Large-Scale Multi-Frequency Capacitive Micromachined Ultrasonic Transducer (CMUT) Arrays for Ultrasound Medical Imaging and Therapeutic Applications

by

Mohammad Maadi

A thesis submitted in partial fulfillment of the requirements for the degree of

Doctor of Philosophy

in

Microsystems and Nanodevices

Department of Electrical and Computer Engineering
University of Alberta

Abstract

Ultrasonic transducers capable of operating over multiple frequency bands could have several interesting medical applications including multi-resolution multi-depth imaging for point-of-care ultrasound, imaging-therapy, super-harmonic contrast agent imaging, super-resolution imaging, image-guided drug delivery, and ultra-wideband ultrasound and photoacoustic imaging. However, multi-frequency arrays are difficult to realize using conventional piezoelectric transducer technology. Here, closely packed interlaced capacitive micromachined ultrasonic transducers (CMUTs) with different membrane sizes are designed to create multi-frequency arrays. CMUTs, compared to their piezoelectric counterparts, are a novel type of ultrasonic transducer that have wider bandwidth, sensitive receive performance, and offer natural integration with electronics. Besides, they do not suffer from self-heating problems which can apply many limitations for piezoelectric transducers. By applying a bias voltage, an electrostatic attraction force occurs between the top and bottom electrodes of the CMUT. The membrane is suspended over the gap until the bias voltage reaches the snap-down value which is named collapse voltage. The resonance frequency is determined by the size and thickness of the membrane. Thus, by interlacing membranes of different sizes, multi-frequency capabilities are realized.

This thesis aims to address unmet needs for multi-frequency ultrasound arrays by comprehensive modeling, fabrication, and testing. Modeling developments include equivalent circuit models for large arrays of membranes, including the interaction of membranes. Previously, the theory for mutual acoustic interactions was developed for similar radiators, but not membranes of different sizes. Following development of analytical expressions for calculating the self- and mutual radiation impedance between dissimilar circular membranes, a fast and precise lumped equivalent circuit model for designing large-scale multi-frequency ultrasound realistic arrays was developed for both circular and square membranes.

We also developed nanofabrication methods for novel multi-frequency CMUT arrays using a modified silicon-nitride sacrificial release process. We showed the feasibility of designed and fabricated multi-frequency arrays for several applications including multi-scale imaging, contrast agent imaging, etc. Aiming to further improve acoustic output, we then developed next-generation large-scale multi-gap multi-frequency CMUT arrays. In these arrays, low-frequency sub-elements have larger gap-sizes to permit a larger range of membrane motion for generating more acoustic power. Compared to low-frequency sub-elements, high-frequency cells are made with smaller gap-sizes to make them more sensitive to echoes coming back from the objects in receive mode. These arrays are designed to increase the acoustic power by a factor of 2-3 times. We additionally propose strategy to increase the acoustic power by applying electrical impedance matching networks to each CMUT element. By transmitting with low-frequencies and receiving nonlinear echoes from microbubble contrast agents with high-frequency sub-arrays, the proposed new technology may have applications for pre-clinical and clinical contrast imaging to permit background-free detection of contrast agents. Such background reduction compared to current methods could prove important for future targeted molecular imaging applications. Other applications of the arrays could include image-guidance with high-frequency sub-arrays and therapeutic modes with low-frequency sub-arrays. Such therapeutic modes could include high-intensity ultrasound based thermal or mechanical ablation, ultrasound-assisted drug release from acoustically-active carriers, and ultrasound-assisted permeabilization of tissues including the blood-brain barrier.

Preface

This thesis is an original work by Mohammad Maadi. Chapters 3 through 10 contain work that has either been published in or submitted to a peer-reviewed journal or conference. These chapters contain minor modifications from the original papers to adhere to the thesis format. The original publication and co-author contributions for each of the thesis chapters is detailed as follows.

Chapter 3 of this thesis has been published as [M. Maadi, R. K. W. Chee, and R. J. Zemp, "Mutual Radiation Impedance for Modeling of Multi-Frequency CMUT Arrays," in Ultrasonics Symposium (IUS), 2015 IEEE International, Taipei, Taiwan, 21-24 Oct. 2015], and [M. Maadi, and R. J. Zemp, "Self and Mutual Radiation Impedances for Modeling of Multi-Frequency CMUT Arrays," IEEE Trans. Ultrason., Ferroelect., Freq. Control, vol. 63, no. 9, pp. 1441–1454, Sept. 2016]. I was responsible for analytical calculations, design, data collection, data analysis, and manuscript composition. R. K. W. Chee contributed to data collection and R. J. Zemp was the supervisory author and was involved with concept formation and manuscript composition.

Chapter 4 of this thesis has been published as [M. Maadi, and R. J. Zemp, "Self and Mutual Radiation Impedances for Modeling of Multi-Frequency CMUT Arrays," IEEE Trans. Ultrason., Ferroelect., Freq. Control, vol. 63, no. 9, pp. 1441–1454, Sept. 2016], and [M. Maadi, and R. J. Zemp, "Modelling of Large-Scale Multi-Frequency CMUT Arrays with Circular Membranes," in Ultrasonics Symposium (IUS), 2016 IEEE International, Tours, France, 18-21 Sept. 2016]. I was responsible for analytical calculations, modelling, design, data collection, data analysis, and manuscript composition. R. J. Zemp was the supervisory author and was involved with concept formation and manuscript composition.

Chapter 5 of this thesis has been prepared by M. Maadi, and R. J. Zemp. I was responsible for design, modifying the process flow, fabrication, characterization, and manuscript composition. R. J. Zemp was the supervisory author and was involved with concept formation and manuscript composition.

Chapter 6 of this thesis has been published as [M. Maadi, and R. J. Zemp, "A Nonlinear Large Signal Equivalent Circuit Model for a Square CMUT Cell," in Ultrasonics Symposium (IUS), 2017 IEEE International, Washington, D.C., USA, 6-9 Sept. 2017], and [M. Maadi, and R. J. Zemp, "A Nonlinear Lumped Equivalent Circuit Model for a Single Un-Collapsed Square CMUT Cell," IEEE Trans. Ultrason., Ferroelect., Freq. Control, vol. 66, no. 8, pp. 1340–1351, Aug. 2019]. I was responsible for analytical calculations, modelling, design, data collection, data analysis, fabrication and characterization of the transducers, and manuscript composition. R. J. Zemp was the supervisory author and was involved with concept formation and manuscript composition.

Chapter 7 of this thesis has been partially published as [M. Maadi, B. Greenlay, C. Ceroici, and R. J. Zemp, "Multi-frequency CMUT imaging arrays for multi-scale imaging and imaging-therapy applications," in Ultrasonics Symposium (IUS), 2017 IEEE International, Washington, D.C., USA, 6-9 Sept. 2017], and the major part of this chapter has been prepared by M. Maadi, C. Ceroici, and R. J. Zemp, "Large-Scale Multi-Frequency CMUT Arrays for Multi-Band Ultrasound Imaging Applications," (Submitted in July 2019). I was responsible for design, modelling, fabrication, and characterization of the transducers, experimental results, data collection, data analysis, and manuscript composition. B. Greenlay designed the interface electronics for imaging and contributed to the fabrication of transducers. C. Ceroici was responsible for ultrasound imaging, and R. J. Zemp was the supervisory author and was involved with concept formation and manuscript composition.

Chapter 8 of this thesis has been published as [M. Maadi, C. Ceroici, and R. J. Zemp, "Electrical Impedace Matching of CMUT Cells," in Ultrasonics Symposium (IUS), 2015 IEEE International, Taipei, Taiwan, 21-24 Oct. 2015]. I was responsible for modelling of transducers, simulation, design, data collection, data analysis, and manuscript composition. C. Ceroici contributed to modelling, and R. J. Zemp was the supervisory author and was involved with concept formation and manuscript composition.

Chapter 9 of this thesis has been prepared by M. Maadi, and R. J. Zemp and presented as a talk in Ultrasonics Symposium (IUS), 2019 IEEE International, Glasgow, Scotland, 6-9 Oct. 2019. I was responsible for design, developing the process flow, fabrication, and characterization. R. J. Zemp was the supervisory author and was involved with concept formation.

Chapter 10 of this thesis has been presented as a talk by M. Maadi, C. Ceroici, T. Kaddoura, and R. J. Zemp, “Microbubble Contrast Agent Imaging Using Multi-Frequency CMUT Arrays,” in Ultrasonics Symposium (IUS), 2018 IEEE International, Kobe, Japan, 22-25 Oct. 2018. I was responsible for design, modelling, fabrication, and characterization of the transducers, experimental results, data collection, data analysis, and conference presentation composition. T. Kaddoura and C. Ceroici were responsible for preparing the code of ultrasound imagining, and R. J. Zemp was the supervisory author and was involved with concept formation and conference presentation composition.

To Leila, my lovely spouse, Nargess, my cute daughter,

and my precious family and friends

Acknowledgement

This work is in part supported by the Natural Sciences and Engineering Research Council of Canada (NSERC CHRPJ 462510, NSERC RGPIN 355544 Zemp), the Canadian Institutes of Health Research (CIHR CPG 134739), nanoBridge, Alberta Innovates Technology Futures, and MITACS (MI MEPF IT04591).

Hereby, I would like to give my best thanks to my Supervisor, Prof. Dr. Roger Zemp for all his support, patience, and encouragement during my PhD. Thank you for guiding me in my growth as an academic and professional. Your passion and ambition in your career have been inspirational and insightful. Thank you for the incredible mentorship you have shown me. I would not be here today without your continued support of my endeavors and interests. I would also like to give my thanks to the members of my supervisory committee, Dr. Manisha Gupta and Dr. Anastasia Elias for guiding me to improve my PhD thesis.

I would also express my gratitude to all of my lab colleagues in Zemp Research Group who helped me a lot by providing a nice research environment. In particular, Benjamin Greenlay, Christopher Ceroici, Tarek Kaddoura, and Ryan Chee.

I would also express my warmest thanks to my parents, family, and my lovely daughter Nargess who helped me emotionally during my life and studies at University of Alberta.

My PhD has been a challenging but rewarding adventure that would not have been the same without the amazing colleagues and friends that have journeyed with me. Thank you to everyone who has been a part of this period in my life in any way. Your companionship and interactions, big or small, have helped shape me and brighten my life.

Above all I would like to give my special thanks to my wife Leila for her love and constant support, for all the late nights and early mornings, for all the moments I left her alone to work on my research, and for keeping me sane over the past few years. Thank you for making my dreams and occupying my heart. Thank you for being a great mother for our pretty and cute daughter Nargess. But most of all, thank you for being my best friend. I owe you everything.

Contents

List of Figures

FIGURES

List of Tables

TABLES

Chapter 1

Introduction

1.1 Motivation for Multi-Frequency Transducers

This thesis concerns design, modelling, fabrication, and testing of multi-frequency capacitive micromachined ultrasonic transducers (CMUTs). Most commercially available ultrasound transducers are piezoelectric and operate around frequencies specified by the thickness of the piezoelectric material. However, they are not suitable for operating in multiple distinct frequency bands [1]. Multi-frequency transducers may have applications on several areas. For example, emerging handheld and wireless probes could prove to be a disruptive technology for point of care imaging but current transducer technology requires separate probes for separate clinical applications [2]. Proposed multi-frequency transducers could eventually replace such multiple probes with a single multi-use system. This is because low-frequencies of ultrasound penetrate tissues much deeper than higher-frequencies but provide coarser spatial resolution. The demand for portable handheld ultrasound is enormous with a multi-billion-dollar market. The ability to use a single probe for whole body imaging could prove to be strategically very important for emerging portable ultrasound markets.

A second possible application of multi-frequency transducers may be microbubble contrast agent imaging. Currently, microbubbles are used as vascular contrast agents which scatter ultrasound more than blood [3]. However, it is sometimes difficult to differentiate microbubble signatures from background tissues. While this is not a significant problem for imaging blood flow in large vessels, imaging microbubble in the microcirculation is less discriminative. This is especially true for imaging targeted contrast imaging applications where microbubbles are conjugated with targeting molecules and where targeted microbubbles adhere to vascular endothelial markers. In this case, microbubbles are not moving relative to the tissue. Nonlinear imaging strategies such as harmonic imaging, pulse-inversion harmonic imaging, and amplitude modulation aim to exploit the strong nonlinearity of microbubble oscillations to differentiate bubbles from tissues [4]. However, nonlinear ultrasound propagation creates tissue contrast that competes with microbubble contrasts. Emerging superharmonic contrast strategies transmit at low-frequencies and receive at high-frequencies, where tissue harmonics are negligible [5], [6]. Such strategies have shown superior contrast-to-background ratios. However, the transducer technology for such an application is immature, with most studies performed using single elements and annular array mechanically scanned transducers. Our proposed multi-frequency arrays could provide superharmonic imaging capabilities without mechanical scanning requirements and may enable future real-time targeted molecular imaging clinical applications.

Additional applications of multi-frequency arrays may include imaging therapy applications. For example, such arrays may enable ultrasound image-guided high intensity focused ultrasound (HIFU) treatment [7]. Here, low-frequencies are typically used for tissue heating and ablation while high-frequency arrays are need for high-resolution imaging.

This thesis concerns the design, modeling, fabrication, and testing of multi-frequency CMUT arrays to address some of the applications noted above. A number of challenges to this objective needed to be overcome. These included lack of accurate analytic and computational models for CMUTs with differing membrane sizes, complex array design, and challenging fabrication. Challenges also included achieving reliable device performance and challenges in obtaining sufficiently high output powers. This thesis directly works to address these challenges to realize practical multi-frequency arrays for next-generation ultrasound applications. A summary of some of these challenges is discussed next.

1.1.1 Multi-Frequency CMUT Design and Simulation

A realistic CMUT array consists of many single transducers interacting with each other. For design and fabrication of CMUT arrays we need a fast and precise model for instantaneous static and dynamic analysis to obtain the design parameters of CMUT cells and arrays including the thickness and size of the membranes, effective gap height, snap-down voltage, insulator thickness, element width, pitch and kerf sizes. Although the finite element method (FEM) is a powerful technique for the analysis of the CMUT cells, it only can be utilized for the arrays with very low number of cells and it is practically impossible to analyze large arrays. Lumped element equivalent circuit models aim to analyze the behavior of the full array using the knowledge of the self and mutual acoustic impedances. In this method, each CMUT element is modeled as a circuit with electrical components and impedance matrix is used to model the interactions between the CMUT cells. However, FEM is still used for validating of developed circuit models. It can be deduced that three ports including electrical, mechanical and acoustical are needed together to model the CMUT completely and accurately. The circuit parameters depend on the shape, size of the membrane, specification of the CMUT and the medium. Orcad PSpice or Advanced Design System (ADS) programs can be used for simulation of the CMUT arrays however, ADS is mostly preferred because of its capability in modeling of the frequency dependent problems. Koymen et al. were provided an improved large signal equivalent circuit model that can predict the entire behavior of a circular CMUT cell in an array [8]. However, we need a model to include both low- and high-frequency CMUT cells with acoustic interactions and such models did not exist prior to this work.

The first challenge for modelling of multi-frequency CMUT arrays was developing a fully comprehensive analytical expression for including the effects of mutual radiation impedance on array designs which is caused by the sound pressure field produced by one cell and exerting a force upon the other transducers. The mutual radiation impedance in multi-frequency CMUT arrays defines the cross-talk between the CMUT cells of dissimilar size. To make the model even faster we should obtain a very precise approximated version of the mutual radiation impedance expressions using polynomial fitting techniques. Then, the approximate and exact expressions should be implemented in an impedance matrix (Z-matrix) and the matrix is integrated with non-linear lumped equivalent circuit models. Three interacting physical ports including electrical, mechanical and acoustic domains must be included precisely in an accurate circuit model of a CMUT cell. Most of previous models assumed the acoustic port only as a resistive load [9], [10].

CMUT arrays have previously been designed and fabricated using different membrane shapes including circular [11], square [12]-[14], hexagonal [15], etc. CMUTs with square membranes have been widely used and make better use of active wafer real-estate compared to transducers with circular membranes. However, the lumped equivalent circuit modeling of these devices is more complex, and most of previous work focused on finite element analysis (FEA), which is time-consuming and practically intractable for large CMUT arrays. For designing and fabrication of CMUT arrays with square membranes, we need a precise and fast equivalent circuit model which is based on accurate approximations of membrane deflection and velocity profiles as well as self-radiation impedance, for which there are no known analytical closed-form solutions [16]. Work in this thesis address both models of square membranes and models of circular membranes of different sizes.

1.1.2 Multi-Frequency CMUT Fabrication and Characterization

Our group pioneered multi-frequency CMUT arrays with square membranes [17], which were outsourced, however, as there was no in-house process for fabricating such arrays. Moreover, with progress in modeling and optimization, we needed a way to fabricate optimized arrays and compare them with models. We developed custom process flows for in-house fabrication of large-scale multi-frequency and multi-gap multi-frequency CMUT arrays with modifications in the fabrication process. Multi-frequency CMUT arrays can be fabricated using sacrificial release [18] or wafer-bonding processes [19]. In the sacrificial release process, a vacuum gap is formed under a suspended membrane, while in wafer-bonding process, a prime wafer is bonded to a SOI (silicon on insulator) wafer after making the cavities on the prime wafer. We focused on sacrificial release-based fabrication process flow because it allows more control over each step with high yields. These are three challenges, to make such a complicated device in a research-based facility is the large number of steps needed, need for tight control over film thicknesses, and dangers of process failure due to over-etching etc. To overcome these challenges, significant work was needed to calibrate each system and to monitor each process step. For fabrication of our arrays, we need to perform 6-7 steps of lithography with almost 50 fabrication steps. The alignments in each lithography step were critical.

Adapting and developing the process technologies for fabrication of large-scale multi-frequency and multi-gap multi-frequency CMUT arrays with high yields allows our research group to fabricate these devices in-house with more flexibility and control over every step at low cost. Moreover, it accelerates the fabrication of new multi-frequency devices for different applications by minimizing the process defects.

1.2 Major Contributions

Chapters 3 to 10 consist of research done during the course of this thesis, some of which have been published, submitted or under-submission in peer-reviewed scientific journals. The major contributions for chapters 3 to 10 are described as follows. Co-author contributions have previously been described in the preface. The following only describes the novelty and impact of each publication.

Chapters 3 and 4. M. Maadi, and R. J. Zemp, "Self and Mutual Radiation Impedances for Modeling of Multi-Frequency CMUT Arrays," *IEEE Transactions on Ultrasonics, Ferroelectrics, and Frequency Control*, vol. 63, no. 9, pp. 1441–1454, Sept. 2016.

Multi-frequency capacitive micromachined ultrasonic transducers (CMUTs) consist of interlaced large and small membranes for multiband operation. In modeling these devices, accurate and computationally efficient methods are required for computing self- and mutual-acoustic-radiation impedances. However, most previous works considered mutual-acoustic impedance between radiators of identical size. A need was thus found to revisit the fundamental framework for mutual-acoustic impedance for its applicability to radiators, especially flexural disks, of differing size. The Bouwkamp integral method is used to achieve infinite series expressions for self- and mutual-acoustic radiation impedances. Polynomial-fitting-based approximate relations of the mutual-acoustic impedance are developed for arbitrary array geometries and are in good agreement with exact expressions. The derived mutual-acoustic impedance is incorporated into equivalent circuit models of multi-frequency CMUTs showing excellent agreement with finite element modeling. The results demonstrate that mutual-acoustic interactions significantly impact device performance. The framework presented here may prove valuable for future design of multi-frequency arrays for novel multiscale imaging, superharmonic contrast imaging, and image therapy applications.

Chapters 5 and 6. M. Maadi, and R. J. Zemp, "A Nonlinear Lumped Equivalent Circuit Model for a Single Un-Collapsed Square CMUT Cell," *IEEE Transactions on Ultrasonics, Ferroelectrics, and Frequency Control*, vol. 66, no. 8, pp. 1340-1351, Aug. 2019.

An accurate nonlinear lumped equivalent circuit model is used for modeling of capacitive micromachined ultrasonic transducers (CMUTs). Finite-element analysis (FEA) is a powerful tool for the analysis of CMUT arrays with a small number of cells while with the harmonic balance (HB) analysis of the lumped equivalent circuit model, the entire behavior of a large-scale arbitrary CMUT array can be modeled in a very short time. Recently, an accurate nonlinear equivalent circuit model for uncollapsed single circular CMUT cells has been developed. However, the need for an accurate large-signal circuit model for CMUT cells with square membranes motivated us to produce a new nonlinear large-signal equivalent circuit model for uncollapsed CMUT cells. In this paper, using analytical calculations and FEA as the tuning tool, a precise large signal equivalent circuit model of square CMUT dynamics was developed and showed excellent agreement with finite-element modeling (FEM) results. Then, different CMUT single cells with square and circular membranes were fabricated using a standard sacrificial release process. Model predictions of resonance frequencies and displacements closely matched experimental Vibrometer measurements. The framework presented here may prove valuable for future design and modeling of CMUT arrays with square membranes for ultrasound imaging and therapy applications.

Chapter 7. M. Maadi, C. Ceroici, and R. J. Zemp, "Large-Scale Multi-Frequency CMUT Arrays for Multi-Band Ultrasound Imaging Applications," *IEEE Transactions on Ultrasonics, Ferroelectrics, and Frequency Control*, (Submitted in July 2019).

Multi-frequency Capacitive Micromachined Ultrasonic Transducers (CMUTs) are introduced for multi-scale imaging applications, where a single array transducer can be used for both deep low-resolution imaging and shallow high-resolution imaging. These transducers consist of low- and high-frequency membranes interlaced within each sub-array element. They are fabricated using a modified sacrificial release process. Successful performance is demonstrated using wafer-level Vibrometer testing, as well as acoustic testing on wirebonded dies consisting of arrays of 2- and 9-MHz elements of up to 64 elements for each sub-array. The arrays are demonstrated to provide multi-scale, multi-resolution imaging using wire phantoms.

Chapters 8, 9, and 10. M. Maadi, C. Ceroici, and R. J. Zemp, "Microbubble Contrast Agent Imaging Using Multi-Frequency CMUT Arrays," *IEEE Transactions on Ultrasonics, Ferroelectrics, and Frequency Control*, (Under-submission).

Ultrasonic transducers capable of operating over multiple frequency bands could have several interesting medical applications including imaging-therapy, super-harmonic contrast agent imaging, super-resolution imaging, image-guided drug delivery, and ultra-wideband ultrasound and photoacoustic imaging. Recently we introduced CMUT-based large-scale multi-frequency transducers for multi-scale imaging applications. These arrays can be used for microbubble contrast agent imaging applications in which low-frequencies are typically needed in transmission, while higher-frequencies are required in receive mode. Nonlinear micron-scale gas-scored agents strongly scatter ultrasound to enhance the contrast in the body. Pulse inversion or amplitude modulation techniques may be used to reject the signal coming back from linear scatterers. The contrast agent imaging can be improved even more by design and fabricating of next-generation of multi-frequency CMUT arrays with different gap sizes for large and small membranes. In these arrays the low-frequency membranes have larger gap sizes compared to high-frequency cells to drive them harder to generate more acoustic power. Electrical impedance matching networks along with acoustic lens can be utilized to increase the acoustic power even more.

1.3 Organization of Thesis

Chapter 2 contains background information and references to previous works which is necessary for understanding the research done in this thesis. First, it provides an overview of capacitive micromachined ultrasonic transducers (CMUTs) and then focuses on previously designed and fabricated multi-frequency ultrasonic arrays for different applications. Chapter 3 demonstrates the self- and mutual radiation impedance analytical and comprehensive calculations for design and modeling of large-scale multi-frequency CMUT arrays. Chapter 4 discusses the implementation of obtained expressions on developed nonlinear lumped equivalent circuit model to show the feasibility of developed model for designing large-scale multi-frequency CMUT arrays. Chapter 5 details the fabrication and characterization of large-scale multi-frequency CMUT arrays using a modified standard sacrificial release process. Chapter 6 also illustrates developed nonlinear lumped equivalent circuit model for a single un-collapsed CMUT cell with square membrane. Chapter 7 proves the feasibility of designed and fabricated large-scale multi-frequency CMUT arrays for multi-band ultrasound imaging applications. Chapter 8 contains design and fabrication of electrical impedance matching networks for CMUT arrays to provide more acoustic power. Chapter 9 demonstrates the feasibility of designed and fabricated multi-frequency CMUT arrays for micro-bubble contrast agent imaging applications. Chapter 10 discusses the design, fabrication and characterization of next-generation multi-gap multi-frequency CMUT arrays for generating more acoustic power. Finally, chapter 11 contains a summary of the thesis and future works.

References

[1] D. N. Stephens, D. E. Kruse, A. S. Ergun, S. Barnes, X. M. Lu, and K. W. Ferrara, “Efficient array design for sonotherapy,” *Phys. Med. Biol.*, vol. 53, no. 14, pp. 3943–3969, Jul. 2008.

[2] M. K. Chirala, P. Huynh, J. Ryu, and Y. Kim, “A 128-ch Δ-Σ ADC based mixed signal IC for full digital beamforming Wireless handheld Ultrasound imaging system,” *37th Annual International Conference of the IEEE Engineering in Medicine and Biology Society (EMBC)*, pp. 1339-1342, Milan, 2015.

[3] Mohanty, Kaustav, et al. “Ultrasound multiple scattering with microbubbles can differentiate between tumor and healthy tissue in vivo,” *Physics in Medicine & Biology*, vol. 64, no. 11, May 2019.

[4] H. Hasegawa, H. Tanaka, T. Takezaki and S. Machida, “Amplitude modulated pulse inversion technique for high SNR of tissue harmonic imaging using CMUT,” *IEEE International Ultrasonics Symposium (IUS)*, Washington, DC, 2017.

[5] J. Ma, K. H. Martin, P. A. Dayton, and X. Jiang, “A preliminary engineering design of intravascular dual-frequency transducers for contrast-enhanced acoustic angiography and molecular imaging,” *IEEE Trans Ultrason Ferroelectr Freq Control,* vol. 61, pp. 870-80, May 2014.

[6] B. D. Lindsey, K. H. Martin, P. A. Dayton, J. Ma, Zhuochen Wang, and X. Jiang, “Dual-frequency intravascular ultrasound imaging of microbubble contrast agents: Ex vivo and in vivo demonstration,” *IEEE International Ultrasonics Symposium (IUS)*, Taipei, Taiwan, 2015.

[7] S. Dingjie, et al. “Thrombolysis using multi-frequency high intensity focused ultrasound at MHz range: an in vitro study,” *Physics in Medicine & Biology*, vol. 60, no. 18, Sept. 2015.

[8] H. Koymen, et al. “An Improved Lumped Element Nonlinear Circuit Model for a Circular CMUT Cell”, *IEEE Transactions on Ultrasonics, Ferroelectrics, and Frequency Control*, vol. 59, no.8, pp. 1791-1799, 2012.

[9] I. Ladabaum, X. Jin, H. T. Soh, A. Atalar, and B. T. Khuri-Yakub. “Surface micromachined capacitive ultrasonic transducers,” *IEEE Transactions on Ultrasonics, Ferroelectrics, and Frequency Control*, vol. 45, no. 3, pp.678–690, 1998.

[10] A. Caronti, G. Caliano, A. Iula, and M. Pappalardo. “An accurate model for capacitive micromachined ultrasonic transducers,” *IEEE Transactions on Ultrasonics, Ferroelectrics, and Frequency Control*, vol. 49, no. 2, pp.159–168, 2002.

[11] M. Maadi, and R. J. Zemp, “A Nonlinear Lumped Equivalent Circuit Model for a Single Un-Collapsed Square CMUT Cell,” IEEE Trans. Ultrason., Ferroelect., Freq. Control, vol. 66, no. 8, pp. 1340-1351, Aug. 2019.

[12] B. A. Greenlay, and R. J. Zemp, “Fabrication of Linear Array and Top-Orthogonal-to-Bottom Electrode CMUT Arrays with a Sacrificial Release Process,” *IEEE Trans. Ultrason. Ferroelectr. Freq. Control*, vol. 64, no. 1, pp. 93-107, Jan. 2017.

[13] M. Maadi, R. Chee, and R. J. Zemp, “Mutual radiation impedance for modeling of multi-frequency CMUT arrays,” *IEEE International Ultrasonics Symposium (IUS),* Taipei, pp.1-4, 21-24 Oct. 2015.

[14] M. Maadi, B. Greenlay, C. Ceroici, and R. J. Zemp, “Multi-frequency CMUT imaging arrays for multi-scale imaging and imaging-therapy applications,” *IEEE International Ultrasonics Symposium (IUS)*, Washington, D.C., USA, 6-9 Sept. 2017.

[15] B. Bayram et al., “Dynamic analysis of capacitive micromachined ultrasonic transducers,” *IEEE Trans. Ultrason. Ferroelectr. Freq. Control* , vol. 52, no. 12, pp. 2270-2275, Dec. 2005.

[16] M. F. la Cour, T. L. Christiansen, J. A. Jensen, and E. V. Thomsen, “Electrostatic and small-signal analysis of CMUTs with circular and square anisotropic plates,” *IEEE Trans. Ultrason. Ferroelectr. Freq. Control*, vol. 62, no. 8, pp. 1563-1579, Aug. 2015.

[17] A. Kshirsagar et al. “Multi-frequency CMUT arrays for imaging-therapy applications,” *IEEE International Ultrasonics Symposium (IUS)*, Prague, Czech Republic, 2013.

[18] A. Sampaleanu, P. Zhang, A. Kshirsagar, W. Moussa, and R. J. Zemp, “Top-orthogonal-to-bottom-electrode (TOBE) CMUT arrays for 3-D ultrasound imaging,” *IEEE Trans. Ultrason., Ferroelectr., Freq. Control*, vol. 61, no. 2, pp. 266–276, Feb. 2014.

[19] P. Zhang, G. Fitzpatrick, T. Harrison, W. Moussa, and R. J. Zemp, “Double-SOI wafer-bonded CMUTs with improved electrical safety and minimal roughness of dielectric and electrode surfaces,” *J. Microelectromech. Syst.*, vol. 21, no. 3, pp. 668–680, Jun. 2012.

Chapter 2

Background

2.1 Ultrasound Transducers

The audible range of human hearing is roughly between 20 Hz - 20 kHz. Any frequencies greater than the higher limit of that range ($> 20\ kHz$) is called ultrasound. Ultrasound is used for a variety of applications including medical imaging or sonography and therapeutic, non-destructive testing of products and structures, detecting invisible flaws (e.g. oil pipes), cleaning, mixing, and accelerating chemical processes (e.g. removing of baked photoresist in acetone), and detecting the obstacles and distance measurements in automobile industries. For medical ultrasound applications in diagnostic radiology, transducers with frequencies between 2 to 15 MHz are normally used. Higher frequency transducers are used for the superficial body structures since they have lower wavelengths and attenuate faster. However, low-frequency transducers are used for deeper imaging applications since they have longer wavelengths. Medical ultrasound transducers contain more than one operating frequency. Fig. 2.1 summarizes the resonance frequencies of typical ultrasound transducers for different medical applications.

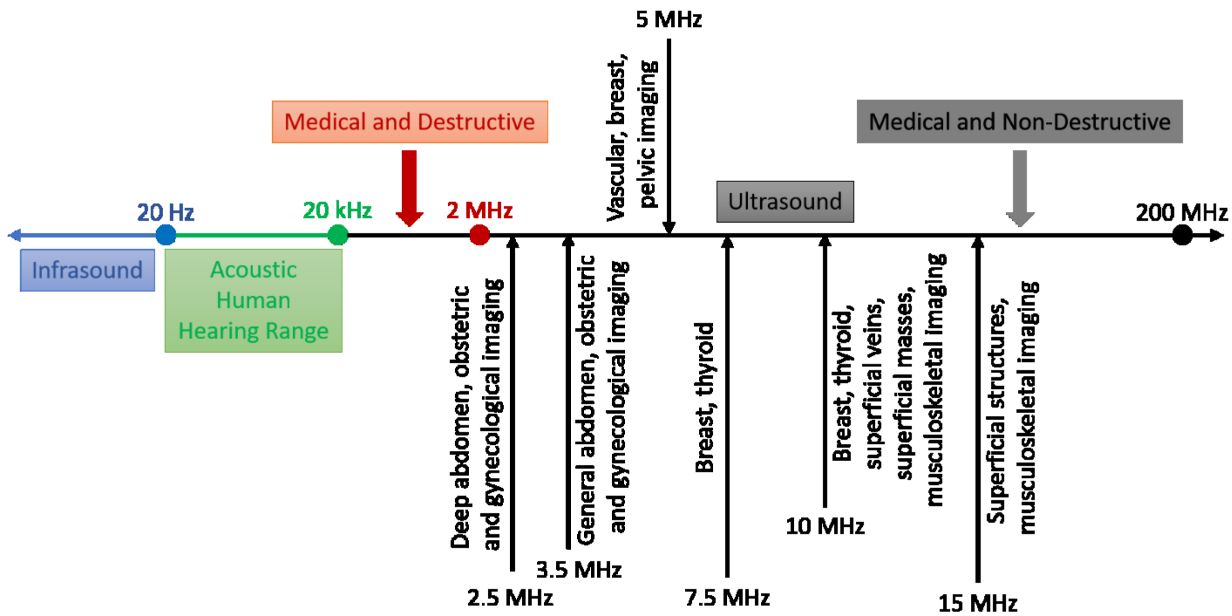

Fig. 2.1. Ultrasound frequencies for different medical applications.

Microelectromechanical Systems (MEMS) have found great commercial success in multiple industries and research areas. Here we provide background and literature review on MEMS-based ultrasound transducers. These primarily include piezoelectric micromachined transducers (PMUTs) and capacitive micromachined ultrasound transducers (CMUTs).

2.2 Micromachined Ultrasound Transducers (MUTs)

Micromachined ultrasound transducers (MUTs) enable the fabrication of a large array devices at low cost. In fact, a micromachined ultrasound array is composed of many microscopic ultrasound single elements. Piezoelectric and capacitive ultrasound transducers are the most well-known structures that are used for medical applications. MUTs provide better acoustic coupling, better integration with electronics, and lower fabrication costs [1].

A single micromachined ultrasound transducer is composed of a membrane suspended on heavily doped silicon substrate (Fig. 2.2). The membrane of a MUT is designed and fabricated in various shapes, sizes and with several materials (e.g. Si_3N_4) for different types of applications. By applying a bias voltage between the membrane and the substrate, the membrane is attracted by the electrostatic force toward the substrate [2]. If the transducer is excited using the combination of

AC and DC signals around the resonance frequency of the device, large membrane displacement and then significant acoustic pressure is obtained.

Fig. 2.2. Fundamental schematic of a micromachined ultrasound transducer (MUT).

2.2.1 Piezoelectric Transducers

Piezoelectric transducers operate based on piezoelectricity principle. The front side of the piezoelectric material is covered by metal. When mechanical stress is applied, electrical potential is generated across the material and when these crystals are applied with external electric field, a mechanical strain is produced in the crystals (Fig. 2.3). The direction of the applied stress including compressive and tensile defines the polarity of the produced charges.

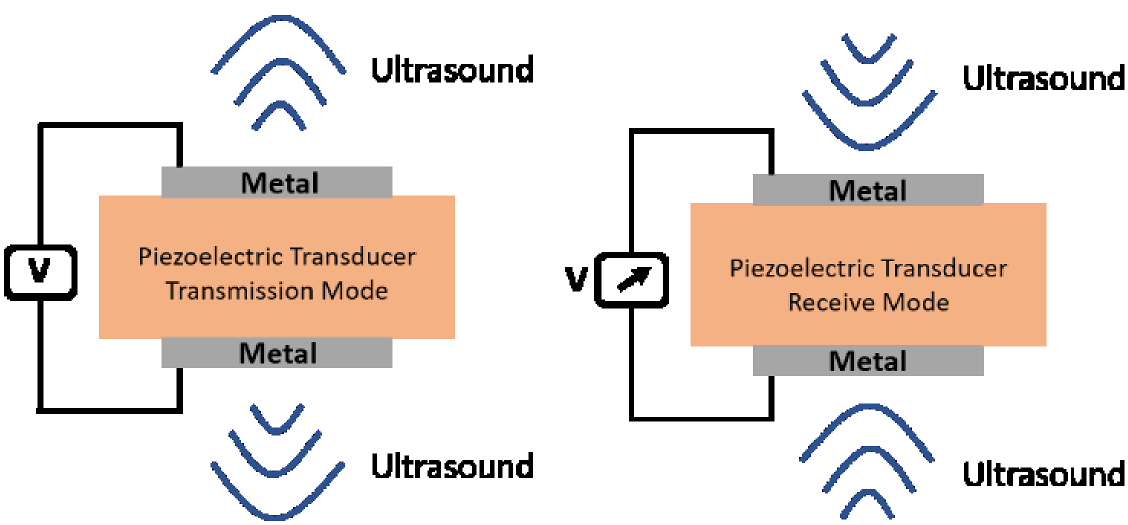

Fig. 2.3. The principle operation of a piezoelectric transducer in transmit and receive modes.

Piezoelectric transducers are inherently narrowband and have several applications including biomedical imaging [3], nondestructive evaluation (NDE) [4], structural health monitoring (SHM) [5], etc. However, for broadband applications such as medical imaging and acoustic emission detection we need to apply acoustic impedance matching networks [6]. The resonance frequency of a piezoelectric transducer is defined by the thickness of the material. To obtain as much energy as possible, an impedance matching layer is needed between the element and the front side of the transducer. Hence, to make a multi-frequency piezoelectric transducer we need materials with different thicknesses and matching layers which make the fabrication of the device challenging.

Ultrasonic transducers can be modelled using finite element method (FEM) and equivalent circuit modeling. The KLM [7], [8], the network [9], [10], and the Butterworth-Van Dyke (BVD) [11] models are the most well-known lumped equivalent circuits for modelling of Piezoelectric transducers. The KLM model is mostly suitable for mechanical designing of the transducer since it works based on physical parameters. On the other hand, both network and BVD models operate based on the input impedance information of the transducer without having any knowledge of the transducer's physical parameters. Fig. 2.4. Demonstrates the BVD model of a single resonance frequency and multi-frequency piezoelectric ultrasound transducer where C_0 is electrical capacitance of the transducer and RLC network defines the mechanical properties of the piezoelectric transducer [6].

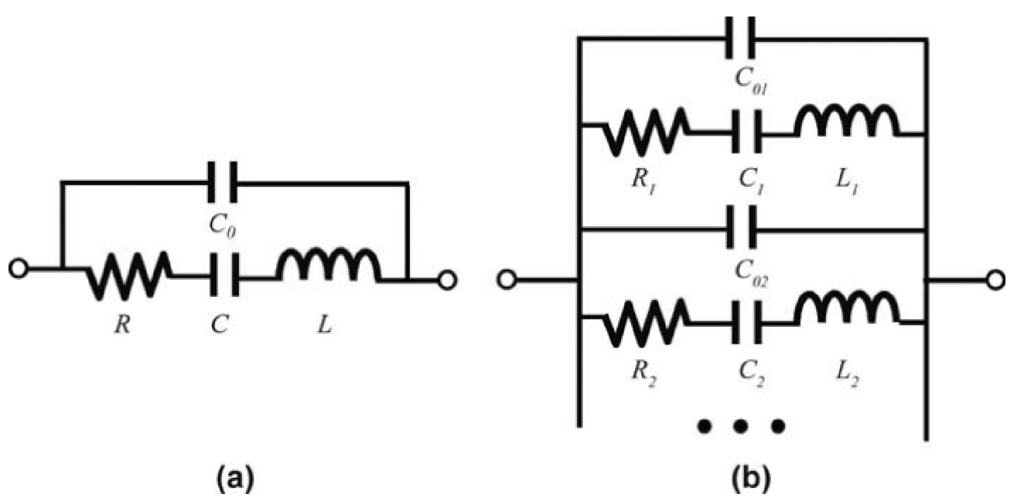

Fig. 2.4. Butterworth-Van Dyke (BVD) model of (a) a single-frequency and (b) multi-frequency piezoelectric ultrasound transducer. © 2011 IEEE.

2.2.2 Piezoelectric Micromachined Ultrasonic Transducers (PMUTs)

PMUTs are MEMS-based piezoelectric ultrasonic transducers which have wider bandwidth, better acoustic coupling with water, reduced voltage requirements, and capability of integration with electronics compared to traditional bulk-PZT thickness-mode piezoelectric ultrasound transducers, particularly for 2D arrays. Moreover, since PMUTs have small sizes, high operational frequencies (e.g. >20 MHz) and low fabrication costs, they can be used for high frequency application instead of conventional bulk-PZT transducers [12]-[14]. Bulk-PZT transducers are based on the thickness-mode motion of a piezoelectric ceramic plate (e.g. PZT). However, PMUTs use the flexural motion of a coupled thin membrane and piezoelectric layer, e.g. Polyvinylidene fluoride (PVDF) [15].

As shown in Fig. 2.5, a PMUT cell consists of a flexural piezoelectric membrane suspended over a gap which can be deformed with an applied electrical excitation [16]. First, an oxide layer is grown on a SOI wafer followed by metal sputtering and patterning. Then PZT material is deposited followed by top-metal sputtering and dry etching of the metal. The PZT is then patterned using wet etching technique. The top oxide and silicon is etched using DRIE until the buried oxide layer. Then, the back oxide is patterned and etched away after pattering the back-silicon using wet etching techniques. More details about the process flow can be found in [16].

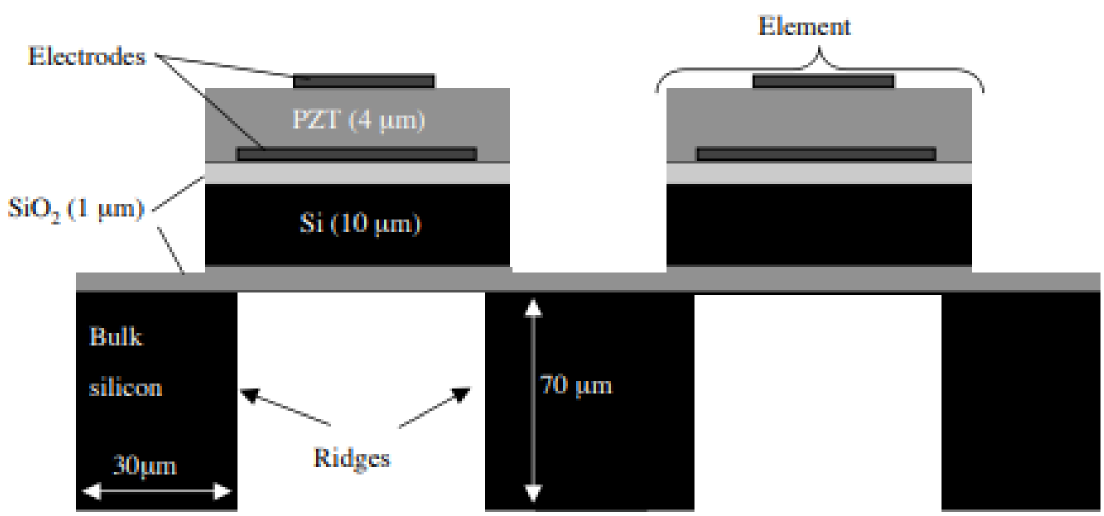

Fig. 2.5. Cross-sectional diagram of a single PMUT on a SOI wafer. © 2006 IEEE.

2.2.3 Capacitive Micromachined Ultrasonic Transducers (CMUTs)

CMUTs are novel types of ultrasound transducers that have wide bandwidth and promising performance. For therapeutic applications, they have the important advantage that they do not suffer from self-heating problems which are a current limitation with piezoelectric transducers. The basic schematic of a CMUT is given in Fig. 2.6. The bottom electrode is fixed without any movement, but the top electrode is a thin flexible and movable plate with the thickness of t_m suspended over a vacuum gap. The membrane of the CMUT is typically made by silicon-nitride or silicon. The radius (a) of the plate (or width L in the case of a square membrane) is on the order of tens of micrometers, the thickness of the membrane (t_m) in the order of microns, and the thickness of the insulator layer (t_i) and gap distances (t_g) in the order of tens to hundreds of nanometers [17]. There is a conductive layer on top of the membrane which enables the electrical excitation of the CMUT. Partial top electrode is used for generating several types of CMUTs with different time dependent capacitances.

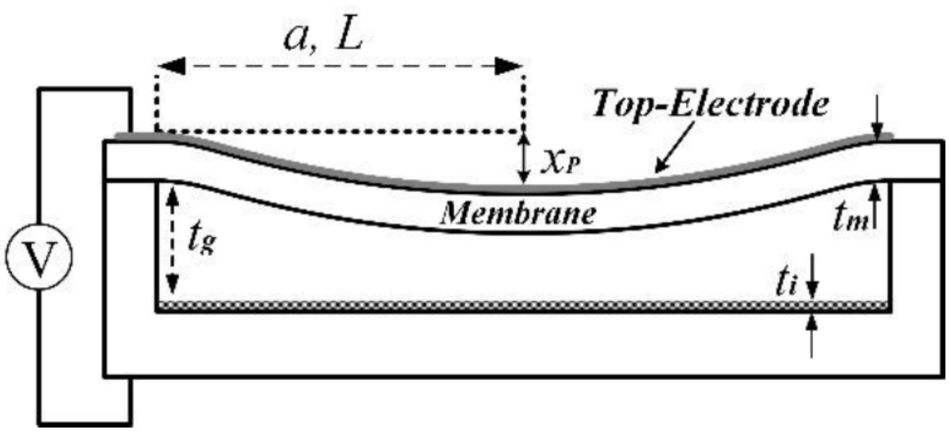

Fig. 2.6. Cross-sectional view of the circular and square CMUT geometry with applied voltage and dimensional parameters.

Three operational modes of CMUTs are conventional, collapsed and collapsed-snapback which are determined by the applied bias voltage. When a DC bias voltage is applied between top and bottom electrodes, the electrostatic force generated by the electric field attracts the movable plate towards the substrate. Due to stiffness of the plate, the mechanical restoring force and electrostatic force cancel each other out at a distance between the electrodes where the movable plate finds its new position. A voltage transient is applied to generate the ultrasound waves. Conversely, if the membrane of a biased CMUT is subjected to ultrasonic waves, an electrical current is generated. The amplitude of the generated signal is a function of the bias voltage, the capacitance of the device and frequency of the incident wave.

When the electrostatic force overcomes the restoring mechanical force, the membrane will collapse onto the substrate which happens at a specific DC voltage and is called the snap-down or collapse voltage. The collapse voltage is proportional to the gap height of the cell and should be considered during design and modelling of the array. Due to non-uniformity in fabrication parameters across the wafer, the snap-down voltage of each single transducer can be slightly different from the neighboring cells.

CMUT arrays are fabricated using sacrificial release [18] or wafer-bonding process [19]. In sacrificial release process, a cavity is formed under a thin membrane by selectively etching the sacrificial layer. On the other hand, in wafer-bonding process, first the gaps are formed on a prime wafer and then is bonded to a SOI wafer. More details about the fabrication steps is explained in chapters 5 and 10 and can be found in [20]. Compared to wafer-bonding process, sacrificial release process has poor control over the uniformity and more complexity of the fabrication. However, in sacrificial release process there is more flexibility to make devices with different gap and membrane sizes in a single wafer which is more attractive for our multi-gap multi-frequency applications.

2.3 Electromechanical Modeling of a CMUT

Electromechanical modeling of CMUT arrays is critical for optimizing the performance of the design before fabrication. Three interacting physical ports including electrical, mechanical, and acoustical domains must be included precisely in an accurate model of a CMUT cell. Finite element method (FEM) is a powerful technique for the analysis of the CMUT cells but it only can be utilized for the arrays with a few number of cells and it is practically impossible to analyze large-scale arrays.

Lumped equivalent circuit models aim to analyze the behavior of the full array using the knowledge of the self- radiation impedance and mutual acoustic interactions between CMUT cells through the immersion and air-coupled mediums which is caused by the sound pressure field produced by one CMUT and exerting a force upon the other cells. The radiation impedance, Z, of a radiator is determined by dividing the total radiated power, P, from the transducer by the square of the absolute value of an arbitrary nonzero reference velocity, V [21]. In this method, each CMUT cell is modeled as a circuit with electrical components and the impedance matrix is used to model the interactions between the CMUT cells. The equivalent circuit parameters depend on the deflection profile of the membrane, specification of the CMUT, and the medium. Orcad PSpice or Advanced Design System (ADS) programs can be used for simulation of the CMUT arrays. However, ADS is mostly preferred because of its capability in modeling of the frequency dependent problems. Some previous simplified models only focused on including the electrical and mechanical parameters of a CMUT by assuming the acoustical port as a resistive load [22], [23]. Recently, the exact values of the self- and mutual radiation impedances for the flexural circular disks with the same sizes were analyzed, modeled, and included in the CMUT array simulations [21]. H. Koymen et al. were provided an improvement on a previously designed large signal equivalent circuit models that can predict the entire behavior of a circular CMUT cell [24]. The model is based on the basic geometry of a circular CMUT cell with a partial electrode that is shown in Fig. 2.7.

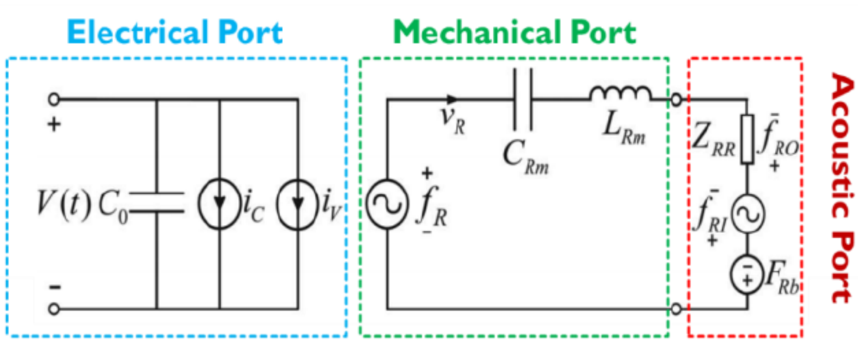

Fig. 2.7. CMUT Large signal equivalent circuit model including three interacting physical domains. © 2012 IEEE.

As given in Fig. 2.7, the large signal equivalent circuit can model three interacting physical domains of the CMUTs in which C_{Rm} and L_{Rm} are the compliance and the mass of the membrane, respectively and the acoustic domain has been included into the model by using Z_{RR} as the radiation impedance of the CMUT cell. For reception operations, small signal model of the CMUT cell can be used by deriving the model from the large signal model. Fig. 2.8 shows the small signal equivalent circuit of the CMUT in which C_{RS} and C_{0d} are the spring softening capacitor and capacitance of the deflected membrane, respectively. More details about the large and small signal equivalent circuit models can be found in [24].

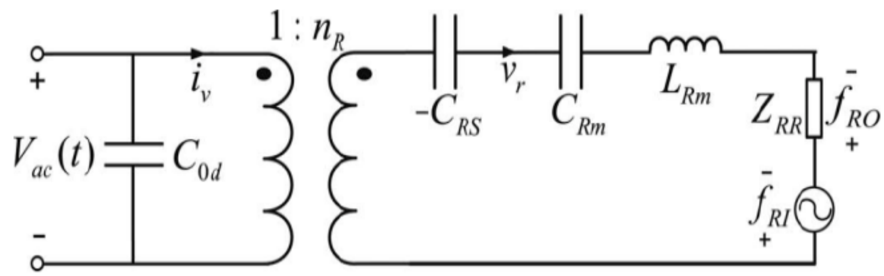

Fig. 2.8. CMUT small signal equivalent circuit model. © 2012 IEEE.

2.4 Multi-Frequency Ultrasound Transducers

Closely packed interlaced CMUTs with different membrane sizes create multi-frequency arrays that would make possible the high-resolution imaging at shallow depths and lower resolution in deeper tissues. In such transducer architectures, flexural membranes of different sizes are interlaced on a scale smaller than the shortest acoustic wavelength to mitigate grating lobe artifacts without sacrificing the resolution. Multi-frequency CMUTs offer broad-band effective fractional bandwidth. Photoacoustic imaging will greatly benefit from ultra-wide bandwidth transducers which are difficult to obtain with traditional piezoelectric transducers. Applications for such emerging transducer technology may include image-guided high-intensity focused ultrasound therapy [25]–[27], multiband photoacoustic imaging [28], [29], and novel microbubble contrast agent imaging techniques including super-harmonic imaging (involving transmission of low frequencies and receiving high frequencies for exceptional contrast-to-tissue ratios) [30]–[32], tissue harmonic imaging [33], [34], image-guided drug delivery [35]–[37], nanodroplet phase-change imaging methods [38], image-guided ultrasound-aided biomarker and extracellular vesicle release [39], [40], multiscale multiresolution imaging [41], and other unique applications [42]. Furthermore, multi-frequency arrays can be used to make portable wireless probes for multiple applications. Portable handheld pocket-sized ultrasound scanners could have a major impact in point-of-care medical imaging for both specialists and non-specialists. However, for use in multiple clinical applications, ultrasound transducers of different frequencies are typically needed to address different depth and resolution scales. To enable a portable ultrasound unit with broad applications, we propose novel multi-frequency ultrasound array technology. Traditionally, ultrasound arrays are manufactured from piezoelectric materials, which operate around a fixed frequency band. In contrast, we introduce MEMS-based ultrasound transducers consisting of interlaced membranes of different sizes. Large membranes are similar to low-pitched drums, whereas small membranes produce higher frequencies. This technology thus enables high-quality ultrasound scans at different operating frequencies and depths. This technology also has applications to emerging imaging-therapy and contrast-agent imaging systems. In modeling multi-frequency devices, accurate and computationally efficient methods are required for computing self- and mutual-acoustic-radiation impedances. However, most previous works considered mutual-acoustic impedance between radiators of identical size. A need was thus found to revisit the fundamental framework for mutual-acoustic impedance for its applicability to radiators, especially flexural disks, of differing size.

Several kinds of ultrasonic transducers have recently been provided for multi-frequency ultrasound imaging applications. In 2013, Guiroy et al. have demonstrated a mechanically-scanned transducer with two elements operating at resonance frequencies of 4 MHz and 14 MHz [32]. Similarly, as shown in Fig. 2.9, two active layers were mechanically bonded in series and poled in opposite directions to form a micromachined PMN-PT 1–3 composite based multi-frequency transducer, operating at 17.5 and 35 MHz for harmonic imaging applications [43]. Due manufacturing challenges, PZT materials have limitations for being used at high frequencies, hence PMN-PT materials have been increasingly utilized over PZT traditional ceramics. In this design, for generating f_0 as the first resonance frequency, both active layers are electrically connected in parallel and are excited by the same signal for behaving as a single active element and during receiving the ultrasound wave, the front layer receive most of the signal with a resonance frequency of $2f_0$ (twice the transmission frequency), because the thickness of the active layer has been divided into two parts.

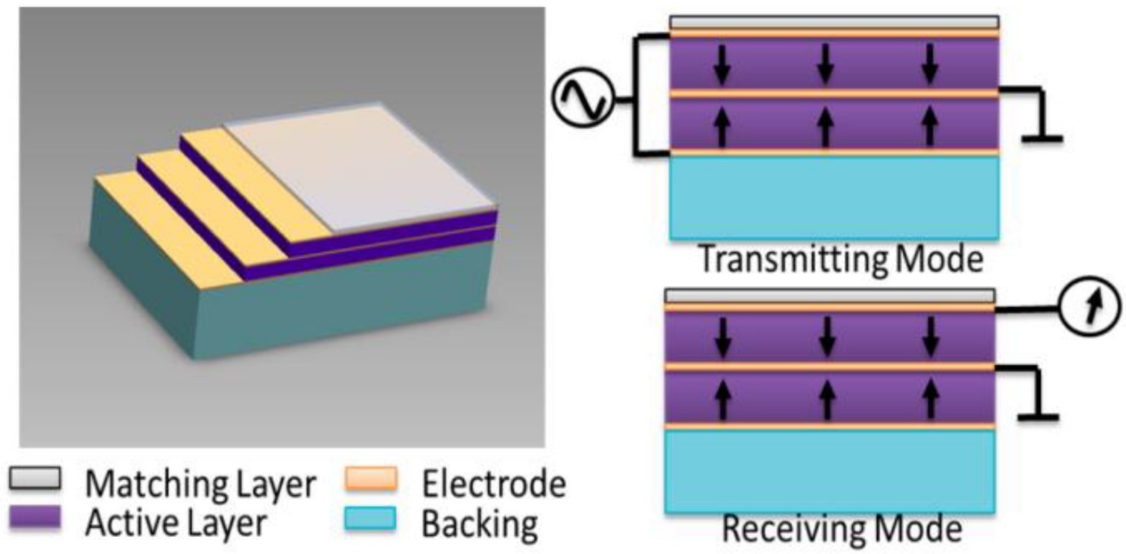

Fig. 2.9. (Left) Schematic of the multi-layer, multi-frequency transducer. (Right) the operation of the device for transmission and receive. © 2013 IEEE.

Jiang's group presented the multi-frequency intravascular ultrasound (IVUS) piezoelectric transducer designed for super-harmonic imaging applications (Fig. 2.10). This device was designed for providing the beams with co-aligned transmit and receive signals operating at resonance frequencies of 6.5 MHz and 30 MHz [44]. The contrast of intravascular ultrasound imaging has been enhanced with microbubbles in phantom. The dual-frequency design helps to minimize the detected tissue backscatter.

The ultrasound imaging technology has affected the field of molecular science by achieving an admirable progress during past decades with the development of the contrast agents [45]. By the combination of ultrasound imaging technology and specific contrast agents, targeted ultrasound techniques would be able to assess the molecular or genetic signatures for diseases. Targeted ultrasound contrast agents have proved some advantages compared with traditional blood pool agents including earlier detection and characterization of disease, higher sensitivity and specificity compared with non-targeted contrast agents. Due to the relatively small impedance differences between red blood cells and plasma, the blood is two to three orders of magnitude less echogenic than tissue. Therefore, for detecting the echoes from capillaries, a contrast agent is needed.

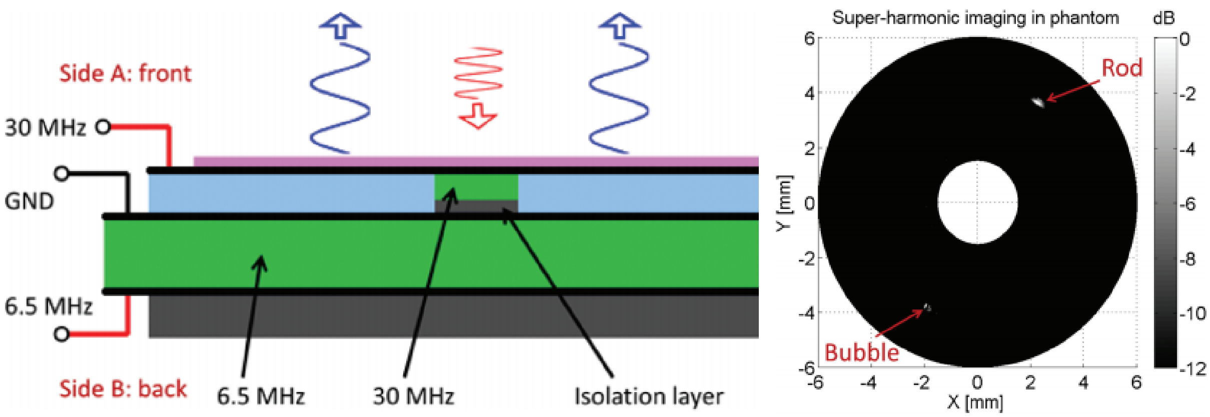

Fig. 2.10. Multi-frequency intravascular ultrasound (IVUS) transducer for super-harmonic imaging. © 2014 IEEE.

In acoustic angiography, as a new high-frequency contrast agent imaging technique [46], the microbubbles are excited near resonance frequency and the high-frequency signal is detected with sufficient bandwidth separation. Using this technique, both high resolution and high contrast to noise ratio (CNR) can be achieved. The traditional contrast imaging techniques are not effective anymore because they only employ the high frequency (35 to 50 MHz) transducers while the nonlinear detection strategies for contrast agent imaging are most effective near the resonance frequency of microbubbles contrast agents (1 to 10 MHz) [47]. In fact, the resolution and CTR can be further improved only if the microbubbles are excited near resonance frequencies and the receive signal is detected at least three times higher than the transmit center frequency [48]. This technique is called super-harmonic, ultra-broadband, or transient imaging which has admirable advantages over sub-harmonic or harmonic contrast intravascular ultrasound (IVUS).

Multi-frequency technique demonstrates its capabilities to detect contrast agents in 200 μm vessels in ex vivo using porcine arteries and vessels with diameters smaller than 200 μm in vivo without using multiple pulses. 3D rendering of vessel networks of chicken embryo vasculature was obtained by performing maximum intensity projections on volumetric datasets (Fig. 2.11) [49].

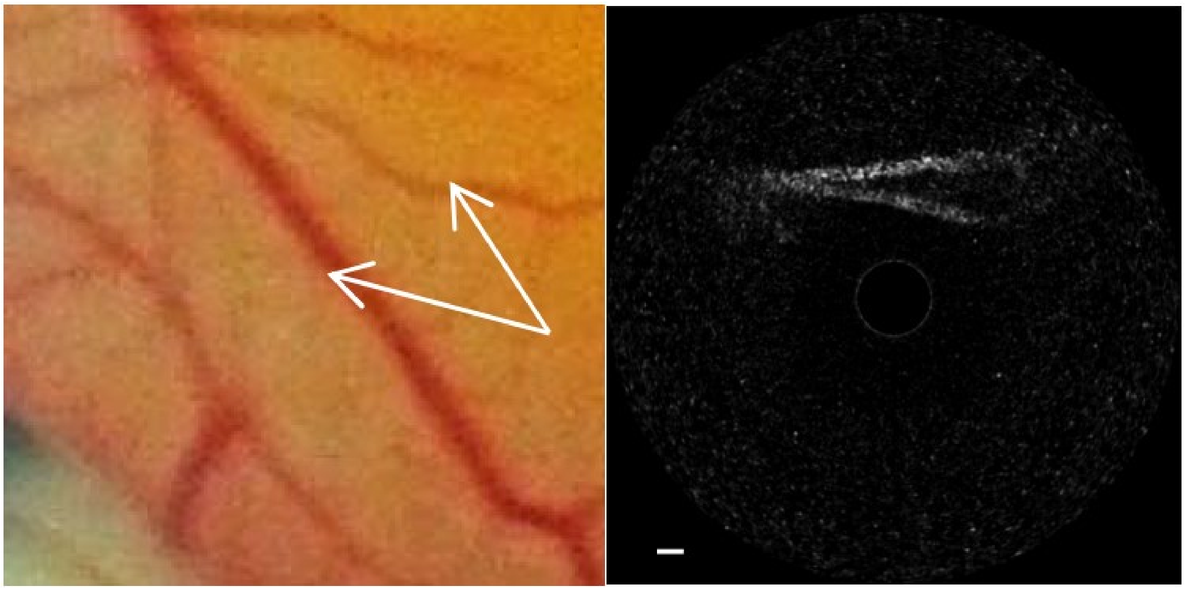

Fig. 2.11. (Left) Optical photograph (arrows indicate vessels of interest) and (Right) dual-frequency images of microvasculature in the CAM in a chicken embryo. Scale bar indicates 1 mm. © 2015 IEEE.

Lindsey et al presented an alternative strategy for ultrasound molecular imaging based on super-harmonic signals produced by microbubbles [50]. The contrast agents were excited near the low resonance frequency (4 MHz) and the super-harmonic echoes were received at a much higher frequency (30 MHz). Multi-frequency super-harmonic imaging can be partially destructive to microbubbles [51]. Since the focal spot is larger for the low-frequency transducers than the high frequency elements, this makes some challenges in implementation of the super-harmonic molecular imaging. However, the super-harmonic echoes can be produced in response to multiple pulses, if the microbubbles are the same [51], [52]. Fig. 2.12 demonstrates the high-resolution imaging of the microbubbles targeted to the $\alpha_v\beta_3$ integrin in an implanted rat fibrosarcoma using an imaging technique which forms images using only the super-harmonic echoes of microbubbles. Acoustic angiography image volumes, as a reference for vascular structure, superimposed images of bound microbubbles which persisted sufficiently long in vivo to allow for the formation of high resolution super-harmonic molecular images. Combined molecular and vascular imaging can be valuable for comparing targeting locations and microvascular anatomy in pre-clinical studies. Additional information on microvascular morphology can be obtained by combining a higher resolution molecular image with a registered angiography-like image.

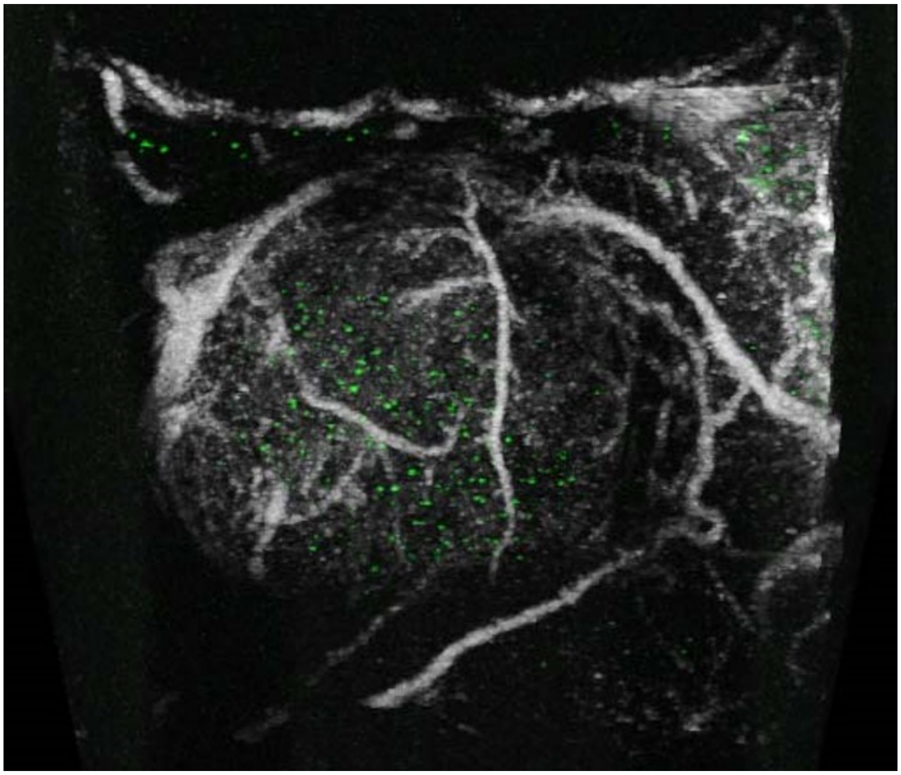

Fig. 2.12. Illustrative acoustic angiography molecular image acquired in an implanted rat fibrosarcoma. $\alpha_v\beta_3$integrin expression is shown in green, microvascular information is shown in white. © 2015 IEEE.

S. Li et al developed a dual-frequency probe consisting of 50 transmission transducers (3 MHz) and 100 receiving elements (18 MHz) for real-time contrast imaging or super-harmonic imaging of microbubbles ("acoustic angiography") for prostate cancer assessment using a multi-channel imaging system [53].

The resonance frequency of piezoelectric transducers is defined by the thickness of the material which makes it difficult to interlace several frequencies. In addition, different impedance matching layers are needed for different frequencies. On the other hand, the resonance frequency of CMUTs are simply defined by the size and thickness of the membrane. Moreover, CMUT arrays have demonstrated better performance compared to piezoelectric transducers but there still have not been many works for multi-frequency application. Eames et al. [54] demonstrated the feasibility of implementing partial-height stand-off structures within the device vacuum-gap that divide the device membrane into smaller sub-membranes in collapse mode to generate high-frequency ultrasound signals (Fig. 2.13). However, CMUTs do not stand for a long time in collapse mode and may stop working permanently.

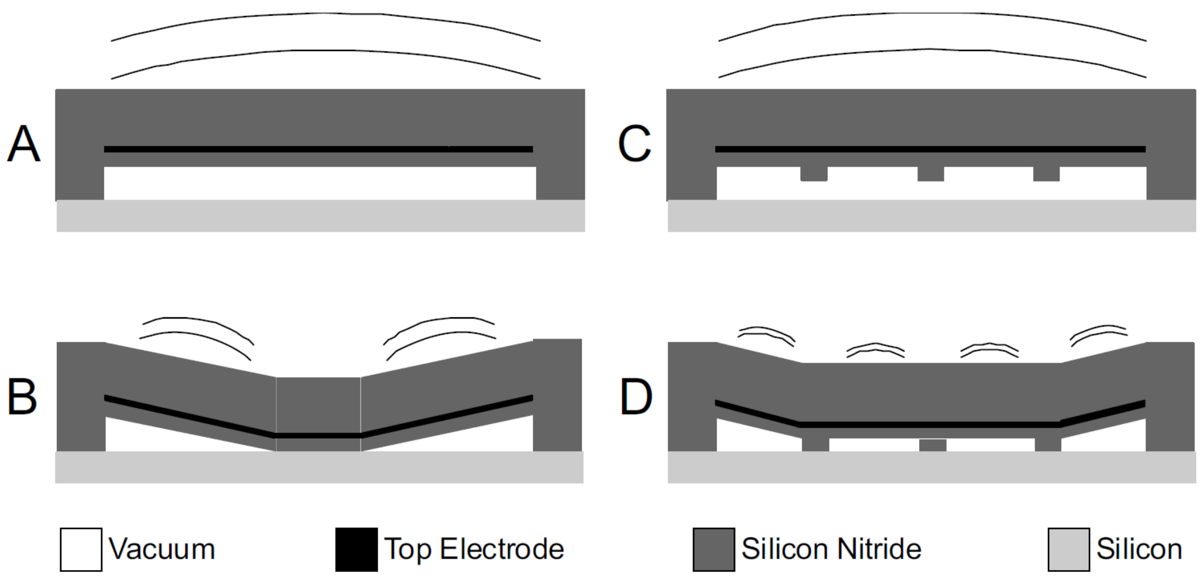

Fig. 2.13. (A) Conventional CMUT in un-collapse mode configuration to generate low-frequency signals, (B) Conventional CMUT in collapse mode to generate high-frequency signals, (C) dual-frequency device designed with stand-offs operating at low-frequency, (D) collapsed dual-frequency device operating at high-frequency. © 2010 IEEE.

References

[1] D. A. Horsley et al., "Piezoelectric micromachined ultrasonic transducers in consumer electronics: The next little thing?," *IEEE 29th International Conference on Micro Electro Mechanical Systems (MEMS)*, Shanghai, pp. 145-148, 2016.

[2] I. Ladabaum, B. T. Khuri-Yakub, D. Spoliansky, and M. I. Haller, "Micromachined Ultrasonic Transducers (MUTs)," *IEEE Proce. Ultrason. Symp*, vol. 1, pp. 501–504. Nov. 1995.

[3] R. S. C. Cobbold. (2007). *Foundations of Biomedical Ultrasound*. Oxford University Press, New York.

[4] A. Grandt, *Fundamentals of Structural Integrity*. Hoboken, NJ: Wiley, 2003.

[5] V. Giurgiutiu, *Structural Health Monitoring with Piezoelectric Wafer Active Sensors*. New York, NY: Academic, 2007.

[6] H. Huang and D. Paramo, "Broadband electrical impedance matching for piezoelectric ultrasound transducers," *in IEEE Transactions on Ultrasonics, Ferroelectrics, and Frequency Control*, vol. 58, no. 12, pp. 2699-2707, Dec. 2011.

[7] L. Wu, and Y. Chen, "PSPICE approach for designing the ultrasonic piezoelectric transducer for medical diagnostic applications," *Sens. Actuators A*, vol. 75, no. 2, pp. 186–198, May 1999.

[8] M. Castillo, P. Acevedo, and E. Moreno, "KLM model for lossy piezoelectric transducers," *Ultrasonics*, vol. 41, no. 8, pp. 671–679, Nov. 2003.

[9] D. Callens, C. Bruneel, and J. Assaad, "Matching ultrasonic transducer using two matching layers where one of them is glue," *NDT & E Int.*, vol. 37, no. 8, pp. 591–596, Dec. 2004.

[10] G. R. Lockwood, and F. S. Foster, "Modeling and optimization of high-frequency ultrasound transducers," *IEEE Trans. Ultrason. Ferroelectr. Freq. Control*, vol. 41, no. 2, pp. 225–230, Mar. 1994.

[11] L. Svilainis, V. Dumbrava, and G. Motiejunas, "Optimization of the ultrasonic excitation stage," in *30th Int. Conf. Information Technology Interfaces*, Dubrovnik, Croatia, pp. 791–796, Jun. 2008.

[12] F. Akasheh, T. Myers, J. D. Fraser, S. Bose, and A. Bandyopadhyay, "Development of Piezoelectric Micromachined Ultrasonic Transducers," *Sensors and Actuators A Phys.*, vol. 111, no. 2, pp. 275-287, 2004.

[13] P. Muralt et al., “Piezoelectric Micromachined Ultrasonic Transducers Based on PZT Thin Films,” *IEEE Trans. Ultra. Ferroelectr. Freq. Contr.*, vol. 52, no. 12, pp. 2276-2288, 2005.

[14] Z. H. Wang et al., “Fabrication and Characterization of Piezoelectric Micromachined Ultrasonic Transducers with Thick Composite PZT Films,” *IEEE Trans. Ultra. Ferroelectr. Freq. Contr.*, vol. 52, no. 12, pp. 2289-2297, 2005.

[15] S. Trolier-McKinstry, and P. Muralt, “Thin film piezoelectrics for MEMS,” *Journal of Electroceramics*, vol. 12, no. 1-2, pp. 7-17, 2004.

[16] B. Belgacem, F. Calame and P. Muralt, “Piezoelectric Micromachined Ultrasonic Transducers based on PZT films,” *15th ieee international symposium on the applications of ferroelectrics*, Sunset Beach, NC, pp. 326-331, 2006.

[17] D. R. Chou, “Piezoelectric Micrimachined Ultrasound Transducer for Medical Imaging,” *Ph.D. Thesis*, Duke University, 2011.

[18] A. Sampaleanu, P. Zhang, A. Kshirsagar, W. Moussa, and R. J. Zemp, “Top-orthogonal-to-bottom-electrode (TOBE) CMUT arrays for 3-D ultrasound imaging,” *IEEE Trans. Ultrason., Ferroelectr., Freq. Control*, vol. 61, no. 2, pp. 266–276, Feb. 2014.

[19] P. Zhang, G. Fitzpatrick, T. Harrison, W. Moussa, and R. J. Zemp, “Double-SOI wafer-bonded CMUTs with improved electrical safety and minimal roughness of dielectric and electrode surfaces,” *J. Microelectromech. Syst.*, vol. 21, no. 3, pp. 668–680, Jun. 2012.

[20] B. T. Khuri-Yakub and O. Oralkan, “Capacitive micromachined ultrasonic transducers for medical imaging and therapy,” *J. Micromech. Microeng.*, vol. 21, no. 5, pp. 54004–54014, 2011.

[21] M. N. Senlik, S. Olcum, H. Koymen, and A. Atalar. “Radiation impedance of an array of circular capacitive micromachined ultrasonic transducers,” *IEEE Trans. Ultra. Ferroelectr. Freq. Contr.*, vol. 57. no. 4, pp. 969–976, 2010.

[22] I. Ladabaum, X. Jin, H.T. Soh, A. Atalar, and B.T. Khuri-Yakub, “Surface micromachined capacitive ultrasonic transducers,” *IEEE Trans. Ultra. Ferroelectr. Freq. Contr.*, vol. 45, no. 3, pp. 678–690, 1998.

[23] A. Caronti, G. Caliano, A. Iula, and M. Pappalardo. “An accurate model for capacitive micromachined ultrasonic transducers,” *IEEE Trans. Ultra. Ferroelectr. Freq. Contr.*, vol. 49, no 2, pp.159–168, 2002.

[24] H. Koymen, A. Atalar, E. Aydogdu, C. Kocabas, H.K. Oguz, and S. Olcum, A. Ozgurluk and A. Unlugedik, “An Improved Lumped Element Nonlinear Circuit Model for a Circular CMUT Cell”, *IEEE Transactions on Ultrasonics, Ferroelectrics, and Frequency Control*, vol. 59, no. 8, pp. 1791-1799, 2012.

[25] Y-S. Kim, “Advances in MR imaging-guided high-intensity focused ultrasound therapy,” *Int. J Hyperthermia*. Vol. 31, pp. 225-232, 2015.

[26] M. R. Pfeffer, T. Rabin, Y. Inbar, A. Hananel, and R. Catane, “Image-guided high-intensity focused ultrasound in the treatment of cancer,” *In Image-Guided Cancer Therapy*, Springer, New York, pp. 79-99, 2013.

[27] A. Ranjan et al., “Image-guided drug delivery with magnetic resonance guided high intensity focused ultrasound and temperature sensitive liposomes in a rabbit Vx2 tumor model,” *Journal of controlled release*, vol. 158, pp. 487-494, 2012.

[28] S. P. Gautieri, “Photo-acoustic, multi-band, multi-cavity gas detection system,” *U.S. Patent*, No. 8,806,916. (19 August 2014).

[29] S. Autrey, G. Posakony, J. Amonette, and N. Foster-Mills, “Multi-band transducer for photoacoustic detection,” *U.S. Patent*, No. 20,010,018,848. (6 September 2001).

[30] S. Unnikrishnan, and A. L. Klibanov, “Microbubbles as ultrasound contrast agents for molecular imaging: preparation and application,” *Am. J. Roentgenology*, vol. 199, pp. 292-299, 2012.

[31] V. R. Stewart, and P. S. Sidhu, “New directions in ultrasound: microbubble contrast,” *The British journal of radiology*, vol. 79, pp. 188-194, 2014.

[32] A. Guiroy et al., “Dual frequency transducer for nonlinear contrast agent imaging,” *IEEE Trans. Ultrason. Ferroelectr. Freq. Control*, vol. 60, pp. 2634–2644, 2013.

[33] C. C. Shen, and C. H. Lin, “Chirp-encoded excitation for dual-frequency ultrasound tissue harmonic imaging,” *IEEE Trans. Ultrason. Ferroelectr. Freq. Control*, vol. 59, pp. 2420-2430, 2012.

[34] E. Ohno, H. Kawashima, S. Hashimoto, H. Goto, and Y. Hirooka “Current status of tissue harmonic imaging in endoscopic ultrasonography (EUS) and EUS-elastography in pancreatobiliary diseases,” *Digestive Endoscopy*, vol. 27, pp. 68-73, 2015.

[35] T. Ojha, L. Rizzo, G. Storm, F. Kiessling, and T. Lammers, "Image-guided drug delivery: preclinical applications and clinical translation," *Expert opinion on drug delivery*, vol. 12, pp. 1203-1207, 2015.

[36] M. Thanou, M. Wright, M. Centelles, and W. Gedroyc, "Image guided focused ultrasound delivery of macromolecular drugs in tumours," *Journal of Therapeutic Ultrasound*, vol. 3, pp. 75-76, 2015.

[37] M. Thanou, M. Wright, and M. Centelles, "Nanoparticles for image guided focused ultrasound drug delivery," *Cancer Research*, vol. 74, pp. 5398-5398, 2014.

[38] P. S. Sheeran, J. E. Streeter, L. B. Mullin, T. O. Matsunaga, and P. A. Dayton, "Toward ultrasound molecular imaging with phase-change contrast agents: an in vitro proof of principle," *Ultrasound in medicine and biology*, vol. 39, pp. 893-902, 2013.

[39] S. E. Ahmed, A. M. Martins, and G. A. Husseini, "The use of ultrasound to release chemotherapeutic drugs from micelles and liposomes," *Journal of drug targeting*, vol. 23, pp. 16-42, 2014.

[40] Y. Lin et al., "Application of Molecular Imaging Technologies in Antitumor Drug Development and Therapy," *Current pharmaceutical design*, vol. 21, pp. 2136-2146, 2015.

[41] G. Ku, X. Wang, G. Stoica, and L. V. Wang, "Multiple-bandwidth photoacoustic tomography," *Physics in Medicine and Biology*, vol. 49, pp. 1329–1338, 2004.

[42] K. H. Martin, B. D. Lindsey, J. Ma, M. Lee, S. Li, F. S. Foster, X. Jiang, and P. A. Dayton, "Dual-frequency piezoelectric transducers for contrast enhanced ultrasound imaging," *Sensors*, vol. 14, pp. 20825-20842, 2014.

[43] S. Li, W. Huang, X. Jiang, X. Jian, and Y. A. Cui, "dual-layer micromachined PMN-PT 1–3 composite transducer for broadband ultrasound imaging," *In Proceedings of the 2013 IEEE International Ultrasonics Symposium, Prague, Czech*, vol. 10, pp. 781–784, 21–25 July 2013.

[44] J. Ma, K. Martin, P. A. Dayton, and X. Jiang, "A preliminary engineering design of intravascular dual-frequency transducers for contrast-enhanced acoustic angiography and molecular imaging," *IEEE Trans. Ultrason. Ferroelectr. Freq. Control*, vol. 61, pp. 870–880, 2014.

[45] P. A. Dayton, and K. W. Ferrara. "Targeted imaging using ultrasound," *Journal of magnetic resonance imaging*, vol. 16, no. 4, pp. 362-377, 2002.

[46] R. C. Gessner, C. B. Frederick, F. S. Foster, and P. A. Dayton, “acoustic angiography: a new imaging modality for assessing microvasculature architecture,” *Int. J. Biomed. Imaging*, vol. 2013, art. no. 936593, 2013.

[47] J. d. Kasprzak, B. Paelinck, F. J. Ten cate, W. B. Vletter, n. de Jong, d. Poldermans, a. Elhendy, a. Bouakaz, and J. r. roelandt, “comparison of native and contrast-enhanced harmonic echocardiography for visualization of left ventricular endocardial border,” *Am. J. Cardiol.*, vol. 83, no. 2, pp. 211–217, 1999.

[48] B. D. Lindsey, J. D. Rojas, K. Heath Martin, S. E. Shelton, and P. Dayton, “Acoustic characterization of contrast-to-tissue ratio and axial resolution for dual-frequency contrast-specific acoustic angiography imaging,” *Ultrasonics, Ferroelectrics, and Frequency Control, IEEE Transactions on*, vol. 61, pp. 1668-1687, 2014.

[49] Lindsey, Brooks D.; Martin, K.Heath; Dayton, Paul A.; Ma, Jianguo; Zhuochen Wang; Jiang, Xiaoning, “Dual-frequency intravascular ultrasound imaging of microbubble contrast agents: Ex vivo and in vivo demonstration,” *in Ultrasonics Symposium (IUS)*, pp.1-4, 21-24 Oct. 2015.

[50] Lindsey, Brooks D.; Shelton, Sarah E.; Tsuruta, James K.; Dayton, Paul A.; Foster, F.Stuart, “Molecular acoustic angiography: Demonstration of in vivo feasibility for high resolution superharmonic ultrasound molecular imaging,” *in Ultrasonics Symposium (IUS)*, pp.1-3, 21-24 Oct. 2015.

[51] B. D. Lindsey, J. D. Rojas, and P. A. Dayton, “On the Relationship between Microbubble Fragmentation, Deflation and Broadband Superharmonic Signal Production,” *Ultrasound Med Biol*, vol. 41, pp. 171125, 2015.

[52] D. E. Kruse and K. W. Ferrara, “A new imaging strategy using wideband transient response of ultrasound contrast agents,” *IEEE Transactions on Ultrasonics Ferroelectrics and Frequency Control*, vol. 52, pp. 1320-1329, Aug. 2005.

[53] Li, Sibo; Kim, Jinwook; Zhuochen Wang; Jiang, Xiaoning; Kasoji, Sunny; Lindsey, Brooks; Dayton, Paul A., “A 3 MHz/18 MHz dual-layer co-linear array for transrectal acoustic angiography,” *in Ultrasonics Symposium (IUS)*, pp.1-4, 21-24 Oct. 2015.

[54] M. D. C. Eames, T. J. Reck, and J. A. Hossack, “Selectable frequency CMUT with membrane stand-off structures,” *IEEE International Ultrasonics Symposium*, pp. 2814-2817, 2009.

Chapter 3

Self and Mutual Radiation Impedances for Multi-Frequency CMUT Arrays

In modeling multi-frequency CMUT arrays, accurate and computationally efficient methods are required for computing self- and mutual-acoustic-radiation impedances. However, most previous works considered mutual-acoustic impedance between radiators of identical size. A need was thus found to revisit the fundamental framework for mutual-acoustic impedance for its applicability to radiators, especially flexural disks, of differing size. The framework presented here may prove valuable for future design of multi-frequency arrays for novel multi-scale imaging, super-harmonic contrast imaging, and image therapy applications. The comprehensive analytical calculation of self- and mutual radiation impedance for the flexural disks with dissimilar sizes is summarized by Maadi et al. in the published journal paper titled “Self and Mutual Radiation Impedances for Modeling of Multi-Frequency CMUT Arrays” and the conference paper titled “Mutual Radiation Impedance for Modeling of Multi-Frequency CMUT Arrays” which is presented here.

3.1 Introduction

Mutual acoustic impedance refers to the ratio of force or integrated pressure exerted by one radiator to the resulting velocity on another radiator. It is important and non-negligible when considering arrays of closely spaced transducer elements and can govern their interaction. Much of the previous work regarding mutual acoustic impedance [1] originated in the 1960s with the work of Pritchard [2] and Porter [3] and has since been widely used. This work primarily focused on mutual acoustic impedance between identical piston and flexural disk radiators. However, multi-frequency transducers including multi-frequency interlaced capacitive micromachined ultrasonic transducers (CMUTs) are an emerging transducer technology [4]. CMUTs are membrane-based transducers microfabricated using sacrificial release [5] or wafer-bonding methods [6]. In such transducer architectures, flexural membranes of different sizes are interlaced on a scale smaller than the shortest acoustic wavelength so as to mitigate grating lobe artifacts. Applications for such emerging transducer technology may include image-guided High-Intensity-Focused-Ultrasound (HIFU) therapy [7]-[9], multi-band photoacoustic imaging [10-11], novel microbubble contrast agent imaging techniques including super-harmonic imaging (involving transmission of low frequencies and receiving high frequencies for exceptional contrast-to-tissue ratios) [12]-[14], tissue harmonic imaging [15], [16], image-guided drug-delivery [17]-[19], nanodroplet phase-change imaging methods [20], image-guided ultrasound-aided biomarker and extracellular vesicle release [21], [22], multi-scale-multi-resolution imaging [23], and other unique applications [24].

Because membranes of different sizes must be considered in multi-frequency CMUTs, the mutual acoustic impedance analysis is more complex than the case of identical radiators. Chan [25] proposed a framework for calculating mutual acoustic impedance for radiators of different sizes, however, the framework was computationally burdensome and some inaccuracies in the analysis resulted. In particular, we point out that results of Chan's analysis, in the limiting case of identically-sized membranes, agree with Porters gold-standard results only for the case of pistons, but not, for clamped edge flexural disks. For example, discrepancies are seen when comparing values computed using Chan's Eq. (16) to those in Table VI of Porter's paper. The need for accurate and computationally efficient methods of estimating mutual acoustic impedance for different-sized membranes motivated us to produce a new framework presented in this work. We present a new set of tractable expressions for self- and mutual acoustic impedances applicable to multi-frequency transducers and identically-sized membranes. In each step for more validation, the expressions are reduced to the case of identical disks and compared with Pritchard and Porter expressions. Additionally, improved-accuracy fast approximations are developed to aid large-scale simulations of next-generation transducers.

Recently, H. Koymen and et al developed an accurate equivalent circuit model for uncollapsed single CMUT cells with partial and full electrodes [26] which built on previous work [27]-[32] but included full nonlinear behavior and accounted for CMUT layout. In this research we used the model developed in [26] and modified it to simulate multi-frequency CMUT arrays by incorporating the newly-developed expressions for mutual acoustic impedance, building on our conference paper [33] which included experimental comparisons with square membrane multi-frequency arrays. The effects of mutual acoustic interactions are validated using Finite Element Method (FEM) simulations. Model predictions of the membrane displacement amplitude and phase, resonance frequency and total electrical conductance closely matched 3D FEM analysis.

The framework developed for modeling mutual acoustic impedance and multi-frequency arrays should prove important for designing next-generation multi-frequency transducers which exhibit ultra-wide bandwidths and which can be tailored for photoacoustic or ultrasound imaging-therapy applications. The simulation tools enable layout-level CMUT architectures to be translated into predictions of operating frequencies, bandwidth, collapse voltages, membrane displacement and velocity, acoustic output pressure and electrical conductance, among other important design factors and array performance metrics. The work presented here is also fundamentally important for understanding interactions between dissimilar radiators.

3.2 Background

Given an array of N radiators, the force on the n^{th} due to radiation from each of the others may be written in the form of

$$f_n = \sum_{m=1}^{N} Z_{nm} v_m \tag{3.1}$$

where v_m is the average surface velocity of the m^th radiator and Z_{nm} is the mutual radiation impedance between the m^th and n^th radiators, while Z_{nn} denotes the self-radiation impedance of the n^th radiator. The net radiation impedance of one radiator $Z_n \equiv f_n/v_n$ is a function of the velocities of the other radiators:

$$Z_n = Z_{nn} + Z_{n1}\left(\frac{v_1}{v_n}\right) + Z_{n2}\left(\frac{v_2}{v_n}\right) + \cdots + Z_{nN}\left(\frac{v_N}{v_n}\right), \tag{3.2}$$

and is in general complex: $Z_n = R_n + jX_n$, where R_n and X_n are the real and imaginary parts of the net radiation impedance, respectively. If each of the radiators normally operates with a baffle surface of which also contains each of the other radiators, then the mutual radiation impedance Z_{nm} will be a function of only the two elements m and n, independent of all others. Accordingly, in such cases, it is sufficient to calculate the mutual acoustic impedance between only two radiators at a time.

Previous work by Pritchard, Porter, and Chan approached the calculation of mutual acoustic impedance by using a method termed the Bouwkamp method [34]. In this method they considered two radiators at a time and calculated the mechanical radiation impedance Z_0 of the combined radiators. Then, they separated the contributions of the associated self- and mutual acoustic impedances.

The complex mechanical radiation impedance Z_0 of two radiators is defined as the total force over the set of radiators ($f_0 = f_1 + f_2$) divided by the surface velocity v_0, (i.e. $Z_0 = f_0/v_0$). Pritchard pointed out that no loss of generality will result if both radiators are assumed to vibrate in phase with $v_0 = v_1 = v_2$, because we can always re-scale the values of the mutual acoustic impedances using Eq. (3.2) to compute net impedances Z_1 and Z_2. Then $Z_0 = Z_1 + Z_2$ and with identical radiators $Z_1 = f_1/v_1 = Z_2 = f_2/v_2 = Z_{11} + Z_{12}(v_2/v_1)$.

The Bouwkamp method of calculating Z_0 involves integrating the directional factor $|K(\theta, \varphi)|^2$ over real and complex angels as follows:

$$Z_0 = \rho c \frac{S^2}{4\pi^2} k^2 \frac{|\bar{v}|^2}{|v_0|^2} \int_0^{2\pi} \int_0^{(\pi/2)+j\infty} |K(\theta,\varphi)|^2 \sin\theta d\theta d\varphi \tag{3.3}$$

where ρc is the characteristic impedance of the medium, S is the total active area of the radiating disk, k is the wavenumber of the radiated sound, $|v_0|$ is the magnitude of the vibrating velocity and $|\bar{v}|$ is the magnitude of the average radiating surface velocity. Note that the average velocity is computed over the membrane surface and may be different depending on the edge-clamping condition. We set up the problem in a similar way but additionally consider a new framework and structure of approximations which leads to new useful results.

3.3 System Definition and Directional Characteristic of the Overall Radiating System

The self and mutual acoustic radiation impedance will be calculated for two circular disks of different sizes vibrating in phase in an infinite rigid plane. As shown in Fig. 3.1, the disks are of radii a_1 and a_2 separated by a distance of d. To calculate the self- and mutual acoustic impedances, we must compute the directional factor of the overall system.

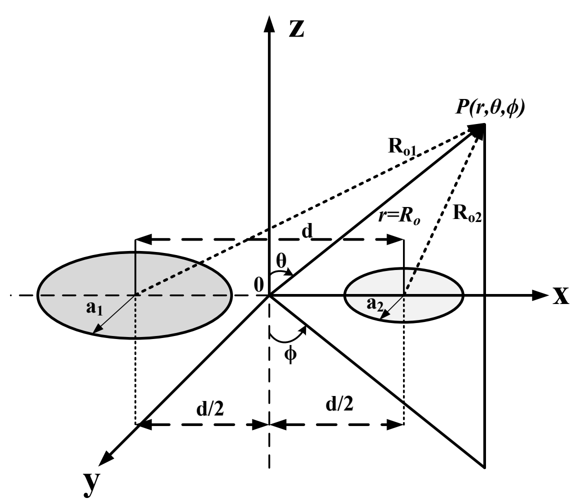

Fig. 3.1. System Coordination for calculation of self and mutual radiation impedance between two disks of different membrane sizes.

3.3.1 Directional Factor Computations

The magnitude of the directional characteristic or directional factor $|K(\theta,\varphi)|$ of the overall system comprising the two disks of different sizes is defined as [3];

$$|K(\theta,\varphi)| = \left|\frac{\text{The total farfield sound pressure}}{\text{The total field pressure on the axis}}\right| = \left|\frac{P}{P_{on-axis}}\right| = \left|\frac{P_1+P_2}{P_{on-axis}}\right| \tag{3.4}$$

where P is the total farfield sound pressure produced by disks number one (P_1) and number two (P_2) on the observation point of $P(r,\theta,\emptyset)$ and by using the Eq. (3.33)-a of Cobbold [35], it can be written as

$$P = P_1 + P_2 = \frac{i\omega\rho_0 v_0 a_1^2}{2R_{0_1}} e^{-ikR_{0_1}} D_1(\theta) + \frac{i\omega\rho_0 v_0 a_2^2}{2R_{0_2}} e^{-ikR_{0_2}} D_2(\theta) \tag{3.5}$$

where ω is the angular frequency, ρ_0 is the density of the medium, v_0 is the velocity amplitude, $a_1$and a_2 are the radii of the disk number one and number two, k is the wavenumber, R_{0_1} and R_{0_2} are the distances from the center of the disks to the observation point of $P(r,\theta,\emptyset)$ and finally $D(\theta)$ is the farfield pressure directivity function which can be defined for different types of circular disks as;

$$D(\theta) = \frac{\sum_{\mu=1}^{3} \beta_\mu \frac{J_\mu(kasin\theta)}{(kasin\theta)^\mu}}{\sum_{n\ even} \frac{\alpha_n}{n+2}} \tag{3.6}$$

where β_μ is expressed in terms of even numbers of deflection curve coefficients that are defined by boundary conditions of the radiators while $\alpha_{2n+1} = 0$. Table 3.I provides the β_μ values and deflection curve coefficients of some well-known radiators using Table IV of Porter and Eq. (12) of Chan papers;

$$
\begin{aligned}
\beta_1 &= \alpha_0 + \alpha_2 + \alpha_4, \\
\beta_2 &= -2(\alpha_2 + 2\alpha_4), \qquad (3.7) \\
\beta_3 &= 8\alpha_4.
\end{aligned}
$$

TABLE 3.I. DEFLECTION CURVE COEFFICIENTS AND β VALUES FOR DIFFERENT TYPES OF DISKS.

Case	α_0	α_2	α_4	β_1	β_2	β_3
Piston	1	0	0	1	0	0
Clamped edge	1	-2	1	0	0	8
Exact supported edge	1	-1.2453	0.2453	0	1.5094	1.9624
Appr. supported edge*	1	-1	0	0	4	0
Finite supported edge	1	-1.8	1	0.2	-0.4	8

*Appr. supported edge approximation leads to simpler analysis of supported edge conditions.

Note that when the above values are substituted into Eq. (3.6), we obtain the expressions for K in Table IV of Porter, which is reproduced in this section as Table 3.II, and included for convenience. When the source is a piston ($\beta_1 = 1$ and $\beta_2 = \beta_3 = 0$), $D(\theta)$ reduces to Eq. (3.33)-b of Cobbold [35] for the directivity function of a piston in the farfield.

TABLE 3.II. Values of the Farfield Pressure Directivity Function for Various Types of Circular Disks.

Disk Type	$D(\theta)$
Piston	$2\,\dfrac{J_1(kasin\theta)}{(kasin\theta)}$
Approximate supported edge	$8\,\dfrac{J_2(kasin\theta)}{(kasin\theta)^2}$
Clamped edge	$48\,\dfrac{J_3(kasin\theta)}{(kasin\theta)^3}$
Point source	1

The on-axis pressure can be calculated from Eq. (3.5) while $R_{0_1} = R_{0_2}$ and $\theta = 0$. Consequently, $D_1(0) = D_2(0) = 1$ and,

$$|P_{on-axis}| = \frac{\omega\rho_0 v_0(a_1^2 + a_2^2)}{2R_{0_1}}\alpha_4. \tag{3.8}$$

To calculate the net acoustic radiation impedance Z_0, first we need to find a comprehensive expression for the $|K(\theta,\varphi)|^2$ while $|R_{0_1}| \cong |R_{0_2}|$ when the observation point is far from the radiators. The details are set forth in Appendix A.1, and the final result which is valid for any types of circular disks of different sizes can be given in the form of,

$$\begin{aligned}|K(\theta,\varphi)|^2 = \{&a_1^4 {D_1}^2(\theta) + a_2^4 {D_2}^2(\theta)\\ &+ 2a_1^2 a_2^2 D_1(\theta) D_2(\theta)[\cos(kdsin\theta sin\varphi)]\}/(a_1^2 + a_2^2)^2\end{aligned} \tag{3.9}$$

Note that the $K(\theta,\varphi)$ depends not only on the disk radii, directivity functions, angular and azimuthal variables but also the center to center distance d. If the two radiators are identical ($a_1 = a_2 = a$) and $D_1(\theta) = D_2(\theta) = D(\theta)$, the $|K(\theta,\varphi)|^2$ expression reduces to

$$\begin{aligned}|K(\theta,\varphi)|^2 &= D^2(\theta)\left\{\frac{1+\cos(kdsin\theta sin\varphi)}{2}\right\}\\ &= D^2(\theta)\left\{\frac{1+\cos(2\frac{\pi d}{\lambda}sin\theta sin\varphi)}{2}\right\}\end{aligned} \tag{3.10}$$

By using the trigonometric relation $\cos(\alpha) = \sqrt{\frac{1+\cos(2\alpha)}{2}}$ and considering the disks as two separated pistons, the Eq. (3.10) reduces to the square of Eq. (7) of Pritchard. Alternatively, the directional characteristic of the overall radiator comprising two identical pistons can be found simply by multiplication of the directivity function of a single disk and two point sources.

Thus

$$|K(\theta,\varphi)| = D(\theta)cos\left(\frac{\pi d}{\lambda}sin\theta sin\varphi\right) = 2\,\frac{J_1(kasin\theta)}{(kasin\theta)}cos\left(\frac{\pi d}{\lambda}sin\theta sin\varphi\right) \tag{3.11}$$

3.4 Net Radiation Impedance

By considering that, the radiating surface area of the overall plane radiator (S) is the total surface area of the circular disk number 1 ($S_1 = \pi a_1^2$) and disk number 2 ($S_2 = \pi a_2^2$), the net radiation impedance of the overall system using the Bouwkamp method [2] can be written as

$$Z_0 = Z_1 + Z_2 = \rho c \frac{(S_1 + S_2)^2}{4\pi^2} k^2 \int_0^{2\pi} \int_0^{(\pi/2)+j\infty} |K(\theta,\varphi)|^2 \, sin\theta d\theta d\varphi \tag{3.12}$$

Without loss of generality, when $v_1 = v_2$, then $Z_0 = Z_{11} + Z_{22} + Z_{12} + Z_{21}$ where the Z_{11} is the self-radiation impedance of the disk number 1, Z_{22} is the self-radiation impedance of the disk number 2 and Z_{12} and Z_{21} are the mutual-radiation impedances between disk number 1 and number 2.

If we consider that two circular radiators are vibrating in phase with each other in the infinite rigid plane [25] and by substituting the comprehensive expression of the $|K(\theta,\varphi)|^2$ in Eq. (3.12),

$$\begin{aligned} Z_0 &= Z_{11} + Z_{22} + 2Z_{12} \\ &= \rho c \frac{k^2}{4} \int_0^{2\pi} \int_0^{(\pi/2)+j\infty} \left\{ a_1^4 {D_1}^2(\theta) + a_2^4 {D_2}^2(\theta) \right. \\ &\left. + 2a_1^2 a_2^2 D_1(\theta) D_2(\theta) \times [\cos{(kdsin\theta sin\varphi)}] \right\} sin\theta d\theta d\varphi \end{aligned} \tag{3.13}$$

where the first two terms, which is independent of the spacing d, are identified as the self-radiation impedances of the first (Z_{11}) and second disks (Z_{22}), respectively

$$\begin{aligned} Z_{11} &= \rho c \frac{k^2}{4} \int_0^{2\pi} \int_0^{(\pi/2)+j\infty} \left\{ a_1^4 {D_1}^2(\theta) \right\} sin\theta d\theta d\varphi \, , \\ Z_{22} &= \rho c \frac{k^2}{4} \int_0^{2\pi} \int_0^{(\pi/2)+j\infty} \left\{ a_2^4 {D_2}^2(\theta) \right\} sin\theta d\theta d\varphi . \end{aligned} \tag{3.14}$$

and the last term, which is dependent of the spacing d, can be defined as the total mutual radiation impedance between two separated circular disks.

$$Z_{12} = Z_{21} = \rho c \frac{k^2}{4} \int_0^{2\pi} \int_0^{(\pi/2)+j\infty} \{a_1^2 a_2^2 D_1(\theta) D_2(\theta) \times [\cos{(kdsin\theta sin\varphi)}]\} sin\theta d\theta d\varphi \tag{3.15}$$

3.4.1 Self-Radiation Acoustic Impedance

By using Eq. (3.14) and according to the provided details in Appendix A.2, the self-radiation impedance Z_{nn} (n is the number of the radiator) can be written as

$$\begin{aligned} Z_{nn} &= R_{nn} + j\,X_{nn} \\ &= \rho c (\pi a_n^2) \frac{(ka_n)^2}{2} \left\{ \int_0^{(\pi/2)} {D_n}^2(\theta) sin\theta d\theta + \int_{(\pi/2)+j0}^{(\pi/2)+j\infty} {D_n}^2(\theta) sin\theta d\theta \right\} \end{aligned} \tag{3.16}$$

3.4.2 Mutual Radiation Acoustic Impedance

According to Eq. (3.15) and the provided details in Appendix A.3, the mutual radiation impedance Z_{12} can be written as Eq. (3.17). This expression is obtained by solving the integral of Eq. (A.12) which has been solved in Pitchard's Appendix section using Eqs. (A1)-(A4) and can be applied directly to obtain

$$\begin{aligned} Z_{12} &= R_{12} + j\,X_{12} \\ &= \frac{\rho c (\pi a_1^2)(ka_2)^2}{2\left(\sum \frac{\alpha_n}{n+2}\right)^2} \sum_{\mu=1}^{3} \sum_{\nu=1}^{3} \beta_\mu \gamma_\nu \\ &\times \frac{1}{(ka_1)^\mu (ka_2)^\nu} \left\{ \sum_{m=0}^{\infty} \sum_{n=0}^{\infty} \frac{\Gamma\left(m+n+\frac{1}{2}\right)}{\pi^{\frac{1}{2}} m!\, n!} \left(\frac{a_1^m a_2^n}{d^{m+n}}\right) \right. \\ &\left. \times J_{\mu+m}(ka_1) J_{\nu+n}(ka_2) \times \zeta_{m+n^{(2)}}(kd) \right\} \end{aligned} \tag{3.17}$$

where the $\zeta_{m+n^{(2)}(kd)}$ is defined by spherical Bessel functions of $\psi_{m+n}(kd)$ and $X_{m+n}(kd)$,

$$\begin{aligned}\zeta_{m+n^{(2)}}(kd) &= \psi_{m+n}(kd) + jX_{m+n}(kd) \\ &= (\frac{\pi}{2kd})^{\frac{1}{2}}\left[J_{m+n+\frac{1}{2}}(kd) + j(-1)^{m+n}J_{-m-n-\frac{1}{2}}(kd)\right] \\ &= (\frac{\pi}{2kd})^{\frac{1}{2}} \times H_{m+n+\frac{1}{2}^{(2)}}(kd)\end{aligned} \tag{3.18}$$

Table 3.III summarizes some of the key analytical results of this work. Eq. (16) of Chan's paper [25] shows the same result for only the case of piston disks, but for supported edge and clamped edge flexural disks, the results must be different. Our results agree with Porter's when both disks are identical. To illustrate this, we analytically verified equivalency, and used MATLAB to verify that our results agree with those computed using Porter's expressions to within numerical precision for $ka_1 = ka_2 = 1$.

TABLE 3.III. MUTUAL RADIATION IMPEDANCE FOR DIFFERENT TYPES OF RADIATORS.

Case	Mutual Radiation Impedance ($Z_{12} = Z_{21}$)
Piston	$Z_{12} = 2\rho c(\pi a_1 a_2) \times M$
Approx. supported edge	$Z_{12} = \frac{32\rho c\pi}{k^2} \times M$
Clamped edge	$Z_{12} = \frac{1152\rho c\pi}{k^4 a_1 a_2} \times M$

$$M = \sum_{m=0}^{\infty}\sum_{n=0}^{\infty}\frac{\Gamma\left(m+n+\frac{1}{2}\right)}{\pi^{\frac{1}{2}}m!\,n!}\left(\frac{a_1^m a_2^n}{d^{m+n}}\right) \times J_{m+T}(ka_1)J_{n+T}(ka_2) \times \zeta_{m+n^{(2)}}(kd)$$

*The value of T in M expression is equal to 1, 2 and 3 for piston, approximate supported edge and clamped edge, respectively.

For $0.01 < ka_1 = ka_2 < 6$, Fig 3.2 shows the normalized variation of the mutual radiation resistance, R_{12}, and reactance, X_{12}, as a function of ka for three well-known disk types when two disks are closely packed ($kerf = radius/10$). As can be observed the values of the mutual radiation impedance are different for piston and clamped edge disks. Since the CMUTs should be considered as clamped edge disks, the equation found by Chan, which is only valid for pistons, cannot be used for modeling of the CMUTs.

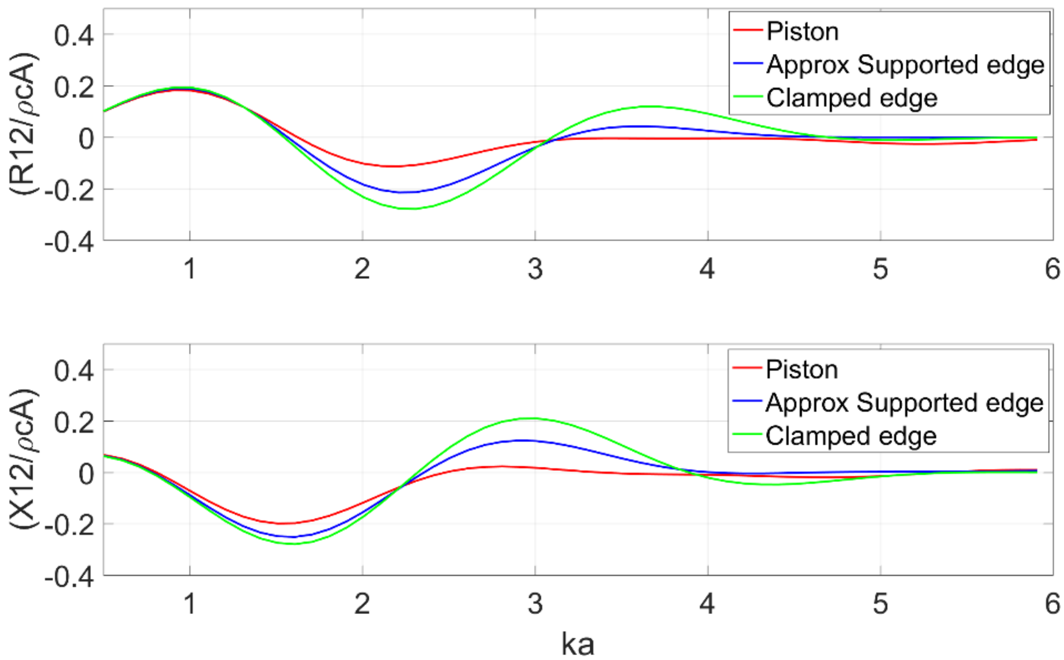

Fig. 3.2. Normalized mutual radiation impedance to $\rho c A$, as a function of ka, for two circular disks including piston, approximate supported edge and clamped edge in an infinite rigid plane, where ρc is the characteristic impedance of the medium and A is the total active area of the radiating disk. The graphs have been obtained using the equations of Table 3.III.

3.5 Additional Approximations for Mutual Radiation Impedance between CMUTs

For CMUT array modeling and any type of arrays with many numbers of vibrating disks, the mutual radiation impedance between all pairs of cells must be considered which ends up with a very large impedance matrix. Consequently, the calculation of the mutual impedance using the exact expression can be very time consuming, especially for large-scale array simulations. Hence, achieving an accurate yet computationally efficient approximation of the exact solution is valuable.

First, we obtain an approximate expression for small ka_1 and ka_2 values ($ka_{1,2} < 0.05$). The approximate expressions are obtained for piston and clamped edge disks under two conditions. The first is when the disks are separated by a distance large relative to the radius and all terms of order $\left(\frac{a}{d}\right)$ and higher are neglected. Second approximate condition can be considered when $\left(ka_{1,2}\right)^2 \ll 1$.

By applying the approximate conditions, new expressions are obtained for piston and clamped edge disks when the production of the wavenumber and radius are much smaller than unity. More details are provided in Appendix A.4.

$$Z_{12-Piston-approx.} = R_{12} + j\,X_{12} = \rho c(\pi a_1^2)\frac{(ka_2)^2}{2}\left\{\frac{\sin(kd)}{kd} + j\frac{\cos(kd)}{kd}\right\} \tag{3.19}$$

For two identical piston radiators, the Eq. (3.19) reduces to Eq. (16) of the Pritchard paper.

Similarly, according to the β_μ and γ_ν values of the clamped edge radiators and the provided details in Appendix A.4,

$$\begin{aligned} Z_{12-Clamped\,edge-approx.} &= R_{12} + j\,X_{12} \\ &= \frac{1152\rho c\pi a_1^2(ka_2)^2}{(ka_1)^3(ka_2)^3}\left\{\frac{\sin(kd)}{kd} + j\frac{\cos(kd)}{kd}\right\}J_3(ka_1)J_3(ka_2) \end{aligned} \tag{3.20}$$

According to Eq. (A.18) of Appendix A, the piston approximate Eq. (3.19) can still be valid for clamped edge disks too if we only consider the first order terms of the series expansion of the Bessel functions $J_3(ka_1)$ and $J_3(ka_2)$.

Moreover, the root-mean-square (rms) value of the mutual radiation impedance is calculated as Eq. (3.19) which reduces to the Eq. (3) of Kagan et al [36] when $a_1 = a_2$.

$$\frac{Z_{12}}{\rho c(\pi a_1^2)} = \frac{5}{9}\times\frac{(ka_2)^2}{2}\left\{\frac{\sin(kd)}{kd} + j\frac{\cos(kd)}{kd}\right\} \tag{3.21}$$

Fig. 3.3 shows the normalized exact and approximate mutual radiation impedance between two clamped edge disks for $ka_1 = ka_2 = ka = 1$, after applying only condition 1 and both conditions 1 and 2 simultaneously. The approximations show a good agreement with exact expressions when $ka = 1$ which means better conformity for $ka \ll 1$. However, it can be observed that, after applying the second condition, the imaginary graph of the approximate expression deviates slightly from the exact one for small kd values.

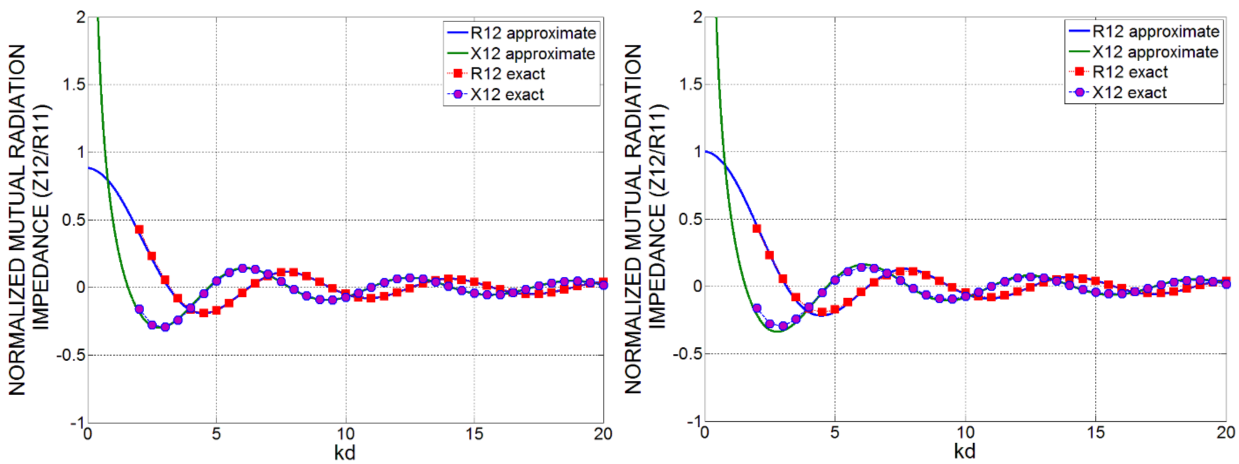

Fig. 3.3. Normalized exact and approximate mutual radiation impedance to $R_{11} = \frac{1}{2}\rho c S(ka)^2$, as a function of relative center to center spacing kd, for two circular clamped edge disks after applying only condition 1 and both condition 1 and 2 simultaneously. The exact plots were drawn using the clamped edge relation of Table 3.III and two separate approximate graphs were obtained by Eqs. (3.19) and (3.20).

3.5.1 Approximate Mutual Radiation Impedance for the disks of the Same Sizes

The obtained approximate relations can only be in good agreement for $ka_{1,2} < 0.5$. However, for identical disks, an accurate approximation for mutual radiation impedance can be obtained for $0.5 < ka < 5.5$ as,

$$Z_{12} = R_{12} + j\,X_{12} = \frac{\rho c(\pi a^2)}{2}\left\{A(ka)\left[\frac{\sin(kd)}{kd}\right] + jB(ka)\left[\frac{\cos(kd)}{kd}\right]\right\} \tag{3.22}$$

where the $A(ka)$ and $B(ka)$ polynomial coefficients are provided in Table A.I of Appendix A.5 using the tenth-order polynomial curve fitting method, for two types of disks that are mostly used in CMUT applications.

$$A(ka) = \sum_{n=0}^{10} a_n\,(ka)^n,$$

$$B(ka) = \sum_{n=0}^{10} b_n\,(ka)^n. \tag{3.23}$$

For $ka > 5.5$, the Z_{12} is negligible compared to the self-radiation impedances of Z_{11} and Z_{22} and can be ignored. For calculating the rms values of the mutual radiation impedance, the final obtained Z_{12} values are multiplied by the factor of $5/9$ [36].

3.5.2 Approximate Mutual Radiation Impedance for Clamped Edge Disks (e.g. CMUTs) of Different Membrane Sizes

Eq. (3.19) can still be used for calculating the mutual radiation impedance between two disks (e.g. CMUTs) of different membrane sizes for very small $ka_{1,2}$ values ($ka_{1,2} < 0.05$). However, for $ka_{1,2} > 0.05$ and the disks with different membrane sizes, the accurate approximation can be found separately for small ($0.05 < ka_{1,2} < 0.8$) and large ($0.8 < ka_{1,2} < 6$) $ka_{1,2}$ values as,

$$Z_{12} = R_{12} + j\,X_{12}$$
$$= \frac{\rho c(\pi {a_1}^2)}{2}\left\{A(ka_1, ka_2)\left[\frac{\sin(kd)}{kd}\right] + jB(ka_1, ka_2)\left[\frac{\cos(kd)}{kd}\right]\right\} \tag{3.24}$$

where the $A(ka_1, ka_2)$ and $B(ka_1, ka_2)$ polynomial coefficients are provided separately in Tables A.II and A.III of Appendix A.5 for abovementioned $ka_{1,2}$ intervals. Please note that, the $0.05 < ka_{1,2} < 0.8$ is only used when both ka_1 and ka_2 values are in this interval and for the rest of the cases beyond this range, we use the second sets of coefficients. Fig. 3.4 shows the real and imaginary polynomial coefficients for all required ka_1 and ka_2 values. These approximations are obtained using five by five degree of polynomial surface fitting method with R-squared of 99.98% and used for modeling of CMUT arrays in following section.

$$A(ka_1, ka_2) = \sum_{i=0}^{5}\sum_{j=0}^{5} a_{ij}\,(ka_2)^i\,(ka_1)^j,$$
$$B(ka_1, ka_2) = \sum_{i=0}^{5}\sum_{j=0}^{5} b_{ij}\,(ka_2)^i\,(ka_1)^j. \tag{3.25}$$

As mentioned before, for $ka_{1,2} > 6$, the mutual radiation impedance of the clamped edge disks is negligible compared to self-radiation impedances and can be ignored.

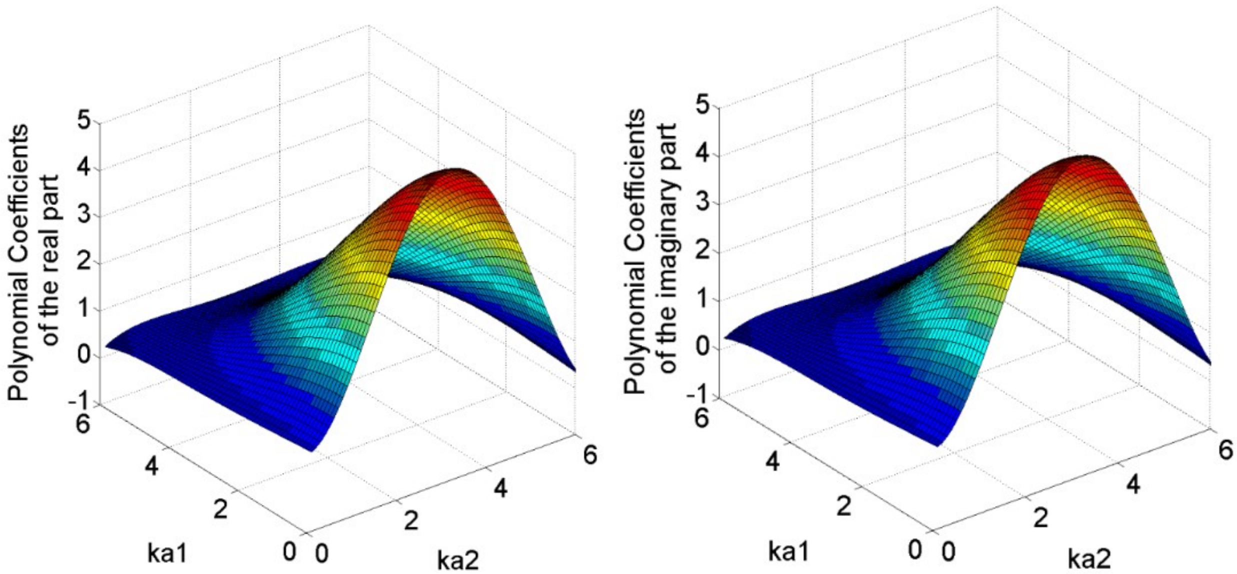

Fig. 3.4. $A(ka_1, ka_2)$ and $B(ka_1, ka_2)$ from Eq. (25) for $0.01 < ka_1, ka_2 < 6$. $A(ka_1, ka_2)$ and $B(ka_1, ka_2)$ are polynomial coefficients of the real (right) and imaginary (left) parts of the approximate mutual radiation impedance expression Eq. (3.24) of clamped edge disks of different membrane sizes.

3.6 Conclusion

The framework developed here offers key results for both self and mutual acoustic radiation impedance and very accurate approximations applicable to arrays of membranes which do not necessarily have the same size and may be especially applicable to multi-frequency CMUT arrays. A comprehensive expression, Eq. (3.9), is obtained for directional factor $|K(\theta,\varphi)|$ of two circular disks radiating in an infinite rigid plane. The method can be expanded for any types of membranes with different shapes including square and rectangular membranes. A generalized series solution, Eq. (3.17), is achieved for self and mutual acoustic radiation impedance between two flexural disks of different membrane sizes, vibrating in phase, in an infinite rigid plane. The obtained expressions can be easily used for the disks with the same membrane sizes by considering a_1 equal to a_2. While many works utilize Eqs. (3.19) or (3.20) as an approximation for identical-membranes, Eq. (3.24) offers a simple extension of this approximation for different sized membranes. Eqs. (3.22) and (3.24) offer improved accuracy over Eqs. (3.19) or (3.20) at little more computational cost owing to pre-calculated values for fitting coefficients.

Since transducers are usually composed of large arrays of closely interlaced cells, modeling to include their exact mutual effects could be extremely computationally costly and time-consuming. Besides offering computational savings, we believe our methods to be the first accurate analysis of flexural disk membranes and other non-piston radiators when considering non-identical radii. Additionally, approximation Eq. (3.24) offers considerable intuition. For sufficiently spaced radiators of different size, the mutual acoustic impedance is simply a scaled version of the mutual acoustic impedance between identical radiators, with the scaling factor related to the new area of the differing disk.

Present work is limited to mutual acoustic radiation impedance when membranes have the same phase. Future work should aim to generalize these results and will also aim to incorporate these new expressions for mutual acoustic impedance into accurate and efficient multi-frequency array simulations of multi-frequency CMUTs and may be key to optimizing their design and guide their implementation.

References

[1] C. H. Sherman, and J. L. Butler, "Transducers and Arrays for Underwater Sound," *Springer*, New York, 2007, Chap. 5, pp. 230-243.

[2] R. L. Pritchard, "Mutual acoustic impedance between radiators in an infinite rigid plane," *J. Acoust. Soc. Am.*, vol. 32, pp. 730-737, 1960.

[3] D. T. Porter, "Self-and Mutual-Radiation Impedance and Beam Patterns for Flexural Disks in a Rigid Plane," *J. Acoust. Soc. Am.*, vol. 36, pp. 1154-1161, 1964.

[4] A. Kshirsagar, R. Chee, A. Sampaleanu, A. Forbrich, D. Rishi, W. Moussa, and R. J. Zemp, "Multi-frequency CMUT arrays for imaging-therapy applications," *IEEE International Ultrasonics Symposium (IUS)*, pp. 1991-1993, 2013.

[5] A. Sampaleanu, P. Zhang, A. Kshirsagar, W. Moussa, and R. J. Zemp, "Top-orthogonal-to-bottom-electrode (TOBE) CMUT arrays for 3-D ultrasound imaging," *IEEE Trans. Ultrason. Ferroelectr. Freq. Control*, vol. 61, no. 2, pp. 266-276, 2014.

[6] P. Zhang, G. Fitzpatrick, T. Harrison, W. Moussa, and R. J. Zemp, "Double-SOI wafer-bonded CMUTs with improved electrical safety and minimal roughness of dielectric and electrode surfaces," *Journal of Microelectromechanical Systems*, vol. 21, no. 3, pp. 668-680, 2012.

[7] Y-S. Kim, "Advances in MR imaging-guided high-intensity focused ultrasound therapy," *Int. J Hyperthermia*, Vol. 31, pp. 225-232, 2015.

[8] M. R. Pfeffer, T. Rabin, Y. Inbar, A. Hananel, and R. Catane, "Image-guided high-intensity focused ultrasound in the treatment of cancer," *In Image-Guided Cancer Therapy*, Springer, New York, pp. 79-99, 2013.

[9] A. Ranjan et al., "Image-guided drug delivery with magnetic resonance guided high intensity focused ultrasound and temperature sensitive liposomes in a rabbit Vx2 tumor model," *Journal of controlled release*, vol. 158, pp. 487-494, 2012.

[10] S. P. Gautieri, "Photo-acoustic, multi-band, multi-cavity gas detection system," *U.S. Patent*, No. 8,806,916. (19 August 2014).

[11] S. Autrey, G. Posakony, J. Amonette, and N. Foster-Mills, "Multi-band transducer for photoacoustic detection," *U.S. Patent*, No. 20,010,018,848. (6 September 2001).

[12] S. Unnikrishnan, and A. L. Klibanov, “Microbubbles as ultrasound contrast agents for molecular imaging: preparation and application,” *Am. J. Roentgenology*, vol. 199, pp. 292-299, 2012.

[13] V. R. Stewart, and P. S. Sidhu, “New directions in ultrasound: microbubble contrast,” *The British journal of radiology*, vol. 79, pp. 188-194, 2014.

[14] A. Guiroy, A. Novell, E. Ringgaard, R. Lou-Moeller, J. M. Gregoire, A. P. Abellard, T. Zawada, A. Bouakaz, and F. Levassort, “Dual frequency transducer for nonlinear contrast agent imaging,” *IEEE Trans. Ultrason. Ferroelectr. Freq. Control*, vol. 60, pp. 2634–2644, 2013.

[15] C. C. Shen, and C. H. Lin, “Chirp-encoded excitation for dual-frequency ultrasound tissue harmonic imaging,” *IEEE Trans. Ultrason. Ferroelectr. Freq. Control*, vol. 59, pp. 2420-2430, 2012.

[16] E. Ohno, H. Kawashima, S. Hashimoto, H. Goto, and Y. Hirooka “Current status of tissue harmonic imaging in endoscopic ultrasonography (EUS) and EUS-elastography in pancreatobiliary diseases,” *Digestive Endoscopy*, vol. 27, pp. 68-73, 2015.

[17] T. Ojha, L. Rizzo, G. Storm, F. Kiessling, and T. Lammers, “Image-guided drug delivery: preclinical applications and clinical translation,” *Expert opinion on drug delivery*, vol. 12, pp. 1203-1207, 2015.

[18] M. Thanou, M. Wright, M. Centelles, and W. Gedroyc, “Image guided focused ultrasound delivery of macromolecular drugs in tumours,” *Journal of Therapeutic Ultrasound*, vol. 3, pp. 75-76, 2015.

[19] M. Thanou, M. Wright, and M. Centelles, “Nanoparticles for image guided focused ultrasound drug delivery,” *Cancer Research*, vol. 74, pp. 5398-5398, 2014.

[20] P. S. Sheeran, J. E. Streeter, L. B. Mullin, T. O. Matsunaga, and P. A. Dayton, “Toward ultrasound molecular imaging with phase-change contrast agents: an in vitro proof of principle,” *Ultrasound in medicine and biology*, vol. 39, pp. 893-902, 2013.

[21] S. E. Ahmed, A. M. Martins, and G. A. Husseini, “The use of ultrasound to release chemotherapeutic drugs from micelles and liposomes,” *Journal of drug targeting*, vol. 23, pp. 16-42, 2014.

[22] Y. Lin et al., “Application of Molecular Imaging Technologies in Antitumor Drug Development and Therapy,” *Current pharmaceutical design*, vol. 21, pp. 2136-2146, 2015.

[23] G. Ku, X. Wang, G. Stoica, and L. V. Wang, "Multiple-bandwidth photoacoustic tomography," *Physics in Medicine and Biology*, vol. 49, pp. 1329–1338, 2004.

[24] K. H. Martin, B. D. Lindsey, J. Ma, M. Lee, S. Li, F. S. Foster, X. Jiang, and P. A. Dayton, "Dual-frequency piezoelectric transducers for contrast enhanced ultrasound imaging," *Sensors*, vol. 14, pp. 20825-20842, 2014.

[25] K. C. Chan, "Mutual acoustic impedance between flexible disks of different sizes in an infinite rigid plane," *J. Acoust. Soc. Am.*, vol. 42, pp. 1060-1063, 1967.

[26] H. Köymen, A. Atalar, E. Aydoğdu, C. Kocabas, H. K. Oğuz, S. Olcum, A. Ozgurluk, and A. Ünlügedik, "An improved lumped element nonlinear circuit model for a circular cMUT cell," *IEEE Trans. Ultrason. Ferroelectr. Freq. Control*, vol. 59, no. 8, pp. 1791–1799, 2012.

[27] I. ladabaum, X. Jin, H. soh, a. atalar, and b. Khuri-yakub, "surface micromachined capacitive ultrasonic transducers," *IEEE Trans. Ultrason. Ferroelectr. Freq. Control*, vol. 45, no. 3, pp. 678–690, May 1998.

[28] H. Koymen, M. senlik, A. Atalar, and S. Olcum, "Parametric linear modeling of circular cMUT membranes in vacuum," *IEEE Trans. Ultrason. Ferroelectr. Freq. Control*, vol. 54, no. 6, pp. 1229–1239, Jun. 2007.

[29] A. Lohfink and P.-C. Eccardt, "linear and nonlinear equivalent circuit modeling of cMUTs," *IEEE Trans. Ultrason. Ferroelectr. Freq. Control*, vol. 52, no. 12, pp. 2163–2172, Dec. 2005.

[30] D. Certon, F. Teston, and F. Patat, "a finite difference model for CMUT devices," *IEEE Trans. Ultrason. Ferroelectr. Freq. Control*, vol. 52, no. 12, pp. 2199–2210, dec. 2005.

[31] I. O. Wygant, M. Kupnik, and B. T. Khuri-yakub, "analytically calculating membrane displacement and the equivalent circuit model of a circular cMUT cell," *in Proc. IEEE Ultrasonics Symp.*, nov. 2008, pp. 2111–2114.

[32] C. Meynier, F. Teston, and D. Certon, "A multiscale model for array of capacitive micromachined ultrasonic transducers," *J. Acoust. Soc. Am.*, vol. 128, no. 5, pp. 2549-2561, 2010.

[33] M. Maadi, R. Chee, and R. J. Zemp, "Mutual radiation impedance for modeling of multi-frequency CMUT arrays," *IEEE International Ultrasonics Symposium (IUS)*, pp.1-4, 21-24 Oct. 2015.

[34] C. J. Bouwkamp, Phil. Research Repts 1, pp. 262-264, 1946.

[35] R. S. C. Cobbold. (2007). Foundations of Biomedical Ultrasound. *Oxford University Press*, New York, Chap. 3, pp. 155-163.

[36] H. Oguz, A. Atalar, and H. Koymen, "Equivalent circuit-based analysis of CMUT cell dynamics in arrays," *IEEE Trans. Ultrason. Ferroelectr. Freq. Control*, vol. 60, pp. 1016-1024, 2013.

Chapter 4

Modeling of Large-Scale Multi-Frequency CMUT Arrays with Circular Cells

Simulation of the multi-frequency arrays is challenging because of the need to incorporate mechanical, electrical, and acoustic aspects of device performance, including so-called mutual-acoustic impedance (or interaction) between elements. Traditional finite-element simulations take many hours for a single membrane but could take many days to model hundreds of thousands of membranes. Moreover, the interaction between elements of different sizes had not previously been modelled. To address these challenges, new large-scale lumped element simulations were developed integrating a new mutual acoustic impedance framework. This approach was able to model the multi-frequency arrays with close agreement to experiments. A lumped equivalent circuit model approach for simulating large-scale multi-frequency CMUT membranes with circular membranes is summarized by Maadi et al. in the published journal paper titled “Self and Mutual Radiation Impedances for Modeling of Multi-Frequency CMUT Arrays” and the conference paper titled “Modelling of Large-Scale Multi-Frequency CMUT Arrays with Circular Membranes” which is presented here.

4.1 Introduction

Using obtained expressions in Chapter 3, an appropriate radiation impedance matrix (Z-matrix) is generated. The Z-matrix contains the self-radiation impedance of each single CMUT cell and the mutual radiation impedance between every pairs of cells with arbitrary membrane sizes. The large signal equivalent circuit model of a clamped circular CMUT cell has been developed in [1] by considering assumptions that the array is in an infinite, rigid plane baffle [2] and that higher order modes of the cells are neglected [3]. We used the same large-signal equivalent-circuit model, but account for different-sized membranes. As demonstrated in Fig. 4.1, several cells are combined using the new Z-matrix. The main goal of this work is to extend the equivalent circuit modelling to large-scale simulations of realistic multi-frequency CMUT arrays. The model may prove useful in engineering next-generation multi-frequency CMUT transducers.

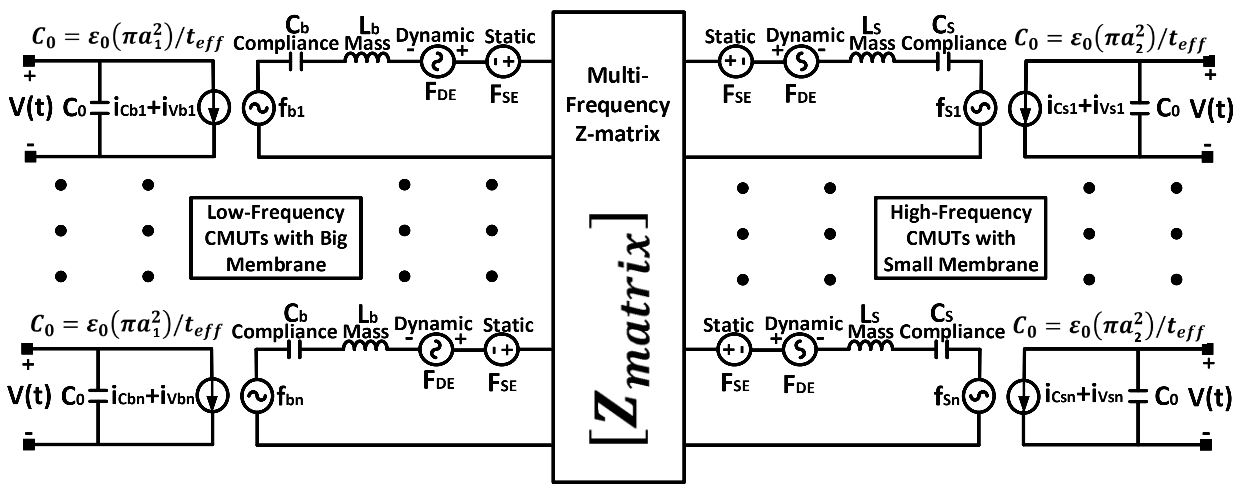

Fig. 4.1. Equivalent circuit diagram of interlaced n- high-frequency and n- low-frequency CMUT cells for multi-frequency applications. By driving all electrical ports with the same signal, we model multi-frequency arrays where all top electrodes are electrically connected, and all bottom electrodes are electrically connected to the same driving signal.

4.2 Modelling of Multi-Frequency CMUT Arrays

In this section, several types of multi-frequency CMUT arrays with different sized membrane radii were simulated to illustrate the significance of membrane size on array performance. Using the precise and validated large signal model of the single circular un-collapsed CMUT cell and a commercial circuit simulator in the ADS environment (Advanced Design System, Agilent Technologies), the linear and nonlinear responses of the equivalent circuit model of the multi-frequency CMUT arrays are obtained. The model can be used to generate and simulate any types of interlaced CMUT cells with different membrane sizes inside of an array within a few seconds.

ANSYS 3-D FEM analysis is used to validate the equivalent circuit model predictions. In all simulations of this we assumed CMUT cells are immersed in water and silicon nitride is used as their membrane material. 3-D axisymmetric models of CMUTs with smallest periodic portions of them ($1/6th$) are utilized by applying the rigid boundary conditions (Fig. 4.2). For a single CMUT cell, the absorbing boundary layer (FLUID130) should be located at least $0.2\lambda + radius$ away from the center of the element, where λ is defined as the greatest wavelength of the pressure waves for the analysis (speed of sound/f _min) [3]. Higher order 3-D 20-node structural solid elements (SOLID186) that exhibit quadratic displacement behavior are combined with electromechanical transducer elements (TRANS126) under the bottom surface nodes of the CMUT membranes, while a gap value (GAP) and a minimum gap value (GAPMIN) are used to provide ground plane nodes and determine maximum possible deflection before snap-down occurs. Using 3-D axisymmetric acoustic fluid (FLUID30), a fluid loading is included to simulate the dynamic behavior of the CMUTs and model the fluid medium and the interface in fluid/structure interaction. The structural motion is coupled as an acoustic wave in the medium by enabling the fluid/structure flags. More details about the FEM model can be found in [4] and [5] as we based our FEM models on their work. Compared with the ANSYS 3-D FEM results, the obtained responses show close predictions. However, it takes several hours for FEM simulations to be completed, even for elementary groups of a few cells. The modeling and simulation of very large and complicated arrays is almost impossible with FEM analysis. To check the accuracy of the FEM models, we increased the mesh size until the mean square errors of results relative to previous mesh sizes changed negligibly. In addition, we compared our FEM results with previously published FEM simulations [1], [6] for single CMUT cells and CMUT arrays with the same membrane sizes to ensure accuracy.

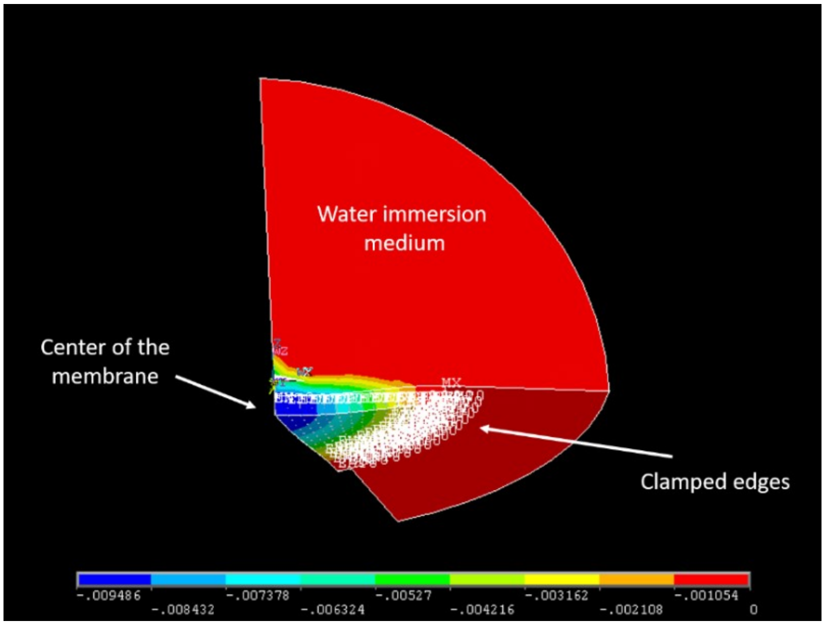

Fig. 4.2. Ansys 3D axisymmetric model of a circular CMUT cell with smallest periodic portion (1/6th) in water immersion medium.

4.2.1 The Effects of the Mutual Radiation Impedance in Closely Packed CMUT Cells of Different Membrane Sizes

To evaluate the effects of the mutual radiation impedance on the frequency response of the CMUT cells, different multi-frequency CMUT arrays are simulated in water immersion mode. Six CMUT cells with different radii and membrane thicknesses are considered to resonate at around 3 MHz and 4.5 MHz in water as large and small cells, respectively. Table 4.I summarizes the physical parameters, DC bias voltages and drive signals of these CMUT cells. Notice that the multi-frequency arrays with larger radii should have thicker membranes to have the same resonance frequencies. First, we use the parameters of the multi-frequency array #2 (Table 4.I) to investigate the effects of the mutual acoustic interactions in detail on each single CMUT cells of 1-cell, 2-cells, 3-cells (Fig. 4.3) and 7-hexagonal arrays (Fig. 4.4). Then, by considering the effects of the mutual interactions on total electrical conductance, G, (the real part of the admittance) of each array, we will compare the results of these different configurations. To calculate conductance, the net current flowing through all membranes is divided by the parallel applied voltage. In ANSYS the current passing through each membrane is found by obtaining the total reaction force data (reaction current of each membrane).

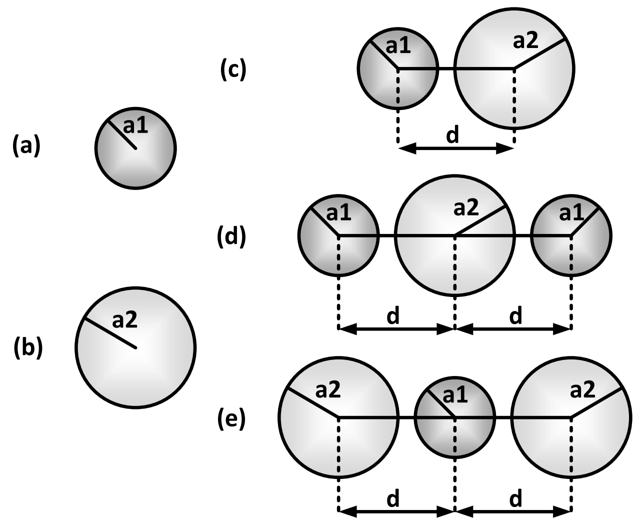

Fig. 4.3. Configuration of single CMUT cells with (a) small, (b) large membranes and CMUT array elements with (c) two cells of different sizes, (d) three cells with the large one at the center and (e) three cells with the small one at the center, located on an infinite rigid baffle.

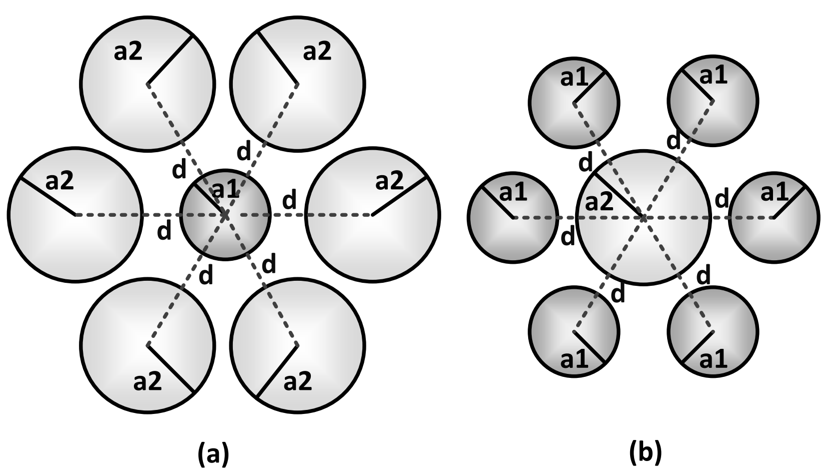

Fig. 4.4. Configuration of 7-cell hexagonal CMUT array elements with (a) the small membrane in the center and (b) large membrane in the center, located on an infinite rigid baffle.

TABLE 4.I. PARAMETERS OF THE CMUT CELLS USED IN EQUIVALENT CIRCUIT MODEL AND FEM SIMULATIONS.

Parameter	Designs		
	Multi-Frequency #1	Multi-Frequency #2	Multi-Frequency #3
Small membrane radius, a_1 (μm)	110 ($\simeq \lambda/3$)	93 ($\simeq \lambda/3.5$)	83 ($\simeq \lambda/4$)
Large membrane radius, a_2 (μm)	129 ($\simeq \lambda/4$)	110 ($\simeq \lambda/4.5$)	98 ($\simeq \lambda/5$)
Center to center distance, d (μm)	259	223	201
Membrane thickness, t_m (μm)	18.75	14	11.4
Insulator thickness, t_i (nm)	100	100	100
Gap height, t_{ga} (nm)	200	200	200
Young's modulus, Y_0 (GPa)	290	290	290
Density, ρ (g/cm^3)	3.1	3.1	3.1
Poisson's ratio, σ	0.263	0.263	0.263
Collapse voltage of small membrane (V)	192	175	163
Collapse voltage of large membrane (V)	142	127	118
Bias voltage, V_{DC} (V)	60	60	60
Driven signal, V_{AC} (V)	1 V peak	1 V peak	1 V peak
Medium	Immersion in water Density of the water is 1.0 (g/cm^3) and speed of sound in water is 1500 m/s. λ is the wavelength in water at 3 MHz and 4.5 MHz for large and small membranes, respectively.		

Fig. 4.5 demonstrates the simulated hexagonal CMUT arrays shown in Fig. 4.4 in Ansys environment.

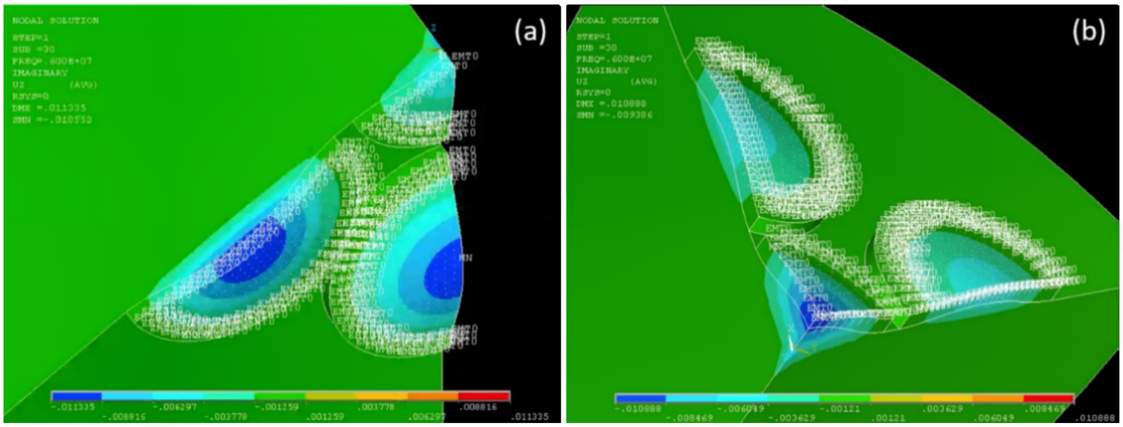

Fig. 4.5. Ansys 3D axisymmetric model of hexagonal CMUT arrays shown in Fig. 4.4 with smallest periodic portion (1/6th) in water immersion medium.

Fig. 4.6 demonstrates the investigation of the mutual radiation impedance on resonance frequency, the amplitude and phase of the peak displacement and the total electrical conductance of considered arrays by using the parameters of the multi-frequency array #2 of Table 4.I. The single small ($a_1 \simeq \lambda_H/3.5$) and large ($a_2 \simeq \lambda_L/4.5$) CMUT cells resonate at around 3 MHz and 4.5 MHz in water immersion mode without having any other cells in proximity. Here λ_H and λ_L are the wavelengths of the resonant frequencies in water. The subscripts are dropped in Table 4.I for notational simplicity. By adding a few more cells with larger and/or smaller membranes, the resonance frequency, the amplitude and phase of the peak displacement of each single cell are changed. For example, the peak displacement amplitude of the single large and small cells with 110 μm and 93 μm radii are 1.219 nm at 3.03 MHz and 0.5307 nm at 4.510 MHz, respectively. When these cells are interlaced together with 223 μm center to center distance (20 μm kerf), the peak displacement amplitude of the large and small cells becomes 1.167 nm at 3.005 MHz and 0.6372 nm at 4.505 MHz, respectively (Fig. 4.6, Two CMUT Cells).

The effects of the mutual acoustic interactions can be observed further when we add more cells with different cell apertures. According to the results, each CMUT membrane is influenced by mutual radiation impedance in a different manner. For instance, the resonance frequencies of large CMUT cells shift to higher frequencies in the array of Fig. 4.4 (a) while it shifts to lower values when we consider the array of Fig. 4.4 (b). This happens because the CMUT cells experience different acoustic loads (different Z-matrix) from the immersion medium.

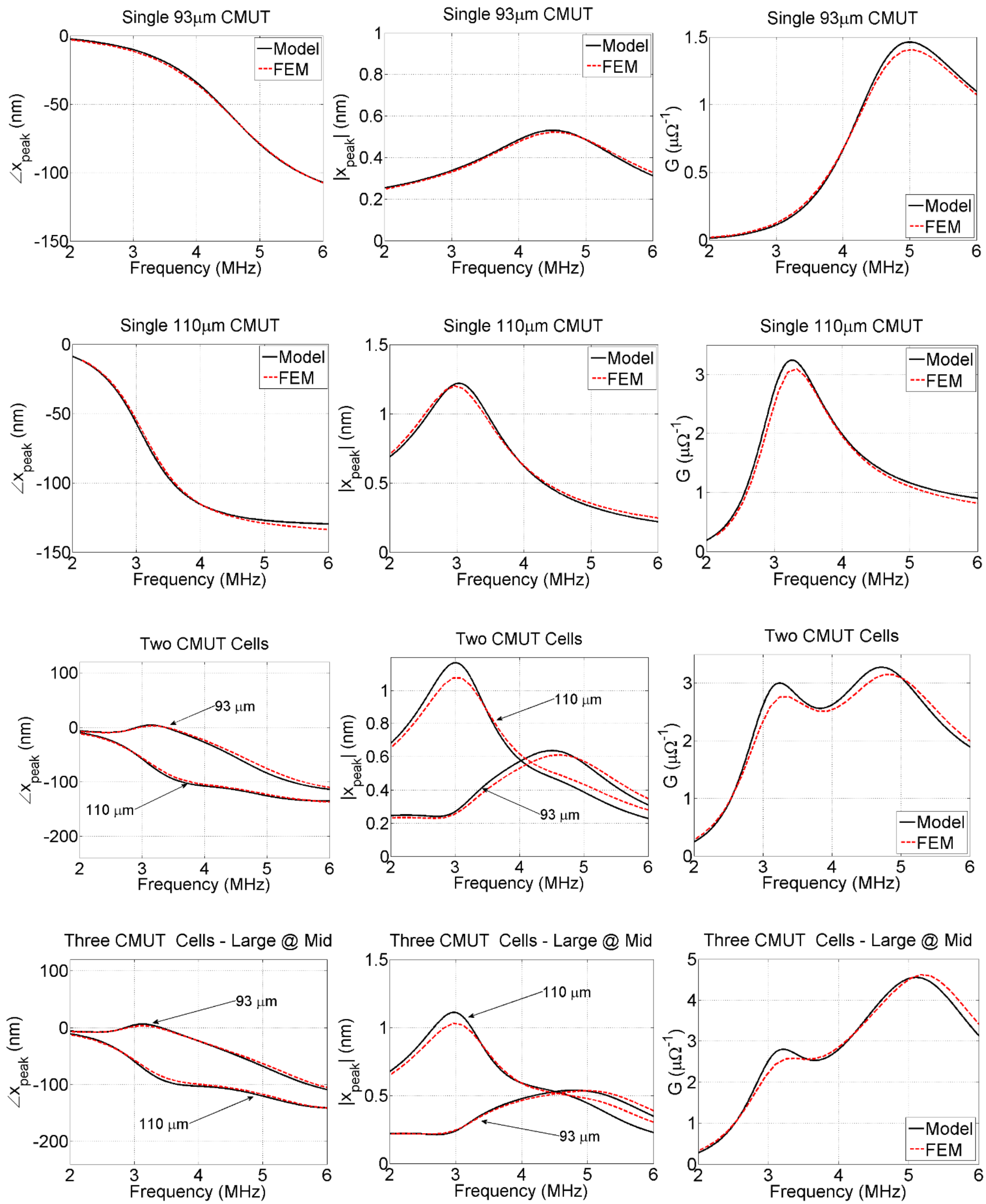

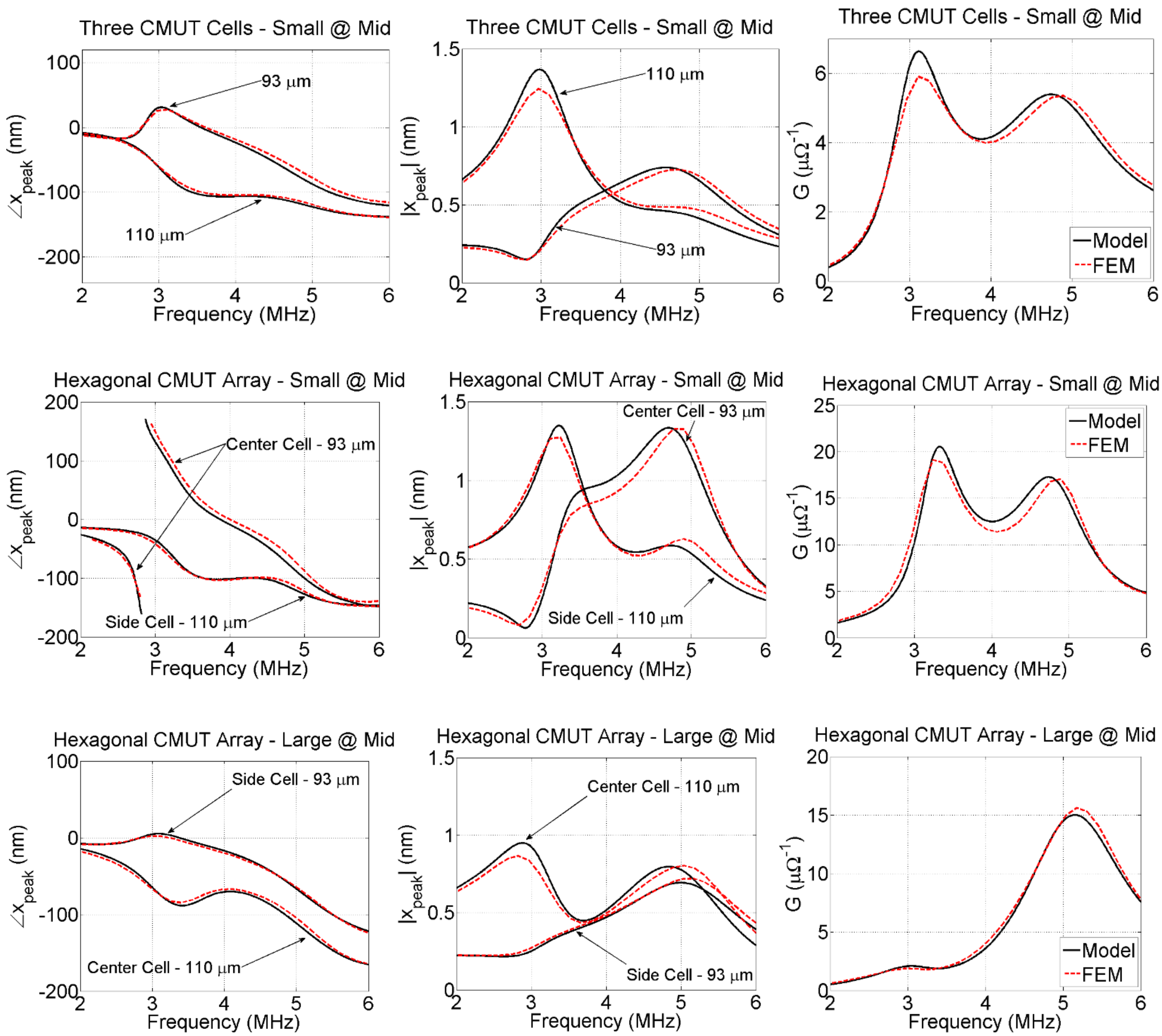

Fig. 4.6. Amplitude and phase of the peak displacement and the total electrical conductance of the single CMUT cells and CMUT array elements with two, three, and seven cells, using the parameters of multi-frequency array #2 (Table 4.I). The cells are located on an infinite rigid baffle and immersed in water.

The total electrical conductance, G, of the parallel connected CMUT cells for all types of array configurations are plotted in the graphs in the right column of Fig. 4.6 using the CMUT parameters of multi-frequency array #2 of Table 4.I. It can be observed that, the peak value of the conductance for single cells changes by adding more cells in its proximity. The effects of mutual radiation impedance on total electrical conductance of different types of arrays (Fig. 4.3 and Fig. 4.4) are evaluated in detail in the following section.

4.2.2 The Effects of the Mutual Acoustic Interactions on Total Conductance of Different CMUT Arrays

Equivalent circuit and FEM simulations are done for multi-frequency arrays #1, #2 and #3 of Table 4.I in water immersion to observe the effects of cell radius and membrane thickness on mutual acoustic interactions in each particular cell configuration on an infinite rigid baffle. The total electrical conductance of the parallel connected multi-sized cells for 2-, 3- and 7-cells with the small membrane centrally located are plotted in Fig. 4.7. The parallel connected multi-sized cells refers to the Figs. 4.3-c, 4.3-e and 4.4-a with 2-, 3- and 7-cells with the small membrane centrally located. The cell spacing information has been provided in Table 4.I as center to center distance, d (μm). As can be observed, the graphs show two different peaks which represent different permanent resonance frequencies. The resonance frequencies with lower and higher values are obtained by larger and smaller membranes, respectively. Based on provided results for different types of arrays, mutual radiation impedance influences each single CMUT cell in different way by shifting their resonance frequencies to lower or higher values. For example, for a_1=110 ($\simeq\lambda/3$), Fig. 4.7 (multi-frequency array #1) shows that there is a shift in the resonance frequency to lower values as the number of cells increases while both Fig. 4.7 (multi-frequency array #2) and (multi-frequency array #3) show a shift to higher frequencies but with different rates. On the other hand, the permanent resonance frequencies of the large cells shift to lower values from 2-cells to 3-cells and they shift to higher values from 2- and/or 3-cells to 7-cells hexagonal arrays. These shifts in permanent resonance frequencies are caused by acoustic coupling of CMUT cells through the medium which is precisely modeled by obtained analytical and approximate expressions with excellent agreement with FEM simulations.

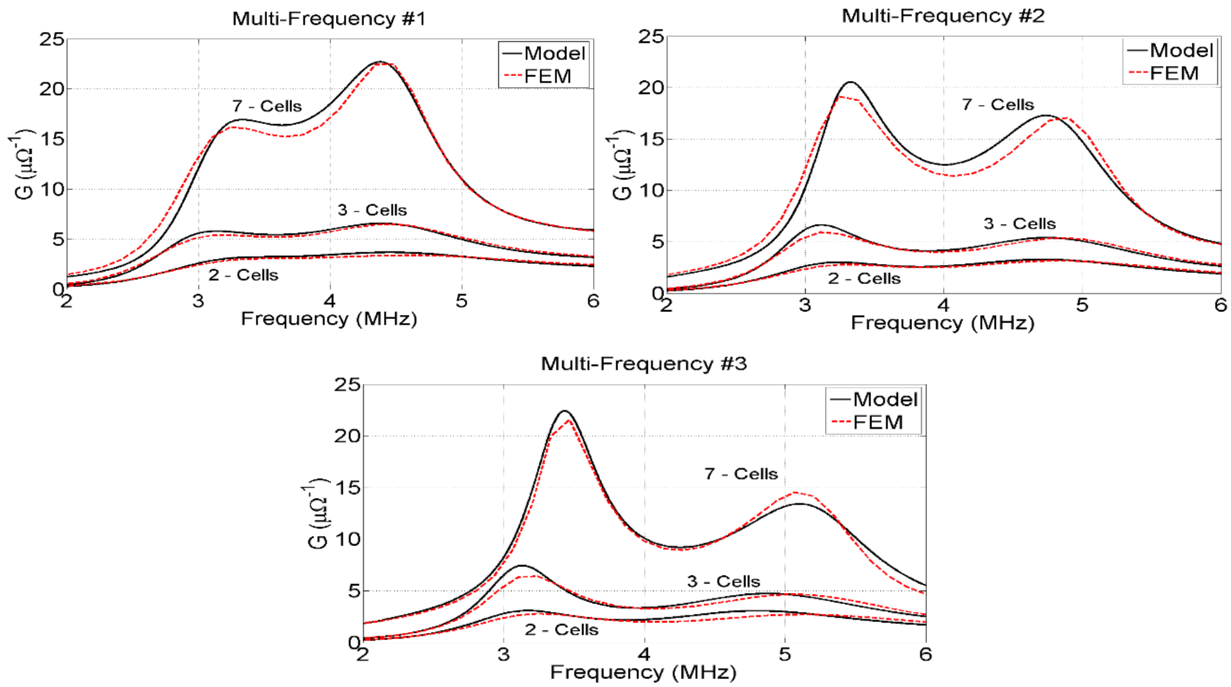

Fig. 4.7. Total electrical conductance of multi-frequency CMUT array elements with 2-, 3- and 7-cells with the small cell at the center, using the parameters of multi-frequency arrays #1, #2 and #3 of Table 4.I, located on an infinite rigid baffle and immersed in water.

4.3 Modelling of Large-Scale Multi-Frequency CMUT Arrays with Circular Membranes

In this section we extend the equivalent circuit modelling to large-scale simulations of realistic multi-frequency CMUT arrays. The model may prove useful in engineering next-generation multi-frequency CMUT transducers. Figure 4.8 shows a large-scale multi-frequency CMUT array including interlaced large and small membranes with low and high resonance frequencies, respectively. The array includes 400 CMUT cells in 20 by 20 configuration in which the center to center distance of the cells is $d = 215\ \mu m$ (kerf = 12 μm) while the radiuses of the large and small transducers are 110 and 93 μm, respectively. Cells with different radii and membrane thicknesses are considered to resonate at around 3 and 4.5 MHz in water immersion mode using the parameters provided in Table 4. II.

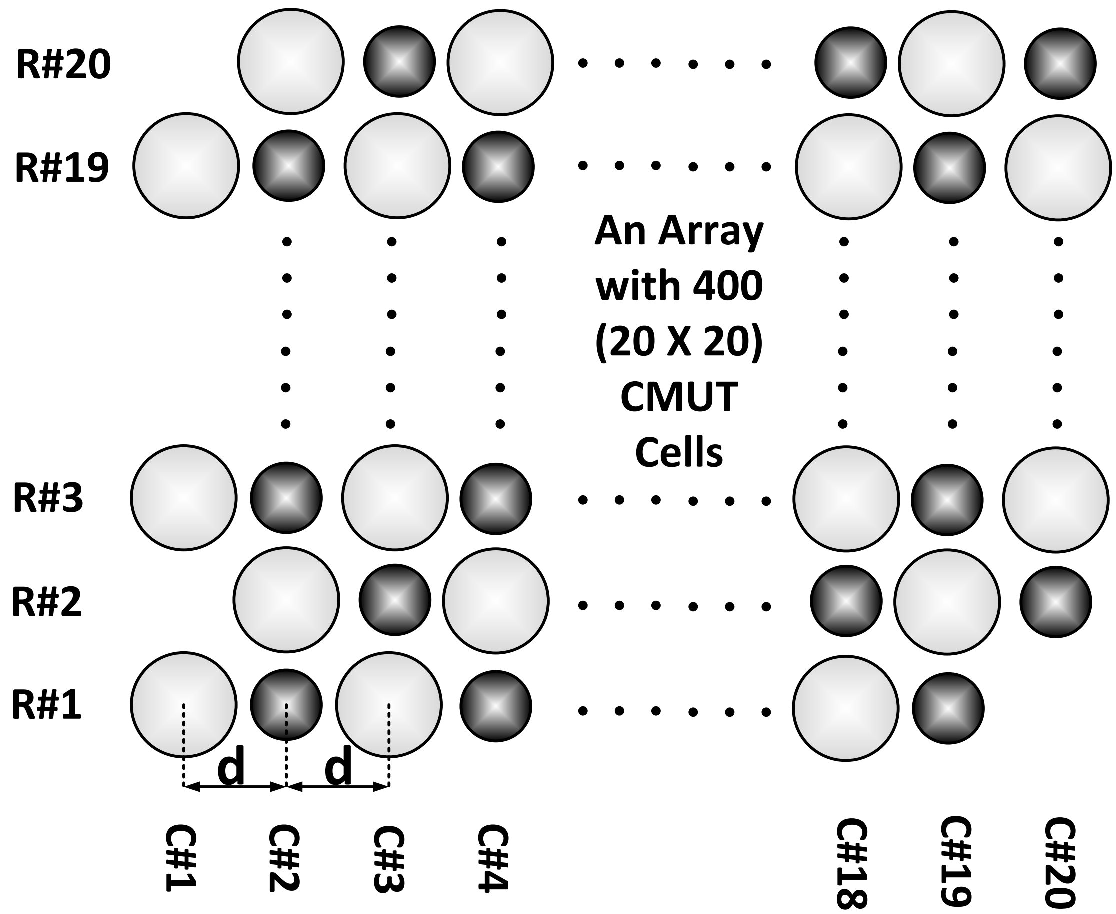

Fig. 4.8. A large-scale multi-frequency CMUT array with 400 cells in 20 by 20 configuration.

Figure 4.9 demonstrates the cross-talking effects between CMUTs with different membrane sizes on their resonance frequencies, the amplitude and phase of the peak displacement, and the total electrical conductance. The phase and amplitude of the peak displacement for four random CMUT cells are shown in Figures 4.9-a and 4.9-b, respectively.

Based on the provided results for cells in different parts of the multi-frequency array, mutual radiation impedance affects each single cell in a different way by shifting the resonance frequencies to higher or lower values. For example, in Figure 4.9-b, the resonance frequency of CMUT#1 shifts from 3 MHz to 3.46 MHz while for CMUT#17 there is a shift from 3 MHz to 3.39 MHz which is less compared to CMUT#1. Moreover, Figure 4.9-b shows shifting from 4.5 MHz to higher values for high-frequency CMUT cells but with different rates.

TABLE 4.II. PARAMETERS OF THE CMUT CELLS USED FOR MODELING OF LARGE-SCALE MULTI-FREQUENCY CMUT ARRAYS.

Parameter	Designs		
	Multi-Frequency Array #1 [3]	Multi-Frequency Array #2	Multi-Frequency Array #3
Small membrane radius, a_1 (µm)	93	89	54
Large membrane radius, a_2 (µm)	110	106	106
Center to center distance, d (µm)	223	201	223
Membrane thickness, t_m (µm)	14	11.4	14
Insulator thickness, t_i (nm)	100	100	100
Gap height, t_{ga} (nm)	200	200	200
Young's modulus, Y_0 (GPa)	290	290	290
Density, ρ (g/cm^3)	3.1	3.1	3.1
Poisson's ratio, σ	0.263	0.263	0.263
Collapse voltage of small membrane (V)	175	191	468
Collapse voltage of large membrane (V)	127	137	137
Bias voltage of small membrane, V_{DC_S} (V)*	60	153	374
Bias voltage of large membrane, V_{DC_L} (V)*	60	110	110
Driven signal, V_{AC} (V)	1 V peak	1 V peak	1 V peak

Medium	Immersion in water Density of the water is 1.0 (g/cm^3) and speed of sound in water is 1500 m/s. *For designs#2 and #3, the applied DC bias voltages are equal to ~80% of the CMUTs collapse voltages.

Figure 4.9-c demonstrates the total electrical conductance G of the parallel connected CMUT cells inside of the array which is calculated by the net current passing through all membranes divided

by the parallel applied voltage. As shown in this figure, the permanent resonance frequencies of the large and small CMUT cells shift to higher values which is caused by acoustic coupling through the medium. Depends on the CMUT parameters, array configuration and shape, mutual radiation impedance influences single cells in different ways [7].

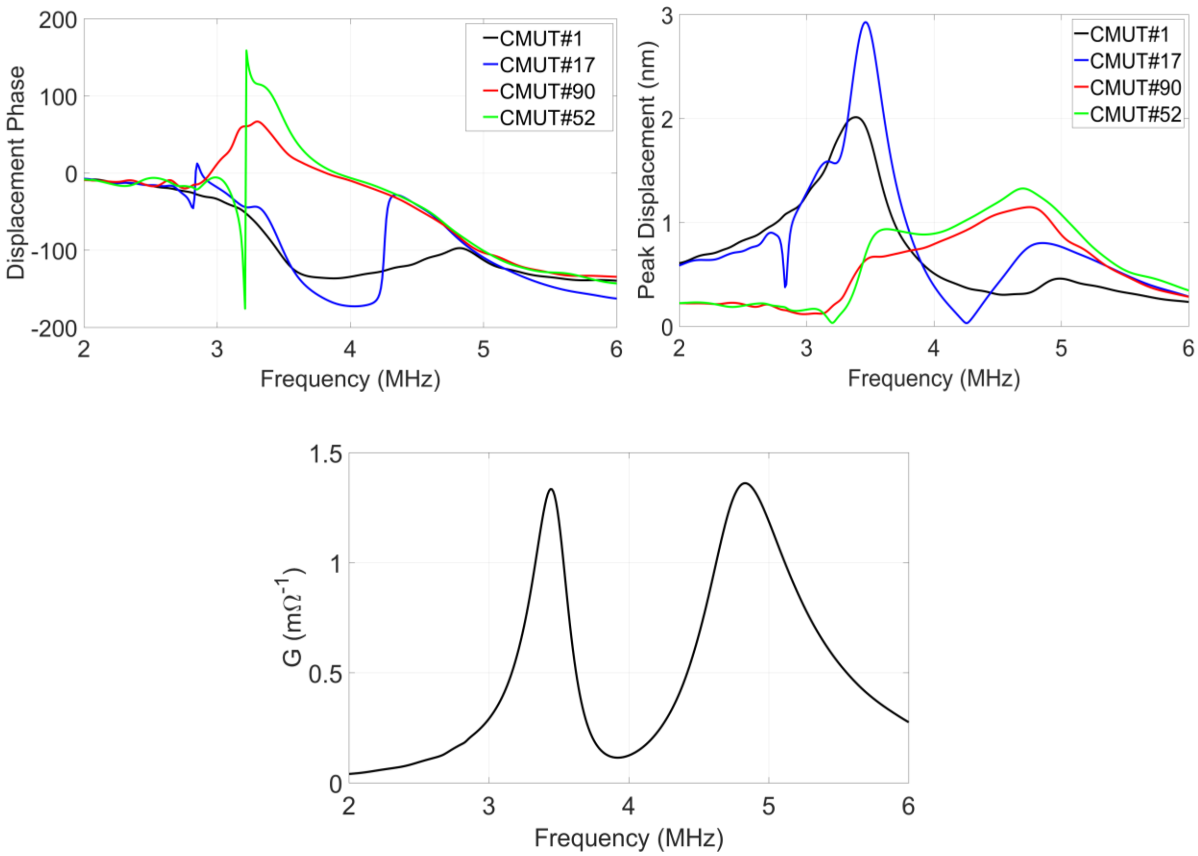

Fig. 4.9. (a) The phase of the peak displacement for random CMUT cells inside of the large-scale multi-frequency array. (b) The amplitude of the peak displacement for random CMUT cells inside of the large-scale multi-frequency array. (c) Total electrical conductance of the parallel connected CMUT cells.

4.4 The Effects of Different Biasing Methods on performance of the Array

In section 4.3, the same AC and DC voltages were applied to low and high frequency CMUT cells in parallel driving mode. In this section, we evaluate the effects of different biasing methods on the performance of the array using the parameters of multi-frequency array #2 and #3 summarized in Table 4.II. Large membranes are designed to resonate around 3 MHz when they are optimally biased at ~80% of their collapse voltages while small membranes have the resonance frequency of 4.5 MHz (multi-frequency array #2) and 15 MHz (multi-frequency array #3) in their optimally biasing voltages.

Figure 4.10 shows the effects of different biasing methods on total electrical conductance of considered large-scale multi-frequency array using different parameters. In first approach, we drive all cells including large and small membranes in parallel mode. The cells with different resonance frequencies are excited with the same AC voltages but with 80% of their collapse voltages which is different for low and high frequency membranes. For example, in Figure 4.10-a, large cells have a DC bias of 110 V while small membranes are biased at 153 V (Table 4.II). In the second method, we grounded the small membranes during driving the low frequency cells and grounded the large cells during exciting the high frequency transducers. Figure 4.10-b repeats the same analysis for a large-scale multi-frequency CMUT array including 3 MHz and 15 MHz cells. As can be observed, the array shows improved performance using the second method.

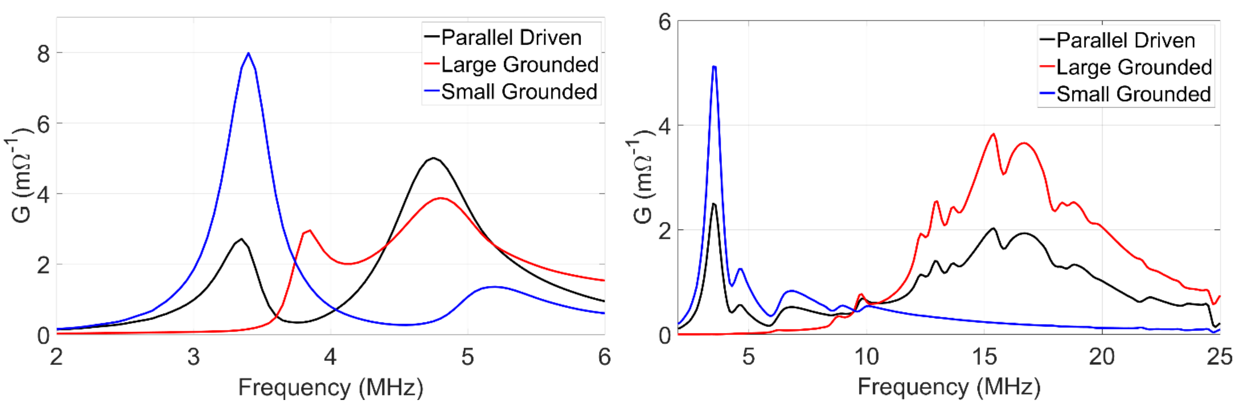

Fig. 4.10. (a) Total electrical conductance of a large-scale multi-frequency CMUT array including 3 MHz and 4.5 MHz transducers using different biasing methods. (b) Total electrical conductance of a large-scale multi-frequency CMUT array including 3 MHz and 15 MHz transducers using different biasing methods.

4.3 Conclusion

An equivalent circuit model was developed for multi-frequency CMUT arrays. The effects of the mutual acoustic interactions for cells of different sizes were evaluated in detail by implementing the obtained expressions into the models. The proposed models provided very precise results with accuracy comparable with FEM analysis but within considerably less time. Approximated versions of the obtained analytical expressions for mutual radiation impedance were used during the simulations. These approximations were used to reduce the simulation time even further. Equivalent circuit simulations run in seconds compared to hours for FEM analysis. Different types of multi-frequency CMUT array configurations with different parameters were designed and simulated. The results proved that, to have an optimum design the CMUT cells should be modeled, simulated and analyzed in an array mode by considering the effects of the mutual radiation interaction.

The proposed nonlinear lumped equivalent circuit model including the effects of the cross-talks between multi-sized CMUT cells was then used to model the large-scale multi-frequency CMUT arrays including interlaced large and small membranes. The model predicts the effects of mutual acoustic impedance on behavior of CMUT cells with different resonance frequencies in any part of the array. The effects of different biasing methods on performance of the arrays were evaluated for different sets of CMUT parameters.

The proposed large-scale circuit model can be used to design, model and fabricate large multi-frequency linear CMUT arrays for ultrasound super-harmonic contrast agent imaging, multi-band photoacoustic imaging, and imaging-therapy applications.

References

[1] H. Köymen, A. Atalar, E. Aydoğdu, C. Kocabas, H. K. Oğuz, S. Olcum, A. Ozgurluk, and A. Ünlügedik, “An improved lumped element nonlinear circuit model for a circular cMUT cell,” *IEEE Trans. Ultrason. Ferroelectr. Freq. Control*, vol. 59, no. 8, pp. 1791–1799, 2012.

[2] D. T. Porter, “Self-and Mutual-Radiation Impedance and Beam Patterns for Flexural Disks in a Rigid Plane,” J. Acoust. Soc. Am., vol. 36, pp. 1154-1161, 1964.

[3] N. M. Senlik, S. Olcum, H. Koymen, and A. Atalar, “Radiation impedance of an array of circular capacitive micromachined ultrasonic transducers,” *IEEE Trans. Ultrason. Ferroelectr. Freq. Control*, vol. 57, no. 4, pp. 969-976, 2010.

[4] H. K. Oguz, “Circuit theory based modeling and analysis of CMUT arrays” *PhD diss.*, Bilkent university, 2013.

[5] S. Olçum, “Deep collapse mode capacitive micromachined ultrasonic transducers.” *PhD diss.*, Bilkent University, 2010.

[6] H. K. Oguz, A. Atalar, and H. Koymen, “Equivalent circuit-based analysis of CMUT cell dynamics in arrays,” *IEEE Trans. Ultrason. Ferroelectr. Freq. Control*, vol. 60, pp. 1016-1024, 2013.

[7] M. Maadi, and R. J. Zemp, “Self and Mutual Radiation Impedances for Modeling of Multi-Frequency CMUT Arrays,” *IEEE Trans. Ultrason., Ferroelect., Freq. Control*, vol. 63, no. 9, pp. 1441–1454, Sep. 2016.

Chapter 5

Design, Fabrication, and Characterization of Multi-Frequency CMUT Arrays Using Sacrificial Release Process

5.1 Introduction

CMUT arrays can be fabricated using sacrificial release [1] or wafer-bonding methods [2]. The basic principle of a process flow based on a standard surface micromachining, particularly sacrificial release process, is to form a gap under a thin membrane by making release holes to access sacrificial layer and then selectively etching the sacrificial layer and releasing the membrane. However, the major problems about the sacrificial release process is the poor control over the uniformity and device parameters, and complexity of the fabrication. On the other hand, wafer bonding process flow aims to have more control on fabrication steps with better repeatability. In this process, two prime and SOI (silicon-on-insulator) wafers are bonded together after forming the gap on a prime wafer by etching the oxide layer. More details about various developed process flows to make CMUT arrays can be found in [3]. We fabricated circular and square CMUT arrays using a silicon nitride sacrificial release process that was recently developed in our group [4] with slight modifications.

5.2 Designed Multi-Frequency CMUT Arrays

Several multi-frequency CMUT arrays were designed with different array parameters. Six different masks were used to finish the fabrication of designed arrays (Fig. 5.1). Table 5.I summarizes the specifications of designed and fabricated devices. These devices were designed for various possible ultrasound imaging and therapeutic applications. In following sections, we showed the feasibility of designed and fabricated arrays for multi-band ultrasound imaging and micro-bubble contrast agent imaging applications.

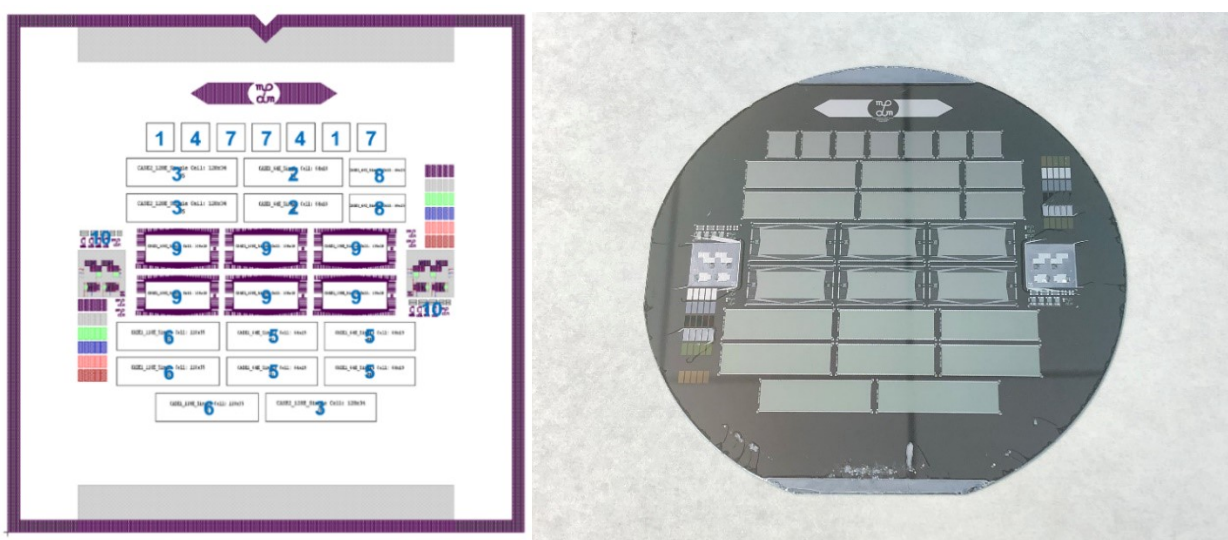

Fig. 5.1. (Left) Final design including 6 masks. (Right) Final fabricated devices using silicon-nitride sacrificial release process.

TABLE 5.I. DESIGNED AND FABRICATED MULTI-FREQUENCY CMUT ARRAY SPECIFICATIONS.

Fabricated Devices						
Design	Resonance Frequency (MHz) and Wavelength* (μm)	Number of Elements	Width of an Element (μm)	Pitch (μm)	Kerf (μm)	Array Size (mm × mm)
1	TX** = 2 & RX** = 8	32	144	184	40	7 × 7
2	λ (Low) = 734.5	64	318	328	10	22 × 7
3	λ (High) = 183.625	128	144	184	40	24.562 × 7
4	TX = 2 & RX = 9	35	131	171	40	7 × 7
5	λ (Low) = 734.5	64	292	302	10	20.348 × 7
6	λ (High) = 163.22	128	131	171	40	22.898 × 7
7		32	141	186	45	7 × 7
8	TX = 2 & RX = 15	64	141	186	45	12.914 × 7
9	λ (Low) = 734.5 λ (High) = 97.93	128	63	108	45	18.354 × 9.418
10	Several Test Devices	N/A	N/A	N/A	N/A	× 4

* The speed of sound in vegetable oil is 1430 m/s.

** TX and RX are transmit and receive frequencies, respectively.

5.3 Fabrication Details of Multi-Frequency CMUT Arrays

Highly conductive ($0.001\ to\ 0.005\ \Omega - cm$) P-type silicon prime wafers were used to make the designed multi-frequency CMUT arrays. First, the wafers were Piranha cleaned in a 3:1 solution of sulphuric acid and hydrogen peroxide and then buffered oxide etching (BOE) was used to remove the native oxide on the wafers. Then we deposited 250nm low-stress low-pressure chemical vapor deposition (LPCVD) thin silicon nitride as insulation layer, 50nm Plasma-enhanced chemical vapor deposition (PECVD) silicon dioxide as an etch-stop layer for reactive ion etching (RIE) of the sacrificial layers and 250nm LPCVD undoped poly-silicon sacrificial layer on cleaned wafers (Fig. 5.2).

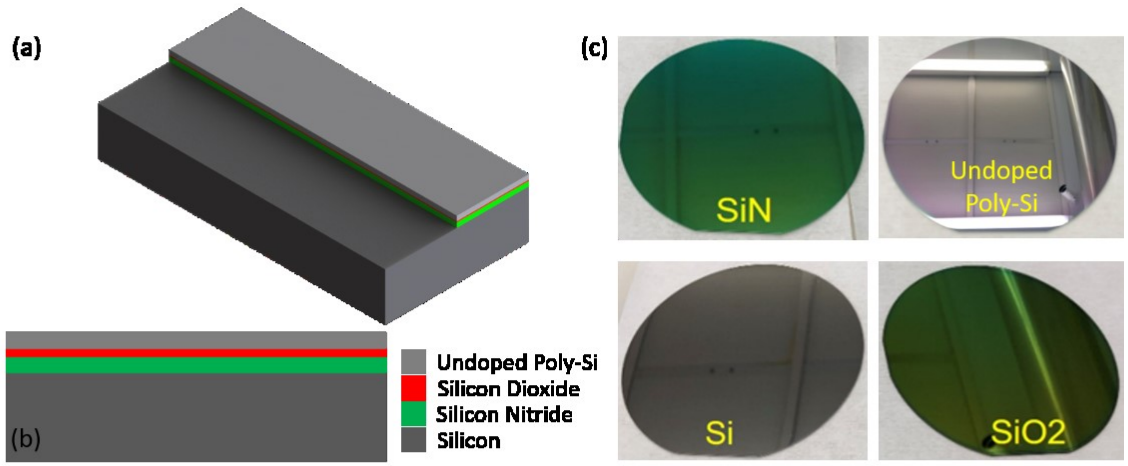

Fig. 5.2. Deposition of thin bottom silicon nitride insulation film, silicon dioxide protection layer and first thick poly-silicon sacrificial layer. (a) 3D cross-sectional view, (b) cross-sectional view, and (c) final wafer with deposited layers.

In next step the wafer is patterned using a highly anisotropic reactive ion etching (RIE) to define the area of the plugs (Fig. 5.3).

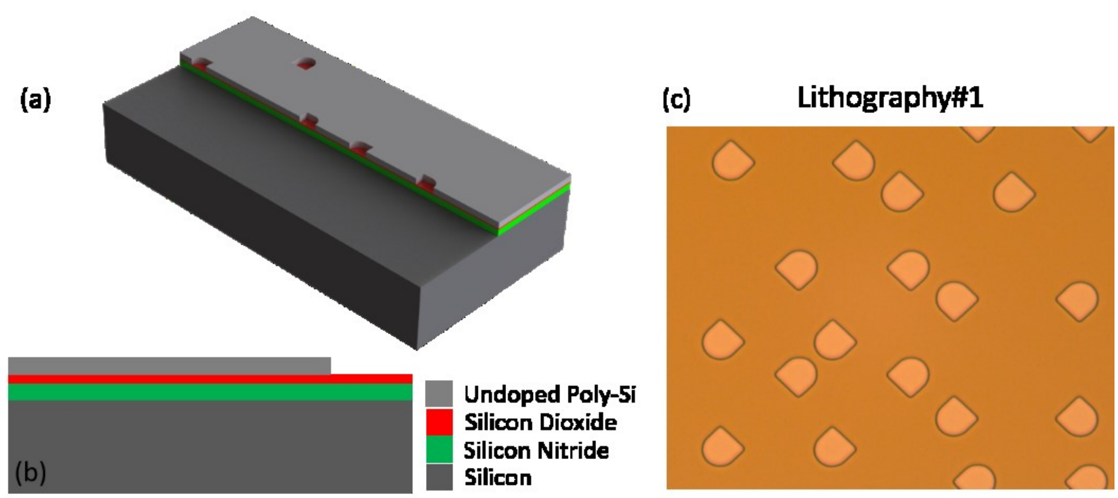

Fig. 5.3. RIE of 250nm un-doped poly silicon. (a) 3D cross-sectional view, (b) cross-sectional view, and (c) microscopic image after lithography#1.

Then another 100nm LPCVD un-doped polysilicon is deposited (Fig. 5.4) as the second sacrificial layer and is patterned to define the low-height etching channels, while slightly increasing the poly-silicon sacrificial layer in the gap area (Fig. 5.5).

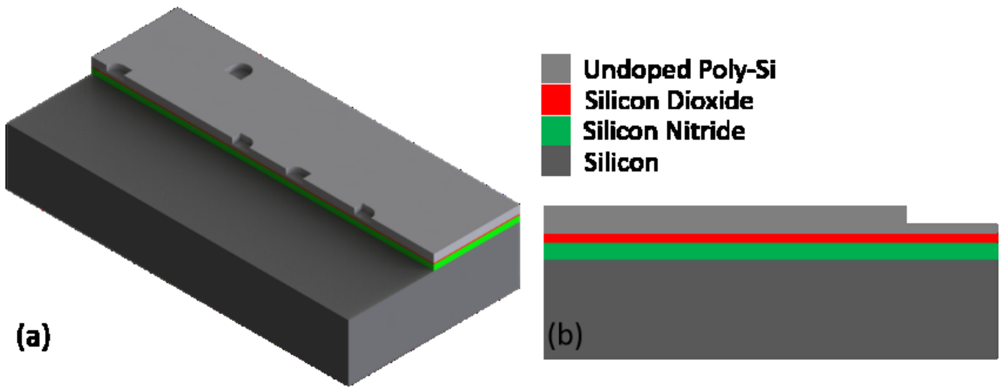

Fig. 5.4. Deposition of second thin poly-silicon sacrificial layer. (a) 3D cross-sectional view, and (b) cross-sectional view.

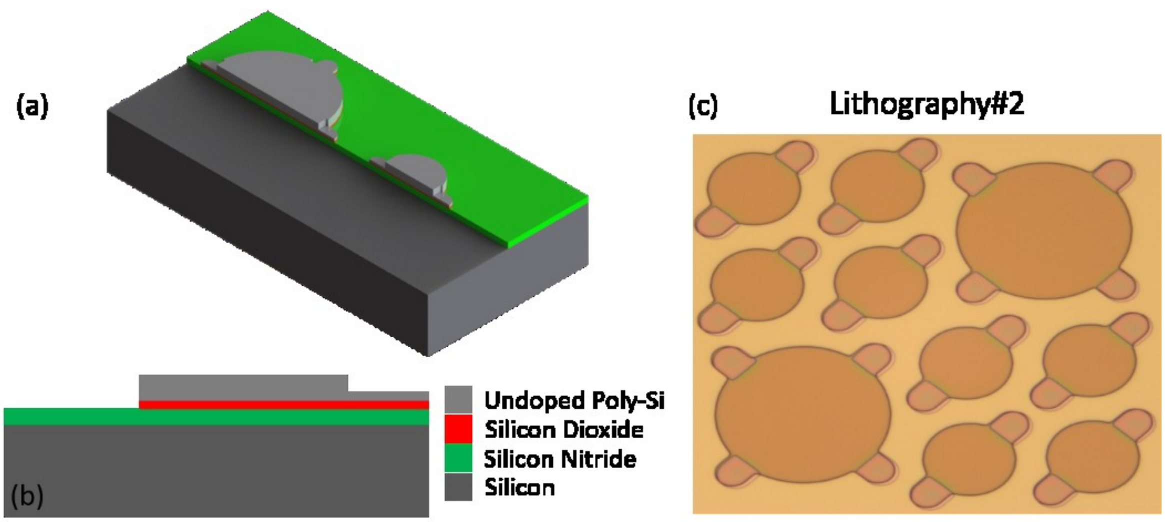

Fig. 5.5. Etching of poly-silicon sacrificial layer followed by a quick BOE of exposed silicon dioxide protection layer. (a) 3D cross-sectional view, (b) cross-sectional view, and (c) microscopic image after lithography#2.

Then Over the patterned poly-silicon sacrificial layer, 1μm LPCVD silicon nitride is deposited as the device membrane (Fig. 5.6).

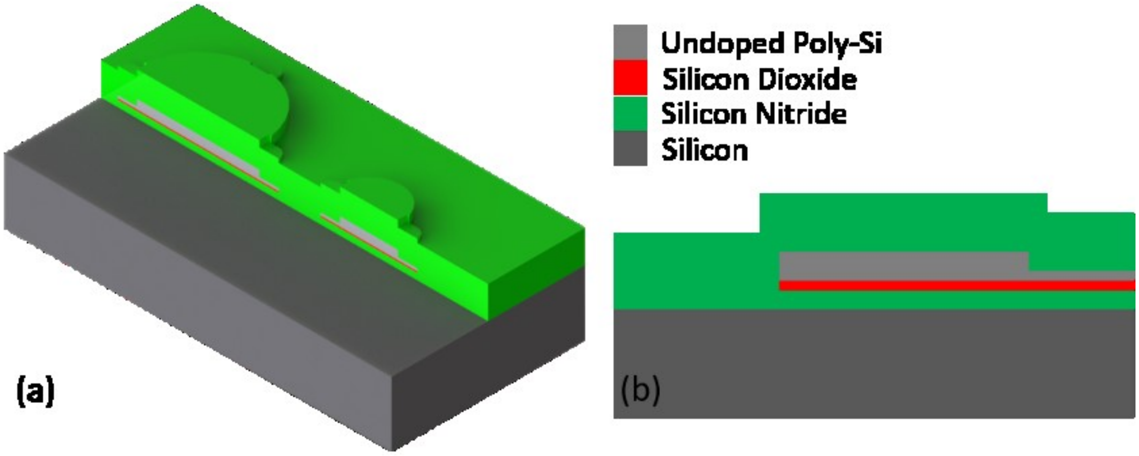

Fig. 5.6. Deposition of thick silicon nitride membrane. (a) 3D cross-sectional view, and (b) cross-sectional view.

To access the poly-silicon sacrificial layer, holes are etched through the membrane (Fig. 5.7). Then the membranes are released by KOH wet etching of combined sacrificial layers (Fig. 5.8). Long KOH etching removes the entire sacrificial layers including 350nm polysilicon and 50nm silicon dioxide layers beneath the gap. To minimize stiction defects, the critical point drying (CPD) step must be done after releasing the membrane.

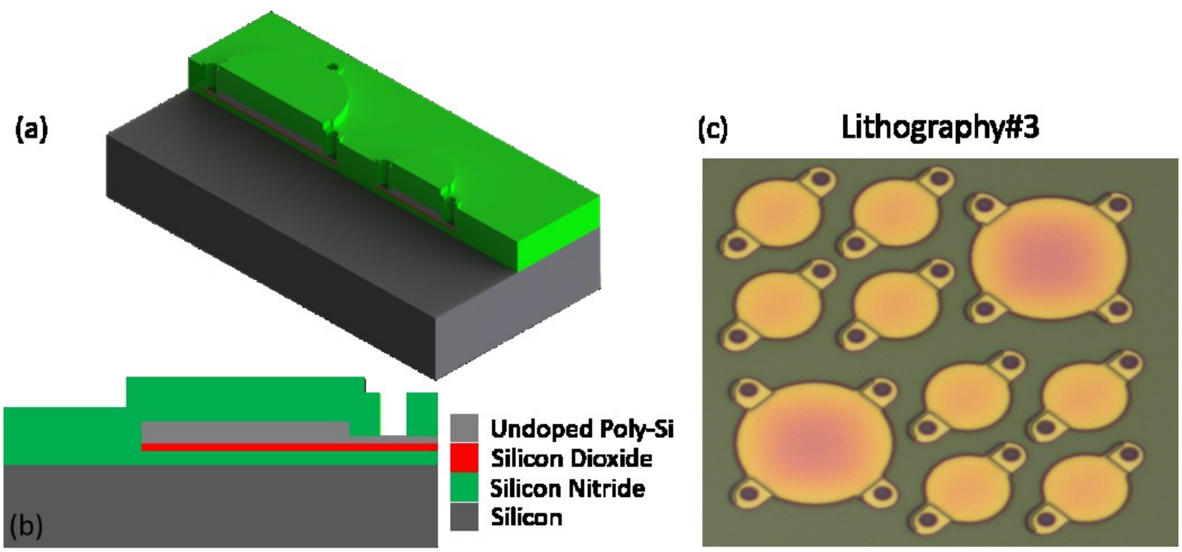

Fig. 5.7. Etching of the silicon nitride membrane to get access to the poly-silicon sacrificial layer. (a) 3D cross-sectional view, (b) cross-sectional view, and (c) microscopic image after lithography#3.

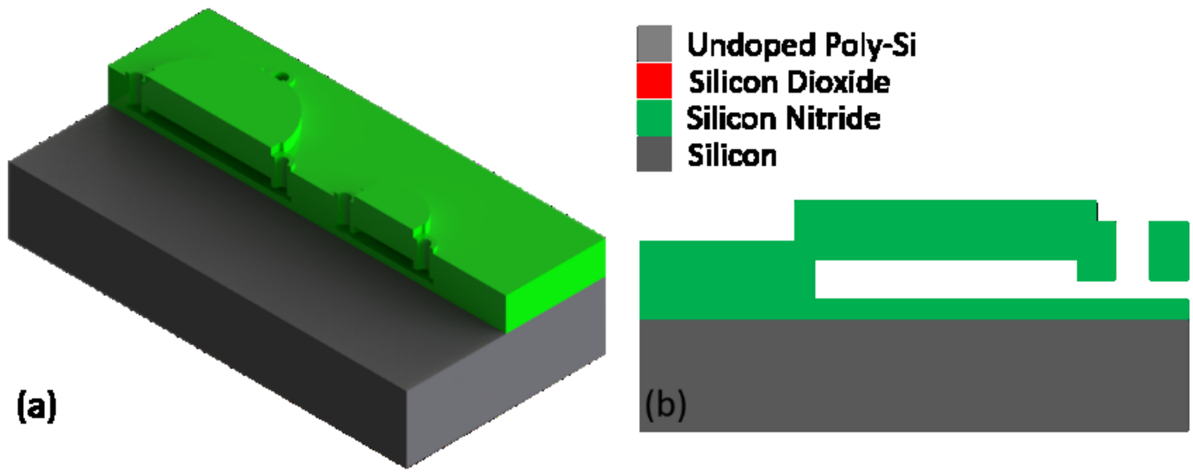

Fig. 5.8. Chemical etching of combined sacrificial layers to release the membrane. (a) 3D cross-sectional view, and (b) cross-sectional view.

A low-stress PECVD silicon dioxide is then deposited to seal the etch holes (Fig. 5.9), which is etched with the combination of dry and wet etching to form the seal plugs without coating the membranes (Fig. 5.10).

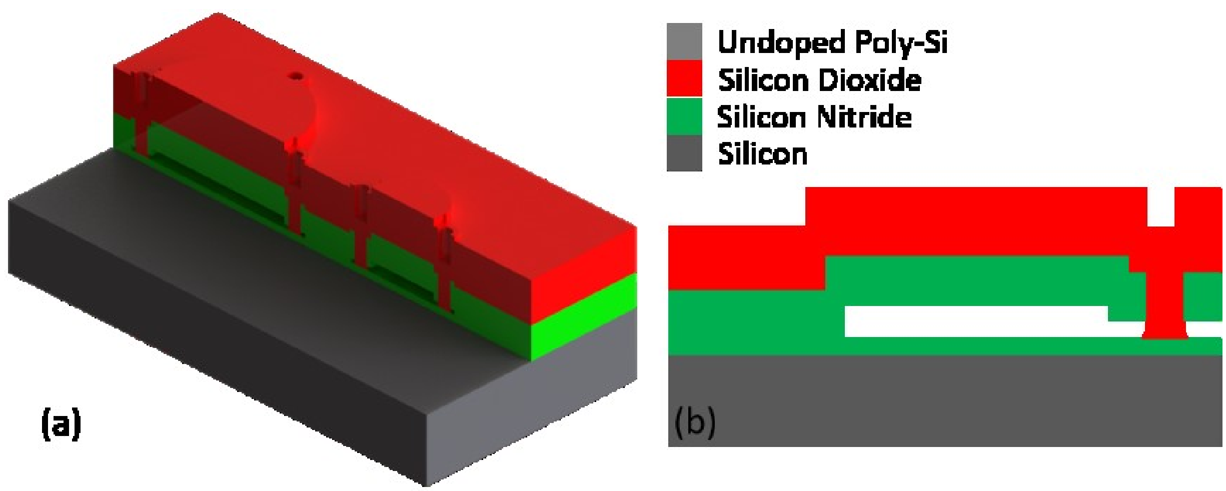

Fig. 5.9. Deposition of silicon dioxide sealing film. (a) 3D cross-sectional view, and (b) cross-sectional view.

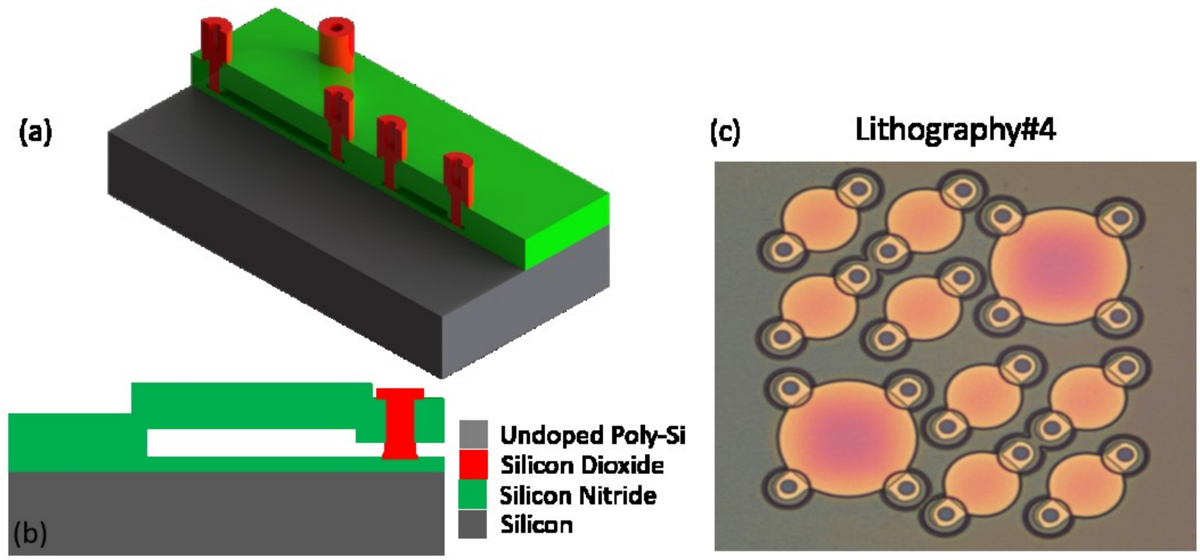

Fig. 5.10. Pattering the silicon dioxide sealing film into plugs. (a) 3D cross-sectional view, (b) cross-sectional view, and (c) microscopic image after lithography#4.

The final step after forming the CMUT cavity and sealing the holes to make the membranes, is defining top and bottom electrodes. Using RIE, bottom electrode holes are etched through the silicon nitride layer to access the substrate which is silicon (Fig. 5.11).

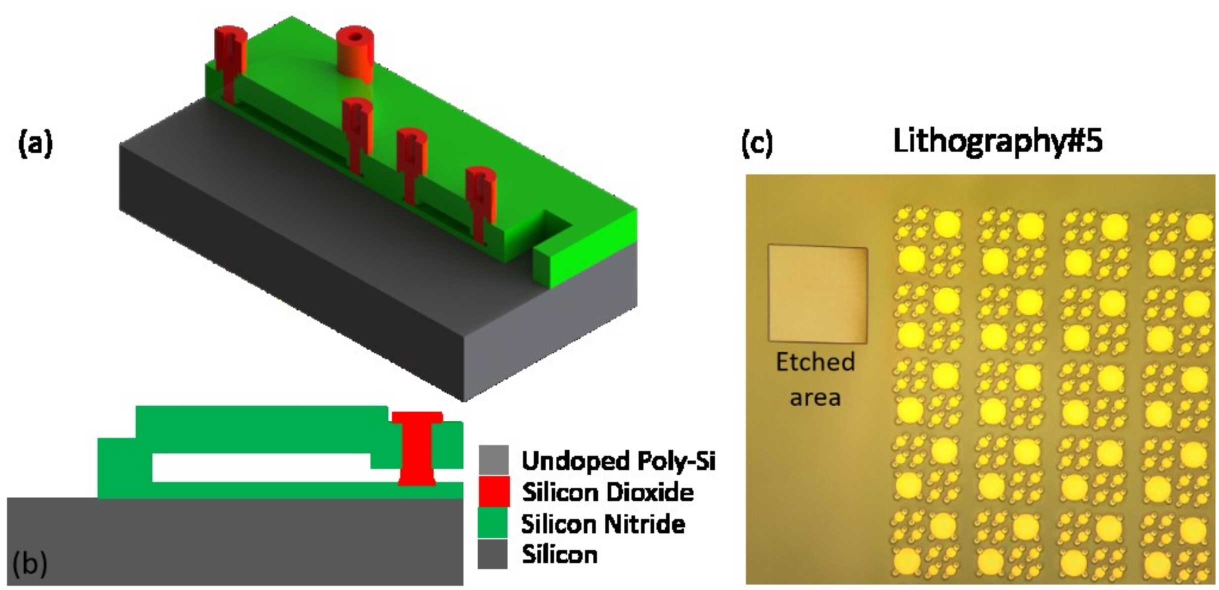

Fig. 5.11. Etching through the silicon nitride film to access the bottom silicon electrode. (a) 3D cross-sectional view, (b) cross-sectional view, and (c) microscopic image after lithography#5.

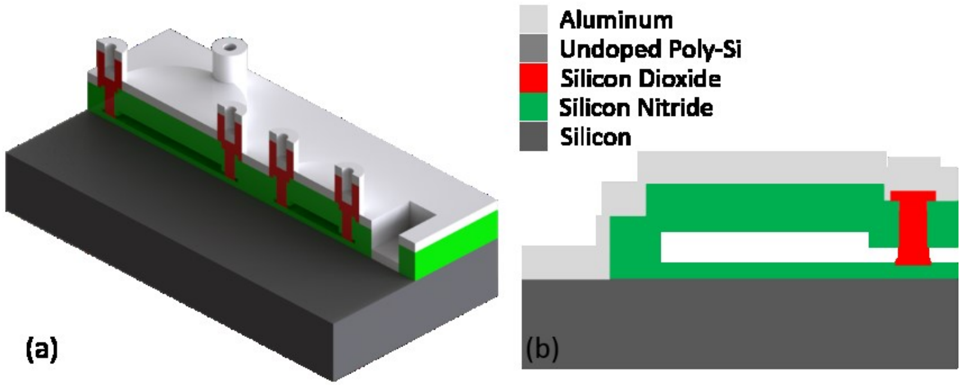

Fig. 5.12. Sputtering the aluminum film. (a) 3D cross-sectional view, and (b) cross-sectional view.

Using a magnetron sputtering system, the entire device is covered by a 400 nm aluminum (Fig. 5.12) and finally, top and bottom electrodes are formed by wet aluminum etching (Fig. 5.13). More details about the fabrication process can be found in [5] and Appendix C.

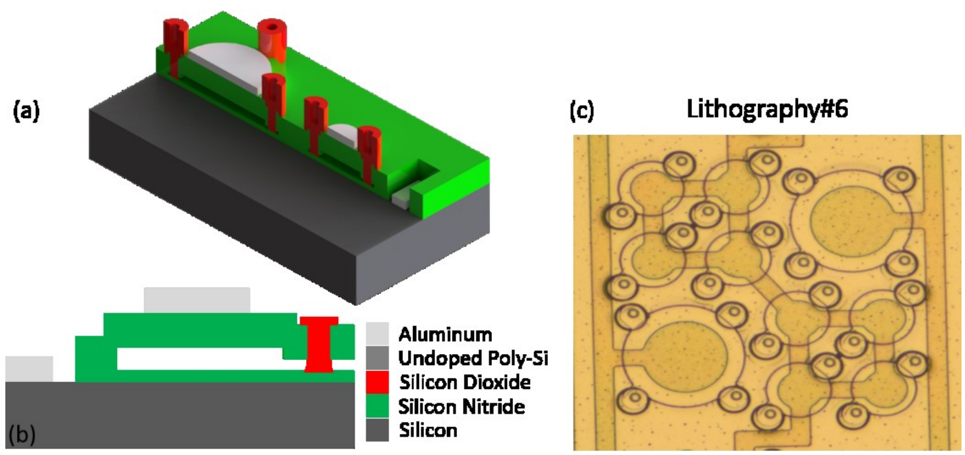

Fig. 5.13. Etching the aluminum layer to form the top and bottom electrodes. (a) 3D cross-sectional view, (b) cross-sectional view, and (c) microscopic image after lithography#6.

5.4 Characterization of Fabricated CMUT Devices

Different characterization tools including Laser Doppler Vibrometer (MSA-500, Polytec), Zygo Optical Profilometer, Olympus Laser Confocal Microscope (OLS3000), Scanning Electron Microscope (Zeiss EVO MA10), Alpha-Step IQ, Filmetrics F50-UV, Helium Ion Microscope

(Zeiss Orion NanoFAB with Ga FIB), Keithley 4200-Semiconductor Characterization System (SCS Analyzer), Thin Film Stress Measurement (FLX 2320), and etc. were used during and after fabrication of our multi-frequency CMUT devices. Fig. 5.14 (a) demonstrates some sample images of fabricated devices using a standard silicon nitride sacrificial release process with slight modifications. Moreover, Fig. 5.14 (b) shows the helium ion microscopy (HIM) of fabricated interlaced multi-frequency CMUT cells with cross-sectional view of a low frequency CMUT cell that was drilled using a Ga focused ion beam (FIB) across the membrane. A laser Doppler Vibrometer (MSA-500, Polytec) was used to wafer-level characterization of low- and high-frequency CMUT cells before dicing them. In following sections, we will show more results about the characterization of fabricated devices.

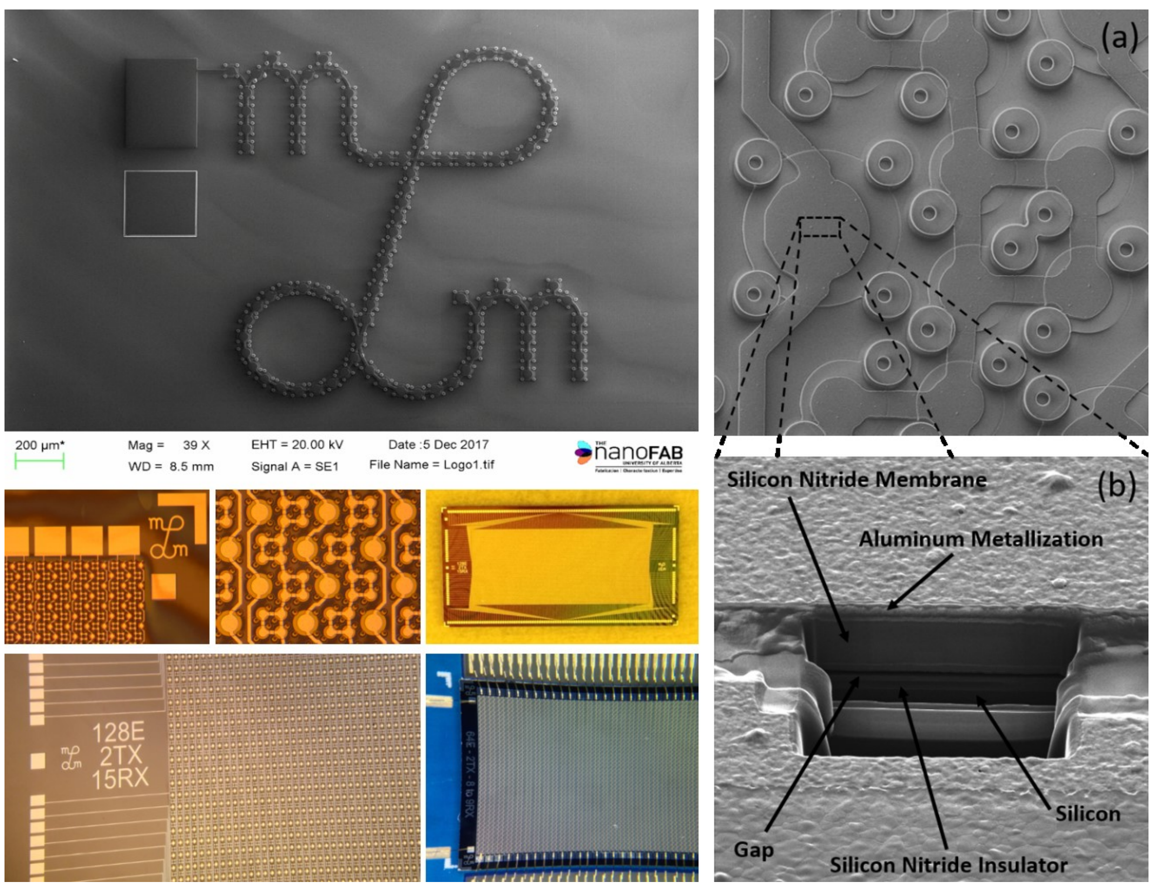

Fig. 5.14. (Left) Final fabricated sample CMUT devices using a standard silicon nitride sacrificial release process. (Right) Helium ion microscopy of (a) fabricated interlaced multi-frequency CMUT cells and (b) labelled cross-sectional view of drilled low-frequency cell using Ga focused ion beam (FIB).

5.5 Conclusion

Various multi-frequency CMUT arrays were designed and fabricated using a standard silicon nitride sacrificial release process with slight modifications. Designed arrays have different combination of low- and high-frequency CMUT parameters for considered ultrasound imaging and therapeutic applications. These large-scale ultrasonic arrays were fabricated completely using the facilities at the nanoFAB of University of Alberta. The arrays are then wire-bonded to custom PCB designs and finally become ready for ultrasound imaging unique applications. Multi-frequency CMUT arrays require six-lithography steps, HMDS, piranha cleans, thermal oxidation, BOE etching, KOH etching, critical point drying, RIE, PECVD, LPCVD, aluminum sputtering, annealing, and etching, along with 80–100 hours of work. These devices were characterized using the Filmetrics system, Alpha-Step IQ profilometer, Keithley semiconductor analyzer, Scanning Electron Microscopy (SEM), Laser Vibrometer, Zygo, Verasonics, Hydrophone measurement and the helium-ion microscope.

References

[1] A. Sampaleanu, P. Zhang, A. Kshirsagar, W. Moussa, and R. J. Zemp, “Top-orthogonal-to-bottom-electrode (TOBE) CMUT arrays for 3-D ultrasound imaging,” *IEEE Trans. Ultrason., Ferroelectr., Freq. Control*, vol. 61, no. 2, pp. 266–276, Feb. 2014.

[2] P. Zhang, G. Fitzpatrick, T. Harrison, W. Moussa, and R. J. Zemp, “Double-SOI wafer-bonded CMUTs with improved electrical safety and minimal roughness of dielectric and electrode surfaces,” *J. Microelectromech. Syst.*, vol. 21, no. 3, pp. 668–680, Jun. 2012.

[3] B. T. Khuri-Yakub and O. Oralkan, “Capacitive micromachined ultrasonic transducers for medical imaging and therapy,” J. Micromech. Microeng., vol. 21, no. 5, pp. 54004–54014, 2011.

[4] B. A. Greenlay, and R. J. Zemp, “Fabrication of Linear Array and Top-Orthogonal-to-Bottom Electrode CMUT Arrays with a Sacrificial Release Process,” *IEEE Trans. Ultrason. Ferroelectr. Freq. Control*, vol. 64, no. 1, pp. 93-107, Jan. 2017.

[5] B. A. Greenlay, “Fabrication and Integration of CMUT Sensors,” MS.c. dissertation, Dept. Elect. Comp. Eng., Univ. of Alberta, Edmonton, Alberta, Canada, 2017.

Chapter 6

A Nonlinear Lumped Equivalent Circuit Model for a Single Un-Collapsed Square CMUT Cell

An accurate nonlinear lumped equivalent circuit model is used for modeling of CMUTs. Finite element analysis (FEA) is a powerful tool for the analysis of CMUT arrays with a few number of cells while with the harmonic balance (HB) analysis of the lumped equivalent circuit model, the entire behavior of a large-scale arbitrary CMUT array can be modelled in a very short time. Recently, an accurate nonlinear equivalent circuit model for un-collapsed single circular CMUT cells has been developed. However, the need for an accurate large-signal circuit model for CMUT cells with square membranes motivated us to produce a new nonlinear large-signal equivalent circuit model for un-collapsed CMUT cells. Using analytical calculations and finite-element-analysis (FEA) as the tuning tool, a precise large signal equivalent circuit model of square CMUT dynamics is summarized by Maadi et al. in the published journal paper titled “A Nonlinear Lumped Equivalent Circuit Model for a Single Un-Collapsed Square CMUT Cell” and the conference paper titled “A Nonlinear Large Signal Equivalent Circuit Model for a Square CMUT Cell” which is presented here. The framework presented here may prove valuable for future design and modelling of CMUT arrays with square membranes for ultrasound imaging and therapy applications.

6.1 Introduction

An accurate nonlinear lumped equivalent circuit model is used for modeling of capacitive micromachined ultrasonic transducers (CMUTs). Finite element analysis (FEA) is a powerful tool for the analysis of CMUT arrays with a few number of cells while with the harmonic balance (HB) analysis of the lumped equivalent circuit model, the entire behavior of a large-scale arbitrary CMUT array can be modelled in a very short time. Recently, an accurate nonlinear equivalent circuit model for un-collapsed single circular CMUT cells has been developed. However, the need for an accurate large-signal circuit model for CMUT cells with square membranes motivated us to produce a new nonlinear large-signal equivalent circuit model for un-collapsed CMUT cells. In this work, using analytical calculations and FEA as the tuning tool, a precise large signal equivalent circuit model of square CMUT dynamics was developed and showed excellent agreement with finite element modeling (FEM) results. Then, different CMUT single cells with square and circular membranes were fabricated using a standard sacrificial release process. Model predictions of resonance frequencies and displacements closely matched experimental Vibrometer measurements. The framework presented here may prove valuable for future design and modelling of CMUT arrays with square membranes for ultrasound imaging and therapy applications.

Capacitive Micromachined Ultrasonic Transducers (CMUTs) have attracted considerable attention in the ultrasound community owing to their potential for mass fabrication and co-integration with electronics [1]-[6]. Additionally, recent efforts have focused on applications not easily addressed with conventional piezoelectric materials, including bias-switchable crossed-electrode 2D arrays [7] and multi-frequency interlaced transducers for acoustic [8]-[11] and photoacoustic imaging applications [12]. Electromechanical modeling of these devices will be critical for optimizing the performance of the arrays.

Much of the previous modeling literature, which is based on Mason's equivalent circuit [13], has focused on circular membranes owing to simplifications associated with cylindrical symmetry

[14]-[16]. In these cases, equivalent-circuit models have proven to be computationally superior over FEM with excellent accuracy. However, FEA is still a powerful tool to predict the nonlinear effects of the CMUT and higher order harmonics.

Square membrane CMUTs have been widely used and make better use of active wafer real-estate compared to circular membranes. Their modeling, however, is more complex [17], and most prior work has relied on FEA, which is time-consuming and practically intractable for large arrays. While static deflection models have been previously presented for square membranes [18]-[21], dynamic lumped equivalent circuit models have only been developed for the small signal regime [17], where important nonlinear behavior is ignored. The Degertekin group developed a 2D Finite-Element hybrid model [22], [23] which is computationally advantageous over the full 3D model, however, computational burden is still non-trivial and the lack of an equivalent circuit model makes co-simulation with electronics difficult.

In this work, a large-signal nonlinear equivalent circuit model is developed for single CMUT cells with square membranes by obtaining new circuit parameters for the model developed in [14]. First, we studied the deflection profile of the square membranes using static FEA and analytical calculations. Then, the nonlinear capacitance of the CMUT was obtained relative to the normalized deflection of the membrane. Using the root mean square (rms) of the plate displacement and velocity, the electrostatic force acting on the membrane was found and compared with circular plates. The membrane rms compliance was found for thin and thick plates and all obtained parameters were implemented in a circuit model. The nonlinear equivalent circuit model is based on accurate approximations of membrane deflection and velocity profiles as well as self-radiation impedance, for which there are no known analytical closed-form solutions [17]. The model is implemented in the commercial circuit simulator Advanced Design System Environment (Agilent Technologies Inc.).

Model predictions of the membrane static deflections for different DC biases, membrane dynamic displacement amplitude and phase, resonance frequency, and total electrical conductance closely matched the 3D FEM analysis for various single square CMUT cells with thin and thick membranes. Then, the results were compared with circular CMUT cells when the half-side-length of the square CMUT is assumed to be equal to the radii of the circular cell. It will be shown that there is a considerable difference between the simulation results of the counterpart circular and square CMUT cells. The fabricated single transducers using a standard sacrificial release process are then compared with circuit simulation results. The predictions for resonance frequencies and displacements show a good agreement with experimental Vibrometer measurement results in air.

While some have used circular CMUT models as an approximation to square membrane models, our research work aims to show some important differences that may make a difference when designing next-generation transducers with maximal real-estate for photoacoustic and ultrasound imaging-therapy applications.

6.2 Nonlinear Lumped Equivalent Circuit Model for a Single Square CMUT Cell

We based our large signal equivalent circuit on the model developed in [14] in which the model parameters are provided for single CMUT devices with circular membranes. However, by considering the same circuit, different circuit parameters are used for the CMUTs with square membranes. The circuit model consists of three interacting physical domains of a CMUT including electrical, mechanical, and acoustical ports (Fig. 6.1).

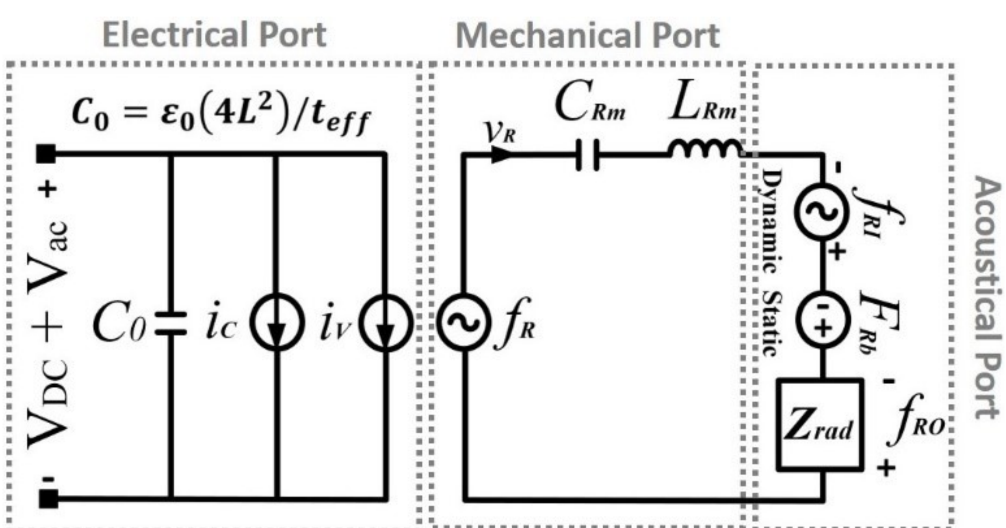

Fig. 6.1. Nonlinear large signal equivalent circuit model of a CMUT with square membrane.

6.2.1 Deflection Profile

Fig 6.2. Shows the basic top and cross-sectional view of a circular and square CMUT cell with an applied voltage. The general form of a square CMUT deflection profile with side-length of 2L can be written as [20]

$$D(x,y,t) = x_p(t)\left[1-\left(\frac{x}{L}\right)^2\right]^2\left[1-\left(\frac{y}{L}\right)^2\right]^2\sum_{n=0}^{N} C_n\left[\left(\frac{x}{L}\right)^2+\left(\frac{y}{L}\right)^2\right]^n \tag{6.2}$$

where L is the half-side-length of the aperture, x and y are the distance accross the plate in two directions, x_p is the displacement at the center of the membrane and C_n coefficients can be adjusted for any design parameters and are determined by FEA.

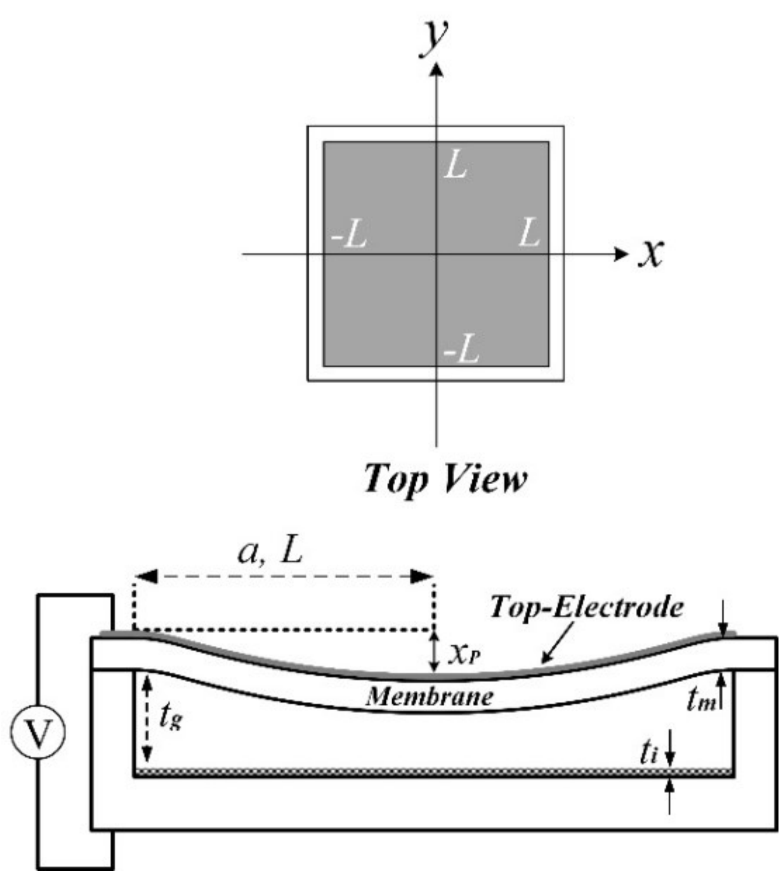

Fig. 6.2. Top and cross-sectional view of the CMUT geometry with applied voltage and dimensional parameters.

Since the analytical deflection calculations for the plates with square membranes are complicated, approximate methods must be used to solve the plate equation. Rahman *et al*. provided a deflection profile for square CMUTs with membrane thickness of 0.5 to 3 μm and half-side-length of 100 to 500 μm [20]. However, the provided expression loses accuracy while the membrane size shrinks to smaller values ($L < 100\ \mu m$). As will be shown later, the CMUT membranes can be considered as thin ($L/t_m \geq 15$) or thick ($L/t_m < 15$) plates. First, the model parameters are achieved by considering the thin plate condition. Then using FEA, the model will be expanded for thick membranes by applying the obtained correction factors to the compliance of the membrane. The approximate deflection profile of a CMUT with a square membrane can be written as

$$D(x,y,t) = x_p(t)\left[1-\left(\frac{x}{L}\right)^2\right]^2\left[1-\left(\frac{y}{L}\right)^2\right]^2\left[1+\beta\left\{\left(\frac{x}{L}\right)^2+\left(\frac{y}{L}\right)^2\right\}\right] \tag{6.2}$$

which is a special case of Eq. (6.1) for $N = 2$. Thomsen *et al*. found the coefficient β for the plates on a silicon (001) substrate and aligned to the [110] direction as [18]

$$\beta = \frac{182 + 143k_2}{1432 + 91k_2} \tag{6.3}$$

where k_2 is the plate coefficient and $\beta_{low} = 0.23920$ and $\beta_{high} = 0.23691$ are obtained for single-crystal silicon with low ($150\ \Omega - cm, \sim 2.8\ \times\ 10^{13}\ cm^{-3}$) and high doping ($3.26\ m\Omega - cm, \sim 2.1\ \times\ 10^{19}\ cm^{-3}$), respectively as defined in [17]. We use $\beta = 0.23691$ in our simulations and found that this provides a reasonable agreement with FEM for a wide range of thin membranes with different materials including silicon nitride which we are mostly intrested in. Fig. 6.3 shows the normalized deflection profile, $D(x,y)/x_p$, of a target thin silicon nitride square membrane ($L = 20\ \mu m, t_m = 1\ \mu m$) versus the normalized diagonal distance from the center of the plate for different biasing voltages in water immersion.

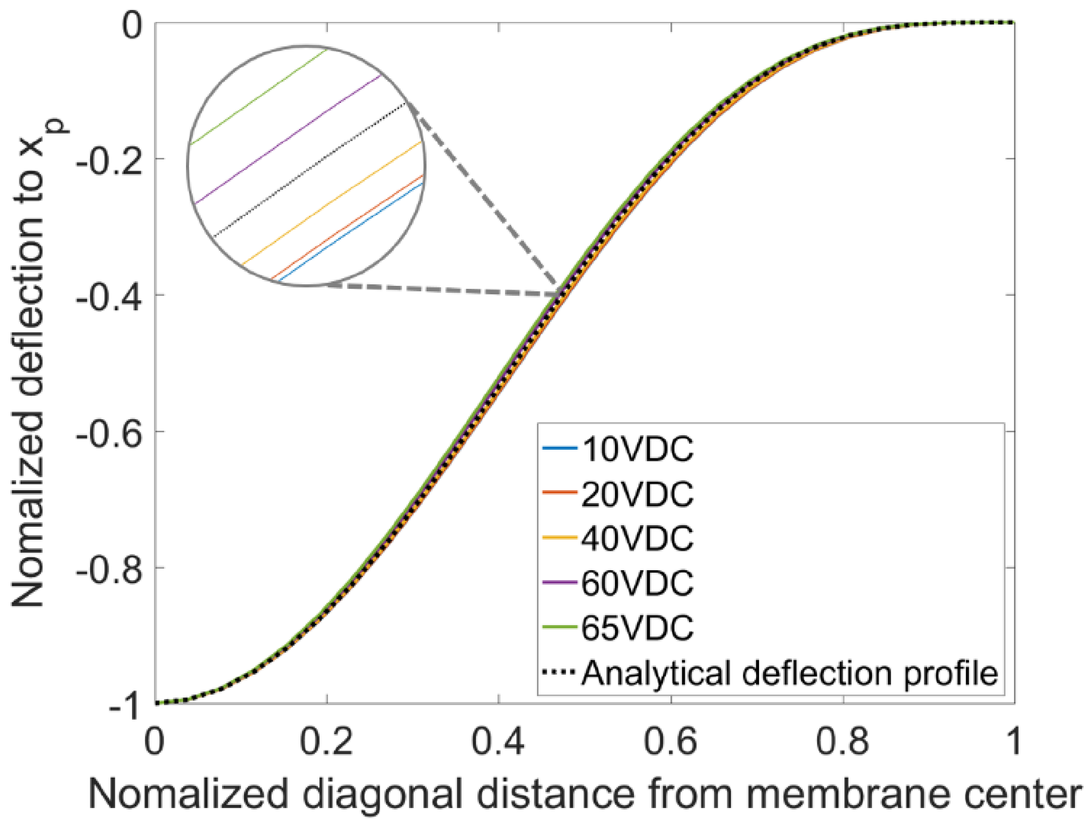

Fig. 6.3. Comparison of finite element analysis (FEA) deflection profile of 1μm silicon nitride diaphragm with the approximate analytical solution, plotted from center to the edge of the plate. $L = 20\ \mu m$ and $t_m = 1\ \mu m$. The silicon nitride membrane parameters are provided in Table 4.I [10, Table IV].

The applied DC voltage is increased until the membrane collapsed at 69 volts. The normalized deflection profile is slightly changed under different bias voltages. However, the approximate analytical solution using $\beta_{high} = 0.23691$ gives us an acceptable deflection profile to start obtaining the nonlinear lumped equivalent circuit parameters of a square CMUT cell. The membrane material parameters of the membrane can be found in [10, Table IV]. For further investigation, the similar analysis was accomplished for different types of thin membranes with different sizes and thicknesses with 60 V DC bias (Fig. 6.4). The collapse voltages for considered three different designs from top to bottom are 69, 82 and 87 volts and the applied 60 V bias is the 87, 73 and 69 percentage of their collapse voltages, respectively.

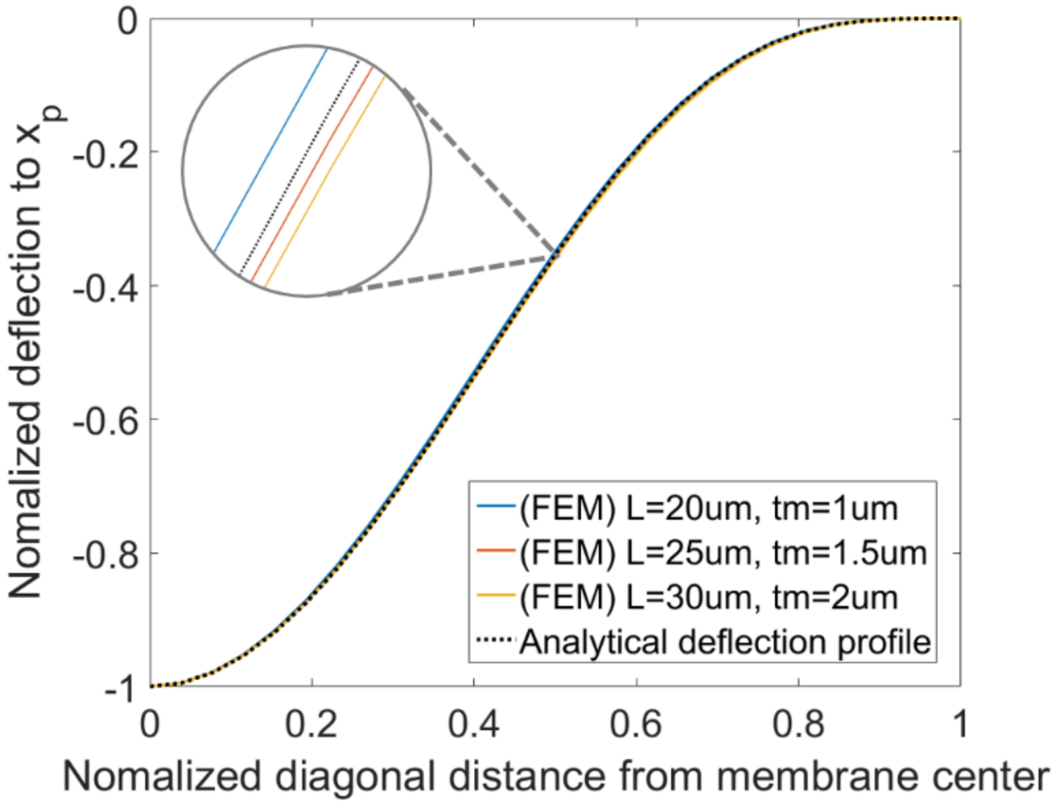

Fig. 6.4. Comparison of finite element analysis (FEA) deflection profile of different silicon nitride membranes with the approximate analytical solution, plotted from center to the edge of the plate. $V_{DC} = 60\,V$.

6.2.2 Capacitance

The capacitance, $\delta C(x,y,t)$, of a concentric narrow square on the membrane with dimension of dx by dy can be expressed as

$$\delta C(x,y,t) = \frac{\varepsilon_0 dxdy}{t_{ge} - D(x,y,t)} \tag{6.4}$$

where $\varepsilon_0 = 8.85 \times 10^{-12}\ F/m$ is the permittivity of the gap in free space and $t_{ge} = t_g + t_i/\varepsilon_r$ is the effective gap height in which ε_r is the relative permittivity of the insulating material, t_g is the thicknesses of the vacuum gap height and t_i determines the insulating layer thickness.

The total capacitance, $C(t)$, of the deflected membrane with full electrode can be written as

$$C(t) = \frac{1}{t_{ge}} \int_{-L}^{L} \int_{-L}^{L} \frac{\varepsilon_0}{1 - \frac{1}{t_{ge}} D(x, y, t)} dxdy \tag{6.5}$$

However, the capacitance can be found for the membranes with a partial electrode of inner half-side-length of L_i and outer half-side-length of L_o. Since there is no analytical solution for the capacitance calculation of the square CMUTs, the integration is performed numerically. Fig. 6.5 shows the analytical solution for a circular membrane with full electrode [14, eq. (2)] and the numerical solutions for the capacitance of a square plate with full and concentric half size electrodes. Please note that for the plates with half size concentric electrodes, the area of the electrode is $2L^2$ and the intervals of the integral in Eq. (6.5) will be from $-\sqrt{2}L/2$ to $\sqrt{2}L/2$.

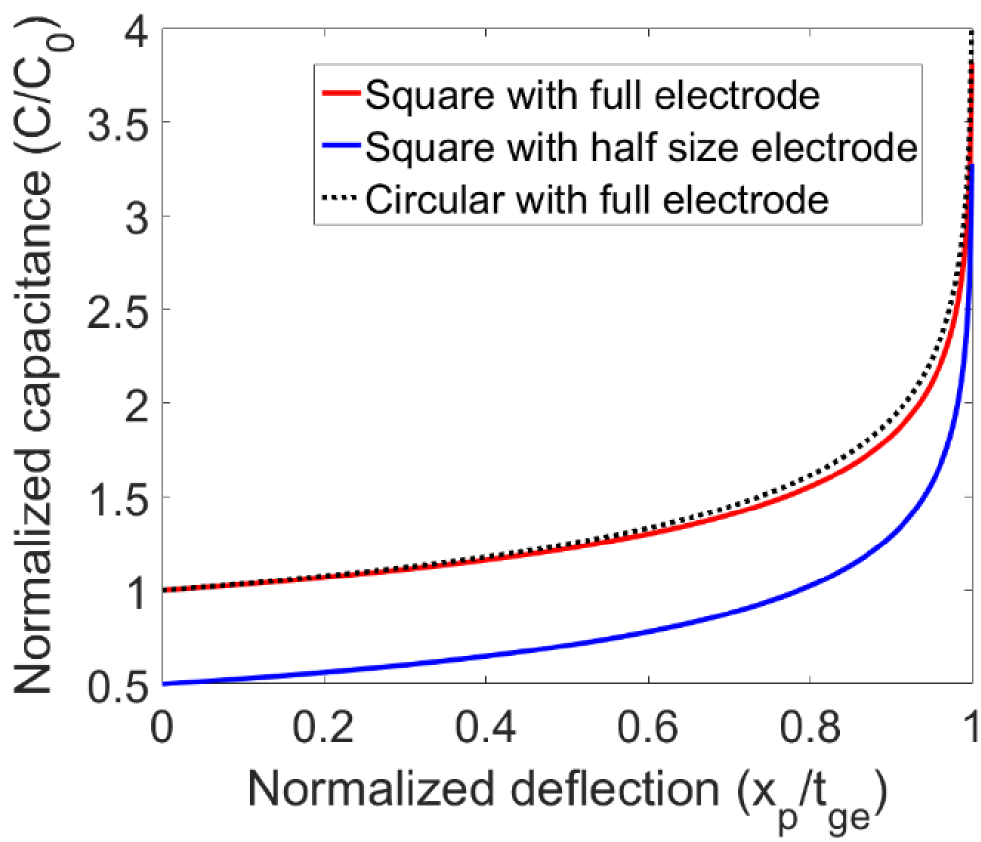

Fig. 6.5. Comparison of normalized total capacitance versus normalized membrane deflection for a circular plate with full electrode and a square membrane with full and concentric half size electrodes.

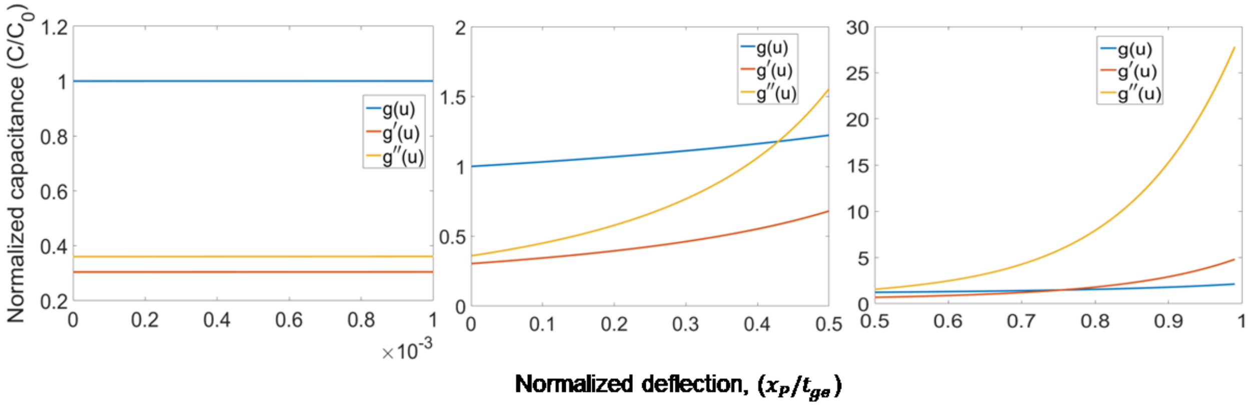

Fig. 6.6. Normalized capacitance of a square plate and its derivatives. (left) for normalized deflection of $0 < (x_p/t_{ge}) < 1e-3$; (mid) $1e-3 < (x_p/t_{ge}) < 0.5$; (right) $0.5 < (x_p/t_{ge}) < 0.99$.

The total capacitance of the deflected membrane with full-area electrodes can be expressed as

$$C(t) = C_0 g\left(\frac{x_p(t)}{t_{ge}}\right) = C_0 g(u) \tag{6.6}$$

where $C_0 = \varepsilon_0 4L^2 / t_{ge}$ is the capacitance at zero deflection and the function $g(u)$, which describes the shape of the capacitance curve, can be found by performing the higher order polynomial fitting to the numerically-obtained solution for three different deflection ranges; i) low deflection $0 < u < 1e-3$, ii) the range below the pull-in distance $1e-3 < u < 0.5$, and iii) the range beyond the pull-in distance of $0.5 < u < 0.99$. Note that Eq. 82 of [17] calculates the normalized pull-in distance as 0.466 without additional pressure loading, which we are rounding to 0.5. Fig. 6.6 demonstrates the numerically obtained solutions for the normalized capacitance of a square plate and its first and second derivatives for three different normalized deflection ranges. The goodness of fitting on obtained graphs is increased dramatically when the polynomial fitting is done separately for divided membrane deflection ranges. The polynomial coefficients of Eq. (6.7) are provided in Table I of the Appendix B.

$$g(u) = \sum_{n=0}^{9} a_n u^n \tag{6.7}$$

Note that for negative values of peak displacement ($x_p(t) < 0$), $g(u)$ will be replaced by $g(-u)$ which is a useful expression for circuit simulators.

6.2.3 RMS, Average and Peak Displacement and Velocity Coefficients

Since the average displacement and velocity measurements are problematic in some cases, the root mean square (rms) velocity distribution on the membrane surface, v_{rms}, is preferred instead of the average velocity, v_{ave}, as the lumped variable at the mechanical side of the circuit [15]. For instance, higher harmonic deflection profiles may generate zero average displacement and velocity. In this case, the mechanical radiation impedance will go to infinity and makes the mechanical port of the lumped model open circuit. This problem can be handled by defining the rms displacement of the square membrane profile as

$$\begin{aligned} x_R(t) &= \sqrt{\frac{1}{4L^2}\int_{-L}^{L}\int_{-L}^{L} D^2(x,y,t)dxdy} \\ &= x_p(t)\sqrt{\frac{16384(92\beta^2 + 572\beta + 1573)}{156080925}} \end{aligned} \tag{6.8}$$

and the average displacement, $x_A(t)$, for the membrane displacement profile given by Eq. (6.1) is

$$x_A(t) = \frac{1}{4L^2}\int_{-L}^{L}\int_{-L}^{L} D(x,y,t)dxdy = x_p(t)\left[\frac{64(2\beta + 7)}{1575}\right] \tag{6.9}$$

Table 6.I, summarizes the displacement rms and average coefficients for low and high doping cases. Please note that, the rms and average displacements, $x_R(t)$ and $x_A(t)$, for the circular membranes are $x_p(t)/\sqrt{5} = 0.4472x_p(t)$ and $x_p(t)/3 = 0.3333x_p(t)$, respectively [14]. For the

rest of this section, we will consider $Coeff_{RMS}$ and $Coeff_{AVG}$ as the membrane rms and average coefficients, respectively (Table 6.I).

TABLE 6.I. DISPLACEMENT RMS AND AVERAGE COEFFICIENTS FOR THE SQUARE PLATES.

β	$x_R(t)$	$x_A(t)$
$\beta_{low} = 0.23691$	$0.42413x_P(t)$	$0.3037x_P(t)$
$\beta_{High} = 0.23920$	$0.42430x_P(t)$	$0.3039x_P(t)$
$x_R(t) = Coeff_{RMS} \times x_P(t)$		
$x_A(t) = Coeff_{AVG} \times x_P(t)$		

According to $v(t) = dx(t)/dt$, the membrane velocity has the same rms and average coefficients as shown for the plate displacement in Table 6.I.

The electrostatic force acting on the small square area $dxdy$ is calculated by taking the derivative of the stored energy in the capacitance with square plates while the CMUT is driven by the combination of DC and AC voltages. The rms force, $f_R(t)$, is given by [14, eq. (6)]

$$f_R(t) = \frac{\partial E(t)}{\partial x_R(t)} \tag{6.10}$$

where the $E(t) = 1/2C(t)V^2(t)$ is the instantaneous energy stored on the capacitance, if $V(t)$ is applied as the voltage across the capacitance. Then the rms force can be written as [14, eq. (7)]

$$f_R(t) = \frac{V^2(t)}{2} \frac{\partial C(t)}{\partial x_R(t)} = \left(\frac{1}{Coeff_{RMS}}\right) \frac{C_0 V^2(t)}{2t_{ge}} g'(u) \tag{6.11}$$

For the CMUTs with full electrodes, Fig. 6.7 depicts the comparison of rms electrostatic force normalized with $C_0V^2(t)/4t_{ge}$ for devices with circular and square membranes.

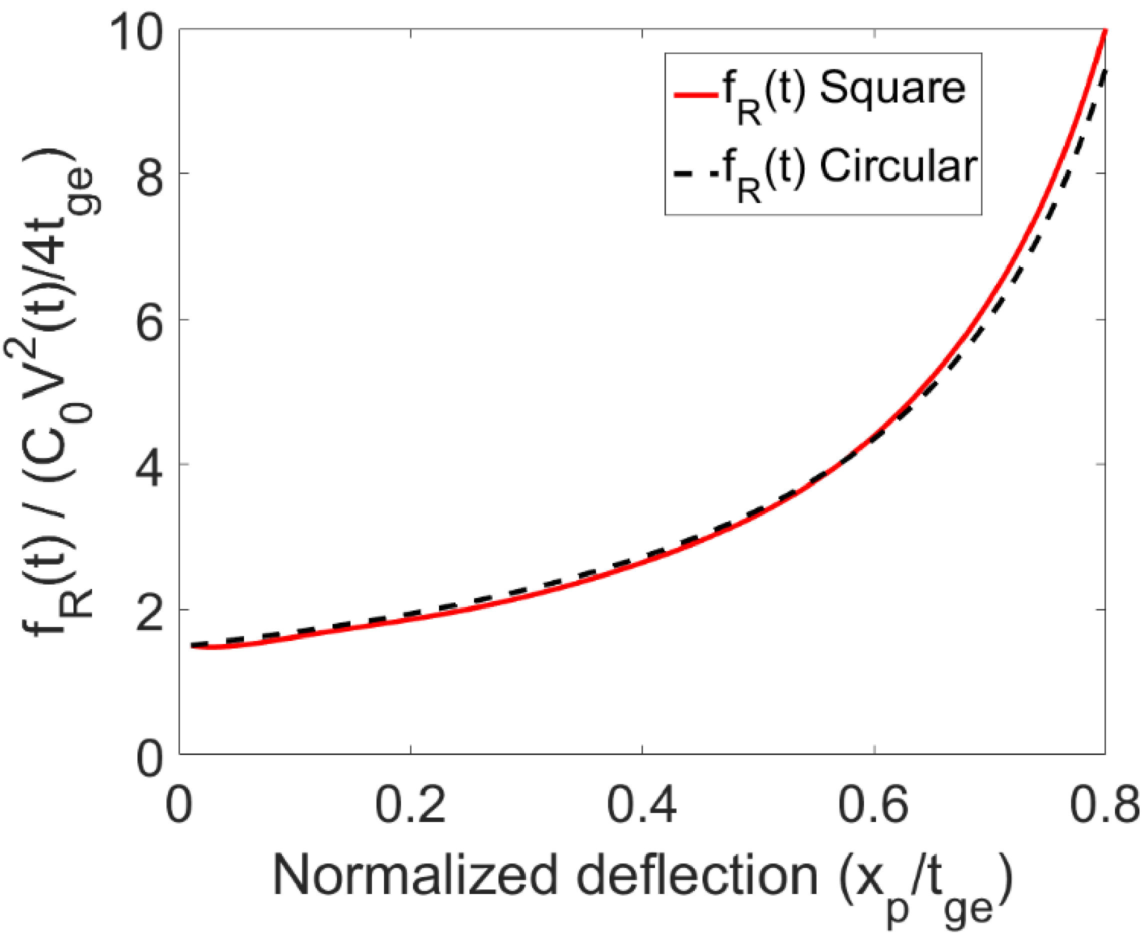

Fig. 6.7. A comparison of rms normalized electrostatic force as a function of normalized membrane deflection.

6.2.4 Compliance and Mass of the Square Membrane

The accuracy of the proposed model depends on the agreement between the parameters of the equivalent circuit model and the actual device parameters. For some of the parameters including the membrane deflection and velocity profiles, we are not able to use the exact form, and for some calculations such as capacitance and mechanical radiation impedance, there is no precise analytical solutions, hence we need to perform numerical calculations or use approximations. Since the device resonance frequency and the snap-down voltage depend on the compliance of the membrane, C_m, and the compliance is related to the membrane physical dimensions (softer compliance for thicker plates), the relation between the compliance and membrane physical dimensions needs to be adequately modelled to compensate the initial thin plate approximation and keep the accuracy of the equivalent circuit for thicker plates.

Yamaner *et al*. used FEM simulation results to develop a correction factor for thick circular plates, applied to the rms compliance of a circular membrane [24, eq. (1)]. Using the same approach, the accuracy of the model is increased by applying different correction factors separately for thin- and thick square membranes.

For the structure shown in Fig. 6.2, the flexural rigidity of the square plate is given by [17, eq. (2)]

$$D = \frac{Y_0 {t_m}^3}{12(1-\sigma^2)} \tag{6.12}$$

where Y_0 is the Young's modulus, t_m is the thickness of the membrane, and σ is the Poission ratio. The linear spring constant of the square membrane is [17]

$$K_S = \frac{768\mathrm{D}}{L^2} \tag{6.13}$$

with compliance given as $C_m = 1/K_S$. As explained in [14], the capacitance in Mason's circuit representating the compliance of the plate, needs to be multiplied by $|v_{rms}|^2/|v_{avg}|^2$ to preserve the resonance frequency in vacuum. Then the rms value of the compliance for devices with square membranes can be written as [24, eq. (7)]

$$C_{Rm} = \left(\frac{Coeff_{RMS}}{Coeff_{AVG}}\right)^2 \frac{(1-\sigma^2)L^2}{64 Y_0 {t_m}^3} \tag{6.14}$$

where $Coeff_{RMS}$ and $Coeff_{AVG}$ are given in Table 6.I.
We previously showed excellent agreement between FEM and equivalent circuit model for circular CMUTs in [10]. The circuit parameters for thin circular membranes are obtained using exact analytical calculations but for thin square membranes, we used approximate deflection profile and numerical calculations to find the nonlinear capacitance of the device. To obtain good agreements

between FEM, model and experimets, two correction factors are obtained by ANSYS 3D FEA for thin ($L/t_m > 15$) and thick ($L/t_m < 15$) membranes and then applied to C_{Rm} separately as [26]

$$C'_{Rm} = C_{Rm}\left[a + b\left(\frac{t_m}{L}\right)^c\right] \tag{6.15}$$

with provided coefficiens in Table 6.II.

TABLE 6.II. COEFFICIENTS OF THE COMPLIANCE CORRECTION FACTOR EQUATION FOR THIN AND THICK MEMBRANES.

Membrane	a	b	c
Thin	1.10628	0.00597	−0.76604
Thick	1.10628	5.305	2.08

In the proposed circuit model of Fig. 6.1, the inductance corresponds to the total mass of the membrane and the rms value is

$$L_{Rm} = \rho(4L^2)t_m \tag{6.16}$$

where ρ is the density of the membrane.

It is necessary to consider the effects of the self-acoustic-radiation impedance on the behaviour of the CMUT especially for immersion media. The radiation impedance, Z, of a radiator is determined by dividing the total radiated power, P, from the transducer by the square of the absolute value of an arbitrary nonzero reference velocity, V [25]. The self-radiation impedance of a flexural circular clamped disk located on an infinite rigid baffle is given in [10, eq. (36)] and [15]. The same expression may be used as an approximation for a square clamped radiator by replacing the area of the circular plate (πa^2) with the area of a square disk ($4L^2$). The self-radiation impedance is implemented in the acoustical port of the circuit model. The choice to use the square area $4L^2$ rather than the circular area πa^2 in the expression for the self- radiation impedance was purely phenomenological and based on model accuracy compared to FEM simulations. This reflects slightly more moving membrane real-estate in the square membrane case compared to the circular membrane case.

The accuracy of the model in static and dynamic conditions are tested for thin and thick plates by comparing the FEM and circuit simulation results for different designs. ANSYS 3D axisymmetric models of CMUTs with quarter periodic sections are utilized by applying the rigid boundary conditions [Fig. 6.8(a)]. More details about the finite element simulations for transducers with circular membranes are provided in [26] as we used the similar method to model and simulate the CMUTs with square membranes. The CMUT is clamped from the side-lengths and considered as a clamped radiator [Fig. 6.8(b)]. Fig. 6.9 shows the comparison of finite element simulations with the results obtained by the circuit model with and without applying the correction factors for the permanent resonance frequency of thin and thick plates in water immersion.

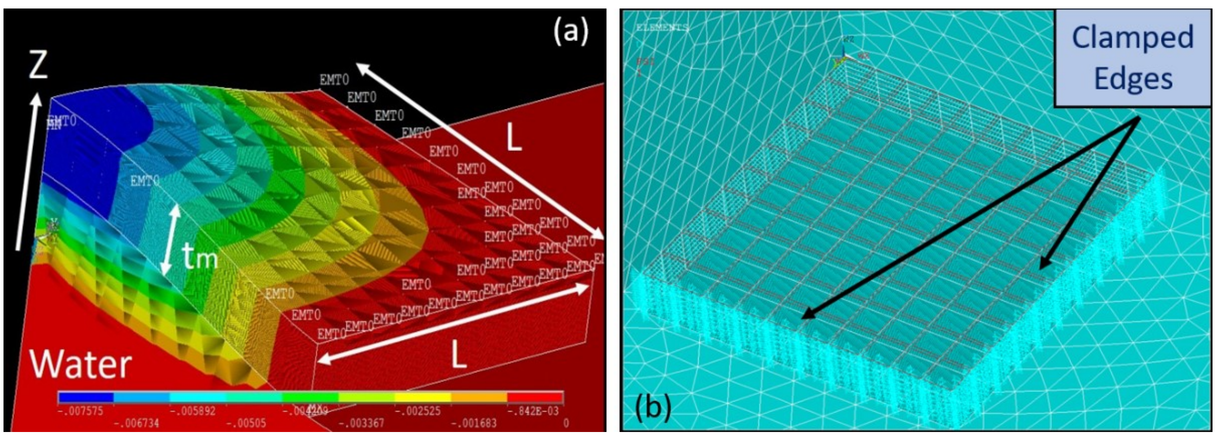

Fig. 6.8. ANSYS 3D axisymmetric models of (a) a CMUT with quarter periodic sections in water immersion medium which is (b) clamped from side-edges.

The permanent resonance frequency of the CMUT is defined as the frequency of the peak total conductance G (the real part of the admittance) [10], [14]. The parameters of [10, Table IV] is used for simulations, except the DC voltage applied is 30V, the half-side-length of the CMUT is considered 30 μm and the thickness of the membrane is swept from 1 to 10 μm. The dynamic simulation results show good agreement with FEM simulations for both thin and thick plates.

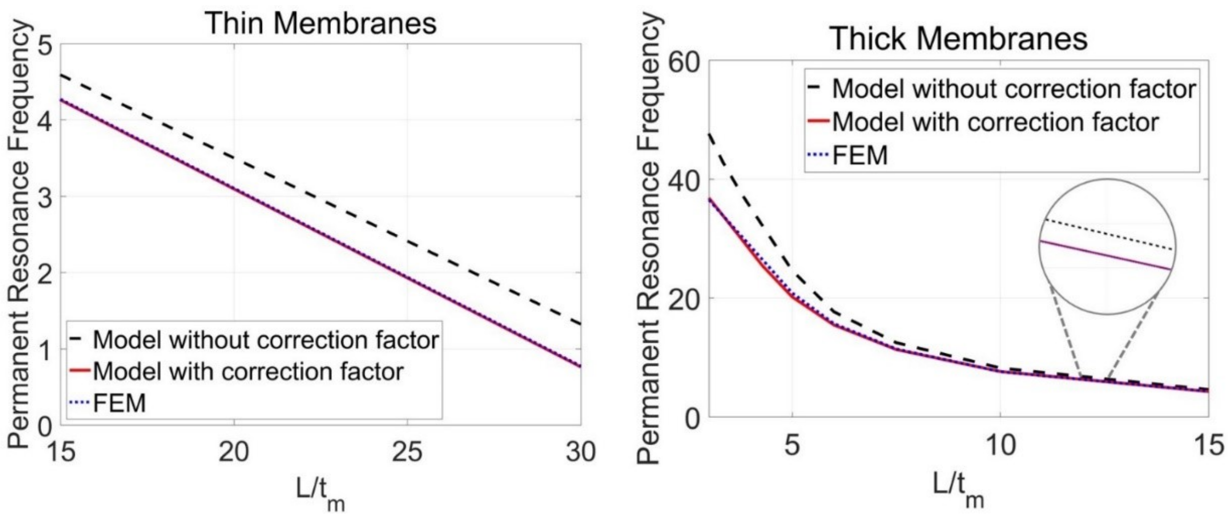

Fig. 6.9. Comparison of FEM with circuit simulation results for permanent resonance frequency of thin and thick plates in water immersion with and without applying the correction factors to the compliance of the membrane. The half-side-length of the device is 30 μm, the thickness of the membrane is swept from 1 to 10 μm and a DC bias of 30V is applied. Device parameters are provided in [10, Table IV].

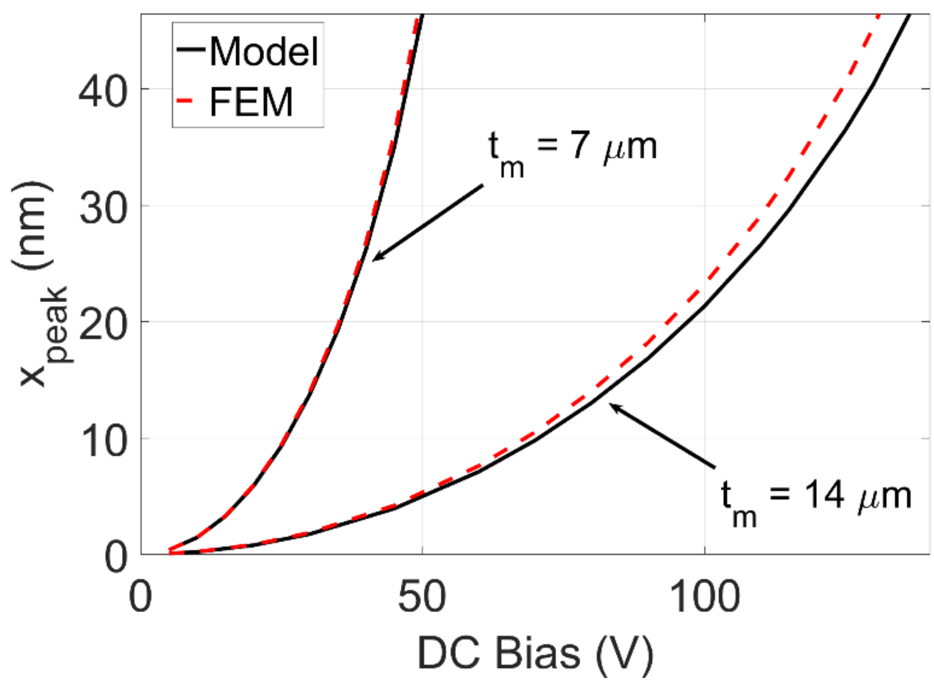

Fig. 6.10. Comparison of peak static deflections of a square CMUT cell with a half-side-length of 93 μm for two thick membranes obtained by FEM and lumped equivalent circuit model using parameters of [10, Table IV] in water immersion.

More investigation is done by testing the accuracy of the model in static conditions for two thick plates ($L = 93\ \mu m$ with 7 and 14 μm thicknesses) by comparing the static deflection obtained by finite element simulations and circuit models for different DC biases in water immersion. As shown in Fig. 6.10, the model can predict the peak static deflection values of a target CMUT cell under different DC biases.

Fig. 6.11 demonstrates the error of the equivalent circuit model simulations for peak displacements compared to FEM for two different designs shown in Fig. 6.10. It is obvious to see that the model is more accurate for thinner membranes which is more desirable for our fabrication purposes. For example, if we bias the considered CMUT cells with 75% of their collapse voltages, the accuracy of the model is more than 97% and 91% for the designs with the thickness of 7 and 14 μm, respectively.

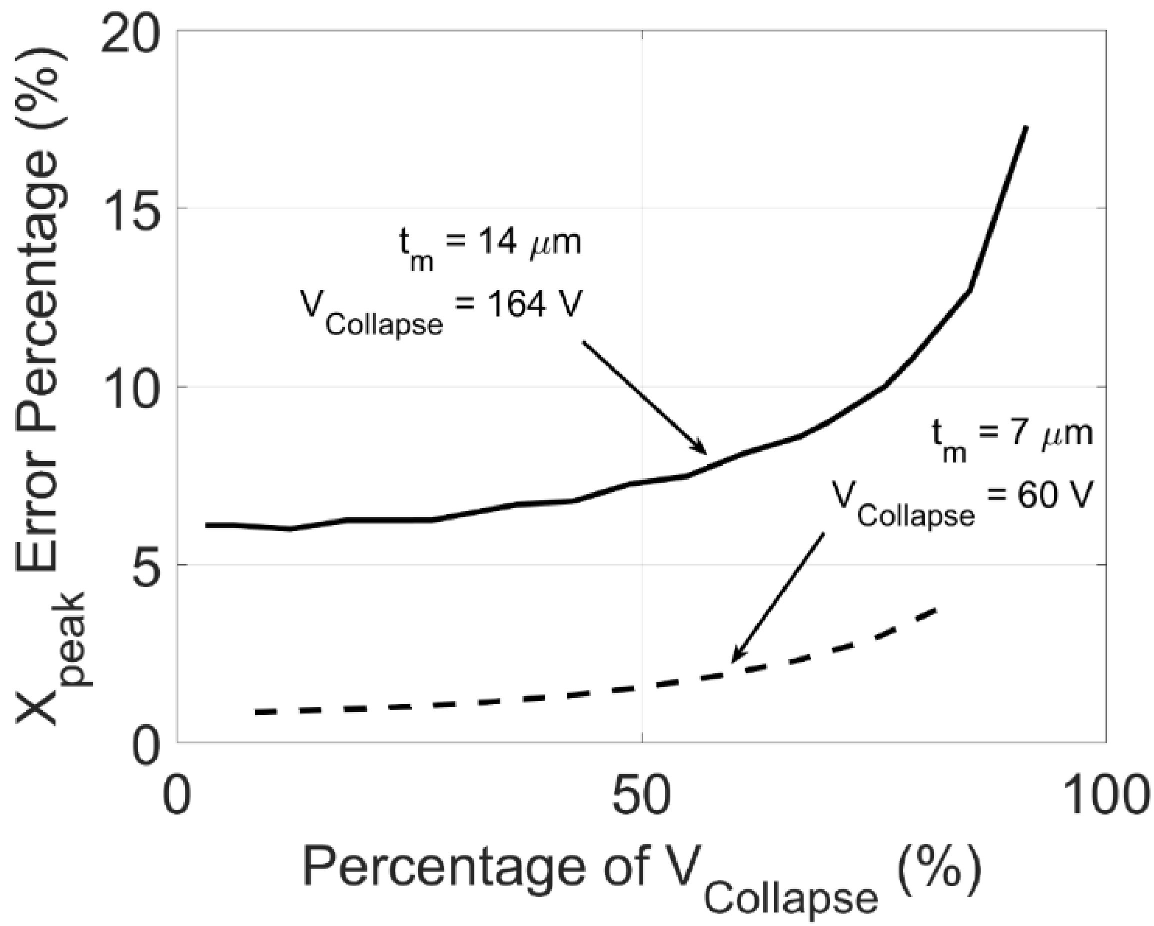

Fig. 6.11. Error analysis of the peak displacement calculations for two different designs shown in Fig. 6.10. The graph shows the accuracy of the proposed equivalent circuit model compared to FEM.

6.3 Comparison with FEM Analysis

In the previous section, the DC performance of the HB circuit model was compared with the finite element static analysis results. Moreover, the large signal electrical conductance of a square CMUT with different design parameters was simulated and compared with FEM. All the circuit simulations were done in water immersion and obtained results were in excellent agreement with FEA. In this section, we will do more dynamic simulations using different CMUT parameters provided in [10, Table IV] and compare with FEM results.

The large signal HB circuit model obtained in [14], [15] for circular CMUT cells may be used as an approximation to model the CMUTs with square membranes by assuming that the half-side-length of the square plate is equal to the radii of the circular membrane. Fig. 6.12 demonstrates the total electrical conductance of two circular and square CMUTs with different membrane sizes, 93 and 110 μm. Using the parameters provided in [10, Table IV], the square CMUTs are modelled in FEM and compared with the circuit simulation results for circular and square devices. As shown, the circuit model with proposed parameters for square CMUTs matches the 3D FEA while the circular approximation does not provide the precise solution. For example, the permanent resonance frequency of a square CMUT cell with the half-side-length of 93 μm and a membrane thickness of 14 μm is 4.22 MHz with the total electrical conductance of 1.96 $\mu\Omega^{-1}$ while the circular model gives the peak total conductance of 1.463 $\mu\Omega^{-1}$ at 5.01 MHz.

For further investigation, we considered two circular and square CMUTs with the same areas. For example, the area of a square CMUT with half-side-length of 93 μm is equal to the area of a circular membrane with radii 105 μm. The results shown in Fig. 6.12 demonstrates that the total electrical conductance of a circular CMUT is more compared to a square membrane with the same area while the resonance frequency shifts to lower values when we replace the circular membrane with a square disk with the same area.

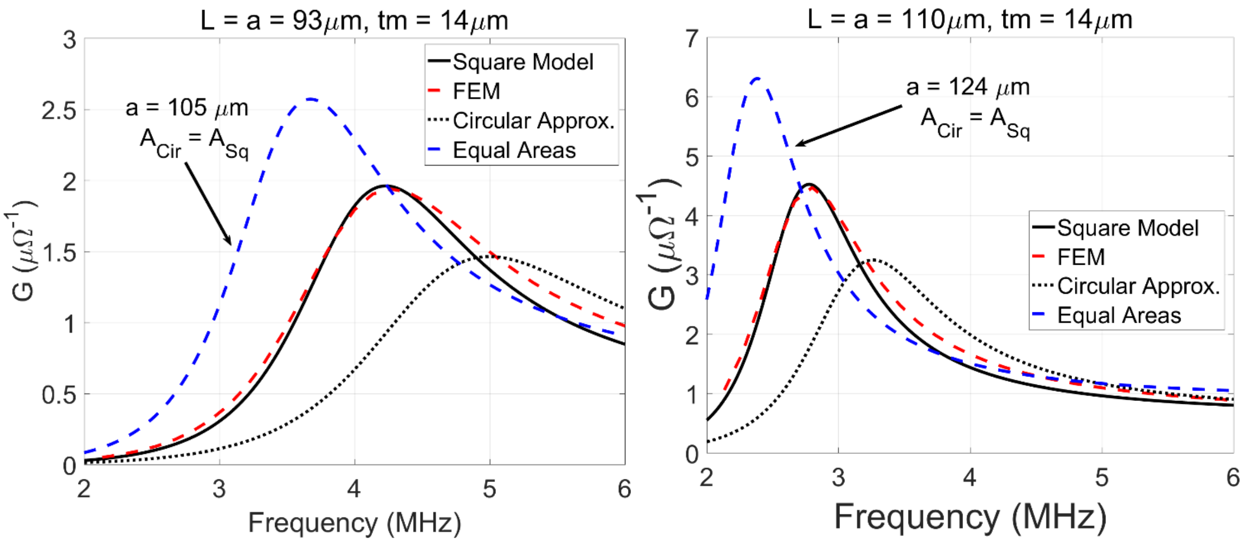

Fig. 6.12. Comparison of total electrical conductance for square and circular CMUT cells with provided parameters in [10, Table IV] when the half-side-length of the square CMUT is assumed to be equal to the radii of the circular membrane and when the circular and square disks have the same areas.

To evaluate the effects of the CMUT physical parameters on the performance of the device, and to show the accuracy of the model in details, more circuit simulations are done in water immersion and compared with FEM. As shown in Fig. 6.13, three CMUTs with L/t_m of 20, 10 and 5 are considered as thin and thick membranes using the same parameters of [10, Table IV]. The simulation results of the square CMUTs are obtained for the phase and amplitude of the peak displacement and the total electrical conductance. Compared to ANSYS 3D FEM results, circuit simulations show close predictions. However, it takes longer for FEM simulations to be completed.

Results thus far are simulated using low 1V AC driving voltages (but with 60V DC bias voltages close to snapdown) where small-signal models may be applicable. However, our model is also applicable to large signal operation. To demonstrate this, we performed simulations similar to those in [14], except using square, rather than circular membranes (Fig. 6.14).

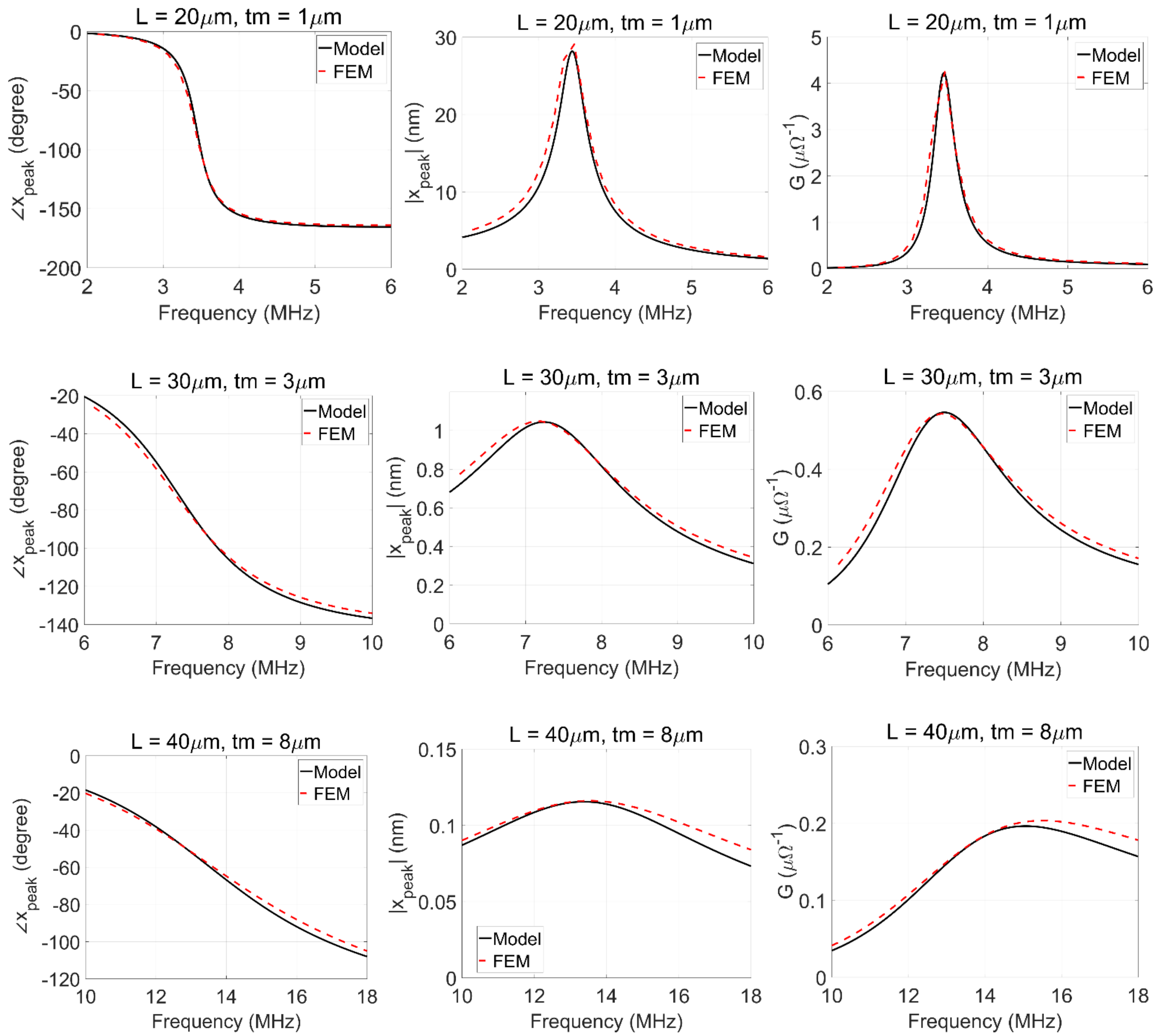

Fig. 6.13. Amplitude and phase of the peak displacement and the total electrical conductance of the single CMUT cells with square membranes for different L/t_m combinations. All simulations are done in water immersion for devices with parameters provided in [10, Table IV].

We used both FEM and our equivalent circuit model to simulate a silicon nitride membrane CMUT cell in water with parameters provided in [10, Table IV]. The modelled driving voltage was 40 V peak AC, swept from 2 to 6 MHz, applied over a 10 V bias. Note that the nearly 70 nm displacement is shown in Fig. 6.14-top is close to one-third of the effective gap size ($g_{eff} = 226\, nm$). Because the applied voltage swings both positive and negative, this would not be a typical operating mode for CMUTs, but this simulation tests the nonlinear capacity of the model under large AC driving conditions.

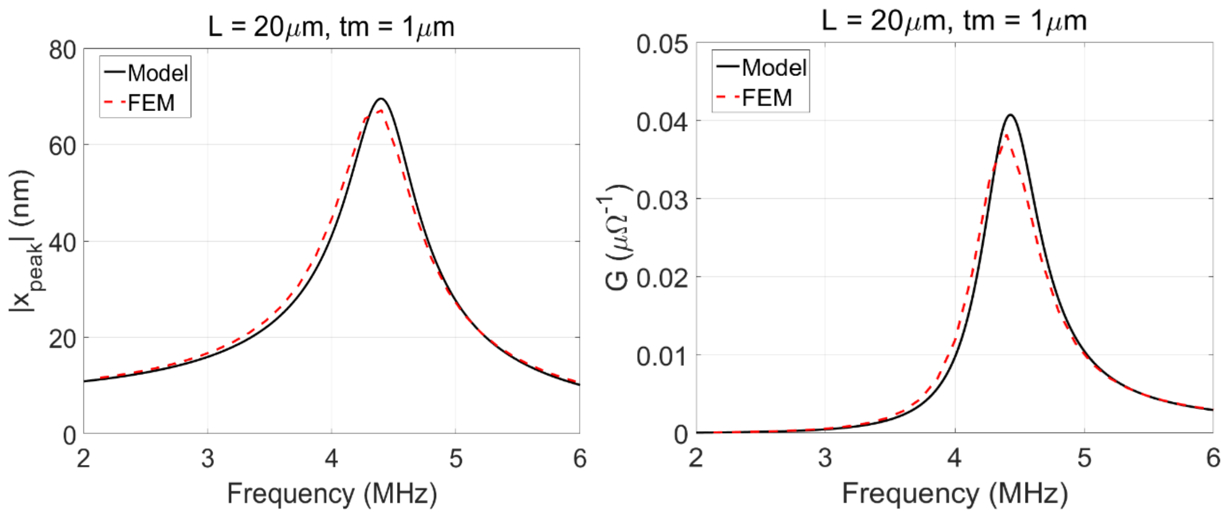

Fig. 6.14. Amplitude and total electrical conductance a of the peak displacement of a silicon nitride membrane CMUT cell in water with parameters provided in [10, Table IV]. A 40 V peak ac signal is applied on a 10 V bias voltage. Large signal response is observed using our finite element (FEM, dashed line) transient analysis and compared with the response of the developed equivalent circuit model shown in Fig. 6.1 (solid line).

6.4 Comparison with Experimental Results

In addition to FEA, the simulation results were validated by comparing the resonance frequencies of designed single CMUT cells with fabricated circular and square transducers using the silicon-nitride sacrificial release process described in section 5. The measurements were made using a Microsystem Analyzer laser Vibrometer (MSA-500, Polytec). A pseudorandom signal, which is equally weighted in all frequencies, was applied to determine the center frequency of the devices in air. Due to the softening of the membrane, the resonance frequency of the CMUTs is shifted to lower frequencies by increasing the DC bias**.** To find the actual resonance frequency, we only applied pseudorandom signals without a DC bias. Figure 6.15 shows the scanning electron microscopy (SEM) image of the fabricated circular and square CMUT cells with provided parameters in Table 6.III. To compare the resonance frequency of the circular and square CMUTs, the radii of the circular devices are considered to be equal to the half-side-length of the square transducers. Circular CMUTs of radius 40, 35, 30, 25 and 20 microns were fabricated, tested and compared with square CMUTs of equivalent half-side-lengths. Table 6.IV shows an excellent agreement between the simulation and experimental results both for circular and square devices. As can be seen, the difference between resonance frequency of the counterpart circular and square CMUTs becomes larger, as the size of the membrane gets smaller.

TABLE 6.III. PARAMETERS OF THE FABRICATED CMUT CELLS USING A SACRIFICIAL RELEASE PROCESS.

Parameter	Values
Membrane material	Silicon Nitride
Membrane thickness, t_m (µm)	~ 1
Insulator thickness, t_i (nm)	~ 150 and 250
Gap height, t_{ga} (nm)	~ 350 - 400
Young's modulus, Y_0 (GPa)	~ 290
Density, ρ (g/cm^3)	~ 3.10
Poisson's ratio, σ	~ 0.263
Bias voltage, V_{DC} (V)	0
Driven signal, V_{AC} (V)	Pseudorandom
Medium	air Density of the air is 1.225 (kg/m^3) and speed of sound in air is 343 m/s.

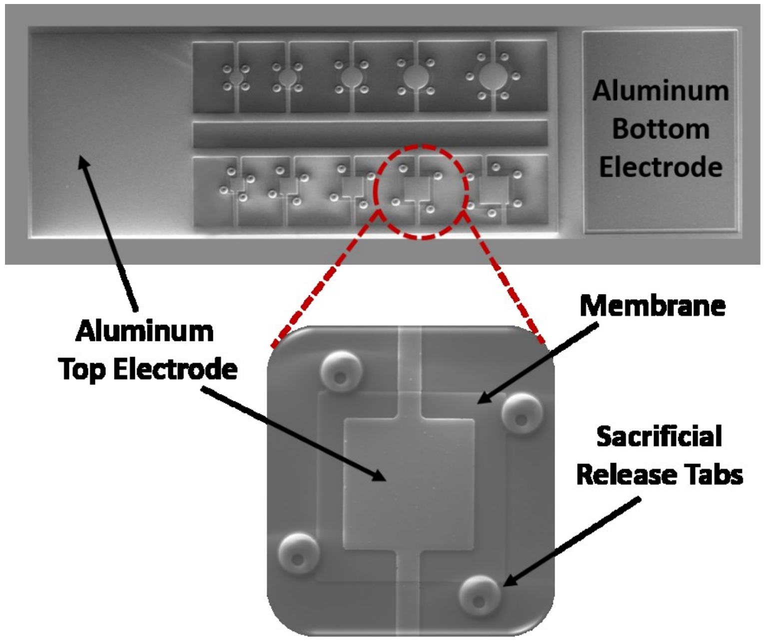

Fig. 6.15. A SEM image of the fabricated CMUTs with circular and square membranes using a standard sacrificial release process. The radii of the circular devices are equal to the half-side-length of the counterpart square CMUTs. Top electrodes of the CMUT cells are connected and all the devices have a common bottom electrode through the silicon substrate.

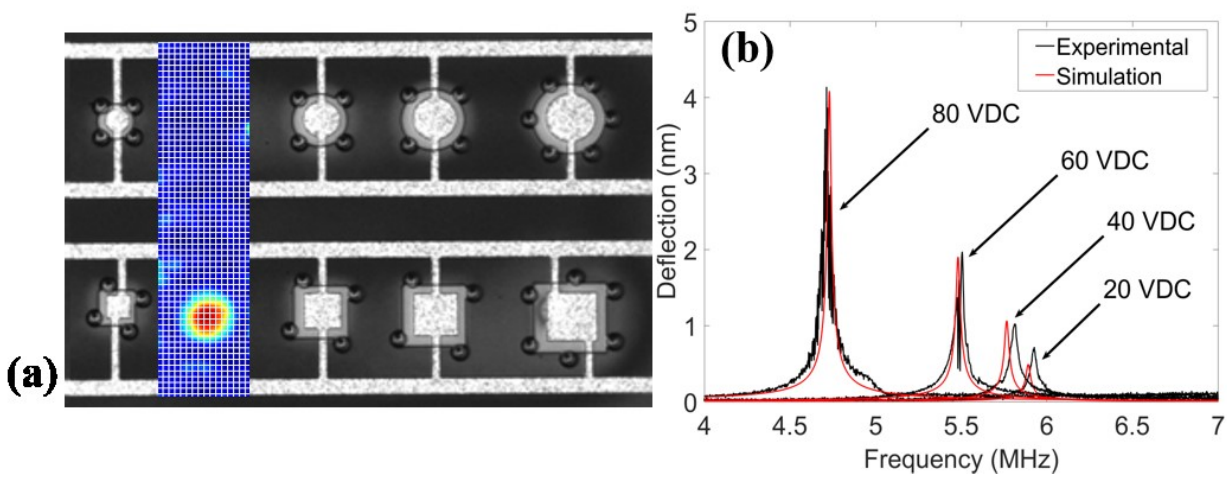

Fig. 6.16. Sample laser Doppler Vibrometer measurements. (a) 2-D scan showing membrane displacement for 40 VDC bias and 1 V Pseudorandom AC signal. (b) Single point measurement using a 1 V Pseudorandom AC signal with different DC biases. Peak represents the optimum resonance frequency of the device for a given DC bias and the frequency is shifted to lower frequencies by increasing the DC bias due to the softening of the membrane.

TABLE 6.IV. COMPARISON OF CIRCUIT SIMULATIONS WITH EXPERIMENTAL RESULTS FOR CMUTS WITH CIRCULAR AND SQUARE MEMBRANES.

CMUT	Half side length* (μm)	Resonance Frequency of Circular Single CMUT Cells		Resonance Frequency of Square Single CMUT Cells		Difference between the Resonance Frequencies of Circular and Square CMUTs using Experiments (MHz)
		Experimental Results (MHz)	Simulation Results (MHz)	Experimental Results (MHz)	Simulation Results (MHz)	
1	40	3.3312	3.263	2.9906	2.679	0.3406
2	35	4.1250	4.265	3.6844	3.515	0.4406
3	30	5.3344	5.544	4.7125	4.582	0.6219
4	25	7.3250	7.607	6.4060	6.307	0.919
5	20	11.1594	11.89	9.5875	9.908	1.5719

*The radii of the circular devices are equal to the half-side-length of the square cells.

We applied a 1 V Pseudorandom signal with different DC biases to a single square CMUT cell with the half-side-length of 25 μm to find the collapse voltage and observe the changes in resonance frequency (Fig. 6.16). As can be seen, due to softening of the membrane, the resonance frequency of the device is shifted to lower frequencies by increasing the DC bias. Using the HB circuit analysis, the snap-down voltage was found to be 93 and 110 volts for the devices with insulator thickness of 150 and 250 nm, respectively. Obtained circuit simulations for the snap-down voltage match with experimental results which are around 90 and 105 volts. We expected to get better agreement between simulation and experimental results when applying low voltages but in Fig. 6.16 we observe better results for higher biases. This may be because of differences between the simulation parameters and the parameters of the actual fabricated devices. These differences may occur due to slight variations during the fabrication process.

6.5 Conclusion

A nonlinear large signal equivalent circuit model was developed for a single un-collapsed CMUT cell with square membranes. The deflection profile of a square plate was studied first and then, the nonlinear capacitance of the square CMUT was obtained using numerical analysis. The polynomial fitting was done on obtained capacitance curves for different normalized deflection areas and the first and second derivatives of the capacitances were calculated. The compliance of the membrane was calculated for thin square plates and then, by comparing the finite element simulations and circuit model, two correction factors are obtained for thin and thick plates and then applied to the compliance. The model was designed and implemented in a circuit simulator and compared with FEM and experimental results. ANSYS 3D FEA was used to validate the equivalent circuit model predictions by performing static, pre-stressed harmonic, and nonlinear transient analysis. The static analysis for calculating the peak deflection of the membrane showed an excellent agreement with FEA. Moreover, the performance of the model was examined for dynamic analysis. The ADS circuit model could predict many intrinsic properties of a square CMUT cell including static deflection, resonance frequency, phase and magnitude of the membrane displacement, membrane velocity, electrical conductance, and collapse voltage with accuracy comparable with FEM but within considerably less time. The results were compared with circular CMUT cells when the half-side-length of the square CMUT is assumed to be equal to the radii of the circular transducer.

Single CMUT cells with silicon-nitride membranes were fabricated using a standard sacrificial release process. The comparison between the ADS circuit simulations and the experimental results showed a good agreement for the resonance frequency and the membrane deflection.

Our model can include atmospheric pressure but has yet to include residual stress of the membrane. Inclusion of these residual stresses and more accurate material and device structural parameters may further improve model accuracy in future work.

Even though we used a circular membrane approximation for the acoustic self-radiation impedance, we used improved accuracy models for square membranes for other lumped circuit elements and found high accuracy when comparing both finite element simulations and experimental results. Future work should consider computational evaluation of the self-radiation impedance of square membranes to compare the incremental accuracy improvement over the circular membrane self- radiation impedance approximation.

The studies presented here could be used as a framework for designing the arrays with square CMUT cells. However, the effects of the mutual-acoustic impedance between the square cells of the same and different sizes should be investigated in detail and implemented into a circuit model as a Z-matrix to evaluate the performance of the array. Future work should aim to expand these results for improved modeling of the multi-frequency CMUT arrays with square cells and their novel applications.

References

[1] B. A. Greenlay, and R. J. Zemp, "Fabrication of Linear Array and Top-Orthogonal-to-Bottom Electrode CMUT Arrays with a Sacrificial Release Process," *IEEE Trans. Ultrason. Ferroelectr. Freq. Control*, vol. 64, no. 1, pp. 93-107, Jan. 2017.

[2] A. S. Erguri, Y. Huang, X. Zhuang, O. Oralkan, G. G. Yarahoglu, and B. T. Khuri-Yakub, "Capacitive Micromachined Ultrasonic Transducers: Fabrication Technology," *IEEE Trans. Ultrason. Ferroelectr. Freq. Control*, vol. 52, no. 12, pp. 2242-2258, Dec. 2005.

[3] B. T. Khuri-Yakub, and O. Oralkan, "Capacitive micromachined ultrasonic transducers for medical imaging and therapy", *J. Micromechan. Microeng.*, vol. 21, no. 5, pp. 054004-054014, May 2011.

[4] P. Zhang, G. Fitzpatrick, T. Harrison, W. Moussa, and R. J. Zemp, "Double-SOI wafer-bonded CMUTs with improved electrical safety and minimal roughness of dielectric and electrode surfaces," *Journal of Microelectromechanical Systems*, vol. 21, no. 3, pp. 668-680, 2012.

[5] M. Maadi, and B. Bayram, "Custom integrated circuit design for ultrasonic therapeutic CMUT array," *Microsystem Technologies*, pp. 1-17, Mar. 2014.

[6] M. Maadi, C. Ceroici, and R. J. Zemp, "Electrical impedance matching of CMUT cells," *IEEE International Ultrasonics Symposium (IUS),* Taipei, pp.1-4, 21-24 Oct. 2015.

[7] A. Sampaleanu, P. Zhang, A. Kshirsagar, W. Moussa, and R. J. Zemp, "Top-orthogonal-to-bottom-electrode (TOBE) CMUT arrays for 3-D ultrasound imaging," *IEEE Trans. Ultrason. Ferroelectr. Freq. Control*, vol. 61, no. 2, pp. 266-276, 2014.

[8] A. Kshirsagar, R. Chee, A. Sampaleanu, A. Forbrich, D. Rishi, W. Moussa, and R. J. Zemp, "Multi-frequency CMUT arrays for imaging-therapy applications," *IEEE International Ultrasonics Symposium (IUS),* pp. 1991-1993, 2013.

[9] M. Maadi, R. Chee, and R. J. Zemp, "Mutual radiation impedance for modeling of multi-frequency CMUT arrays," *IEEE International Ultrasonics Symposium (IUS),* Taipei, pp.1-4, 21-24 Oct. 2015.

[10] M. Maadi, and R. J. Zemp, "Self and Mutual Radiation Impedances for Modeling of Multi-Frequency CMUT Arrays," *IEEE Trans. Ultrason., Ferroelect.*, Freq. Control, vol. 63, no. 9, pp. 1441–1454, Sep. 2016.

[11] M. Maadi, and R. J. Zemp, “Modelling of Large-Scale Multi-Frequency CMUT Arrays with Circular Membranes,” *IEEE International Ultrasonics Symposium (IUS)*, Tours, pp.1-4, 18-21 Sep. 2016.

[12] R. K. W. Chee, P. Zhang, M. Maadi, and R. J. Zemp, “Multifrequency Interlaced CMUTs for Photoacoustic Imaging,” *IEEE Trans. Ultrason., Ferroelect.*, Freq. Control, vol. 64, no. 2, pp. 391–401, Feb. 2017.

[13] W. Mason, *Electromechanical Transducers and Wave Filters,* 2nd ed. New York: Van Nostrand, 1948.

[14] H. Koymen, A. Atalar, E. Aydogdu, C. Kocabaş, H. K. Oguz, S. Olcum, A. Ozgurluk, and A. Unlugedik, “An improved lumped element nonlinear circuit model for a circular CMUT cell,” *IEEE Trans. Ultrason. Ferroelectr. Freq. Control*, vol. 59, no. 8, pp. 1791-1799, Aug. 2012.

[15] H. K. Oguz, S. Olcum, M. N. Senlik, V. Tas, A. Atalar and H. Koymen, “Nonlinear modeling of an immersed transmitting capacitive micromachined ultrasonic transducer for harmonic balance analysis,” *IEEE Trans. Ultrason. Ferroelectr. Freq. Control*, vol. 57, no. 2, pp. 438-447, Feb. 2010.

[16] H. Koymen, M. N. Senlik, A. Atalar and S. Olcum, “Parametric linear modeling of circular cMUT membranes in vacuum,” *IEEE Trans. Ultrason. Ferroelectr. Freq. Control*, vol. 54, no. 6, pp. 1229-1239, June 2007.

[17] M. F. la Cour, T. L. Christiansen, J. A. Jensen, and E. V. Thomsen, “Electrostatic and small-signal analysis of CMUTs with circular and square anisotropic plates,” *IEEE Trans. Ultrason. Ferroelectr. Freq. Control*, vol. 62, no. 8, pp. 1563-1579, Aug. 2015.

[18] E. V. Thomsen, K. Reck, G. Skands, C. Bertelsen, and O. Hansen, “Silicon as an anisotropic mechanical material: Deflection of thin crystalline plates,” *Sens. Actuators,* vol. 220, pp. 347–364, 2014.

[19] F. C. Mbakogu, and M. N. Pavlovic, “Bending of clamped orthotropic rectangular plates: A variational symbolic solution,” *Comput. Struc.,* vol. 77, no. 2, pp. 117–128, Jun. 2000.

[20] M. Rahman, J. Hernandez, and S. Chowdhury, “An improved analytical method to design CMUTs with square diaphragms,” *IEEE Trans. Ultrason. Ferroelectr. Freq. Control*, vol. 60, no. 4, pp. 834-845, Apr. 2013.

[21] Z. Zheng, W. Sun, X. Suo, L. L. Wong, Z. Sun, and J. T. Yeow, "A novel deflection shape function for rectangular capacitive micromachined ultrasonic transducer diaphragms," *Sensing and Bio-Sensing Research,* vol. 5, pp. 62-70, Sept. 2015.

[22] S. Satir, J. Zahorian, and F. L. Degertekin, "A large-signal model for CMUT arrays with arbitrary membrane geometry operating in non-collapsed mode," *IEEE Trans. Ultrason. Ferroelectr. Freq. Control*, vol. 60, no. 11, pp. 2426-2439, Nov. 2013.

[23] J. Zahorian, S. Satir, and F. L. Degertekin, "Analytical-Finite Element hybrid model for CMUT arrays with arbitrary membrane geometry," *IEEE International Ultrasonics Symposium (IUS)*, Dresden, pp. 584-587, 7-10 Oct. 2012.

[24] F. Y. Yamaner, S. Olcum, H. K. Oguz, A. Bozkurt, H. Koymen, and A. Atalar, "High-power CMUTs: design and experimental verification," *IEEE Trans. Ultrason. Ferroelectr. Freq. Control*, vol. 59, no. 6, pp. 1276-1284, Jun. 2012.

[25] N. M. Senlik, S. Olcum, H. Koymen, and A. Atalar, "Radiation impedance of an array of circular capacitive micromachined ultrasonic transducers," *IEEE Trans. Ultrason. Ferroelectr. Freq. Control*, vol. 57, no. 4, pp. 969-976, 2010.

[26] H. K. Oguz, "Circuit theory based modeling and analysis of CMUT arrays," Ph.D. dissertation, Dept. Elect. Electron. Eng., Bilkent Univ., Ankara, Turkey, 2013.

Chapter 7

Multi-Frequency CMUT Imaging Arrays for Multi-Band Imaging and Imaging-Therapy Applications

Multi-frequency CMUT arrays are introduced for multi-scale imaging applications, where a single array transducer can be used for both deep low-resolution imaging and shallow high-resolution imaging. These transducers consist of low- and high-frequency membranes interlaced within each sub-array element. They are fabricated using a modified sacrificial release process. Successful performance is demonstrated using wafer-level Vibrometer testing, as well as acoustic testing on wirebonded dies consisting of arrays of 2- and 9-MHz elements of up to 64 elements for each sub-array. The arrays are demonstrated to provide multi-scale, multi-resolution imaging using wire phantoms. This work is summarized by Maadi et al. in the published conference paper titled "Multi-frequency CMUT imaging arrays for multi-scale imaging and imaging-therapy applications" and a submitted journal paper titled "Large-Scale Multi-Frequency CMUT Arrays for Multi-Band Ultrasound Imaging Applications" which is presented here.

7.1 Introduction

Typical ultrasound transducers operate in a pre-defined frequency band. In the case of piezoelectric transducers, this is predominantly determined by the thickness of the piezo ceramic as well as the backing and other considerations. There is growing interest in multi-frequency transducers for various applications including multi-scale imaging (the focus of this section), image-guided high-intensity focused ultrasound [1], image-guided ultrasound-aided drug delivery [2], super-harmonic contrast agent imaging [3]-[5], etc. Some of these applications have used imaging transducers physically embedded within an aperture in larger therapy transducers. Others have used a scanned single-element high-frequency transducer in an annular low-frequency transducer for low-frequency excitation, and high-frequency reception of super-harmonic signatures from microbubble contrast agents [6]-[11]. Ma *et al.* used a rotating single-element transducer with a high-frequency element (30 MHz) on one side and low-frequency element (6.5 MHz) on the other side [5]. Another approach to multi-frequency transducer design has included stacked low- and high-frequency piezo-composites [12]. In this case, acoustic matching for both low- and high-frequency is difficulty to obtain, and fabrication is non-trivial. Wang *et al.* used this approach to fabricate multi-frequency arrays. However, this approach did not use optimal matching for the low-frequency sub-array.

Capacitive micromachined transducers (CMUTs) are drum-like membranes that are electrostatically actuated to generate ultrasound and detect ultrasound signals by reading out pressure-induced capacitive changes. Operating frequencies of CMUTs are primarily determined by the size and thickness of the membranes. Eames *et al.* created multi-frequency CMUTs by using a pre-collapse mode for low-frequency operation and a collapse-mode for high-frequency operation [13]. However, this approach may suffer from dielectric charging and subsequent reliability issues. Savoia *et al.* fabricated CMUT membranes on piezoelectric transducers using a reverse fabrication process to create multi-frequency transducers [14].

Low frequency transducers exhibit a narrower bandwidth, but with greater energy and more penetration in a material while high frequency devices respond to frequencies below and above the central frequency (wider bandwidth) with less penetration, but better sensitivity to small discontinuities.

Using a different approach, we exploited the fact that CMUT membranes can be made much smaller than the acoustic wavelength(s) generated. We used this property to create multi-frequency CMUT arrays where large- and small membranes were interlaced on a scale smaller than operating wavelengths. This was investigated for multi-band photoacoustic imaging by Chee *et al.* [15]. The modeling of multi-frequency CMUT arrays was reported by our group including the effects of mutual acoustic impedance between dis-similar membranes [16], [17]. Then we showed the feasibility of our model for predicting the behavior of large-scale CMUT arrays [18]. In this section, we report on the design, characterization, and testing of multi-frequency linear arrays for multi-scale imaging purposes. Such arrays could enable both deep-penetration with low-resolution as well as higher-resolution at shallower imaging depth, all with a single transducer. This may have emerging applications for portable and wireless imaging probes which need to be multi-purpose. These arrays may also have applications to imaging-therapy, microbubble contrast agent imaging, etc, although these are not the focus of this paper. We demonstrate promising results indicating the potential for multi-frequency CMUT arrays for next-generation imaging and therapy applications.

7.2 Designed Multi-Frequency CMUT Arrays for Ultrasound Multi-Band Imaging Applications

We used our developed nonlinear equivalent circuit model [17] for predicting the behavior of large-scale multi-frequency CMUT arrays [18]. We aimed to develop 2- and 9-MHz sub-arrays created by interlacing low- and high-frequency membranes. Various large-scale multi-frequency arrays with different parameters were designed to be fabricated on highly conductive silicon prime wafers. Fig. 7.1 shows an example of a designed multi-frequency CMUT array with the parameters provided in Table 7.I.

As shown, the array uses 128 connections, 64 bonding pads for low- and 64 pads for high-frequency, to supply low- and high frequency sub-elements separately. This array was then fabricated and used to show the capability of multi-frequency arrays for multi-scale ultrasound imaging.

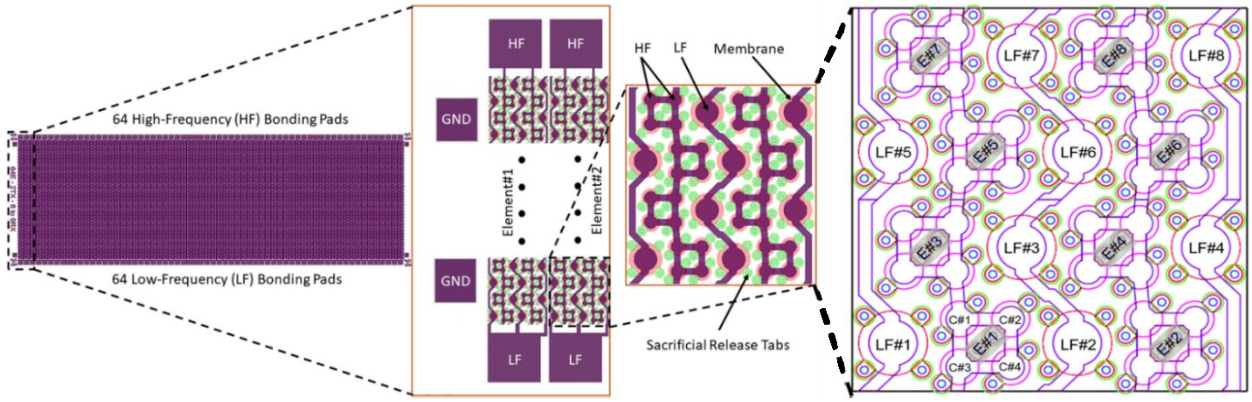

Fig. 7.1. A large-scale multi-frequency CMUT array with 64 low- and 64 high frequency sub-elements.

Fig. 7.2 demonstrates the simulation results of designed multi-frequency CMUT arrays (Fig. 7.1) in oil immersion medium for amplitude and phase of the peak displacement, and the total electrical conductance of single and parallel-connected multi-sized CMUT cells. Based on our simulation results, the resonance frequency of a single low- and high frequency CMUT cells with the parameters provided in Table 7.I and driving them with 85% of their snap-down voltages is 2.455 and 8.365 MHz, respectively [Fig. 7.2(a)]. Fig. 7.2(b) shows the total electrical conductance G of the parallel-connected CMUT cells inside of the array that is calculated by the net current passing through all membranes divided by the parallel-applied voltage. As shown in this figure, the permanent resonance frequencies of large and small membrane array elements are 2.54 and 9.635 MHz, respectively [Fig. 7.2(b)]. Depending on the CMUT parameters, array configuration and shape, mutual radiation impedance between the cells with dissimilar sizes affects each single cell in a different way by shifting the resonance frequencies to low or higher values [Fig. 7.2(c) – (f)]. For example, the resonance frequency of CMUT membrane #4 in Element#5 (E#5-C#4) shifts from 8.365 to 8.16 MHz (lower values) while for high-frequency CMUT membrane #3 in Element#2 (E#2-C#3) there is a shift to 8.84 MHz (higher values). Similarly, the resonance frequency of low-frequency (LF) CMUT membrane #1 (LF#1) shifts from 2.455 to 2.445 MHz (lower values) while for LF#7 there is a shift to 2.525 MHz (higher values).

TABLE 7.I. PARAMETERS OF DESIGNED AND FABRICATED CMUT CELLS USING A SACRIFICIAL RELEASE PROCESS.

Parameter	Values
Membrane material	Silicon Nitride
Large cells radius, a_1 (µm)	~ 26
Small cells radius, a_2 (µm)	~ 15
Number of LF and HF sub-elements	64
Width of LF and HF sub-elements (µm)	~ 292 and 210
Pitch of the elements (µm)	~ 302
Kerf of LF and HF sub-elements (µm)	~ 62 and 79
Array Size (mm × mm)	~ 19.32 × 5.95
Array Size including bonding pads (mm × mm)	~ 19.85 × 6.50
Number of LF and HF cells in each element	152 and 608
Total number of LF and HF CMUT cells in array	48,640
Collapse voltage of single small membrane (V)	401
Collapse voltage of single large membrane (V)	146
Membrane thickness, t_m (µm)	~ 1
Insulator thickness, t_i (nm)	~ 250
Gap height, t_{ga} (nm)	~ 400
Young's modulus, Y_0 (GPa)	~ 290
Density, ρ (g/cm^3)	~ 3.10
Poisson's ratio, σ	~ 0.263
Medium	Vegetable oil immersion Density of the oil is ~ 930 (kg/m^3) and speed of sound in oil is ~ 1430 m/s.

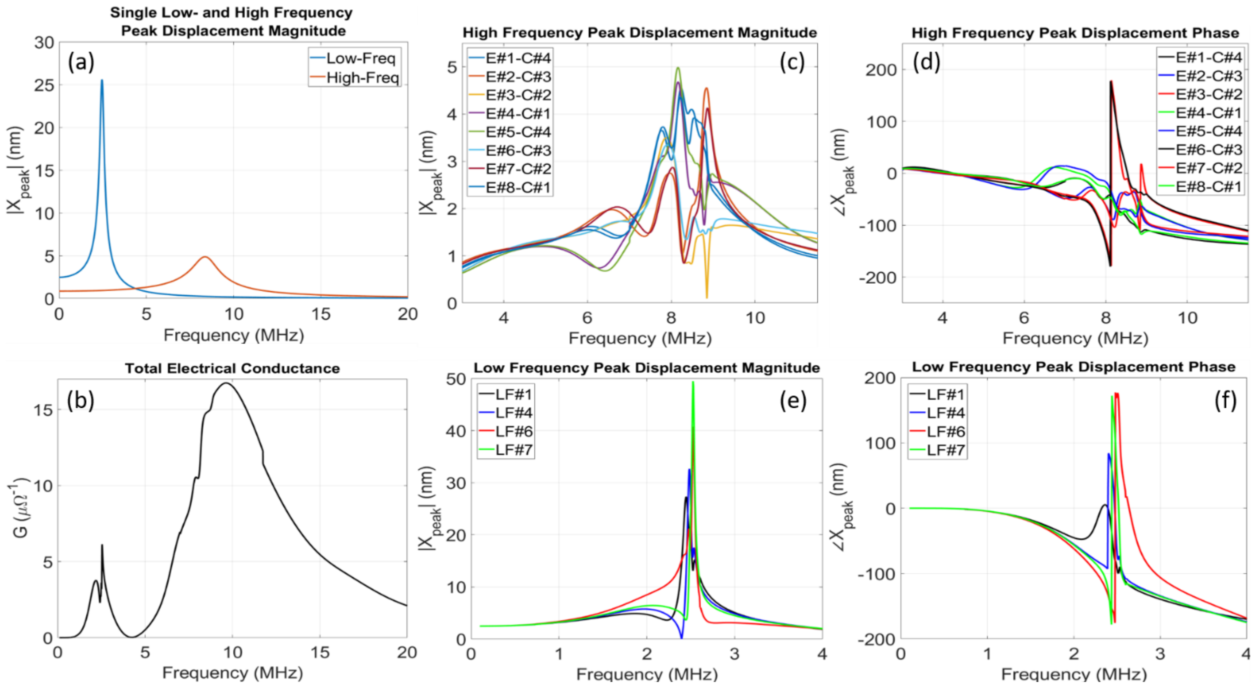

Fig. 7.2. Simulation results of designed multi-frequency CMUT array with parameters provided in Table 7.I. (a) Amplitude of the peak displacement for single low- and high frequency CMUT cells. (b) Total electrical conductance of the parallel-connected multisized CMUT cells. (c) The amplitude of the peak displacement for selected high frequency CMUT cells. (d) The phase of the peak displacement for selected high frequency CMUT cells. (e) The amplitude of the peak displacement for selected low frequency CMUT cells. (f) The phase of the peak displacement for selected low frequency CMUT cells.

Another multi-frequency CMUT array [Fig. 7.3(a)] was designed with square membranes and smaller die areas (7 × 7 mm). This array has 20 elements containing interlaced low- (~ 3 MHz in air) and high-frequency (~ 11 MHz in air) cells with the half-side-length of 41 and 18 µm, respectively [Fig. 7.3(b)]. Each element of the array has three bonding pads including low-frequency, common ground, and high-frequency. Both arrays (large- and small-sized) were fabricated using a modified standard silicon-nitride sacrificial release process. Section 5 explains the fabrication process of these arrays in detail.

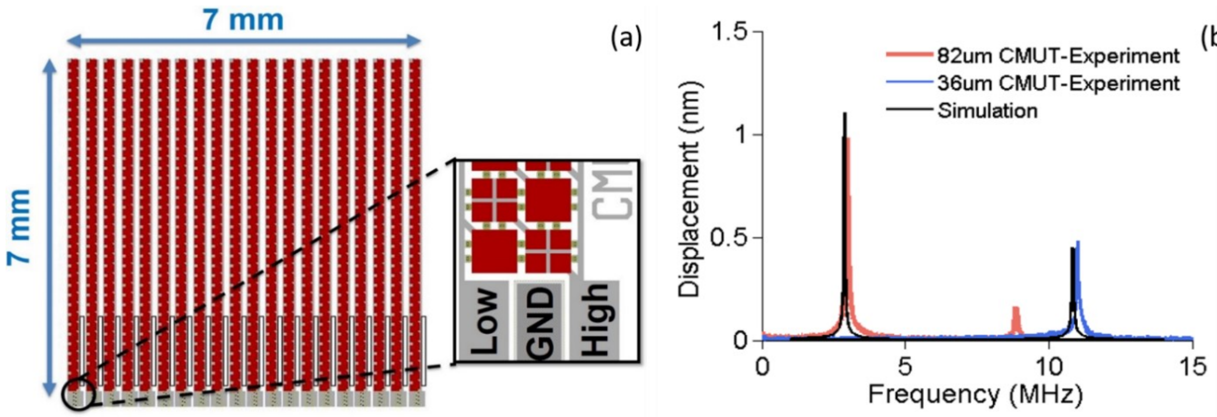

Fig. 7.3. (a) Designed 7 by 7 mm multi-frequency CMUT array with 20 elements and with square membranes. (b) Simulation and experimental results of designed and fabricated array.

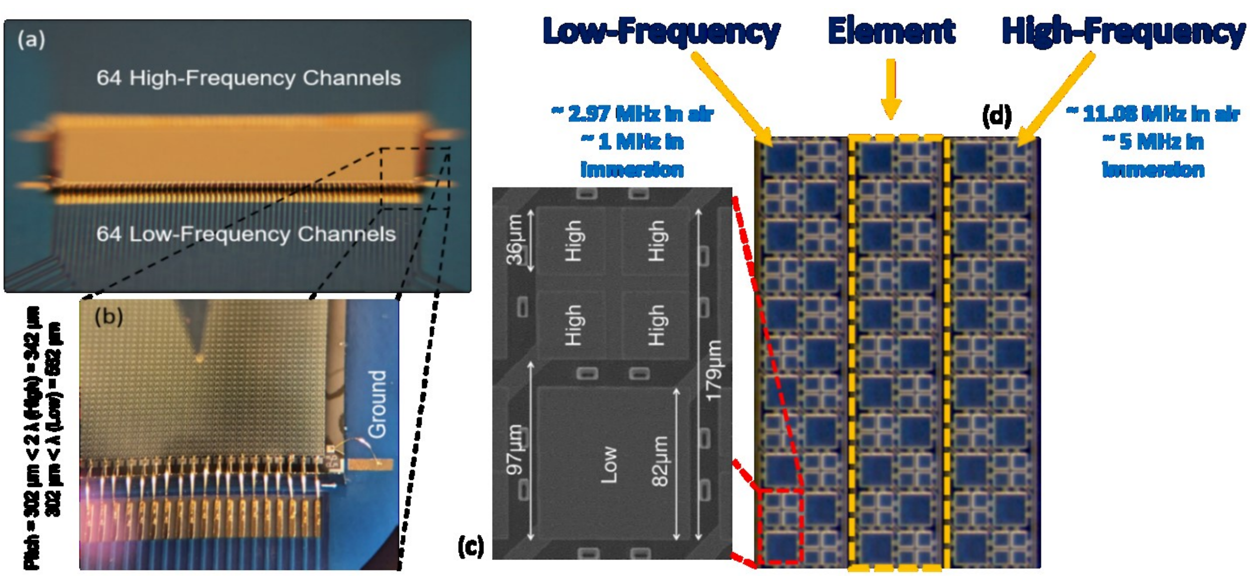

Fig. 7.4. (a) Sixty-four-sub-element multi-frequency CMUT linear array mounted on a custom PCB design. (b) A close-up image of gold wire-bonded low-frequency CMUT elements to a PCB. (c) SEM image of interlaced 82 and 36 μm square CMUT cells. (d) Microscopic image of fabricated 7 × 7 mm array.

7.3 Wafer-Level Characterization and Testing

A laser Doppler Vibrometer (MSA-500, Polytec) was used to image the operation of low- and high-frequency CMUT cells for large-scale (Fig. 7.5) multi-frequency CMUT arrays. The resonance frequency of the cells in air along with their membrane deflection were determined by applying an 8V pseudorandom signal with separate 130 and 250 VDC bias voltages to subarrays of large and small cells, respectively. The maximum membrane deflection for the low-and high-frequency CMUT cells in air were obtained at around 6.6359 and 18.9281 MHz, respectively while our model predictions showed the resonance frequency of 5.74 and 18.99 MHz. The differences between the simulation and experimental results may be due to discrepancies in simulation and fabricated device parameters. Then, using obtained resonance frequencies, a 0.5V sinusoidal signal with 130 and 250 VDC bias was applied to low- and high-frequency subarrays, separately (Fig. 7.5).

Similarly, the operation of small-scale CMUT array was imaged (Fig. 7.6). To determine the resonance frequency of the cells in air, a 3-V pseudorandom signal was applied to subarrays of large and small cells, separately. The maximum membrane deflection for the large and small CMUT cells in air were obtained at around 2.94 and 10.89 MHz, respectively. Then, using obtained resonance frequencies, a 3-V sinusoidal signal with 20 VDC bias was applied to low- and high-frequency subarrays, separately (Fig. 7.6).

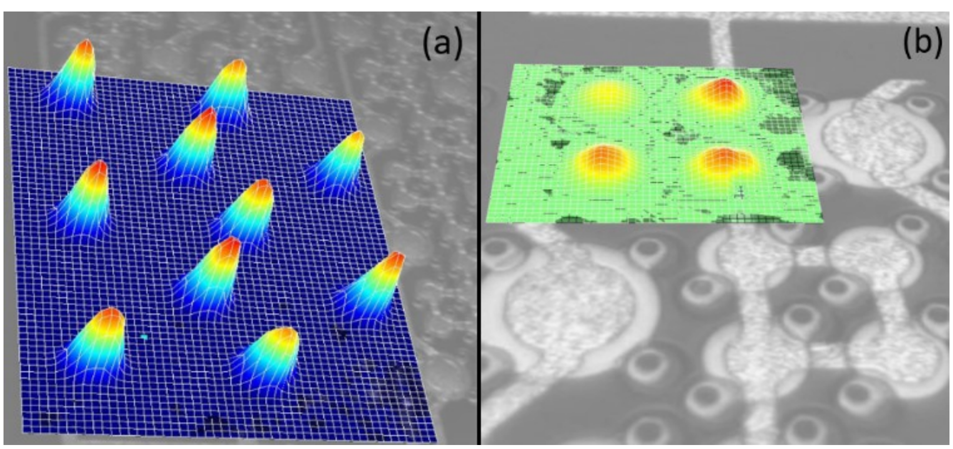

Fig. 7.5. Sample laser Vibrometer measurements of large-scale multi-frequency CMUT array. (a) Actuation of the low-frequency single element subarray including cells with the radius of 26 μm when driven by a 0.5 V sine wave and 130 VDC at 6.6359 MHz. (b) Actuation of the high-frequency single element subarray including cells with the radius of 15 μm when driven by a 0.5 V sine wave and 250 VDC at 18.9281 MHz.

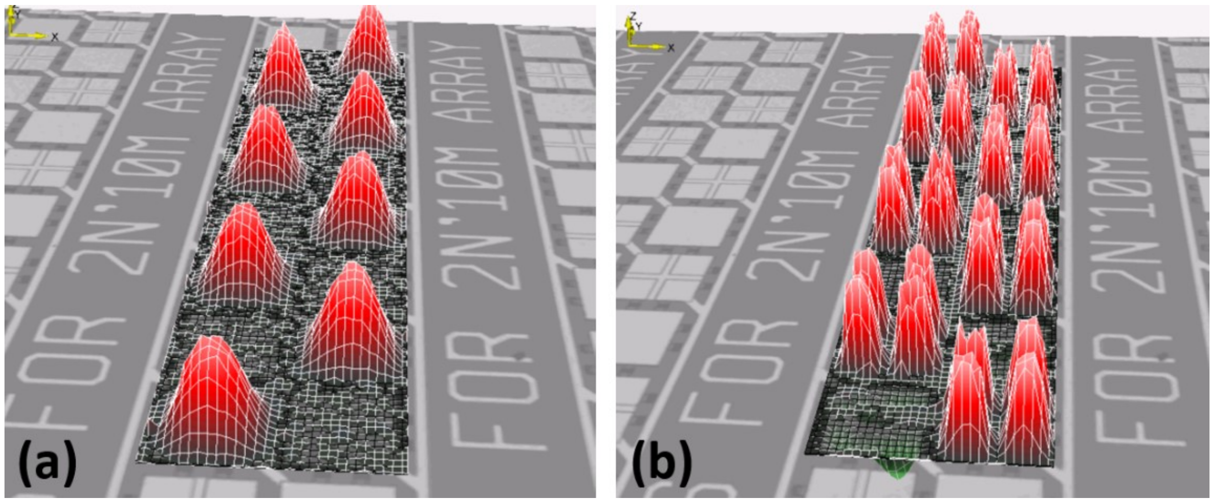

Fig. 7.6. Sample laser Vibrometer measurements of small-scale multi-frequency CMUT array. (a) Actuation of the low-frequency single element subarray including cells with the half-side-length of 41 µm when driven by a 3 V sine wave at 2.94 MHz. (b) Actuation of the high-frequency single element subarray including cells with the half-side-length of 18 µm when driven by a 3 V sine wave at 10.89 MHz.

7.4 Multi-Band Imaging using Large-Scale Multi-frequency CMUT Array

To demonstrate the potential of the multi-frequency devices for multi-scale imaging, we gold wirebonded a multi-frequency CMUT array with 64 low- and 64 high-frequency sub-elements (128 sub-elements in total) to custom printed circuit boards (PCBs) using wedge bonder (Fig. 7.4(a)). This board then mounted into interface boards populated with voltage-protected pre-amplifiers, bias tees, and supply voltage lines (Fig. 7.7), as previously described in [21]. The board has the capability of driving up to 256 elements with separate biasing for low- and high-frequency sub-elements. This was then connected to a Verasonics V1 Ultrasound Research system (Fig. 7.7). Low-frequency and high-frequency sub-arrays were supplied with 130 and 340 VDC, respectively. Additionally, low- and high-frequency elements were driven by a tri-state pulser, with a 100 Vpp, two-cycle waveform designed to approximate sinusoidal pulses matched to the respective element frequencies. Multi-band images were formed using a plane-wave imaging script. Three custom wire-target phantoms with the diameter of 190 μm and the separation of 7 mm, were imaged in a vegetable oil immersion medium.

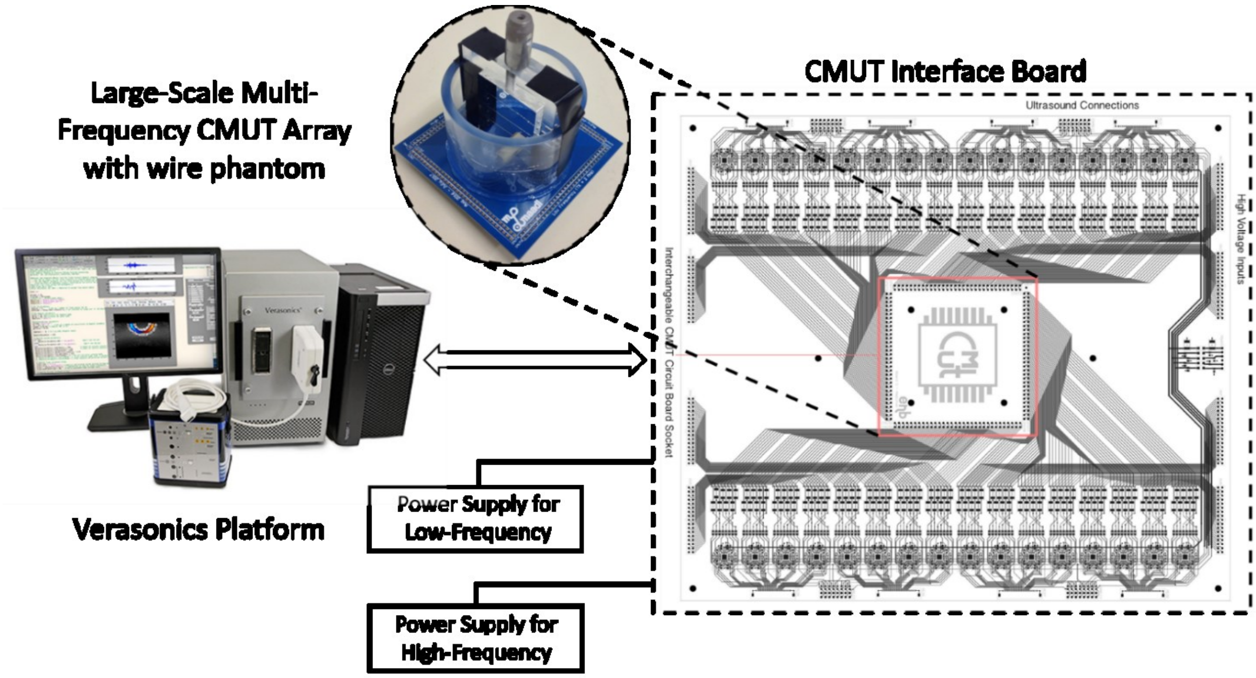

Fig. 7.7. The experimental setup including a wire-bonded 19.85 by 6.50 mm multi-frequency CMUT array to a custom PCB design, three wire phantoms with the diameter of 190 μm and the separation of 7 mm, all immersed in vegetable oil. The PCB is connected to Verasonics V1 platform using designed CMUT interface board with the capability of driving 256 elements through different lines and applying separate DC biases for low- and high-frequency sub-elements for ultrasound imaging.

Imaging results are shown in Fig. 7.8 and resolution measurements are quantified in Table 7.II. As expected, low-frequency sub-arrays were able to image deeper wire-targets with greater signal-to-noise ratios, but with inferior spatial resolution compared to the high-frequency sub-arrays. Fig. 7.9 demonstrates the lateral and axial point spread functions of wire#1 which is 16 mm far from the array.

Theoretical lateral resolutions for the wire at 16 mm depth were calculated as 0.67 and 0.21 mm, for the low- and high-frequency sub-arrays, respectively. These were close to the measured values of 0.61 and 0.31 mm, respectively. For target depths of 23 and 30 mm, theoretical lateral resolutions for low frequency sub-arrays were calculated as 0.97 and 1.26 mm, respectively. Similarly, for high frequency sub-elements, lateral resolutions were computed as 0.29 and 0.37 mm for the second and third wires, respectively. Discrepancies in resolution from the theoretical predictions may in part be due to array imperfections as well as frequency mixing between high- and low-frequency membranes. This has partially been predicted by mutual acoustic impedance considerations, described in our previous work [17]. Moreover, it is hard to detect the second and third wires for high-frequency sub-arrays to measure the resolution.

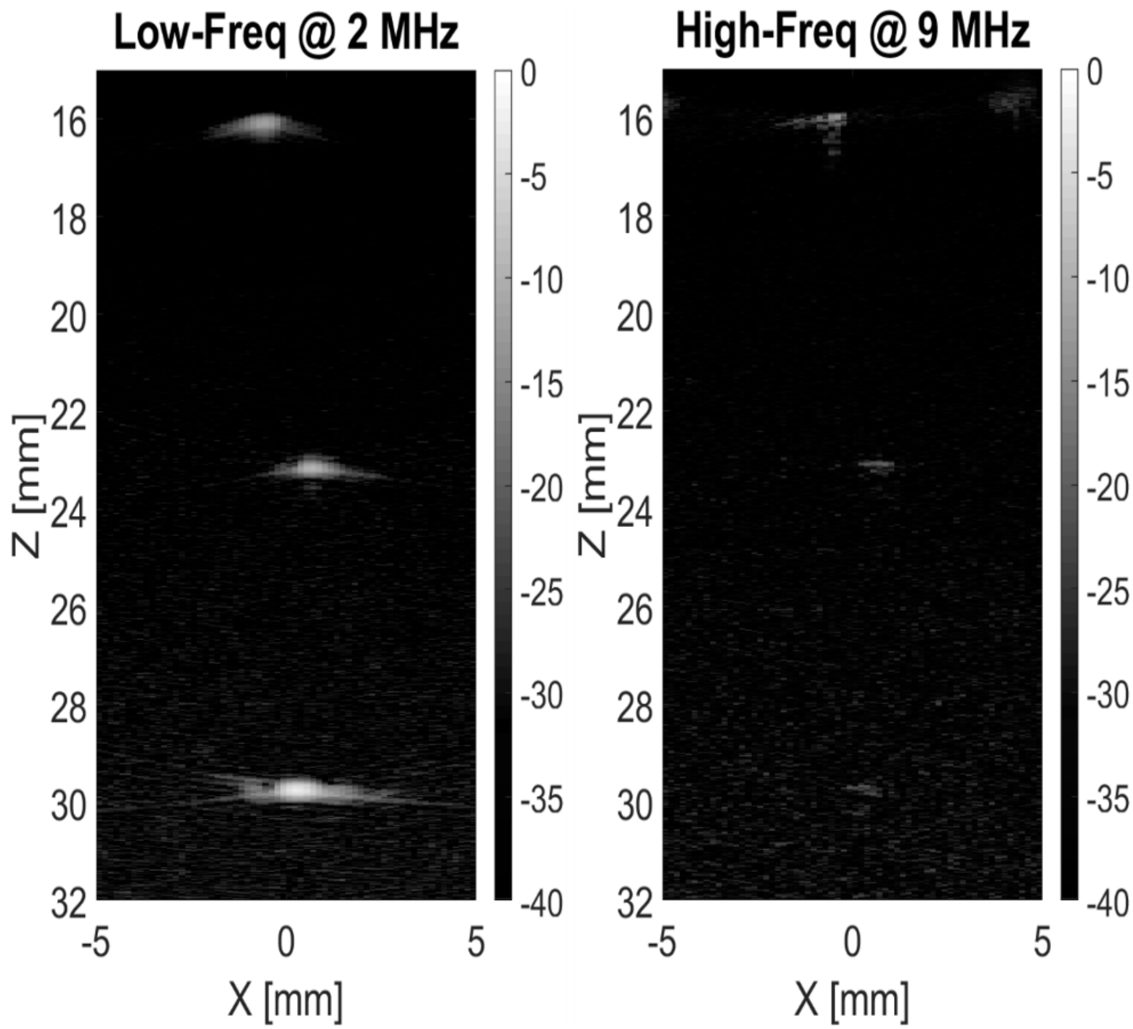

Fig. 7.8. Ultrasound multi-scale imaging of three wire phantoms with the diameter of 190 μm and the separation of 7 mm, using low- and high-frequency interlaced CMUT cells. Low-frequency sub-elements show less resolution, but with better penetration (left) while high-frequency sub-elements provides better resolution, but with less penetration (right).

TABLE 7.II. Resolution and SNR Measurements as a Function of Depth for Low- and High-Frequency Combinations.

Wire distance (mm)	Lateral FWHM Resolution (mm)		Axial FWHM Resolution (mm)		SNR (dB)	
	Low-Frequency	High-Frequency	Low-Frequency	High-Frequency	Low-Frequency	High-Frequency
16	0.61	0.31	0.55	0.21	39.17	39.25
23	0.88	0.67	0.57	0.42	34	26.1
30	1.20	0.90	0.64	0.46	36.73	19.87

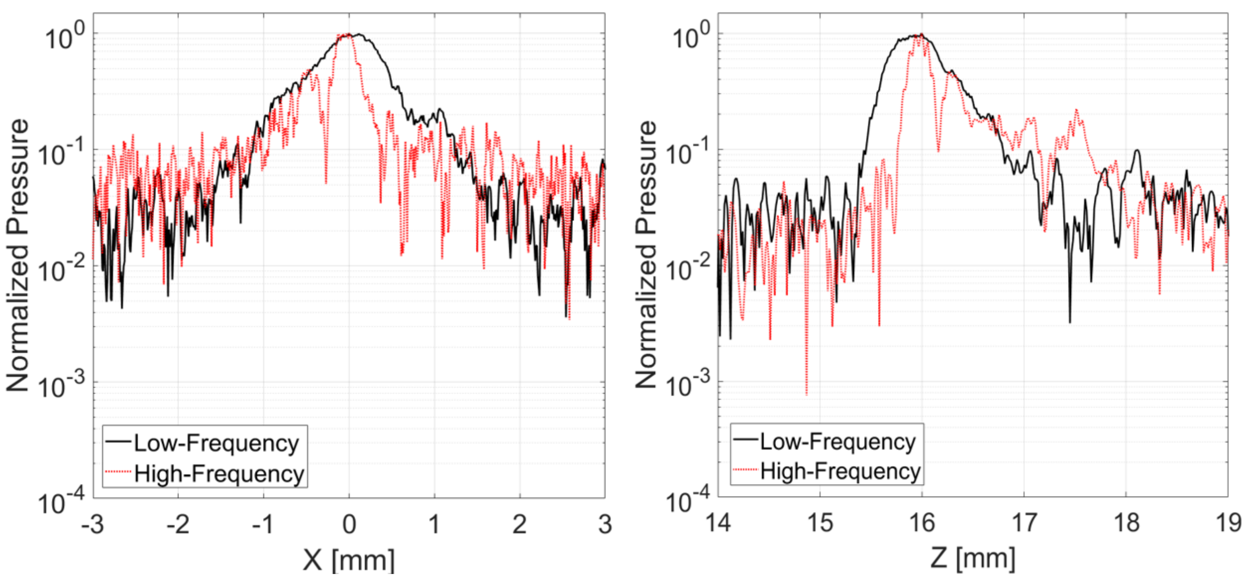

Fig. 7.9. (Left) Lateral and (Right) axial point spread functions of low- and high-frequency sub-elements for the wire of 16 mm far from the array.

7.5 Multi-Band Imaging using Small-Scale Multi-frequency CMUT Array

Similarly, the 7 by 7mm multi-frequency CMUT array was wire-bonded to a custom designed PCB (Fig. 7.10). Using our equivalent circuit model, the resonance frequencies of the low- and high-frequency sub-arrays were obtained as 0.668 MHz at 28 VDC and 4.681 MHz at 140 VDC in oil immersion medium, when 80% of the snap-down voltage was applied. We used separate power supplies to apply 30 VDC and 120 VDC for low- and high-frequency elements, respectively. Flash imaging was used to transmit sinusoidal pulses with frequencies of 1 and 5 MHz using low- and high-frequency CMUT cells and the images are reconstructed using dynamic receive beamforming.

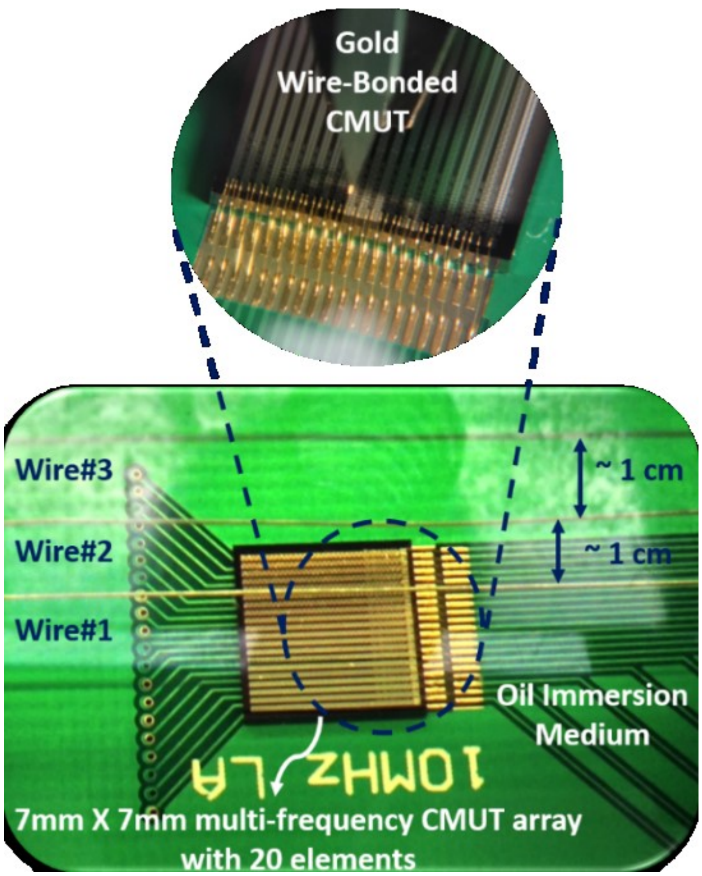

Fig. 7.10. The experimental setup including a gold wire-bonded 7 by 7 mm multi-frequency CMUT array to a custom designed PCB, three wire phantoms with the separation of 0.7 cm, all immersed in vegetable oil.

Fig. 7.11 demonstrates the imaging of three wire phantoms with different low- and high-frequency transmit and receive combinations. First, we transmit the ultrasound signal using low-frequency elements by exciting them at the resonance frequency of 1 MHz and receiving the echoes coming back from the targets using the same low-frequency transducers. Then we switch the elements to high-frequency CMUTs and excite them at resonance frequency of 5 MHz.

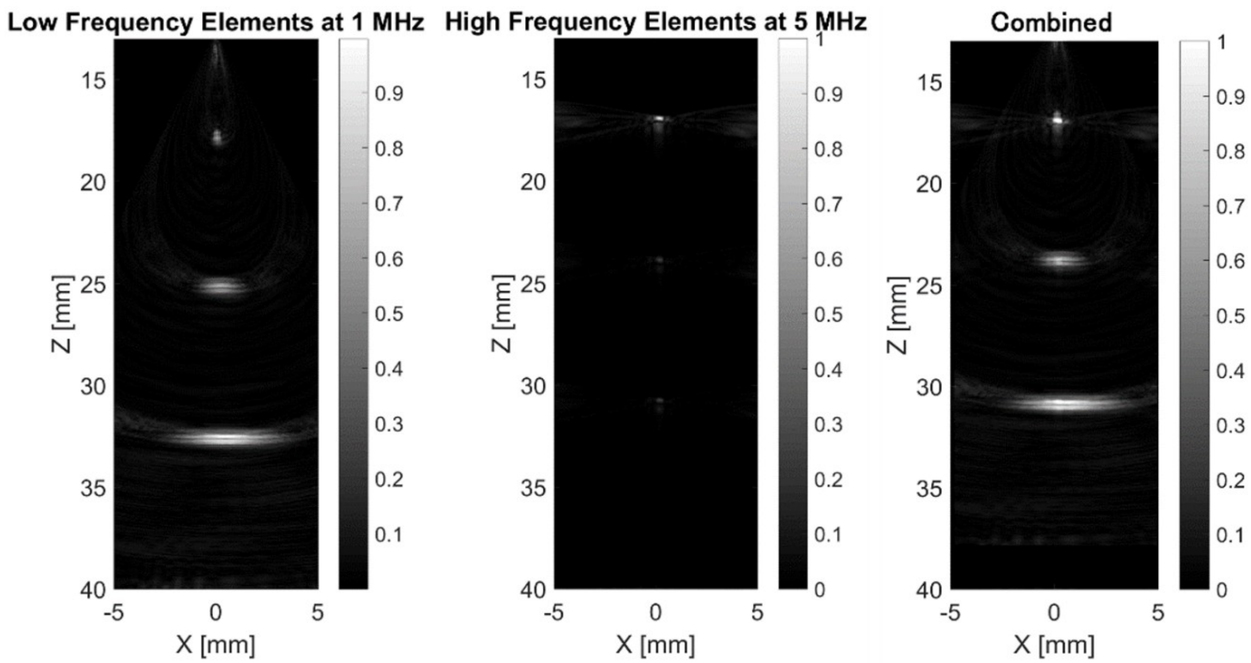

Fig. 7.11. Imaging of three wire phantoms using low- and high-frequency CMUT cells.

As can be seen in Fig. 7.11, the low-frequency elements provide better signal to noise ratio (SNR) for the furthest wire target with less resolution compared to the image obtained by high-frequency elements. On the other hand, the high-frequency elements can be used to obtain high-resolution images for the targets close to the transducer. However, the SNR of the images for the second and third wire phantoms are less compared to the images obtained using low-frequency elements. The combination of low- and high-frequency subarrays may be used to image different depths to keep the good resolution and SNR simultaneously. Table7.III summarizes the azimuthal and axial FWHM (full width at half maximum) resolutions and the SNR of three different images obtained using wire targets.

TABLE 7.III. RESOLUTION AND SNR MEASUREMENTS AS A FUNCTION OF DEPTH FOR LOW- AND HIGH-FREQUENCY COMBINATIONS.

Wire distance (mm)	Azimuthal FWHM Resolution (mm)		Axial FWHM Resolution (mm)		SNR (dB)	
	Low-Frequency	High-Frequency	Low-Frequency	High-Frequency	Low-Frequency	High-Frequency
16	0.66	0.37	0.65	0.15	30.2	36.1
23	1.5	0.361	0.62	0.22	31.3	24.2
30	3.5	0.341	0.52	0.20	34	24

7.6 Discussion

While wideband imaging transducers are becoming more common, multi-frequency transducers with distinct bands of operation have yet to be demonstrated for multi-scale imaging. This work represents a new approach to multi-scale imaging using multi-frequency CMUT arrays. The large-scale arrays are fabricated such that high-frequency sub-arrays have 1.7λ pitch and the low-frequency sub-arrays have 0.5λ pitch while small-scale arrays are designed and fabricated in a scale smaller than the wavelength to ensure the minimization of grating lobes. Grating and sidelobe levels appear to be minimal and could be further reduced with future designs. Some sidelobe artifacts are due to dead elements and other elements that have a sub-optimal sensitivity.

Greater acoustic outputs will be desired for future applications. Currently, using the same gap height for low- and high-frequency sub-arrays of large-scale CMUT array, the maximum acoustic pressure obtained at the transmit-focal-depth of 23 mm was 0.8 MPa peak-to-peak (Fig. 7.12). The normalized frequency spectrum of the received acoustic pressure is show in Fig. 7.13 by applying fast Fourier transform to obtained output pressure signal from hydrophone. It was found that the second harmonic wave resonated at $2f_0$ of 5.8 MHz was around – 14.5 dB with respect to the fundamental harmonic at f_0 of 2.9 MHz.

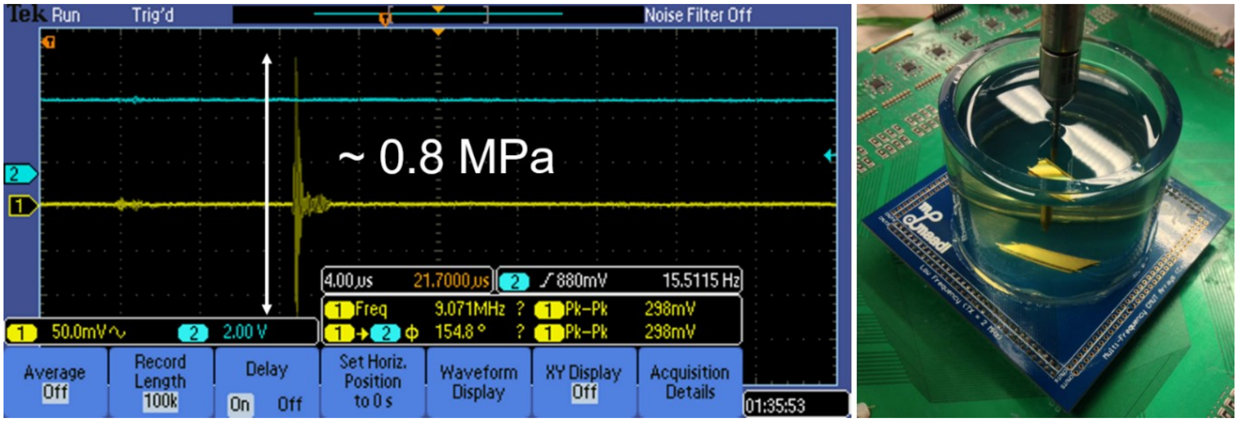

Fig. 7.12. Hydrophone pressure measurement for a 19.85 by 6.50 mm multi-frequency CMUT array on the 23 mm transmit-focal distance of the array.

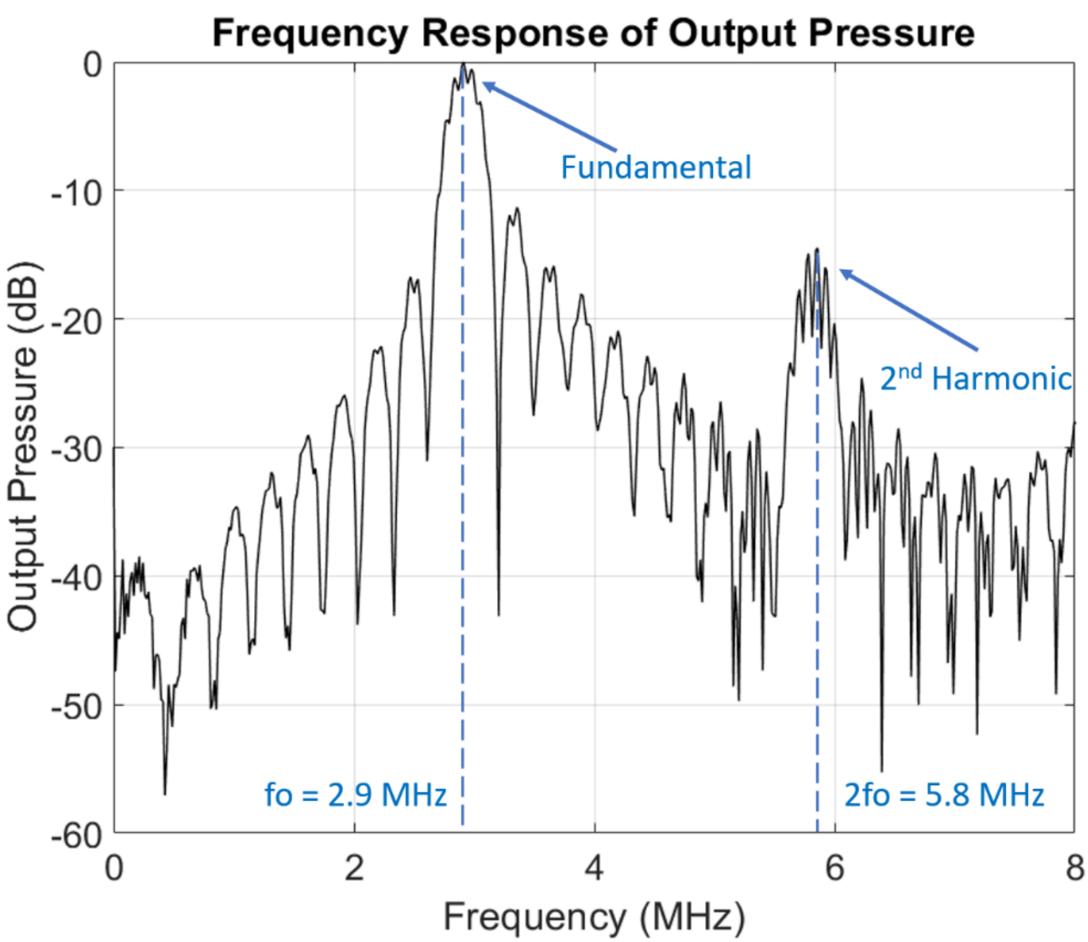

Fig. 7.13. The normalized frequency spectrum of the received output pressure.

Conclusion

Multi-frequency transducers may have several emerging applications including multi-scale imaging, super-harmonic contrast agent imaging and imaging-therapy applications. For imaging-therapy applications low-frequencies are typically needed for therapeutic heating or contrast agent destruction, while higher-frequencies are required for high-resolution imaging. However, development of these multi-frequency transducers is challenging owing to disparate focal zones or difficult acoustic impedance matching. Large- and small-scale multi-frequency CMUT arrays have been designed, fabricated, and characterized as well as tested for multi-scale imaging applications. These arrays consist of low- and high-frequency membranes interlaced on a scale smaller or comparable with acoustic wavelengths. Current devices show promise for emerging multi-scale, multi-resolution imaging, and may have applications to portable and handheld probes that must have multiple functionalities for a variety of imaging applications.

References

[1] C. D. Herickhoff, C. M. Wilson, G. A. Grant, G. W. Britz, E. D. Light, M. L. Palmeri, P. D. Wolf, and S. W. Smith, "Dual-mode IVUS transducer for image-guided brain therapy: Preliminary experiments," *Ultrasound Med. Biol.*, vol. 37, no. 10, pp. 1667–1676, Oct. 2011.

[2] A. L. Klibanov, "Microbubble contrast agents: targeted ultrasound imaging and ultrasound-assisted drug-delivery applications," *Invest. Radiol.*, vol. 41, no. 3, pp. 354–362, Mar. 2006.

[3] K. H. Martin, B. D. Lindsey, J. Ma, M. Lee, S. Li, F. S. Foster, X. Jiang, and P. A. Dayton, "Dual-frequency piezoelectric transducers for contrast enhanced ultrasound imaging," *Sensors*, vol. 14, no. 11, pp. 20825–20842, Nov. 2014.

[4] H. H. Kim, J. M. Cannata, R. Liu, J. H. Chang, R. H. Silverman and K. K. Shung, "20 MHz/40 MHz dual element transducers for high frequency harmonic imaging," *IEEE Trans. Ultrason. Ferroelectr. Freq. Control*, vol. 55, no. 12, pp. 2683-2691, Dec. 2008.

[5] J. Ma, K. Martin, P. A. Dayton, and X. Jiang, "A preliminary engineering design of intravascular dual-frequency transducers for contrast-enhanced acoustic angiography and molecular imaging," *IEEE Trans. Ultrason. Ferroelectr. Freq. Control*, vol. 61, no. 5, pp. 870–880, May 2014.

[6] B. D. Lindsey, J. D. Rojas, K. H. Martin, S. E. Shelton, and P. A. Dayton, "Acoustic characterization of contrast-to-tissue ratio and axial resolution for dual-frequency contrast-specific acoustic angiography imaging," *IEEE Trans. Ultrason. Ferroelectr. Freq. Control*, vol. 61, no. 10, pp. 1668-1687, Oct. 2014.

[7] B. D. Lindsey, K. H. Martin, P. A. Dayton, J. Ma, Zhuochen Wang, and X. Jiang, "Dual-frequency intravascular ultrasound imaging of microbubble contrast agents: Ex vivo and in vivo demonstration," *2015 IEEE International Ultrasonics Symposium (IUS)*, Taipei, pp. 1-4, 21-24 Oct. 2015.

[8] B. D. Lindsey, S. E. Shelton, J. K. Tsuruta, P. A. Dayton, and F. S. Foster, "Molecular acoustic angiography: Demonstration of in vivo feasibility for high resolution superharmonic ultrasound molecular imaging," *2015 IEEE International Ultrasonics Symposium (IUS)*, Taipei, pp. 1-3, 21-24 Oct. 2015.

[9] B. D. Lindsey, J. D. Rojas, and P. A. Dayton, “On the relationship between microbubble fragmentation, deflation and broadband superharmonic signal production,” *Ultrasound Med. Biol.*, vol. 41, no. 6, pp. 1711–1725, Jun. 2015.

[10] D. E. Kruse, and K. W. Ferrara, “A new imaging strategy using wideband transient response of ultrasound contrast agents,” *IEEE Trans. Ultrason. Ferroelectr. Freq. Control*, vol. 52, no. 8, pp. 1320-1329, Aug. 2005.

[11] S. Li et al., “A 3 MHz/18 MHz dual-layer co-linear array for transrectal acoustic angiography,” *2015 IEEE International Ultrasonics Symposium (IUS)*, Taipei, pp. 1-4, 21-24 Oct. 2015.

[12] Z. Wang et al., “Design, Fabrication, and Characterization of a Bifrequency Colinear Array,” *IEEE Trans. Ultrason. Ferroelectr. Freq. Control*, vol. 63, no. 2, pp. 266-274, Feb. 2016.

[13] M. D. C. Eames, T. J. Reck, and J. A. Hossack, “Selectable frequency CMUT with membrane stand-off structures,” *IEEE International Ultrasonics Symposium (IUS)*, Rome, pp. 2814-2817, 20-23 Sep. 2009.

[14] A. Stuart Savoia et al., “Design, Fabrication and Characterization of a Hybrid Piezoelectric-CMUT Dual-Frequency Ultrasonic Transducer,” *2018 IEEE International Ultrasonics Symposium (IUS)*, Kobe, pp. 1-4, 22-25 Oct. 2018.

[15] R. K. W. Chee, P. Zhang, M. Maadi, and R. J. Zemp, “Multifrequency Interlaced CMUTs for Photoacoustic Imaging,” *IEEE Trans. Ultrason., Ferroelect., Freq. Control*, vol. 64, no. 2, pp. 391–401, Feb. 2017.

[16] M. Maadi, R. Chee, and R. J. Zemp, “Mutual radiation impedance for modeling of multi-frequency CMUT arrays,” *IEEE International Ultrasonics Symposium (IUS)*, Taipei, pp. 1-4, 21-24 Oct. 2015.

[17] M. Maadi, and R. J. Zemp, “Self and Mutual Radiation Impedances for Modeling of Multi-Frequency CMUT Arrays,” *IEEE Trans. Ultrason., Ferroelect., Freq. Control*, vol. 63, no. 9, pp. 1441–1454, Sep. 2016.

[18] M. Maadi, and R. J. Zemp, “Modelling of Large-Scale Multi-Frequency CMUT Arrays with Circular Membranes,” *IEEE International Ultrasonics Symposium (IUS)*, Tours, pp. 1-4, 18-21 Sep. 2016.

[19] B. A. Greenlay, and R. J. Zemp, “Fabrication of Linear Array and Top-Orthogonal-to-Bottom Electrode CMUT Arrays with a Sacrificial Release Process,” *IEEE Trans. Ultrason. Ferroelectr. Freq. Control*, vol. 64, no. 1, pp. 93-107, Jan. 2017.

[20] M. Maadi, and R. J. Zemp, “A Nonlinear Lumped Equivalent Circuit Model for a Single Un-Collapsed Square CMUT Cell,” *IEEE Trans. Ultrason., Ferroelect., Freq. Control*, vol. 66, no. 8, pp. 1340–1351, Aug. 2019.

[21] B. A. Greenlay, “Fabrication and Integration of CMUT Sensors,” MS.c. dissertation, Dept. Elect. Comp. Eng., Univ. of Alberta, Edmonton, Alberta, Canada, 2017.

Chapter 8

Electrical Impedance Matching of CMUT Cells

Several impedance matching networks were designed to transfer more power to CMUT arrays. The design, simulation and integration results are summarized by Maadi et al. in the published conference paper titled "Electrical Impedance Matching of CMUT Cells" which is presented here.

8.1 Introduction

Capacitive micromachined ultrasonic transducers (CMUTs) have admirable performance that make them suitable for use in ultrasound imaging and therapeutic applications. Maximizing acoustic power output from CMUTs is of major importance to ensure competitive signal-to-noise ratio. In this work, ADS validated models were used to predict device performance before and after using impedance matching networks. Electrical impedance matching of the large signal models of the CMUT cells were studied in detail. Membrane velocity and acoustic pressure of a single 3MHz CMUT cell, a 2 by 10 linear CMUT array and 6 by 6 CMUT square array were measured and compared with and without matching networks. For a given bias voltage, we found the maximum possible AC drive-level we could apply without collapsing the membrane, then found the mean membrane velocity at this signal drive-level in the cases where a matching network was present or absent. The results show remarkable improvements in output acoustic pressure which can be useful for some imaging and especially ultrasound therapeutic applications. The scattering parameters of a 5 by 100 linear CMUT array were measured using a vector network analyzer. Different kinds of impedance matching networks were designed to transfer more power to the arrays. Experiments show admirable improvements and have a good agreement with simulation results.

CMUTs have a significant reactive component to the input impedance which may result in non-optimal real power dissipated as acoustic energy when transmitting. Impedance matching networks can counteract undesired reactance within specific frequency bands to permit more real power delivery. However, it is unclear how advantageous such matching networks may be if one simply has the option of using a higher transmit level.

In previous works, impedance matching techniques have been used to match the mechanical and acoustical terminals of the ultrasound transducers using physical matching layers [1]-[3]. However, the potential of CMUTs for therapeutic applications using electrical impedance matching networks has not been fully explored. In this section, we performed large signal simulations of CMUT cells and arrays to demonstrate important advantages of using electrical impedance matching networks. Then, using the simulation results and experimental scattering parameters obtained by a vector network analyzer (VNA) the appropriate impedance matching networks are designed. Finally, the scattering parameters are compared in the case where a matching network is present or absent.

8.2 Case Study: Electrical Impedance Matching of a Single CMUT Cell Using the Large Signal Model

Three interacting physical ports including electrical, mechanical and acoustical domains must be included precisely in an accurate model of a CMUT cell. Some previous simplified models only focused on including the electrical and mechanical parameters of a CMUT by assuming the acoustic port as a resistive load [4], [5]. In sections 3 and 4, the exact values of the self and mutual radiation impedances were analyzed, modeled and included in the CMUT array simulations.

As given in Fig. 8.1, the large signal equivalent circuit can model three interacting physical domains of the CMUTs. As shown, the impedance matching network is placed between the VNA and the CMUT input port.

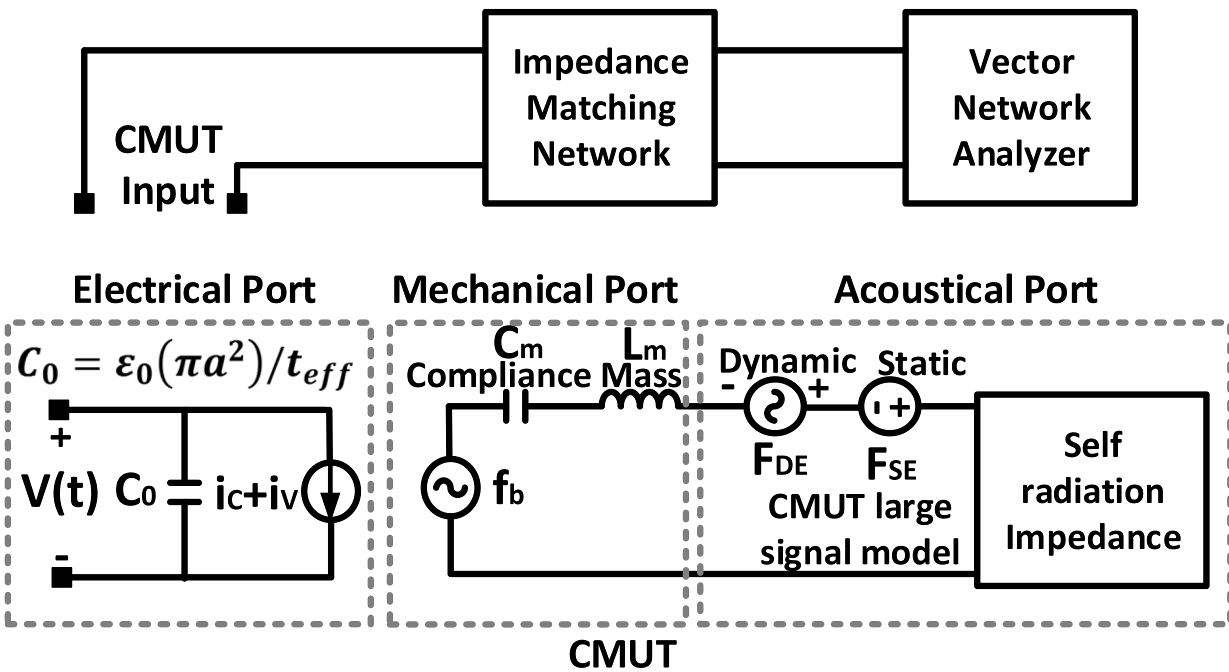

Fig. 8.1. CMUT Large signal equivalent circuit model including three interacting physical domains connected to a VNA by a matching network.

8.3 Input Impedance and Scattering Parameters of a single CMUT Cell with and without Using Impedance Matching Network

The scattering parameters (S-parameters) are used to describe the relationship between the input and output electrical ports of a CMUT cell in which S_{11}, S_{12}, S_{21} and S_{22} parameters represent the input reflection, reverse transmission, forward transmission and output reflection coefficients, respectively. The CMUT is modeled in ADS using the parameters of Table 8.I. As shown in Fig. 8.2 and expected, the CMUT cell is resonating around 3MHz as a pure capacitor (-90°) with considerable imaginary part of input impedance (245.3KΩ) which means the CMUT cell is mostly storing the energy rather than radiating.

TABLE 8.I. CMUT SPECIFICATIONS FOR MODELING IN ADS.

CMUT Parameter	Value
Membrane radius	48 μm
Membrane thickness	4 μm
Top electrode	Full
Gap size	300 nm
Insulating layer	0
Young's modulus	148 GPa
Poisson's ratio	0.177
Density	2329 kg/m^3
Mode	Immersion in water

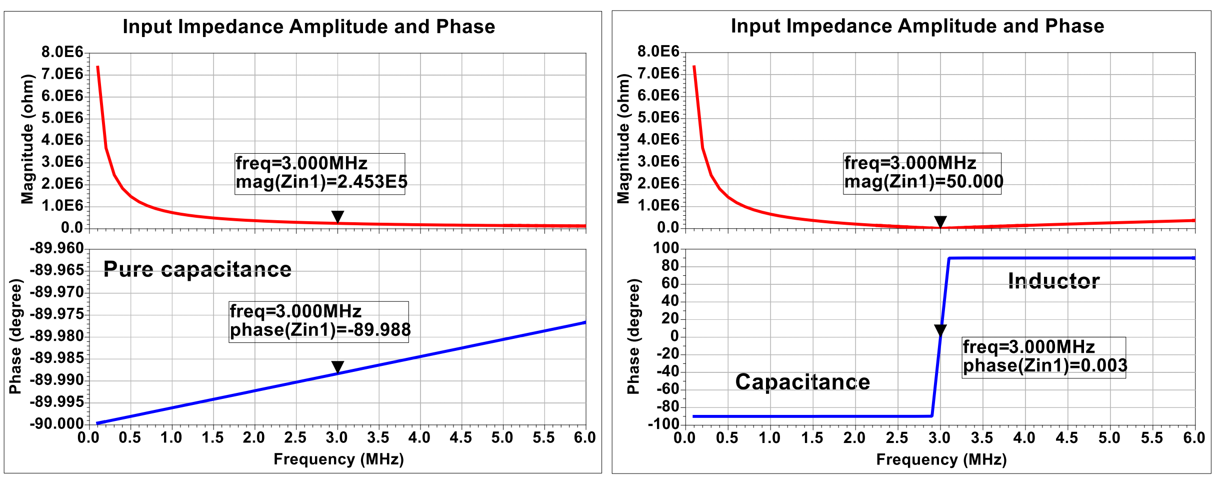

Fig. 8.2. Input impedance magnitude and phase of a 3MHz CMUT cell operating in immersion medium without (Top) and with (Bottom) impedance matching network.

The imaginary part of the input impedance can be cancelled using an appropriate matching network. As shown in Fig. 8.2, the CMUT shows a 50Ω real input impedance around the resonance frequency with negligible reactance (0.003Ω) which means the CMUT is completely matched. The behavior of the CMUT is changed from a capacitor before the center frequency to a pure resistor with almost zero-degree phase and then remains as an inductor with positive reactive impedance above the resonance frequency (Fig. 8.2). The effects of the optimized matching network on the membrane velocity and output pressure is evaluated in following section to observe the performance of the CMUT.

8.4 The Effect of Impedance Matching Network on CMUT Membrane Velocity and Pressure

The optimized matching network is added to CMUT large signal model and then they are used in 2 by 10 linear and 6 by 6 square array configurations.

To evaluate the effect of matching network on membrane velocity and output pressure, the DC voltage is swept from 5V to 110V by 10V step. For each DC value, the CW AC voltage is increased until the snap-down occurs in at least one of the CMUT cells. This is the point that the maximum membrane velocity and consequently maximum pressure is obtained for un-collapsed mode operation. For 2 by 10 linear CMUT array, when the input DC voltage is less than 75V, the average membrane velocity using a matching network is larger than those without (Fig. 8.3-Top). As can be observed, the gap between the matched and unmatched graphs becomes bigger around low DC values and maximum pre-collapsed drive AC signals which makes it possible to get more velocity and then output pressure. Although the average membrane velocity of the unmatched CMUT array is more than the matched one after 75 DC volts, but the values are still dramatically less than those obtained using lower DC voltages. Similar approach is accomplished for a 6 by 6 CMUT square array, but this time the unmatched graph passed the matched one after 60 DC volts. It is obvious that the graph nature is completely dependent on the CMUT cells configuration.

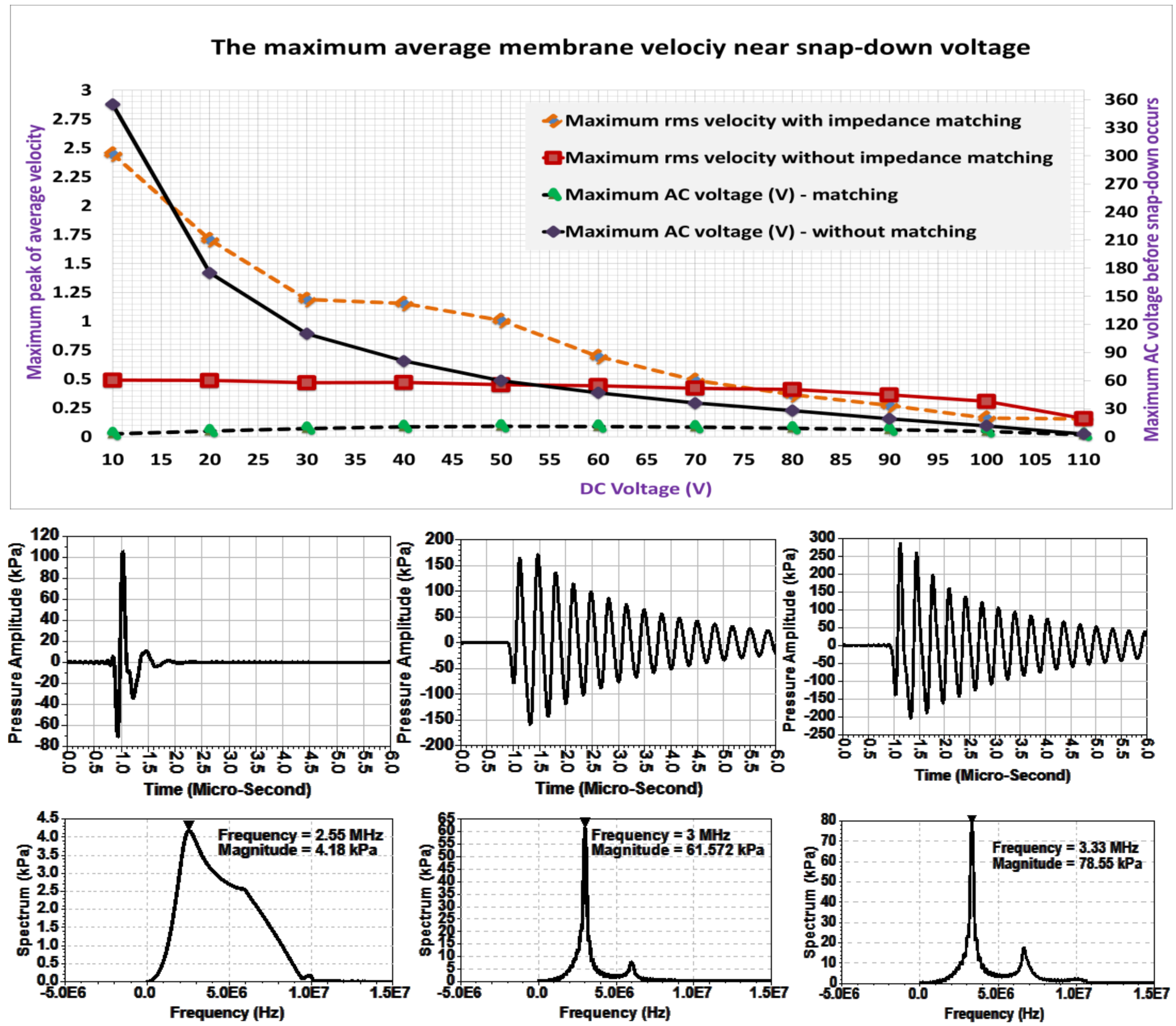

Fig. 8.3. (Top) The maximum average membrane velocity of a 2 by 10 linear CMUT array with 3MHz transducers operating in immersion mode close to snap-down voltage. (Bottom-left) The generated pulse pressure and its spectrum at 583.2μm distance away from the center of the 1080 by 1080 μm^2 array without matching network. (Bottom-mid) The generated pulse pressure and its spectrum at 583.2μm distance away from the center of the 1080 by 1080 μm^2 array with matching network. (Bottom-right) The generated pulse pressure and its spectrum at 583.2μm distance away from the center of the 1080 by 1080 μm^2 array with wide-band matching network.

Due to mutual acoustic impedance effect between the transducers, the mid CMUT cell in 6 by 6 array meets the collapse voltage much sooner, while others are still far from the collapsed mode and we are not able to increase the AC voltage further more to obtain much larger membrane velocities.

Fig. 8.3-bottom shows the time domain pressure pulses generated 583.2µm distance away from the center of the array for impedance matched and unmatched cases. A 6 by 6 CMUT array is excited with a single 100nm single pulse when the voltage is initially kept at 50V and then increased to 70V within the pulse duration. As can be observed, the matched spectrum shows bigger quality factor with almost 15 to 19 times more maximum pressure compared to unmatched CMUT array.

A wide-band matching network was used to increase the bandwidth (Fig. 8.3- Bottom-right). The maximum pressure is enhanced 17kPa compared to the first matching network and the spectrum shows higher values in upper frequencies.

The membrane RMS velocities of matched and unmatched single CMUT elements are compared in Fig. 8.4. The matched CMUT shows dramatically higher velocities (~ 8.5 times) compared to unmatched element while the wide-band matching network has wider response.

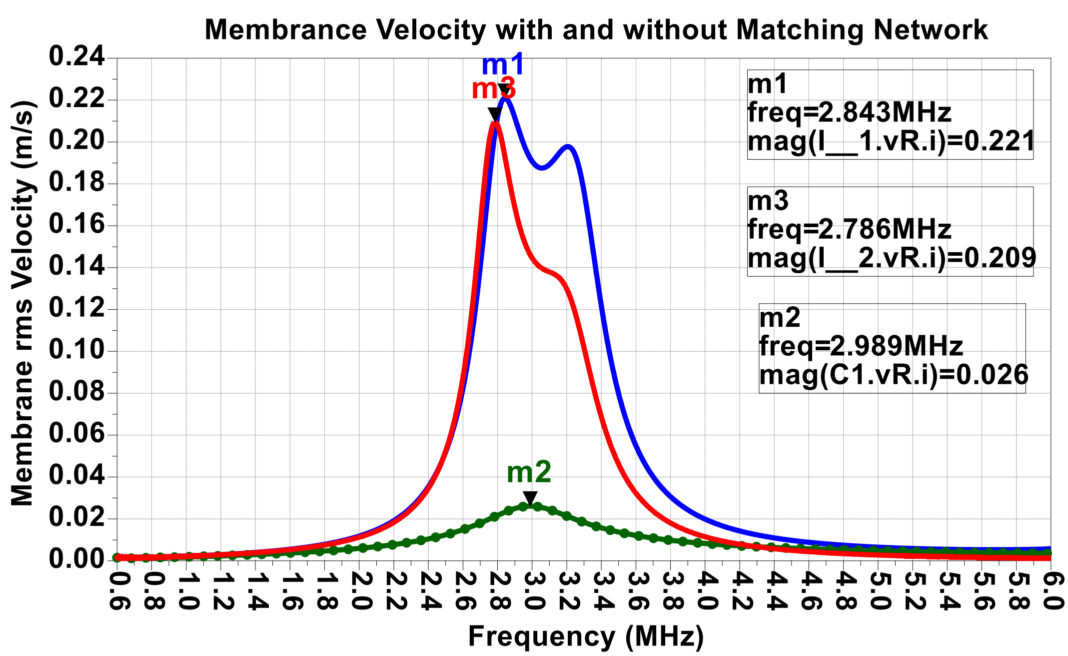

Fig. 8.4. Impedance matching effects on a single membrane RMS velocity. Green dotted line: unmatched, red-dashed line: matched with narrowband network, blue solid line: broadband matching network.

The output pressure of a 6 by 6 square CMUT array is measured at 583.2µm distance away from the center of the array. The voltage is initially kept at 50V and then increased from 10V to 65V with 5V step size within the pulse duration (Fig. 8.5). Depending on the value of the AC voltages, the output power with matching network is enhanced almost 8 to 17 times compared to the array in the absence of matching network. The improvement factor can be increased even more when lower DC voltages are applied to the matched CMUT arrays.

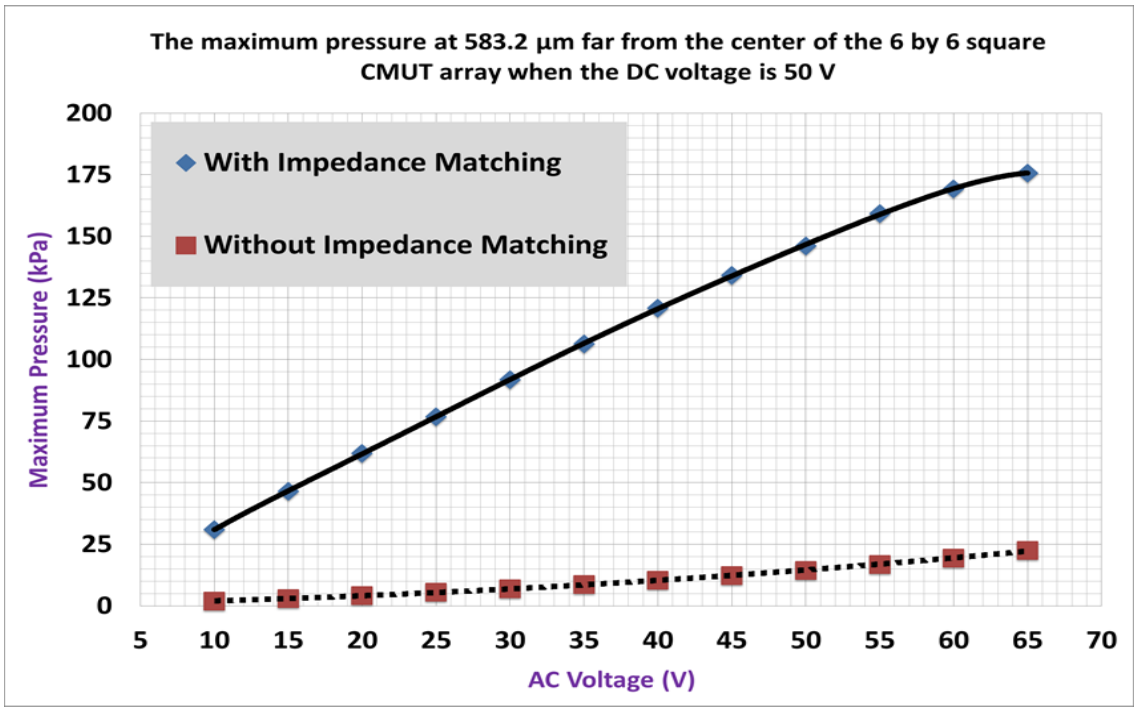

Fig. 8.5. Impedance matching effect on acoustic pressure for a 6 by 6 CMUT square array.

8.5 Experiment

A Vector Network Analyzer (NI PXIe-5632, National Instruments) was used (Fig. 8.6) to measure the scattering parameters of a 5 by 100 linear sacrificial-release CMUT array with architecture similar to those reported in [1]. The scattering parameters of the CMUT array for 5dBm power and different DC voltages were obtained and evaluated in the case where the impedance matching network is present or absent (Fig. 8.7). In fact, the S_{11} parameter indicates how much power is reflected back to the source.

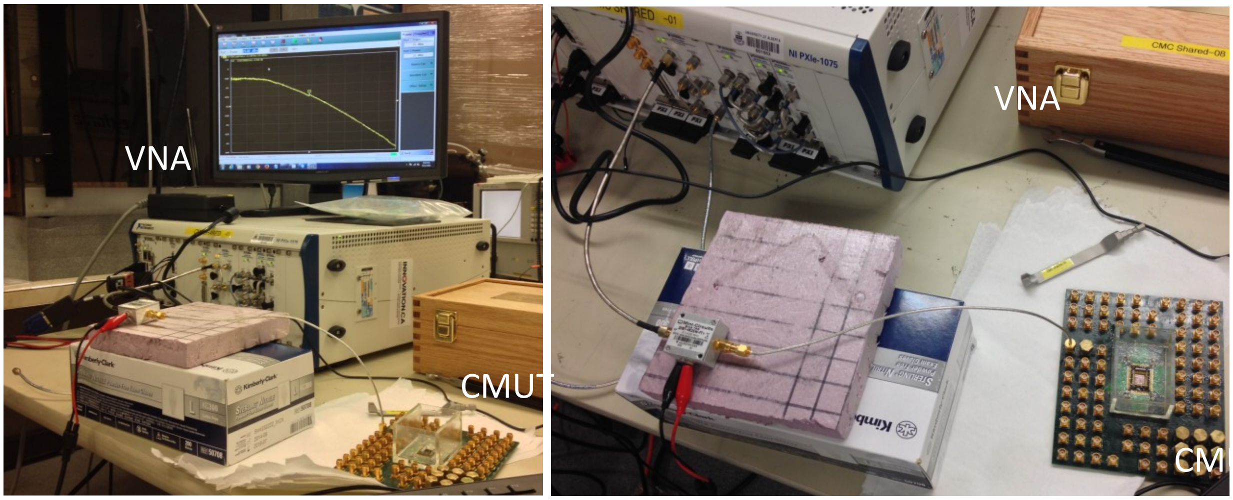

Fig. 8.6. A vector network analyzer (VNA) is connected to a CMUT array.

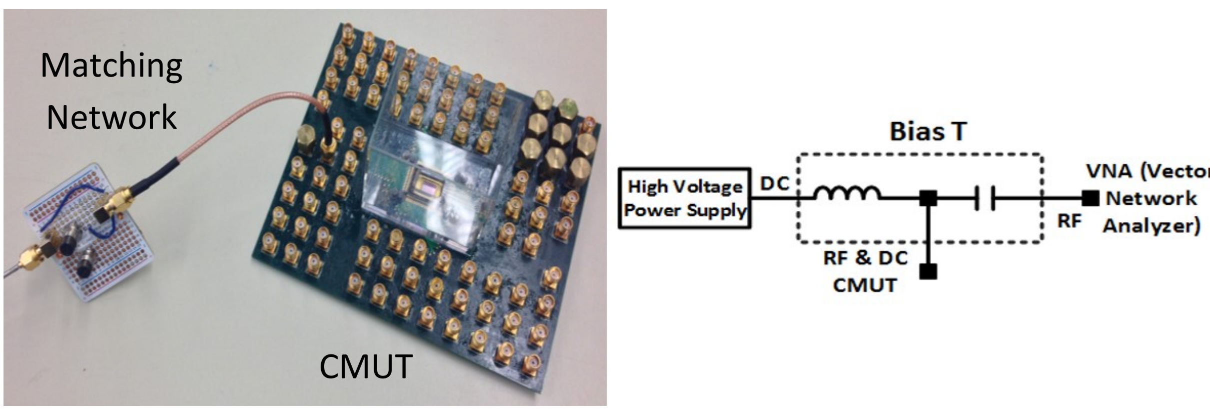

Fig. 8.7. A CMUT array is connected to a VNA with an impedance matching circuit and a bias T was used to apply DC and AC signals together.

In the case with no matching network, the DC voltage was swept from 0V to near the collapse voltage (~80V). Due to the softening of the membrane, the resonance frequency shifted down to lower frequencies by increasing the DC voltage (Fig. 8.8). After obtaining the S_{11} parameters of the CMUT array by VNA, the matching network was designed to decrease that reflected power. Then, the matching network was built and attached to the CMUT array. As shown in Fig. 8.8, the S_{11} was dramatically reduced after using the matching network which means much more power transferred to the CMUT array. The simulation shows a very good agreement compared to the experimental results.

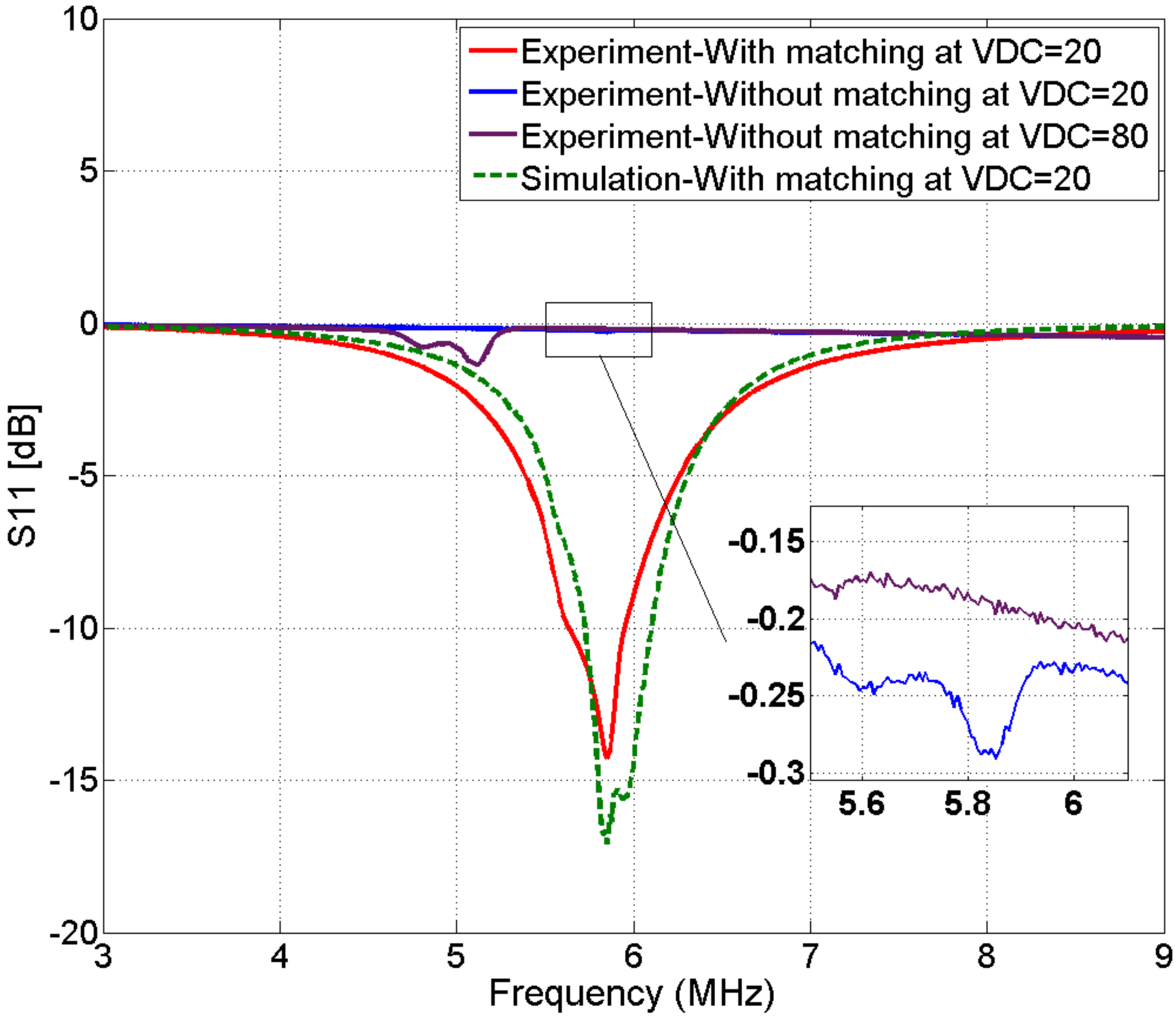

Fig. 8.8. The S_{11} parameter of a 5 by 100 linear CMUT array after applying 5dBm power and different DC voltages with and without using matching network.

8.6 Conclusion

Electrical impedance matching of the large signal models of the CMUT cells were studied in detail. ADS validated models were used to predict the device performance before and after using impedance matching networks. The best-possible RMS velocities associated with maximum pre-collapse drive-signals were significantly higher when a matching network was present. Thus, even if we have the option of driving CMUTs with an arbitrarily high drive-signal, we cannot achieve outputs as high as when we use appropriate matching networks. The output power with a matching network was enhanced dramatically compared to the case when no matching network was used in this case. The scattering parameters of a CMUT array were measured using a network analyzer and then using the obtained data, the matching network was made based on the simulations. The simulations closely match experimental results. Future work will use and optimize different types of matching networks for ultrasound applications.

References

[1] Q. F. Zhou et al. “Self-focused high frequency ultrasonic transducers based on ZnO piezoelectric films.” *Applied physics letters*, vol. 90, no. 11, pp. 113502-113502, 2007.

[2] A. Sevig, and J. W. Sliwa, “Stacked and filled capacitive microelectromechanical ultrasonic transducer for medical diagnostic ultrasound systems,” *U.S. Patent*, No. 6,558,330. 6 May 2003.

[3] M. Celmer, and K. J. Opieliński, “Study of Crosstalk in Linear Ultrasonic Transducer Arrays,” *Acta Acustica united with Acustica*, vol. 101, no. 1, pp. 46-54, 2015.

[4] I. Ladabaum, X. Jin, H.T. Soh, A. Atalar, and B.T. Khuri-Yakub. “Surface micromachined capacitive ultrasonic transducers,” *Ultrasonics, Ferroelectrics and Frequency Control, IEEE Transactions on*, vol. 45, no. 3, pp. 678–690, May 1998.

[5] A. Caronti, G. Caliano, A. Iula, and M. Pappalardo., “An accurate model for capacitive micromachined ultrasonic transducers,” *Ultrasonics, Ferroelectrics and Frequency Control, IEEE Transactions on*, vol. 49, no. 2, pp. 159–168, Aug. 2002.

Chapter 9

Microbubble Contrast Agent Imaging Using Multi-Frequency CMUT Arrays

9.1 Introduction

The ultrasound imaging technology has affected the field of molecular science by achieving an admirable progress during past decades with the development of the contrast agents [1]. By the combination of ultrasound imaging technology and specific contrast agents, targeted ultrasound techniques would be able to assess the molecular or genetic signatures for diseases. Molecular signatures are sets of genes, proteins, genetic variants or other variables that can be used as markers for a particular phenotype. Targeted ultrasound imaging can be used in some important areas such as disease-associated molecular signatures, in vivo delineation of complex molecular mechanisms of disease, detection of gene expression or protein products and localized drug delivery [2].

Targeted contrast agents can be used for site- and disease specific enhancement by utilizing the molecular signatures for various pathologies [3]. Ultrasound contrast agents (UCAs) are localized by molecular signature and using the complimentary receptor ligands [4], [5]. Targeted ultrasound contrast agents have proved some advantages compared with traditional blood pool agents including earlier detection and characterization of disease, higher sensitivity and specificity compared with non-targeted contrast agents. Due to the relatively small impedance differences between red blood cells and plasma, the blood is two to three orders of magnitude less echogenic than tissue. Therefore, for detecting the echoes from capillaries, a contrast agent is needed.

In acoustic angiography, as a new high-frequency contrast agent imaging technique [6], the microbubbles are excited near resonance frequency and the high-frequency signal is detected with sufficient bandwidth separation. Using this technique, both high resolution and high contrast to noise ratio (CNR) can be achieved. Contrast enhanced transcutaneous ultrasound imaging can be used in carotid artery with some limited resolution and motion artifacts [7]. The traditional contrast imaging techniques are not effective anymore because they only employ the high frequency (35 to 50 MHz) transducers while the nonlinear detection strategies for contrast agent imaging are most effective near the resonance frequency of microbubbles contrast agents (1 to 10 MHz) [8]. In fact, the resolution and CTR can be further improved only if the microbubbles are excited near resonance frequencies and the receive signal is detected at least three times higher than the transmit center frequency [9]. This technique is called super-harmonic, ultra-broadband, or transient imaging which has admirable advantages over sub-harmonic or harmonic contrast intravascular ultrasound (IVUS).

9.2 Contrast Agent Imaging Techniques

In Chapter 7 we introduced CMUT-based large-scale multi-frequency transducers for multi-scale imaging applications. These arrays can be used for microbubble contrast agent imaging applications in which low-frequencies are typically needed in transmission, while higher-frequencies are required in receive mode. Nonlinear micron-scale gas-cored agents strongly scatter ultrasound to enhance the contrast in the body. Using traditional piezoelectric transducers, pulse inversion [10] or amplitude modulation [11] techniques have been used to reject the signal coming back from linear scatterers. In the pulse inversion method, two identical pulses are transmitted per image but with opposite polarity. The signal returning from linear scatterers (e.g. tissues) is a scaled version of that which is emitted. Hence, if we add those two inverted signals coming back from the linear scatterers, the output signal will be zero. However, the signals returning from non-linear scatterers such as microbubbles do not cancel, and thus a pure contrast harmonic signal is obtained. In the amplitude modulation technique two pulses are transmitted but the second pulse has half the amplitude of the first pulse. The echoes coming back from linear scatterers will be identical but with different amplitudes. If the amplitude of the second returning signal is doubled and subtracted from the first returning signal, the result will be zero. However, in case of non-linear scatterers reflecting pulses from contrast agents differ in amplitude and shape, thus the output signal will be non-zero.

While pulse inversion and amplitude modulation have enabled contrast enhancement and background tissue suppression, tissue suppression is not perfect because transmitted ultrasound signals experience nonlinear ultrasound propagation and have existing harmonics even when interacting with linear scatterers. One motivation of multi-frequency transducers is improved methods of contrast imaging with greater background suppression. Super-harmonic imaging is one approach that successfully has achieved this aim. Superharmonic imaging uses low-frequency pulses to excite microbubble contrast agents, which are much more nonlinear than tissue. Consequently, harmonics above the 3rd harmonic are negligible due only to nonlinear propagation but are strong due to nonlinear asymmetric microbubble oscillations. The concepts of super-harmonic imaging were first reported by Kruse et al. [12], but these approaches lacked transducers with broad-band capabilities until the Dayton group demonstrated imaging using multi-frequency single-element transducers [13]. Our motivation was to achieve similarly impressive super-harmonic imaging capabilities but with realtime performance by developing multi-frequency arrays which offer electronic, rather than mechanical scanning. To achieve this, we developed multi-frequency CMUT arrays as described in earlier chapters, transmitting at 2 MHz and receiving at 8-9 MHz. As explained before, the resonance frequency of a micro-bubble is defined by the size of the micro-bubble and the material used for making the bubbles. On average, the microbubbles we make have the diameter of ~2 µm which is around the resonance frequency of 2 MHz. Our arrays are designed to receive the third or fourth harmonics of the fundamental 2 MHz excitation. Third or fourth tissue harmonics are known to be negligible, thus our designs should achieve very high contrast to tissue ratios.

One challenge of using CMUTs for nonlinear contrast imaging schemes (including pulse inversion, amplitude modulation and super-harmonic imaging) is the nonlinear output of CMUTs which may generate harmonics in the transmit signal that may confound such schemes.

To ensure the minimization of grating lobes, large- and small CMUT membranes were fabricated in an interlaced fashion such that the pitch of high-frequency sub-arrays were 1λ or 2λ. Arrays of various sizes up to 128 elements were fabricated using a modified sacrificial release process with silicon nitride membranes and then wire-bonded to custom PCB boards mounted onto an interfacing board with voltage-protected pre-amplifiers, connected to a Verasonics programmable ultrasound platform. This system enables real-time imaging and programmable control over low- and/or high-frequency transmission and reception. To demonstrate contrast agent imaging, microbubbles with gas core and lipid shell were injected inside of a tube and then were imaged.

To receive only the signals returning from non-linear scatterers, an alternative to the standard amplitude modulation technique is a subtraction-based contrast-enhanced imaging sequence. The principle is the same as the amplitude modulation technique but with a different implementation [14]-[16]. We first used the odd elements of low-frequency transducers to transmit the signal and received the echoes coming back from the target (S_1) using all high-frequency sub-elements. Then we transmit the ultrasound signal using even elements of the low-frequency sub-arrays and receive the signal (S_2) on all high-frequency elements. Then we use low-frequency sub-arrays to transmit the ultrasound and receive the signal on all high-frequency sub-elements, labelled S_3. If we add signals S_1 and S_2 and then subtract S_3 , the results will only contain the information of non-linear scatterers which is the signal returning from microbubbles in our case (Fig. 9.1). The advantage of this approach over traditional phase- or amplitude modulation schemes for CMUTs is that amplitude modulation can be achieved using aperture apodization, rather than modulating signals from elements. Thus, CMUT nonlinearity is no longer a factor.

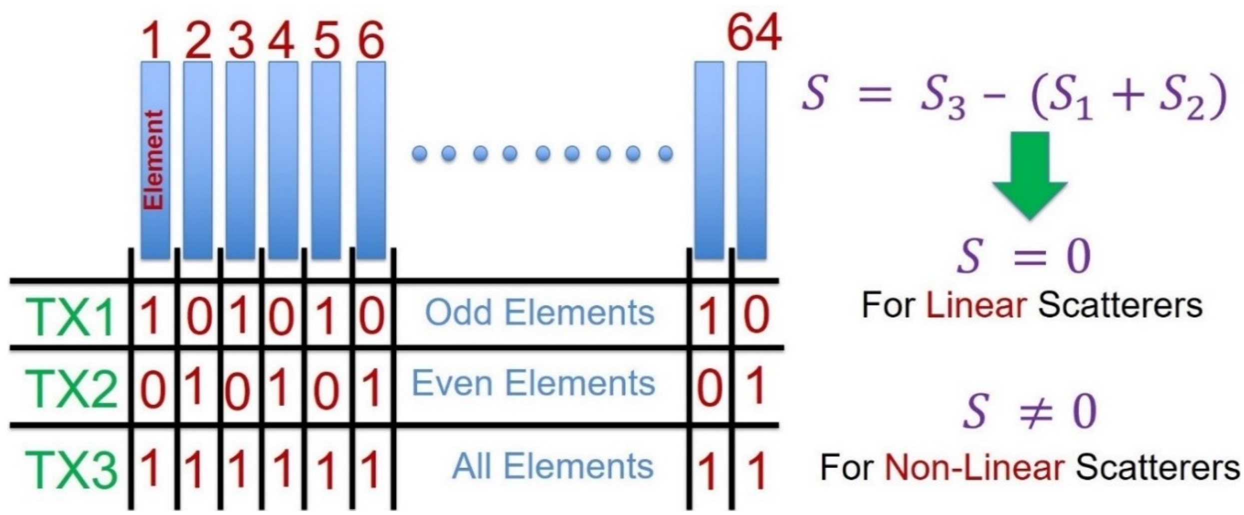

Fig. 9.1. The subtraction technique used for rejecting the signal coming back from linear scatterers.

To demonstrate the potential of subtraction technique used for rejecting the signal coming back from linear scatterers, we used the similar setup showed in Fig. 7.7. A micro-tube phantom was imaged in a vegetable oil immersion medium with and without subtraction technique (Fig. 9.2). Low-frequency and high-frequency sub-arrays as described in Chapter 7 were supplied with 250 and 400 VDC, respectively. Additionally, low- and high-frequency elements were driven by tri-state pulsers in the Verasonics ultrasound platform, with a 200 Vpp, two-cycle waveform designed to approximate sinusoidal pulses matched to the respective element frequencies. A transmit focus was set to 3cm depth, close to the target. Echo data was received on all high-frequency elements then beamformed using conventional delay-and-sum processing to form images shown in Fig. 9.3.

As demonstrated in Fig. 9.3, the empty micro-tube is not visible with the aperture-modulation subtraction technique and we did not receive any signal coming back from linear scatterers. Now if we inject micro-bubbles inside the micro-tube, we only image bubbles as non-linear scatterers as will be described in section 9.3.

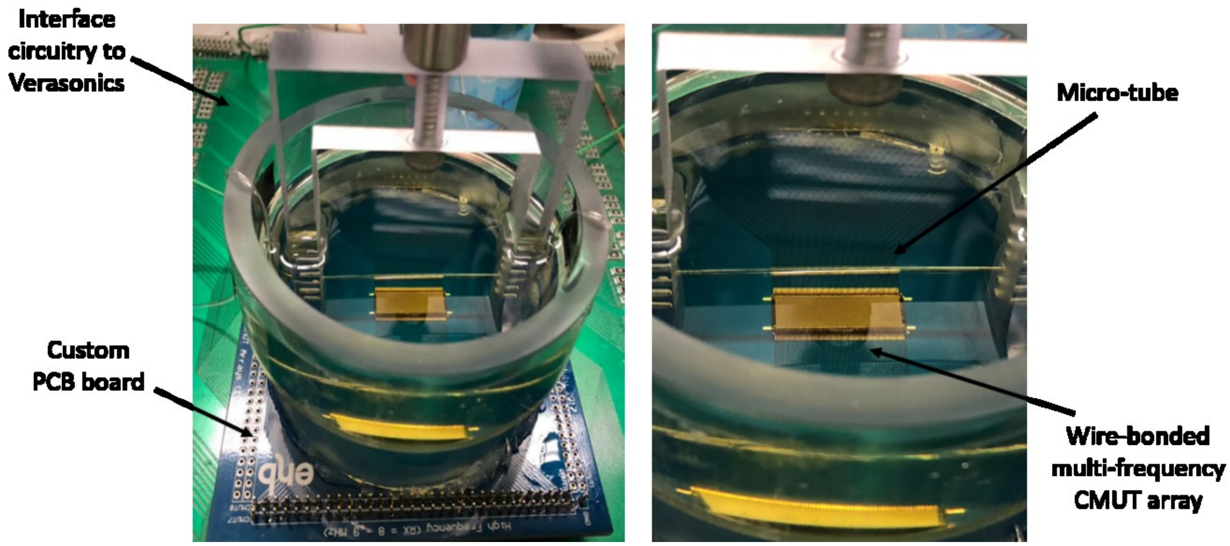

Fig. 9.2. Wire-bonded multi-frequency CMUT array to a custom designed PCB immersed in oil to image a micro-tube phantom. The microbubbles are injected into the tube and imaged.

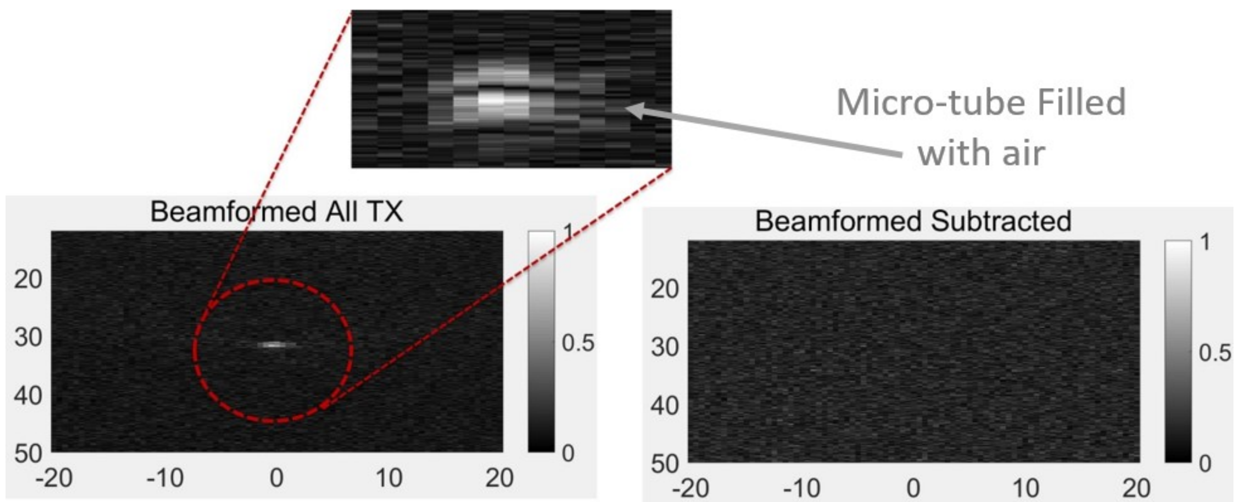

Fig. 9.3. Imaging of a micro-tube phantom in oil immersion medium without (left) and with (right) using subtraction technique explained in Fig. 9.1.

9.3 Microbubble Contrast Agents

The ultrasound contrast agents for our experiments are custom-made perfluoropropane-containing lipid stabilized microbubbles. The lipid shell is composed of 10 mol% 1,2-dipalmitoyl-sn-glycero-3-phosphate (DPPA), 82 mol% 1,2-dipalmitoyl-sn-glycero-3-phosphocholine (DPPC) and, 8 mol% 1,2-dipalmitoyl-sn-glycero-3-phosphoethanolamine-N-[methoxy(polyethylene glycol)-2000] (DPPE-mPEG2k). This formulation was chosen to closely mimic the food and drug administration (FDA) approved definity microbubbles which are currently clinically used for cardiovascular imaging. Microbubble contrast agents were produced in 1mL batches using the following procedure:

1) Aliquot 10 mol% DPPA, 82 mol% DPPC and 8 mol% DPPE-mPEG2k for a final lipid quantity of 0.665 μmol.
2) The chloroform is evaporated under a nitrogen stream for about 1 hour until there is no visible fluid.
3) The lipid pellet is then further dried in a rotary evaporator under vacuum while being maintained at 50°C in a water bath for a minimum of 4 hours. Glass beads are also placed in the rotary evaporator to spread the lipids into a dry film.
4) The dried lipid film is then rehydrated with 1mL degassed 40°C 1:1:8 propylene glycol:glycerin:PBS (volume basis).
5) The solution is heated to 80°C for 1 hour and stored at 4°C for at least 1 day prior to use.
6) 1mL of the solution is transferred to a 2 mL glass vial and the head space is filled with approximately 0.8 mL perfluoropropane.
7) The vial is shaken for 45 seconds in a VialMix (Bristol Myers Squibb) which produces approximately 1e10 microbubbles, majority of which are 1-3 μm in size. They can then be diluted to the required concentration.

9.4 Contrast Agent Imaging: Experimental Results

To show the feasibility of designed and fabricated multi-frequency CMUT arrays, we first filled the micro-tube with water [Fig. 9.4 (a)]. Imaging parameters were similar to those used in Section 9.2 except we used 10 cycles. The high-frequency spectra from water only shows low-frequency harmonics which probably comes from the non-linearity of the CMUT itself. However, when we injected the microbubbles slowly inside the micro-tube using a syringe, we observed more peaks (or so-called super-harmonics) in high-frequency domains which is the response of microbubbles to transmitted signals [Fig. 9.4 (b)]. The signals from the non-linearity of CMUTs can be removed by subtracting the high-frequency spectra of water and micro-bubbles contrast agents [Fig. 9.4 (c)].

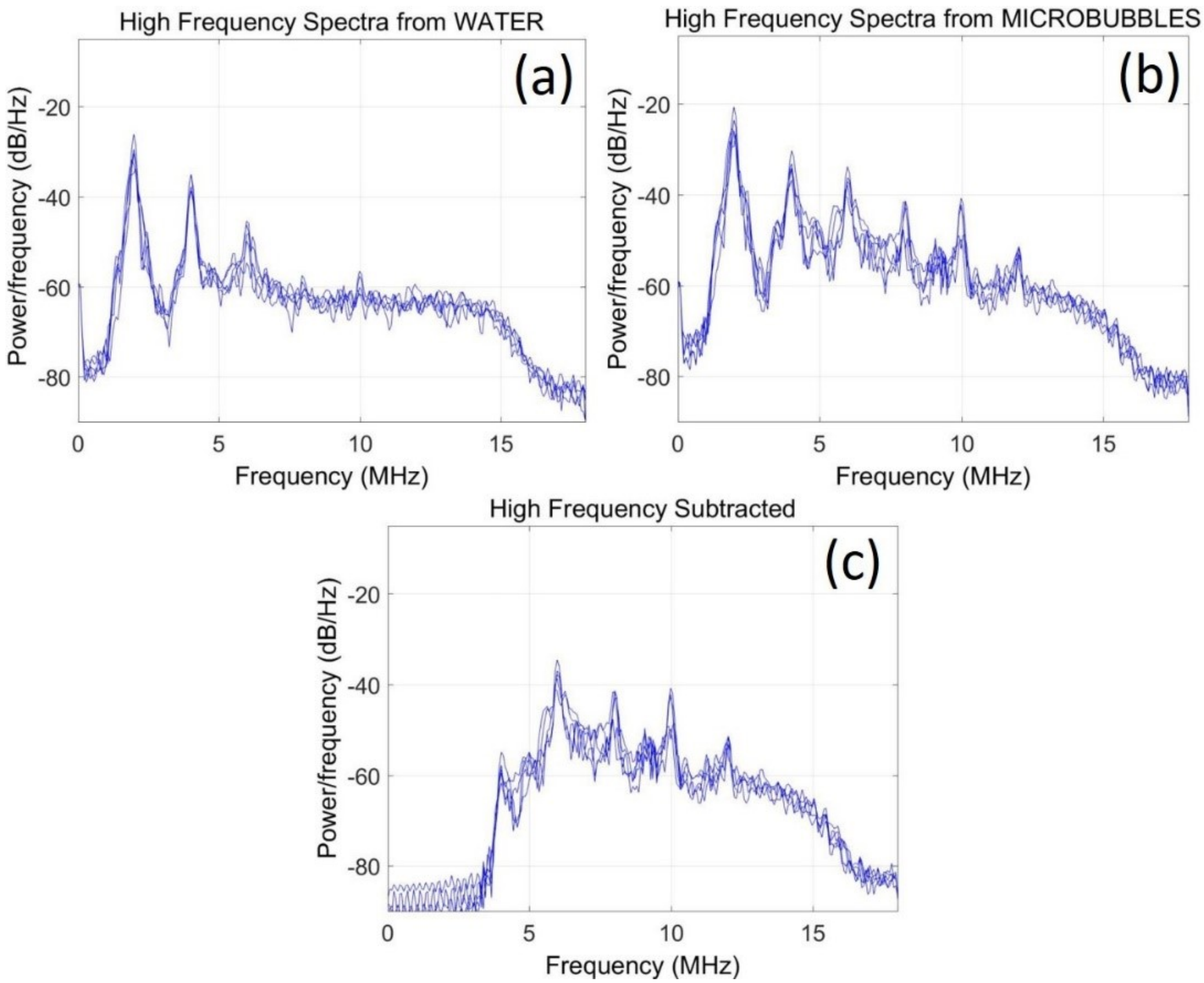

Fig. 9.4. The spectra of high-frequency sub-arrays received from injecting (a) water, (b) micro-bubble contrast agents, and (c) subtracting the signals received from water and micro-bubble returning signals.

Fig. 9.5 demonstrates the super-harmonic images of a micro-tube filled with water and microbubble contrast agents using the prototype of a multi-frequency array. It is obvious to see that we can get stronger signals from non-linear scatterers (microbubbles) compared to water. However, there is still signals returning from linear scatterers which can be improved with further investigations.

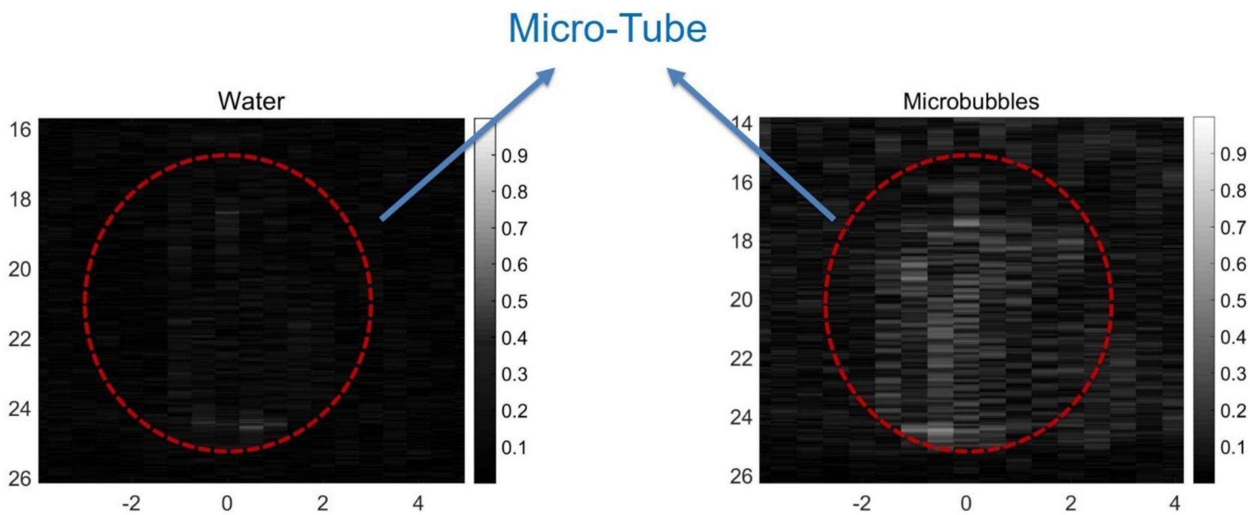

Fig. 9.5. Super-harmonic images of a micro-tube filled with (Left) water and (Right) microbubble contrast agents using the prototype of a multi-frequency array.

9.5 Discussion and Conclusion

Owing to difficulties in obtaining high acoustic pressures without damaging membranes, our imaging experiments with microbubbles used 10 cycles rather than 1 or two, to improve acoustic output at the expense of axial resolution. Future work should aim to improve the design of the CMUTs to enable higher output pressures, which are key to super-harmonic generation. The repetition interval between pulses for the subtraction-based amplitude modulation scheme was 0.1ms, which should minimize any motion-related artifacts, but motion could nevertheless prove to be a confounding source of unwanted background contrast which should be investigated in future work. Once acoustic outputs are better optimized, additional work should also include in vivo imaging of microvaculature with super-harmonic imaging. Recent super-harmonic imaging systems have attracted considerable attention but still use mechanically-scanned multi-frequency single element transducers. Our multi-frequency arrays could enable electronic, rather than mechanical scanning, and thus open up opportunities for emerging clinical applications, which require realtime operation.

Reference

[1] P. A. Dayton, and K. W. Ferrara, “Targeted imaging using ultrasound,” *Journal of magnetic resonance imaging*, vol. 16, no. 4, pp. 362-377, 2002.

[2] A. L. Klibanov, “Targeted delivery of gas-filled microspheres, contrast agents for ultrasound imaging,” *Adv. Drug Deliv Rev.*, vol. 37, pp. 139–157, 1999.

[3] F. A. Jaffer, P. Libby, and R. Weissleder, “Molecular and cellular imaging of atherosclerosis: Emerging applications,” *J. Am. Coll. Cardiol.*, vol. 47, no. 7, pp. 1328–1338, 2006.

[4] R. P. Choudhury, V. Fuster, and Z. A. Fayad, “Molecular, cellular and functional imaging of atherothrombosis,” *Nat. Rev. Drug Discov.*, vol. 3, pp. 913–925, Nov. 2004.

[5] R. Gessner, and P. A. Dayton, “Advances in molecular imaging with ultrasound,” *Mol. Imaging*, vol. 9, pp. 117–127, Jun. 2010.

[6] R. C. Gessner, C. B. Frederick, F. S. Foster, and P. a. Dayton, “Acoustic angiography: a new imaging modality for assessing microvasculature architecture,” *Int. J. Biomed. Imaging*, 2013.

[7] S. B. Feinstein, “Contrast ultrasound imaging of the carotid artery vasa vasorum and atherosclerotic plaque neovascularization,” *J. Am. Coll. Cardiol.*, vol. 48, no. 2, pp. 236–243, 2006.

[8] J. D. Kasprzak, et al., “Comparison of native and contrast-enhanced harmonic echocardiography for visualization of left ventricular endocardial border,” *Am. J. Cardiol.*, vol. 83, no. 2, pp. 211–217, 1999.

[9] B. D. Lindsey, J. D. Rojas, K. Heath Martin, S. E. Shelton, and P. Dayton, “Acoustic characterization of contrast-to-tissue ratio and axial resolution for dual-frequency contrast-specific acoustic angiography imaging,” *IEEE Trans. Ultrason. Ferroelectr. Freq. Control*, vol. 61, pp. 1668-1687, 2014.

[10] C. Shen, Y. Chou, and P. Li, “Pulse inversion techniques in ultrasonic nonlinear imaging,” *Journal of Medical Ultrasound*, vol. 13, no. 1, pp. 3-17, 2005.

[11] R. J. Eckersley, C. T. Chin, and P. N. Burns, “Optimising phase and amplitude modulation schemes for imaging microbubble contrast agents at low acoustic power,” *Ultrasound in medicine & biology*, vol. 31, no. 2, pp. 213-219, 2005.

[12] D. E. Kruse, and K. W. Ferrara, “A new imaging strategy using wideband transient response of ultrasound contrast agents,” *IEEE Transactions on Ultrasonics Ferroelectrics and Frequency Control*, vol. 52, pp. 1320-1329, Aug. 2005.

[13] J. Ma, K. Martin, P. A. Dayton, and X. Jiang, “A preliminary engineering design of intravascular dual-frequency transducers for contrast-enhanced acoustic angiography and molecular imaging,” *IEEE Trans. Ultrason. Ferroelectr. Freq. Control*, vol. 61, pp. 870–880, 2014.

[14] E. Quaia, Ed., *Contrast Media in Ultrasonography*. Berlin, Germany: Springer-Verlag, 2005.

[15] O. Couture, M. Fink, and M. Tanter, “Ultrasound contrast plane wave imaging,” *IEEE Trans. Ultrason., Ferroelectr., Freq. Control*, vol. 59, no. 12, Dec. 2012.

[16] D. Fouan, and A. Bouakaz, “Investigation of classical pulse sequences for contrast-enhanced ultrasound imaging with a cMUT probe,” *IEEE transactions on ultrasonics, ferroelectrics, and frequency control*, vol. 63, no. 10, pp. 1496-1504, Oct. 2016.

Chapter 10

Fabrication and Characterization of Large-Scale Multi-Gap Multi-Frequency CMUT Arrays Using Sacrificial Release Process

10.1 Introduction

Multi-frequency CMUT arrays were demonstrated in previous chapters but suffered from low acoustic output of low-frequency sub-arrays, in part due to the limited range of membrane motion. Additionally, large membranes had the same gap as small membranes, and thus much lower collapse voltages, which imposed limits on how hard these membranes could be driven. Yet, for proposed applications, including super-harmonic contrast imaging and imaging-therapy modes, high acoustic output from low-frequency sub-arrays will be critical. We propose multiple approaches to achieve improved output from low-frequency sub-arrays. One strategy is to create multiple gaps in the fabrication process, with larger gaps for larger membranes. Another strategy is to optimize membrane thickness. Yet another strategy discussed in Chapter 8, is the use of impedance matching networks, which however, come at the cost of more narrow-band operation. An elevationally-focusing acoustic lens can additionally improve focal gains and thus focal pressures. Finally, future work on collapse-mode and collapse-snapback modes could be considered. In this chapter we focus on achieving multiple gap heights for multi-frequency arrays, as well as aim to optimize membrane thickness. Our simulations indicate that these strategies may be used for improving the generated pressure from CMUTs by a factor of $2-3$ times. In our new designs, low-frequency CMUTs will be fabricated with larger gaps to increase the snap-down voltage to drive them harder for generating more pressure while high-frequency transducers will have smaller gaps for making them more sensitive in receive mode. Our goal is that next-generation multi-frequency arrays with multiple-gaps may enable sufficient acoustic output pressures for practical super-harmonic and imaging-therapy applications.

10.2 Design and Simulation Results

We used our developed equivalent circuit model to simulate our designed multi-gap multi-frequency CMUT arrays. Table 10.I summarizes the simulation results for a single large (26 µm) and small (15 µm) circular membranes in vegetable oil immersion medium. As can be observed, the rms membrane velocity is increased 3.8 times from design#1 (our previous multi-frequency CMUT arrays) to design#3 (newly proposed arrays) in large membranes. The simulation results prove that the combination of increasing the gap-size and the membrane thickness can provide more acoustic power.

TABLE 10.I. DESIGN AND SIMULATION RESULTS IN ADS.

Design	Membrane Radius (μm)	Membrane thickness (μm)	Gap size (nm)	Effective gap size (nm)	Membrane Velocity (m/s) @ 80% of snap-down voltage	Peak displacement (nm)	Snap-down voltage (v)
#1	26 (2.43 MHz)	1	400	433	0.151 @ 97VDC + 1VAC 0.983 @ 97VDC + 6.5VAC	22.15 144.0	122
	15 (9 MHz)	1	400	433	0.101 @ 294VDC + 1VAC 0.363 @ 294VDC + 3.6VAC	3.983 143.4	367
#2	26 (2.42 MHz)	1	900	933	0.104 @ 308VDC + 1VAC 2.087 @ 308VDC + 20VAC	15.34 306.7	386
	15 (9 MHz)	1	400	433	0.101 @ 294VDC + 1VAC 0.363 @ 294VDC + 3.6VAC	3.983 143.4	367
#3	26 (4.26 MHz)	1.5	900	933	0.062 @ 567VDC + 1VAC 3.726 @ 567VDC + 60VAC	5.175 310.5	709
	15 (15 MHz)	1.5	400	433	0.065 @ 521VDC + 1VAC 6.122 @ 521VDC + 94VAC	1.532 144.0	651
Medium: Vegetable oil immersion. Density of the oil is ~ 930 (kg/m3) and speed of sound in oil is ~ 1430 m/s. The insulator layer is SiN with the thickness of 250nm and the dielectric constant of 7.5.							

10.3 Fabrication Details of Multi-Gap Multi-Frequency CMUT Arrays

In chapter 5 we explained the fabrication of large-scale multi-frequency CMUT arrays with the same gap sizes for low- and high-frequency sub-elements using a modified standard sacrificial release process. We used six steps of lithography to finish the fabrication of designed arrays. However, for fabrication of multi-gap multi-frequency CMUT arrays we need an additional mask (seven steps of lithography) to define different gap sizes. We used the same silicon nitride sacrificial release process flow with some modifications. Fig. 10.1 summarizes the fabrication steps by providing cross-sectional and microscopic images of each single main step. In summary, a prime silicon wafer is coated with 250nm LPCVD thin silicon nitride as insulation layer, 100nm PECVD silicon dioxide as an etch-stop layer for RIE of the sacrificial layers and 500nm un-doped LPCVD polysilicon sacrificial layer on it [Fig. 10.1(a)]. The first poly-Si layer is patterned using a RIE [Fig. 10.1(b)] to form the additional gap-sizes of the large membranes. Then, another 100nm LPCVD polysilicon layer is deposited [Fig. 10.1(c)] as the second sacrificial layer for large membranes and first sacrificial layer for small CMUT devices. The second deposited poly-Si is then patterned to define the area of the plugs [Fig. 10.1(d)]. The last 200nm LPCVD poly-Si sacrificial layer is deposited [Fig. 10.1(e)] to define the low-height etching channels while increasing the polysilicon sacrificial layer in the gap area [Fig. 10.1(f)]. So far, we defined different gap-sizes of 900 and 400nm for large and small devices, respectively. Over the patterned polysilicon sacrificial layer, 1.5μm low-stress LPCVD silicon nitride is deposited as the device membrane [Fig. 10.1(g)]. To access the polysilicon sacrificial layer, holes are etched through the membrane [Fig. 10.1(h)]. Then, the membranes are released by KOH wet etching of combined sacrificial layers [Fig. 10.1(i)]. Long KOH etching removes the entire sacrificial layers including 900 and 400nm polysilicon and 100nm silicon dioxide layers beneath the gap. Critical point drying (CPD) is then used right after the KOH to minimize the stiction problems in the membranes. A low-stress 2.5μm PECVD silicon dioxide layer is then deposited to seal the etch holes [Fig. 10.1(j)], which is etched to form the sealing plugs without coating the membranes [Fig. 10.1(k)].

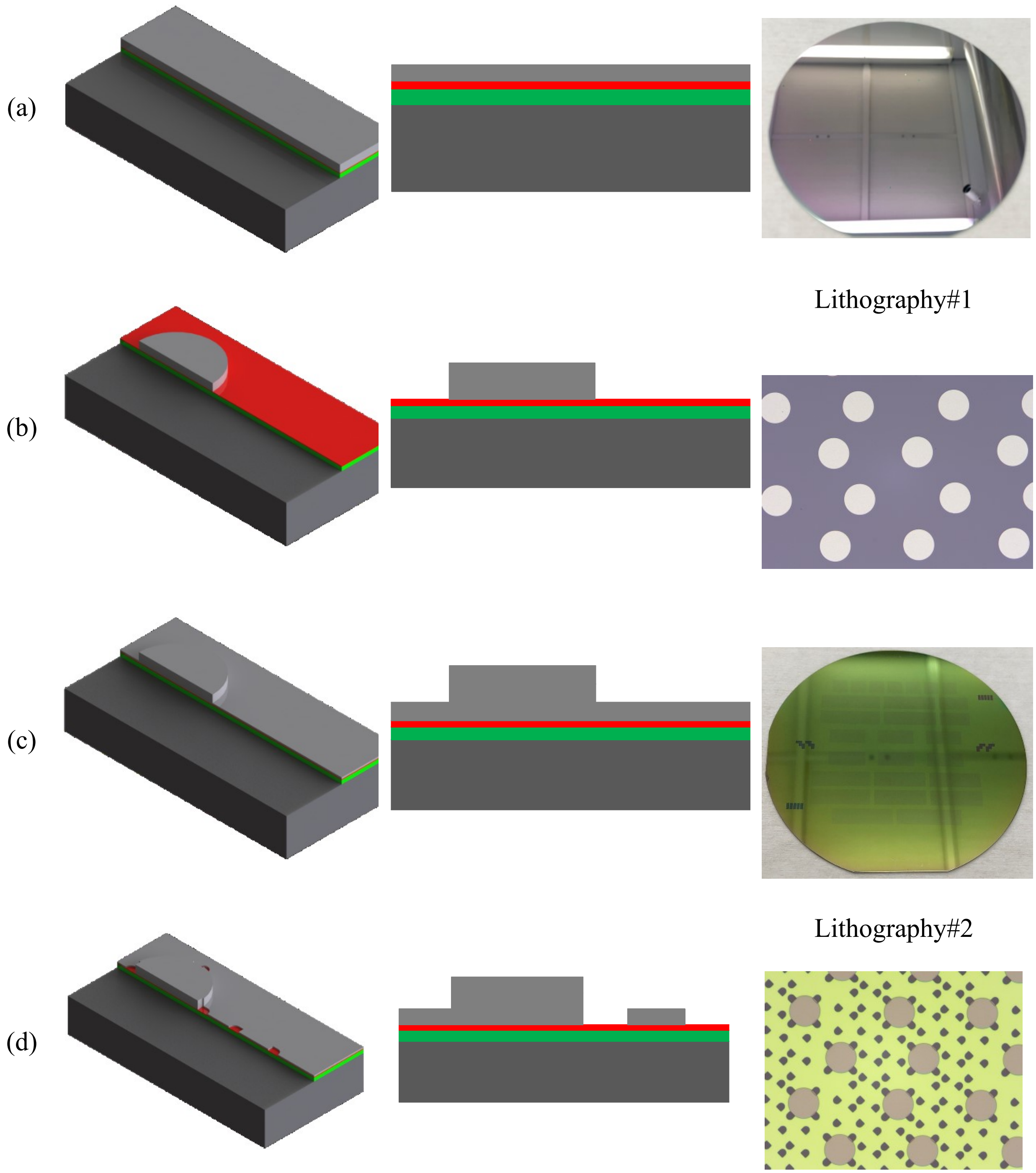
(a)
Lithography#1
(b)
(c)
Lithography#2
(d)

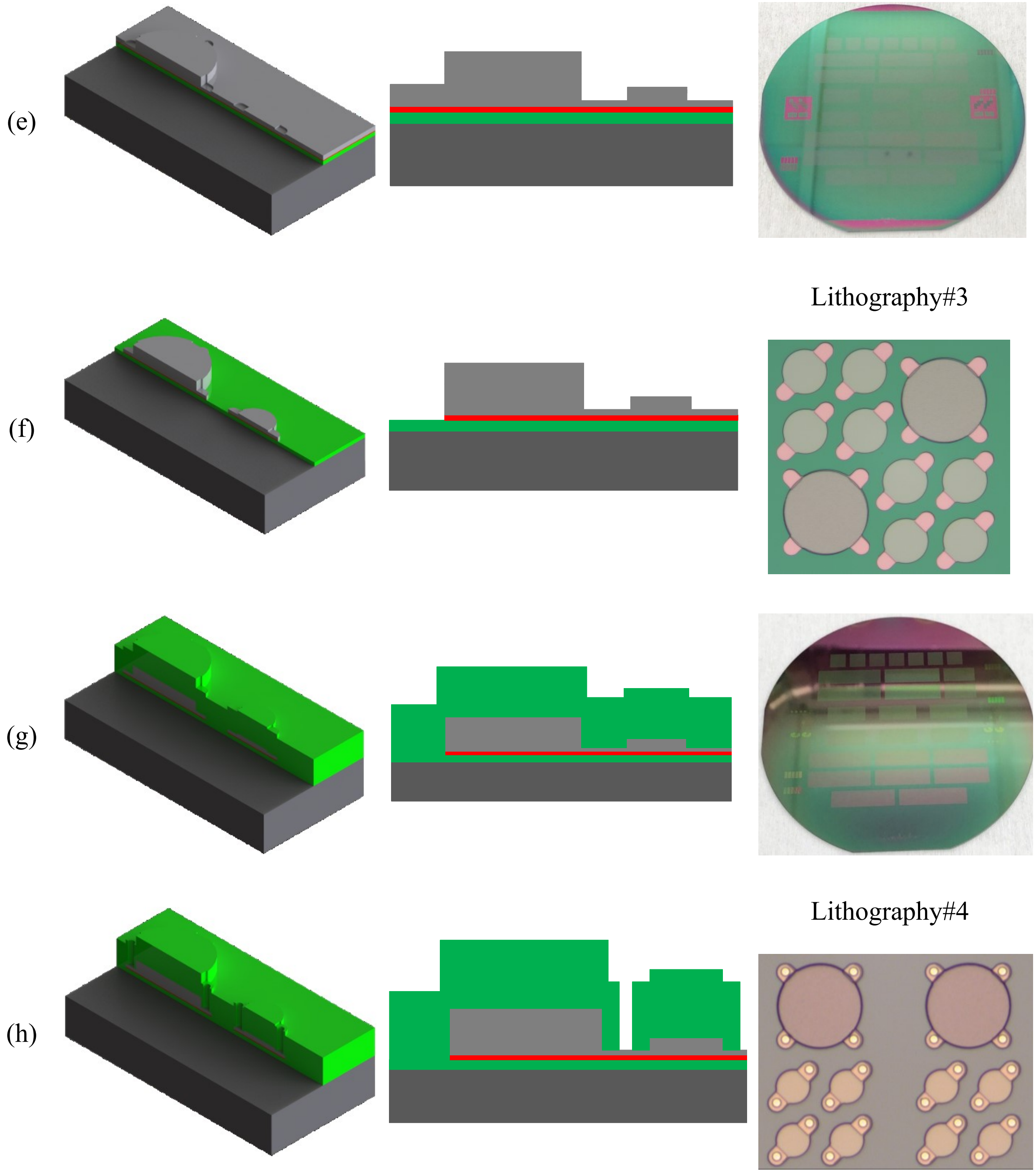
(e)
Lithography#3
(f)
(g)
Lithography#4
(h)

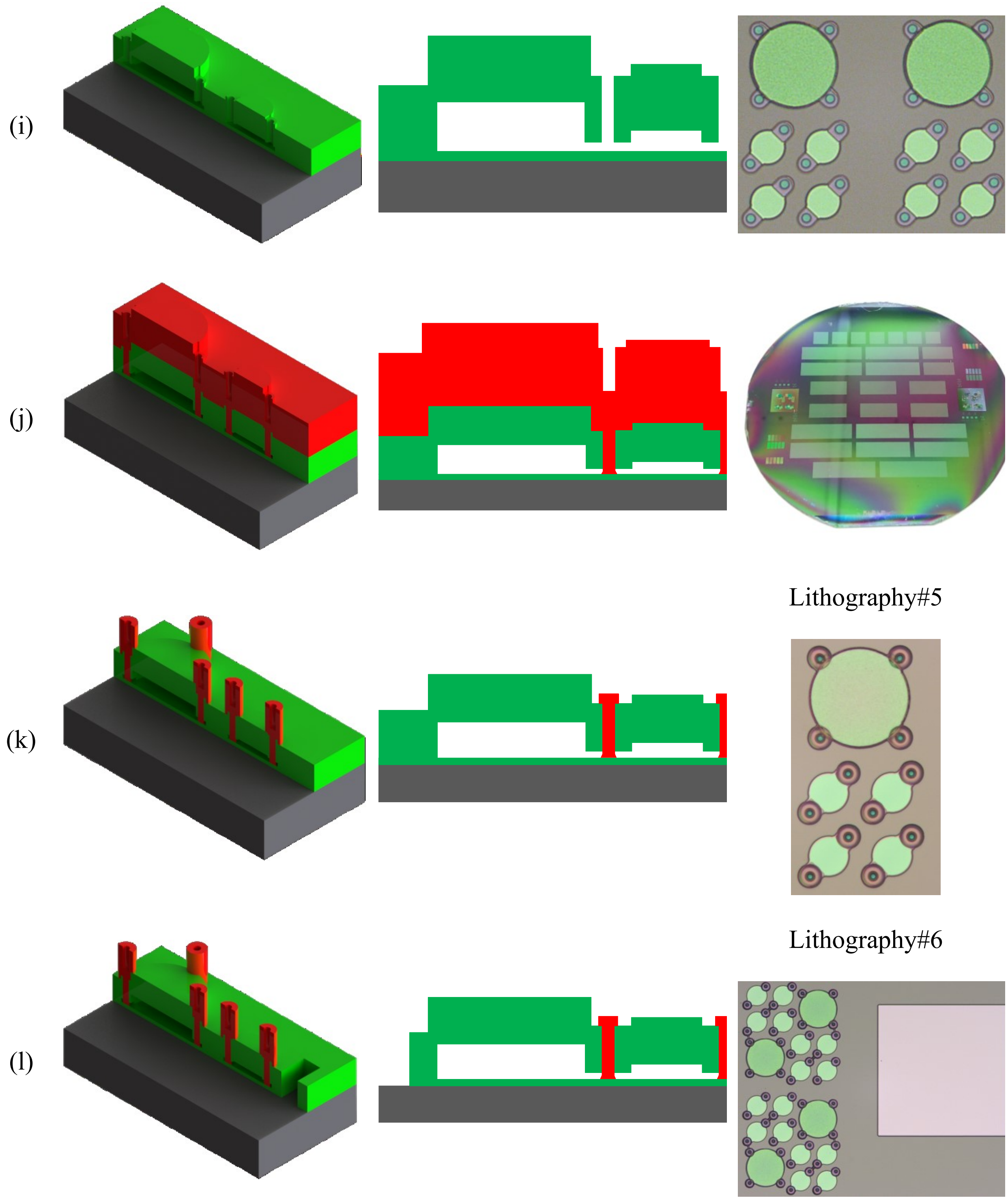

(i)
(j)
Lithography#5
(k)
Lithography#6
(l)

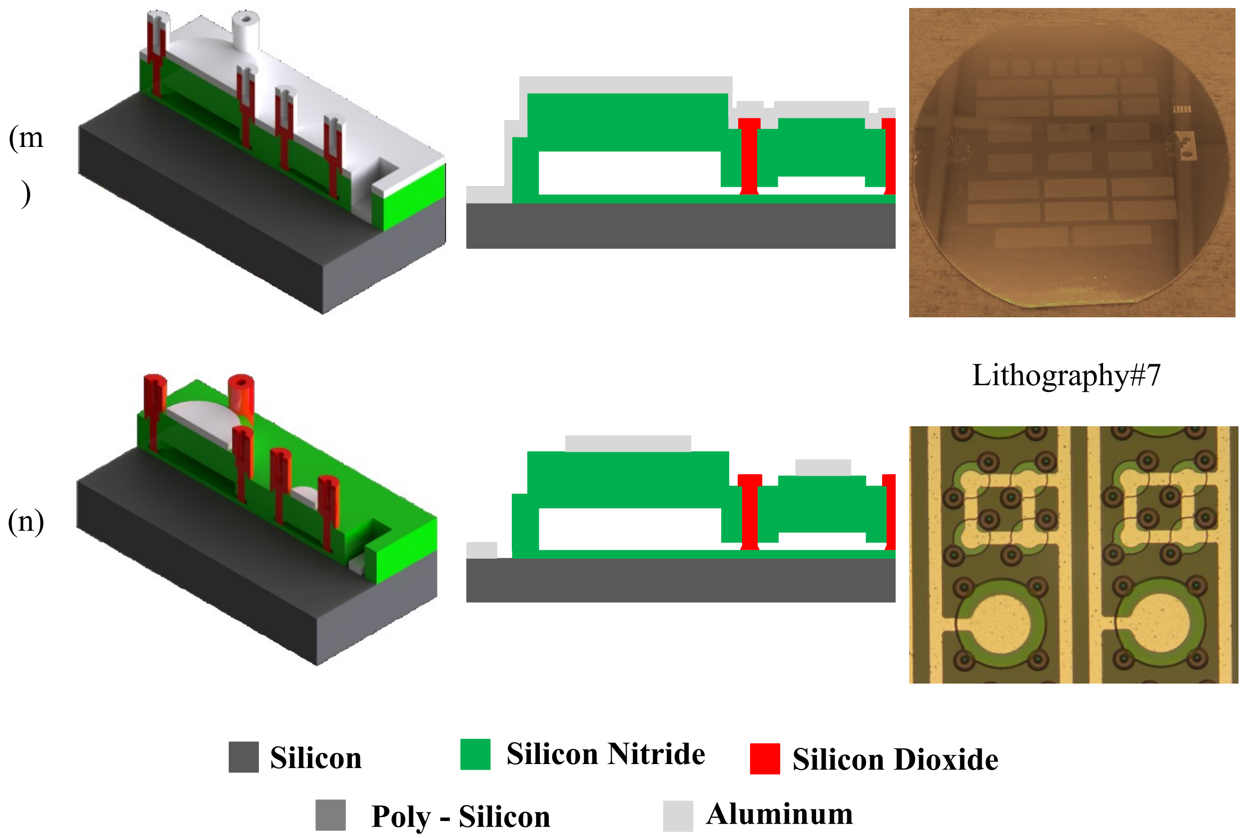

Fig. 10.1. Silicon nitride sacrificial release multi-gap multi-frequency CMUT fabrication process with starting on a highly conductive silicon prime wafer. (a) Deposition of thin bottom silicon nitride insulation film, silicon dioxide protection layer, and first thick polysilicon sacrificial layer. (b) Etching of the first polysilicon sacrificial layer to make the gap-sizes of large membranes bigger. (c) Deposition of the second thin polysilicon sacrificial layer. (d) Etching of polysilicon sacrificial layer to define the plug areas. (e) Deposition of the third polysilicon sacrificial layer. (f) Etching of polysilicon sacrificial layer followed by a quick buffered oxide etch of exposed silicon dioxide protection layer. (g) Deposition of thick silicon nitride membrane. (h) Etching of the silicon nitride membrane to get access to the polysilicon sacrificial layer. (i) Chemical etching of combined sacrificial layers to release the membrane. (j) Deposition of silicon dioxide sealing film. (k) Pattering the silicon dioxide sealing film into plugs. (l) Etching through the silicon nitride film to access the bottom silicon electrode. (m) Sputtering the aluminum film. (n) Etching the aluminum layer to form the top and bottom electrodes.

The final step after forming the CMUT cavity and sealing the holes to make the membranes is defining top and bottom electrodes. Using RIE, bottom electrode holes are etched through the silicon nitride layer to access the substrate which is silicon [Fig. 10.1(l)]. Using a magnetron sputtering system, the entire device is covered by a 400nm aluminum layer [Fig. 10.1(m)] and then the aluminum is annealed in 200 ºC for 3 hours. Finally, top and bottom electrodes are formed by wet aluminum etching [Fig. 10.1(n)]. More details about the fabrication process can be found in Appendix C.

10.4 Characterization of Multi-Gap Multi-Frequency CMUT Arrays

Several steps of characterization have been used during and after the fabrication of multi-gap multi-frequency CMUT arrays. Here, we just show the critical steps of characterization which are vital to make the functional devices. During the DRIE of thick silicon-nitride membranes [Fig. 10.1(h)] the etching should ideally stop in half-way through the poly-Si sacrificial layer to make sure we etched the entire 1.5μm silicon-nitride across the wafer due to non-uniform LPCVD deposition. Laser confocal microscopy can be used to calculate the etch depth and rate. As illustrated in Fig. 10.2, a laser confocal microscope is used to measure the etch depth in plug areas. Since the DRIE etch rate was higher at the edges of the wafer, the results were obtained using an array close to the edge of the wafer. The measurement shows the etch depth of 1.847μm which means we etched the entire thick silicon nitride membrane and 200nm poly-Si sacrificial layer and probably some parts of the silicon nitride insulator. We should be careful of not etching the entire insulation layer.

After completing the fabrication of devices, we test the devices using a laser Doppler Vibrometer (MSA-500 Micro System Analyzer, Polytec) [Fig. 10.3(a)]. A 10V pseudorandom signal was applied to determine the center frequency of the devices in air [Fig. 10.3(b)] and then 10V sinusoidal signal with the frequency of 6.12 MHz was applied and scanned across the array to obtain 3D images of the device oscillation [Fig. 10.3(c)]. Fig. 10.4 shows the helium ion microscopy (HIM) of fabricated interlaced multi-gap multi-frequency CMUT cells.

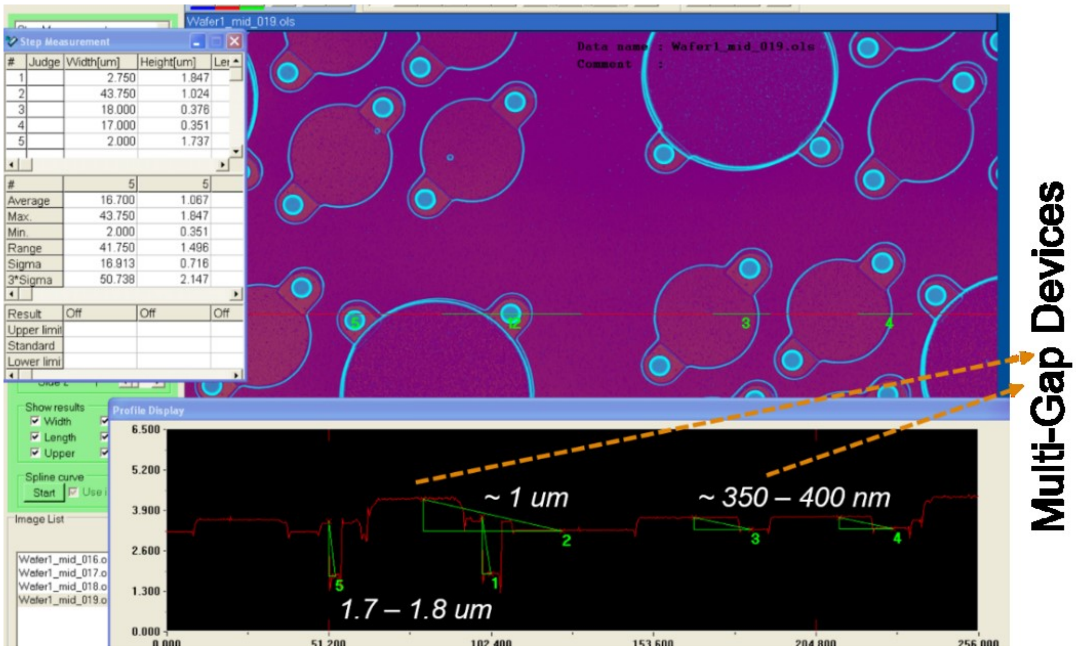

Fig. 10.2. Laser confocal microscope image of a multi-gap multi-frequency CMUT array.

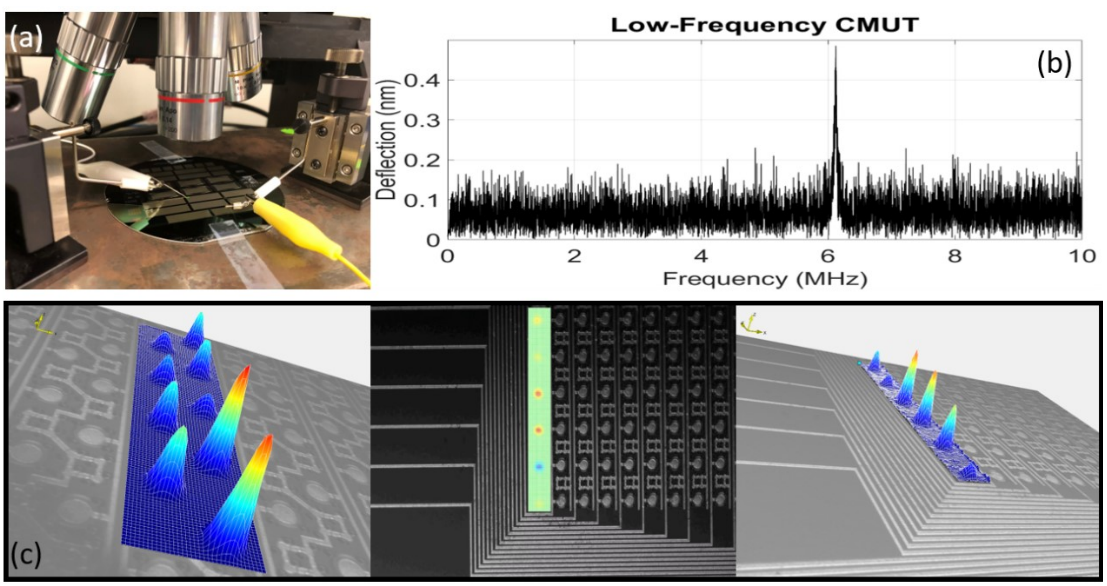

Fig. 10.3. Sample laser Doppler Vibrometer measurements. (a) Fabricated multi-gap multi-frequency CMUT arrays on a highly conductive silicon prime wafer. (b) Actuation of a low-frequency CMUT cell with a 10V Pseudorandom signal to obtain the resonance frequency of the device. (c) Actuation of the sample low-frequency single element subarrays in different parts of the wafer when driven by a 10V sine wave at 6.12 MHz.

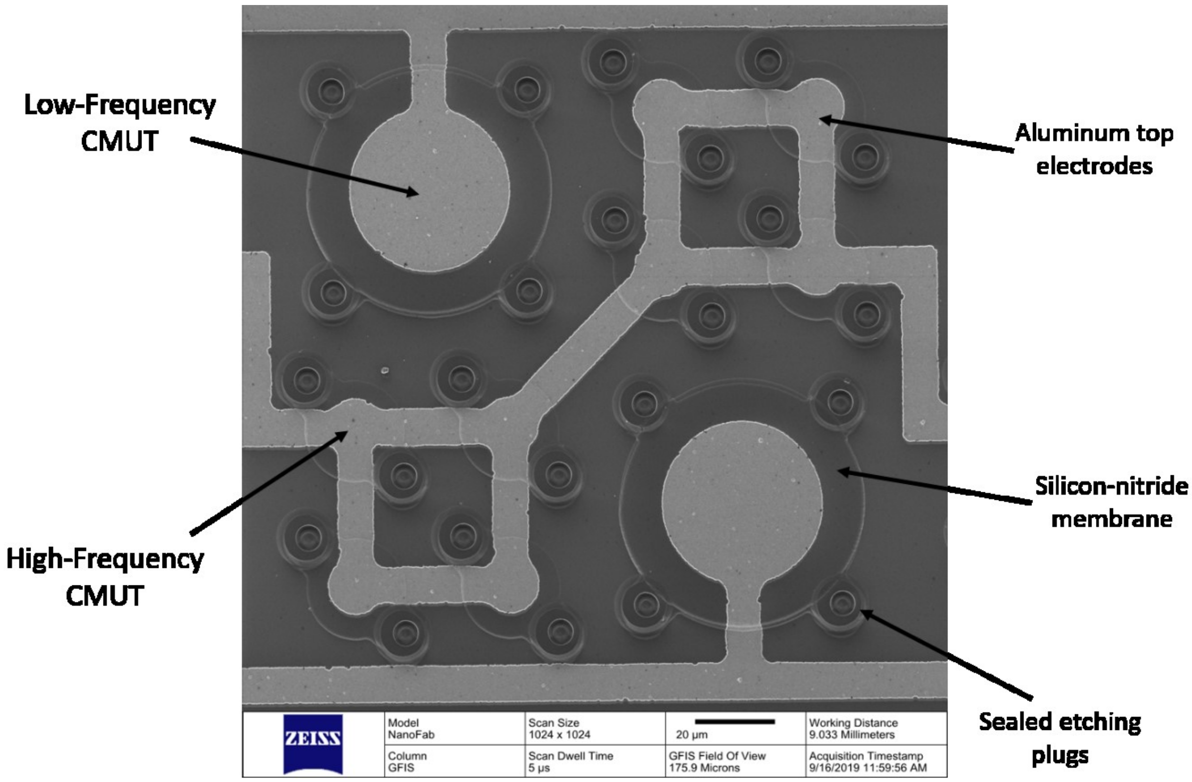

Fig. 10.4. Helium ion microscopy (HIM) of fabricated interlaced multi-gap multi-frequency CMUT cells.

10.5 Current Stage and Future Work

At this stage, we have completed fabrication of several new multi-gap multi-frequency arrays of up to 128 high-frequency elements and 128 low-frequency elements. Preliminary Vibrometer testing demonstrates working devices, however, work is ongoing to demonstrate whether new multi-gap multi-frequency devices offer the promised improvements in acoustic output due to higher snapdown voltages and capacity for higher driving voltages. This work will involve additional Vibrometer testing as well as acoustic output testing and imaging experiments.

Chapter 11

Conclusions and Future Work

Multi-frequency capacitive micromachined ultrasonic transducer (CMUT) arrays are designed by closely packing interlaced membranes of different sizes with applications to imaging-therapy, multi-band imaging, contrast agent imaging and photoacoustic imaging. Designed arrays can be used for making ultrasound wireless probes by having the capability of switching between low- and high-frequency elements for selecting high-resolution images or having more penetration.

In my thesis I have developed modelling, design, fabrication, characterization, interface circuitry and imaging strategies for various possible ultrasound imaging and therapeutic applications. I have proposed precise modelling and design of large-scale multi-frequency CMUT arrays with circular membranes using an equivalent circuit approach for performance analysis of the arrays. First, I developed an analytical and computational framework for studying effects of mutual acoustic impedance. This interaction has not been previously modeled in the case of different-sized membranes. Secondly, I applied the obtained comprehensive expressions to circular CMUT non-linear lumped equivalent circuits. Then, I performed several FEM simulations for arrays with small number of cells and showed that the results match with our developed model. Using the proposed model, one can very rapidly obtain the linear frequency and nonlinear transient response of arrays with an arbitrary number of CMUT cells within a few seconds, whereas FEM simulations take a few hours. Then, I upgraded the model for modelling of large-scale realistic multi-frequency CMUT arrays.

Using our developed equivalent circuit models, a new set of multi-frequency arrays with different specifications were designed for several ultrasound applications and then fabricated using silicon-nitride sacrificial release process. Arrays were characterized and wire-bonded to custom PCB designs. Finally, the devices were integrated with electronics and connected to a Verasonics research ultrasound platform for imaging studies.

I used some of my fabricated multi-frequency arrays for ultrasound multi-band applications. A 7 by 7 mm multi-frequency CMUT array with 20 elements and a 20 by 7 mm array with 64 elements were used to test the feasibility of the designed and fabricated arrays for multi-scale imaging applications. Three wire phantoms with the separation of 0.7 cm were used in oil immersion medium to investigate the performance of the low- and high-frequency elements for different depths. Low-frequency elements showed more penetration while high-frequency CMUTs demonstrates better resolution. The combination of low- and high-frequency devices may be used for a variety of novel imaging and imaging-therapy applications. Fabricated multi-frequency arrays are the first of their kind to demonstrate multi-resolution and multi-depth imaging capabilities and could enable future portable point-of-care ultrasound for a wide array of clinical applications. Novel designed multi-frequency CMUT arrays could be replaced by traditional single-frequency arrays for clinical wireless ultrasound probes.

Since CMUT arrays with square membranes have more fill-factor compared to arrays with circular membranes, a nonlinear large signal equivalent circuit model was developed for a single un-collapsed CMUT cell with square membranes. The model was designed and implemented in a circuit simulator and compared with FEM and experimental results. ANSYS 3D FEA was used to validate the equivalent circuit model predictions by performing static, pre-stressed harmonic, and nonlinear transient analysis. The static analysis for calculating the peak deflection of the membrane showed an excellent agreement with FEA. Moreover, the performance of the model was examined for dynamic analysis. The ADS circuit model could predict many intrinsic properties of a square CMUT cell including static deflection, resonance frequency, phase and magnitude of the membrane displacement, membrane velocity, electrical conductance, and collapse voltage with accuracy comparable with FEM but within considerably less time. The results were compared with circular CMUT cells when the half-side-length of the square CMUT is assumed to be equal to the radii of the circular transducer. Single CMUT cells with silicon-nitride membranes were fabricated using a standard sacrificial release process with slight modifications. The comparison between the ADS circuit simulations and the experimental results showed a good agreement for the resonance frequency and the membrane deflection. The studies presented here could be used as a framework for designing the arrays with square CMUT cells. However, the effects of the mutual-acoustic impedance between the square cells of the same and different sizes should be investigated in detail and implemented into a circuit model as a Z-matrix to evaluate the performance of the array. Future work should aim to expand these results for improved modeling of the multi-frequency CMUT arrays with square cells and their novel applications.

CMUTs have not been known for high acoustic output, but our recent studies show that this may in part be due to highly sub-optimal electric impedance matching. We showed using simulations and preliminary experiments that acoustic output could be improved over 20 times with electrical impedance matching. Additional work aims to optimize CMUTs for high power output. The fundamental things that limit acoustic output of transducers include heating and dielectric breakdown. Heating is problematic for piezoelectric transducers but less so for CMUTs. We propose using a novel CMUT architecture with isolated supports and so-called isolated isolation posts which are essentially electrically-isolated posts that prevent shorting during membrane collapse.

Multi-Frequency CMUTS will be used to obtain high resolution and high contrast ultrasound images. We constructed phantoms with or without contrast microbubble agents and implemented pulse sequences for visualizing these agents with negligible tissue background. Recent harmonic reduction strategies were applied to avoid CMUT and tissue-harmonic nonlinearity. We obtained almost zero signal from linear scatterers. Microbubble contrast agents showed significant amount of nonlinearity in higher frequencies which were detected by high-frequency sub-arrays. The results could be improved dramatically by design and fabrication of novel large-scale multi-gap multi-frequency CMUT arrays with the ability of generating over 1MPa pressure using low-frequency elements.

Most ultrasound transducers operate with a limited bandwidth, minimizing opportunities for multi-depth and novel harmonic imaging applications. Recently, we introduced multi-frequency CMUT arrays where large-membranes, sensitive to low-frequencies, were interlaced amongst small membranes, sensitive to high-frequencies. The interlacing could be achieved on a scale smaller than acoustic wavelengths, thus mitigating side-lobes. However, previous designs had limited transmit power at low-frequencies owing to low-collapse voltages. To achieve higher transmit power levels, we introduce multi-gap multi-frequency CMUT arrays. The large, low-frequency membranes are fabricated with a larger gap, thus enabling higher operating voltages without collapse, and providing a larger range of membrane motions. Multi-frequency CMUT arrays were fabricated using a modified sacrificial release process. Compared to previous multi-frequency devices, an additional mask step was added for separate patterning of large membranes to achieve a larger gap. High-frequency membranes ranged from 12-15 microns radius (8-15MHz in immersion), and low-frequency membranes ranged from 25-30 microns radius (2-4MHz center frequency in immersion). Different sized arrays with 64 and 128 channels for each of the low- and high-frequency sub-arrays were fabricated. Accurate nonlinear CMUT models were used to predict the improvement in transmit pressures. Previous multi-frequency devices produced peak-to-peak output pressures at 2MHz as high as 0.8MPa. By increasing the gap height from 400 to 900 microns and the membrane thickness from 1 to 1.5 microns, the membrane velocity (when biased at 80% of the collapse voltage) and driving at higher AC voltages, we predicted a 2-4 times improvement in output pressure. Future work should aim to use next-generation multi-gap multi-frequency CMUT arrays for super-harmonic contrast agent imaging and ultrasound drug-delivery applications.

Future work should aim to mitigate dielectric charging effects. Recently, commercially available fabrication processes have enabled charging-free CMUT operation and these should be exploited. This is important, not only for device reliability, but also charging-free operation may enable collapse- and collapse-snapback modes, which have previously been shown to exhibit much higher acoustic output than pre-collapse operation and exhibit less operational nonlinearity.

The combination of collapse-mode operation, multi-gap architectures, integration of elevationally-focusing acoustic lenses, and novel impedance-matching strategies may enable desired high acoustic outputs for super-harmonic and imaging-therapy applications. Once additional technical challenges have been addressed, exciting new imaging applications may emerge including targeted molecular imaging, super-harmonic super-resolution imaging, and practical point-of-care multi-resolution multi-depth imaging applications.

Wearable ultrasound transducers could open up new possibilities for cardiac ejection fraction monitoring, pulmonary hypertension monitoring and monitoring of response to interventions and therapeutics. Developed sacrificial release process flow may be used for fabrication of flexible multi-frequency CMUT arrays by selectively etching the back silicon-substrate and sputtering the bottom electrode, then using Polydimethylsiloxane (PDMS) as the flexible substrate. However, we need to carefully protect the devices in front side of the wafer from being etched during the wet etching of the silicon-substrate by adhesive bonding the devices to a glass wafer.

Our designed 1D arrays are used for 2D ultrasound imaging applications. Our group recently showed the feasibility of top-orthogonal-to-bottom-electrode (TOBE) 2D single-frequency CMUT arrays for novel 3D ultrasound imaging arrays. Future work should aim to design and fabricate multi-frequency TOBE arrays for 3D multi-band and contrast agent imaging applications. Moreover, the flexible large-scale multi-frequency TOBE CMUT arrays may be designed and fabricated for novel ultrasound applications.

Bibliography

D. N. Stephens, D. E. Kruse, A. S. Ergun, S. Barnes, X. M. Lu, and K. W. Ferrara, "Efficient array design for sonotherapy," Phys. Med. Biol., vol. 53, no. 14, pp. 3943–3969, Jul. 2008.

M. K. Chirala, P. Huynh, J. Ryu, and Y. Kim, "A 128-ch Δ-Σ ADC based mixed signal IC for full digital beamforming Wireless handheld Ultrasound imaging system," 37th Annual International Conference of the IEEE Engineering in Medicine and Biology Society (EMBC), pp. 1339-1342, Milan, 2015.

Mohanty, Kaustav, et al. "Ultrasound multiple scattering with microbubbles can differentiate between tumor and healthy tissue in vivo," Physics in Medicine & Biology, vol. 64, no. 11, May 2019.

H. Hasegawa, H. Tanaka, T. Takezaki and S. Machida, "Amplitude modulated pulse inversion technique for high SNR of tissue harmonic imaging using CMUT," IEEE International Ultrasonics Symposium (IUS), Washington, DC, 2017.

J. Ma, K. H. Martin, P. A. Dayton, and X. Jiang, "A preliminary engineering design of intravascular dual-frequency transducers for contrast-enhanced acoustic angiography and molecular imaging," IEEE Trans Ultrason Ferroelectr Freq Control, vol. 61, pp. 870-80, May 2014.

B. D. Lindsey, K. H. Martin, P. A. Dayton, J. Ma, Zhuochen Wang, and X. Jiang, "Dual-frequency intravascular ultrasound imaging of microbubble contrast agents: Ex vivo and in vivo demonstration," IEEE International Ultrasonics Symposium (IUS), Taipei, Taiwan, 2015.

S. Dingjie, et al. “Thrombolysis using multi-frequency high intensity focused ultrasound at MHz range: an in vitro study,” Physics in Medicine & Biology, vol. 60, no. 18, Sept. 2015.

D. A. Horsley et al., “Piezoelectric micromachined ultrasonic transducers in consumer electronics: The next little thing?,” *IEEE 29th International Conference on Micro Electro Mechanical Systems (MEMS)*, Shanghai, pp. 145-148, 2016.

I. Ladabaum, B. T. Khuri-Yakub, D. Spoliansky, and M. I. Haller, “Micromachined Ultrasonic Transducers (MUTs),” *IEEE Proce. Ultrason. Symp*, vol. 1, pp. 501–504. Nov. 1995.

R. S. C. Cobbold. (2007). *Foundations of Biomedical Ultrasound*. Oxford University Press, New York.

A. Grandt, *Fundamentals of Structural Integrity*. Hoboken, NJ: Wiley, 2003.

V. Giurgiutiu, *Structural Health Monitoring with Piezoelectric Wafer Active Sensors*. New York, NY: Academic, 2007.

H. Huang and D. Paramo, “Broadband electrical impedance matching for piezoelectric ultrasound transducers,” *in IEEE Transactions on Ultrasonics, Ferroelectrics, and Frequency Control*, vol. 58, no. 12, pp. 2699-2707, Dec. 2011.

L. Wu, and Y. Chen, “PSPICE approach for designing the ultrasonic piezoelectric transducer for medical diagnostic applications,” *Sens. Actuators A*, vol. 75, no. 2, pp. 186–198, May 1999.

M. Castillo, P. Acevedo, and E. Moreno, “KLM model for lossy piezoelectric transducers,” *Ultrasonics*, vol. 41, no. 8, pp. 671–679, Nov. 2003.

D. Callens, C. Bruneel, and J. Assaad, “Matching ultrasonic transducer using two matching layers where one of them is glue,” *NDT & E Int.*, vol. 37, no. 8, pp. 591–596, Dec. 2004.

G. R. Lockwood, and F. S. Foster, “Modeling and optimization of high-frequency ultrasound transducers,” *IEEE Trans. Ultrason. Ferroelectr. Freq. Control*, vol. 41, no. 2, pp. 225–230, Mar. 1994.

L. Svilainis, V. Dumbrava, and G. Motiejunas, “Optimization of the ultrasonic excitation stage,” in *30th Int. Conf. Information Technology Interfaces*, Dubrovnik, Croatia, pp. 791–796, Jun. 2008.

F. Akasheh, T. Myers, J. D. Fraser, S. Bose, and A. Bandyopadhyay, “Development of Piezoelectric Micromachined Ultrasonic Transducers,” *Sensors and Actuators A Phys.*, vol. 111, no. 2, pp. 275-287, 2004.

P. Muralt et al., “Piezoelectric Micromachined Ultrasonic Transducers Based on PZT Thin Films,” *IEEE Trans. Ultra. Ferroelectr. Freq. Contr.*, vol. 52, no. 12, pp. 2276-2288, 2005.

Z. H. Wang et al., “Fabrication and Characterization of Piezoelectric Micromachined Ultrasonic Transducers with Thick Composite PZT Films,” *IEEE Trans. Ultra. Ferroelectr. Freq. Contr.*, vol. 52, no. 12, pp. 2289-2297, 2005.

S. Trolier-McKinstry, and P. Muralt, “Thin film piezoelectrics for MEMS,” *Journal of Electroceramics*, vol. 12, no. 1-2, pp. 7-17, 2004.

B. Belgacem, F. Calame and P. Muralt, “Piezoelectric Micromachined Ultrasonic Transducers based on PZT films,” *15th ieee international symposium on the applications of ferroelectrics*, Sunset Beach, NC, pp. 326-331, 2006.

D. R. Chou, “Piezoelectric Micrimachined Ultrasound Transducer for Medical Imaging,” *Ph.D. Thesis*, Duke University, 2011.

A. Sampaleanu, P. Zhang, A. Kshirsagar, W. Moussa, and R. J. Zemp, “Top-orthogonal-to-bottom-electrode (TOBE) CMUT arrays for 3-D ultrasound imaging,” *IEEE Trans. Ultrason., Ferroelectr., Freq. Control*, vol. 61, no. 2, pp. 266–276, Feb. 2014.

P. Zhang, G. Fitzpatrick, T. Harrison, W. Moussa, and R. J. Zemp, “Double-SOI wafer-bonded CMUTs with improved electrical safety and minimal roughness of dielectric and electrode surfaces,” *J. Microelectromech. Syst.*, vol. 21, no. 3, pp. 668–680, Jun. 2012.

B. T. Khuri-Yakub and O. Oralkan, “Capacitive micromachined ultrasonic transducers for medical imaging and therapy,” *J. Micromech. Microeng.*, vol. 21, no. 5, pp. 54004–54014, 2011.

M. N. Senlik, S. Olcum, H. Koymen, and A. Atalar. “Radiation impedance of an array of circular capacitive micromachined ultrasonic transducers,” *IEEE Trans. Ultra. Ferroelectr. Freq. Contr.*, vol. 57. no. 4, pp. 969–976, 2010.

I. Ladabaum, X. Jin, H.T. Soh, A. Atalar, and B.T. Khuri-Yakub, “Surface micromachined capacitive ultrasonic transducers,” *IEEE Trans. Ultra. Ferroelectr. Freq. Contr.*, vol. 45, no. 3, pp. 678–690, 1998.

A. Caronti, G. Caliano, A. Iula, and M. Pappalardo. “An accurate model for capacitive micromachined ultrasonic transducers,” *IEEE Trans. Ultra. Ferroelectr. Freq. Contr.*, vol. 49, no 2, pp.159–168, 2002.

H. Koymen, A. Atalar, E. Aydogdu, C. Kocabas, H.K. Oguz, and S. Olcum, A. Ozgurluk and A. Unlugedik, “An Improved Lumped Element Nonlinear Circuit Model for a Circular CMUT Cell”, *IEEE Transactions on Ultrasonics, Ferroelectrics, and Frequency Control*, vol. 59, no. 8, pp. 1791-1799, 2012.

Y-S. Kim, “Advances in MR imaging-guided high-intensity focused ultrasound therapy,” *Int. J Hyperthermia*. Vol. 31, pp. 225-232, 2015.

M. R. Pfeffer, T. Rabin, Y. Inbar, A. Hananel, and R. Catane, “Image-guided high-intensity focused ultrasound in the treatment of cancer,” *In Image-Guided Cancer Therapy*, Springer, New York, pp. 79-99, 2013.

A. Ranjan et al., “Image-guided drug delivery with magnetic resonance guided high intensity focused ultrasound and temperature sensitive liposomes in a rabbit Vx2 tumor model,” *Journal of controlled release*, vol. 158, pp. 487-494, 2012.

S. P. Gautieri, “Photo-acoustic, multi-band, multi-cavity gas detection system,” *U.S. Patent*, No. 8,806,916. (19 August 2014).

S. Autrey, G. Posakony, J. Amonette, and N. Foster-Mills, “Multi-band transducer for photoacoustic detection,” *U.S. Patent*, No. 20,010,018,848. (6 September 2001).

S. Unnikrishnan, and A. L. Klibanov, “Microbubbles as ultrasound contrast agents for molecular imaging: preparation and application,” *Am. J. Roentgenology*, vol. 199, pp. 292-299, 2012.

V. R. Stewart, and P. S. Sidhu, “New directions in ultrasound: microbubble contrast,” *The British journal of radiology*, vol. 79, pp. 188-194, 2014.

A. Guiroy et al., “Dual frequency transducer for nonlinear contrast agent imaging,” *IEEE Trans. Ultrason. Ferroelectr. Freq. Control*, vol. 60, pp. 2634–2644, 2013.

C. C. Shen, and C. H. Lin, “Chirp-encoded excitation for dual-frequency ultrasound tissue harmonic imaging,” *IEEE Trans. Ultrason. Ferroelectr. Freq. Control*, vol. 59, pp. 2420-2430, 2012.

E. Ohno, H. Kawashima, S. Hashimoto, H. Goto, and Y. Hirooka “Current status of tissue harmonic imaging in endoscopic ultrasonography (EUS) and EUS-elastography in pancreatobiliary diseases,” *Digestive Endoscopy*, vol. 27, pp. 68-73, 2015.

T. Ojha, L. Rizzo, G. Storm, F. Kiessling, and T. Lammers, “Image-guided drug delivery: preclinical applications and clinical translation,” *Expert opinion on drug delivery*, vol. 12, pp. 1203-1207, 2015.

M. Thanou, M. Wright, M. Centelles, and W. Gedroyc, “Image guided focused ultrasound delivery of macromolecular drugs in tumours,” *Journal of Therapeutic Ultrasound*, vol. 3, pp. 75-76, 2015.

M. Thanou, M. Wright, and M. Centelles, “Nanoparticles for image guided focused ultrasound drug delivery,” *Cancer Research*, vol. 74, pp. 5398-5398, 2014.

P. S. Sheeran, J. E. Streeter, L. B. Mullin, T. O. Matsunaga, and P. A. Dayton, “Toward ultrasound molecular imaging with phase-change contrast agents: an in vitro proof of principle,” *Ultrasound in medicine and biology*, vol. 39, pp. 893-902, 2013.

S. E. Ahmed, A. M. Martins, and G. A. Husseini, “The use of ultrasound to release chemotherapeutic drugs from micelles and liposomes,” *Journal of drug targeting*, vol. 23, pp. 16-42, 2014.

Y. Lin, Z. Y. Chen, F. Yang, J. S. Zhang, Y. X. Wang, J. B. Liu, J. Y. Liao, Y. Y. Liao, Q. L. Zhou, B. C. Li, and H. Y. Liang, “Application of Molecular Imaging Technologies in Antitumor Drug Development and Therapy,” *Current pharmaceutical design*, vol. 21, pp. 2136-2146, 2015.

G. Ku, X. Wang, G. Stoica, and L. V. Wang, “Multiple-bandwidth photoacoustic tomography,” *Physics in Medicine and Biology*, vol. 49, pp. 1329–1338, 2004.

K. H. Martin, B. D. Lindsey, J. Ma, M. Lee, S. Li, F. S. Foster, X. Jiang, and P. A. Dayton, "Dual-frequency piezoelectric transducers for contrast enhanced ultrasound imaging," *Sensors*, vol. 14, pp. 20825-20842, 2014.

S. Li, W. Huang, X. Jiang, X. Jian, and Y. A. Cui, "dual-layer micromachined PMN-PT 1–3 composite transducer for broadband ultrasound imaging," *In Proceedings of the 2013 IEEE International Ultrasonics Symposium, Prague, Czech*, vol. 10, pp. 781–784, 21–25 July 2013.

P. A. Dayton, and K. W. Ferrara. "Targeted imaging using ultrasound," *Journal of magnetic resonance imaging*, vol. 16, no. 4, pp. 362-377, 2002.

R. C. Gessner, C. B. Frederick, F. S. Foster, and P. A. Dayton, "acoustic angiography: a new imaging modality for assessing microvasculature architecture," *Int. J. Biomed. Imaging*, vol. 2013, art. no. 936593, 2013.

J. d. Kasprzak, B. Paelinck, F. J. Ten cate, W. B. Vletter, n. de Jong, d. Poldermans, a. Elhendy, a. Bouakaz, and J. r. roelandt, "comparison of native and contrast-enhanced harmonic echocardiography for visualization of left ventricular endocardial border," *Am. J. Cardiol.*, vol. 83, no. 2, pp. 211–217, 1999.

B. D. Lindsey, J. D. Rojas, K. Heath Martin, S. E. Shelton, and P. Dayton, "Acoustic characterization of contrast-to-tissue ratio and axial resolution for dual-frequency contrast-specific acoustic angiography imaging," *Ultrasonics, Ferroelectrics, and Frequency Control, IEEE Transactions on*, vol. 61, pp. 1668-1687, 2014.

Lindsey, Brooks D.; Shelton, Sarah E.; Tsuruta, James K.; Dayton, Paul A.; Foster, F.Stuart, "Molecular acoustic angiography: Demonstration of in vivo feasibility for high resolution superharmonic ultrasound molecular imaging," *in Ultrasonics Symposium (IUS)*, pp.1-3, 21-24 Oct. 2015.

B. D. Lindsey, J. D. Rojas, and P. A. Dayton, "On the Relationship between Microbubble Fragmentation, Deflation and Broadband Superharmonic Signal Production," *Ultrasound Med Biol*, vol. 41, pp. 171125, 2015.

D. E. Kruse and K. W. Ferrara, "A new imaging strategy using wideband transient response of ultrasound contrast agents," *IEEE Transactions on Ultrasonics Ferroelectrics and Frequency Control*, vol. 52, pp. 1320-1329, Aug. 2005.

Li, Sibo; Kim, Jinwook; Zhuochen Wang; Jiang, Xiaoning; Kasoji, Sunny; Lindsey, Brooks; Dayton, Paul A., "A 3 MHz/18 MHz dual-layer co-linear array for transrectal acoustic angiography," *in Ultrasonics Symposium (IUS)*, pp.1-4, 21-24 Oct. 2015.

M. D. C. Eames, T. J. Reck, and J. A. Hossack, "Selectable frequency CMUT with membrane stand-off structures," *IEEE International Ultrasonics Symposium*, pp. 2814-2817, 2009.

C. H. Sherman, and J. L. Butler, "Transducers and Arrays for Underwater Sound," *Springer*, New York, 2007, Chap. 5, pp. 230-243.

R. L. Pritchard, "Mutual acoustic impedance between radiators in an infinite rigid plane," *J. Acoust. Soc. Am.*, vol. 32, pp. 730-737, 1960.

D. T. Porter, "Self-and Mutual-Radiation Impedance and Beam Patterns for Flexural Disks in a Rigid Plane," *J. Acoust. Soc. Am.*, vol. 36, pp. 1154-1161, 1964.

A. Kshirsagar, R. Chee, A. Sampaleanu, A. Forbrich, D. Rishi, W. Moussa, and R. J. Zemp, "Multi-frequency CMUT arrays for imaging-therapy applications," *IEEE International Ultrasonics Symposium (IUS)*, pp. 1991-1993, 2013.

K. C. Chan, "Mutual acoustic impedance between flexible disks of different sizes in an infinite rigid plane," *J. Acoust. Soc. Am.*, vol. 42, pp. 1060-1063, 1967.

H. Koymen, M. senlik, A. Atalar, and S. Olcum, "Parametric linear modeling of circular cMUT membranes in vacuum," *IEEE Trans. Ultrason. Ferroelectr. Freq. Control*, vol. 54, no. 6, pp. 1229–1239, Jun. 2007.

A. Lohfink and P.-C. Eccardt, "linear and nonlinear equivalent circuit modeling of cMUTs," *IEEE Trans. Ultrason. Ferroelectr. Freq. Control*, vol. 52, no. 12, pp. 2163–2172, Dec. 2005.

D. Certon, F. Teston, and F. Patat, "a finite difference model for CMUT devices," *IEEE Trans. Ultrason. Ferroelectr. Freq. Control*, vol. 52, no. 12, pp. 2199–2210, dec. 2005.

I. O. Wygant, M. Kupnik, and B. T. Khuri-yakub, “analytically calculating membrane displacement and the equivalent circuit model of a circular cMUT cell,” *in Proc. IEEE Ultrasonics Symp.*, nov. 2008, pp. 2111–2114.

C. Meynier, F. Teston, and D. Certon, “A multiscale model for array of capacitive micromachined ultrasonic transducers,” *J. Acoust. Soc. Am.*, vol. 128, no. 5, pp. 2549-2561, 2010.

M. Maadi, R. Chee, and R. J. Zemp, “Mutual radiation impedance for modeling of multi-frequency CMUT arrays,” *IEEE International Ultrasonics Symposium (IUS)*, pp.1-4, 21-24 Oct. 2015.

C. J. Bouwkamp, Phil. Research Repts 1, pp. 262-264, 1946.

R. S. C. Cobbold. (2007). Foundations of Biomedical Ultrasound. Oxford University Press, New York, Chap. 3, pp. 155-163.

H. Oguz, A. Atalar, and H. Koymen, “Equivalent circuit-based analysis of CMUT cell dynamics in arrays,” *IEEE Trans. Ultrason. Ferroelectr. Freq. Control*, vol. 60, pp. 1016-1024, 2013.

H. K. Oguz, “Circuit theory based modeling and analysis of CMUT arrays” *PhD diss.*, Bilkent university, 2013.

S. Olçum, “Deep collapse mode capacitive micromachined ultrasonic transducers.” *PhD diss.*, Bilkent University, 2010.

M. Maadi, and R. J. Zemp, “Self and Mutual Radiation Impedances for Modeling of Multi-Frequency CMUT Arrays,” *IEEE Trans. Ultrason., Ferroelect., Freq. Control*, vol. 63, no. 9, pp. 1441–1454, Sep. 2016.

B. A. Greenlay, and R. J. Zemp, “Fabrication of Linear Array and Top-Orthogonal-to-Bottom Electrode CMUT Arrays with a Sacrificial Release Process,” *IEEE Trans. Ultrason. Ferroelectr. Freq. Control*, vol. 64, no. 1, pp. 93-107, Jan. 2017.

B. A. Greenlay, “Fabrication and Integration of CMUT Sensors,” *MS.c. dissertation*, Dept. Elect. Comp. Eng., Univ. of Alberta, Edmonton, Alberta, Canada, 2017.

A. S. Erguri, Y. Huang, X. Zhuang, O. Oralkan, G. G. Yarahoglu, and B. T. Khuri-Yakub, “Capacitive Micromachined Ultrasonic Transducers: Fabrication Technology,” *IEEE Trans. Ultrason. Ferroelectr. Freq. Control*, vol. 52, no. 12, pp. 2242-2258, Dec. 2005.

M. Maadi, and B. Bayram, “Custom integrated circuit design for ultrasonic therapeutic CMUT array,” *Microsystem Technologies*, pp. 1-17, Mar. 2014.

M. Maadi, C. Ceroici, and R. J. Zemp, “Electrical impedance matching of CMUT cells,” IEEE International Ultrasonics Symposium (IUS), Taipei, pp.1-4, 21-24 Oct. 2015.

M. Maadi, and R. J. Zemp, “Modelling of Large-Scale Multi-Frequency CMUT Arrays with Circular Membranes,” IEEE International Ultrasonics Symposium (IUS), Tours, pp.1-4, 18-21 Sep. 2016.

R. K. W. Chee, P. Zhang, M. Maadi, and R. J. Zemp, “Multifrequency Interlaced CMUTs for Photoacoustic Imaging,” IEEE Trans. Ultrason., Ferroelect., Freq. Control, vol. 64, no. 2, pp. 391–401, Feb. 2017.

W. Mason, Electromechanical Transducers and Wave Filters, 2nd ed. New York: Van Nostrand, 1948.

H. K. Oguz, S. Olcum, M. N. Senlik, V. Tas, A. Atalar and H. Koymen, “Nonlinear modeling of an immersed transmitting capacitive micromachined ultrasonic transducer for harmonic balance analysis,” IEEE Trans. Ultrason. Ferroelectr. Freq. Control, vol. 57, no. 2, pp. 438-447, Feb. 2010.

M. F. la Cour, T. L. Christiansen, J. A. Jensen, and E. V. Thomsen, “Electrostatic and small-signal analysis of CMUTs with circular and square anisotropic plates,” IEEE Trans. Ultrason. Ferroelectr. Freq. Control, vol. 62, no. 8, pp. 1563-1579, Aug. 2015.

E. V. Thomsen, K. Reck, G. Skands, C. Bertelsen, and O. Hansen, “Silicon as an anisotropic mechanical material: Deflection of thin crystalline plates,” Sens. Actuators, vol. 220, pp. 347–364, 2014.

F. C. Mbakogu, and M. N. Pavlovic, “Bending of clamped orthotropic rectangular plates: A variational symbolic solution,” Comput. Struc., vol. 77, no. 2, pp. 117–128, Jun. 2000.

M. Rahman, J. Hernandez, and S. Chowdhury, "An improved analytical method to design CMUTs with square diaphragms," IEEE Trans. Ultrason. Ferroelectr. Freq. Control, vol. 60, no. 4, pp. 834-845, Apr. 2013.

Z. Zheng, W. Sun, X. Suo, L. L. Wong, Z. Sun, and J. T. Yeow, "A novel deflection shape function for rectangular capacitive micromachined ultrasonic transducer diaphragms," Sensing and Bio-Sensing Research, vol. 5, pp. 62-70, Sept. 2015.

S. Satir, J. Zahorian, and F. L. Degertekin, "A large-signal model for CMUT arrays with arbitrary membrane geometry operating in non-collapsed mode," IEEE Trans. Ultrason. Ferroelectr. Freq. Control, vol. 60, no. 11, pp. 2426-2439, Nov. 2013.

J. Zahorian, S. Satir, and F. L. Degertekin, "Analytical-Finite Element hybrid model for CMUT arrays with arbitrary membrane geometry," IEEE International Ultrasonics Symposium (IUS), Dresden, pp. 584-587, 7-10 Oct. 2012.

F. Y. Yamaner, S. Olcum, H. K. Oguz, A. Bozkurt, H. Koymen, and A. Atalar, "High-power CMUTs: design and experimental verification," IEEE Trans. Ultrason. Ferroelectr. Freq. Control, vol. 59, no. 6, pp. 1276-1284, Jun. 2012.

C. D. Herickhoff, C. M. Wilson, G. A. Grant, G. W. Britz, E. D. Light, M. L. Palmeri, P. D. Wolf, and S. W. Smith, "Dual-mode IVUS transducer for image-guided brain therapy: Preliminary experiments," Ultrasound Med. Biol., vol. 37, no. 10, pp. 1667–1676, Oct. 2011.

A. L. Klibanov, "Microbubble contrast agents: targeted ultrasound imaging and ultrasound-assisted drug-delivery applications," Invest. Radiol., vol. 41, no. 3, pp. 354–362, Mar. 2006.

H. H. Kim, J. M. Cannata, R. Liu, J. H. Chang, R. H. Silverman and K. K. Shung, "20 MHz/40 MHz dual element transducers for high frequency harmonic imaging," IEEE Trans. Ultrason. Ferroelectr. Freq. Control, vol. 55, no. 12, pp. 2683-2691, Dec. 2008.

Z. Wang et al., "Design, Fabrication, and Characterization of a Bifrequency Colinear Array," IEEE Trans. Ultrason. Ferroelectr. Freq. Control, vol. 63, no. 2, pp. 266-274, Feb. 2016.

A. Stuart Savoia et al., “Design, Fabrication and Characterization of a Hybrid Piezoelectric-CMUT Dual-Frequency Ultrasonic Transducer,” 2018 IEEE International Ultrasonics Symposium (IUS), Kobe, pp. 1-4, 22-25 Oct. 2018.

M. Maadi, and R. J. Zemp, “A Nonlinear Lumped Equivalent Circuit Model for a Single Un-Collapsed Square CMUT Cell,” IEEE Trans. Ultrason., Ferroelect., Freq. Control, vol. 66, no. 8, pp. 1340–1351, Aug. 2019.

Q. F. Zhou et al. “Self-focused high frequency ultrasonic transducers based on ZnO piezoelectric films,” Applied physics letters, vol. 90, no. 11, pp. 113502-113502, 2007.

A. Sevig, and J. W. Sliwa, “Stacked and filled capacitive microelectromechanical ultrasonic transducer for medical diagnostic ultrasound systems,” U.S. Patent, No. 6,558,330. 6 May 2003.

M. Celmer, and K. J. Opieliński, “Study of Crosstalk in Linear Ultrasonic Transducer Arrays,” Acta Acustica united with Acustica, vol. 101, no. 1, pp. 46-54, 2015.

A. L. Klibanov, “Targeted delivery of gas-filled microspheres, contrast agents for ultrasound imaging,” Adv. Drug Deliv Rev., vol. 37, pp. 139–157, 1999.

F. A. Jaffer, P. Libby, and R. Weissleder, “Molecular and cellular imaging of atherosclerosis: Emerging applications,” J. Am. Coll. Cardiol., vol. 47, no. 7, pp. 1328–1338, 2006.

R. P. Choudhury, V. Fuster, and Z. A. Fayad, “Molecular, cellular and functional imaging of atherothrombosis,” Nat. Rev. Drug Discov., vol. 3, pp. 913–925, Nov. 2004.

R. Gessner, and P. A. Dayton, “Advances in molecular imaging with ultrasound,” Mol. Imaging, vol. 9, pp. 117–127, Jun. 2010.

S. B. Feinstein, “Contrast ultrasound imaging of the carotid artery vasa vasorum and atherosclerotic plaque neovascularization,” J. Am. Coll. Cardiol., vol. 48, no. 2, pp. 236–243, 2006.

C. Shen, Y. Chou, and P. Li, “Pulse inversion techniques in ultrasonic nonlinear imaging,” Journal of Medical Ultrasound, vol. 13, no. 1, pp. 3-17, 2005.

R. J. Eckersley, C. T. Chin, and P. N. Burns, “Optimising phase and amplitude modulation schemes for imaging microbubble contrast agents at low acoustic power,” Ultrasound in medicine & biology, vol. 31, no. 2, pp. 213-219, 2005.

E. Quaia, Ed., Contrast Media in Ultrasonography. Berlin, Germany: Springer-Verlag, 2005.

O. Couture, M. Fink, and M. Tanter, “Ultrasound contrast plane wave imaging,” IEEE Trans. Ultrason., Ferroelectr., Freq. Control, vol. 59, no. 12, Dec. 2012.

D. Fouan, and A. Bouakaz, “Investigation of classical pulse sequences for contrast-enhanced ultrasound imaging with a cMUT probe,” IEEE transactions on ultrasonics, ferroelectrics, and frequency control, vol. 63, no. 10, pp. 1496-1504, Oct. 2016.

Appendix A

Radiation Impedance

A.1 Calculation of the Directional Factor

The comprehensive expression for $|K(\theta,\varphi)|^2$ is obtained from Eq. (3.4) by dividing $|P_1+P_2|^2$ by the on-axis pressure magnitude$|P_{on-axis}|^2$. Thus, for monochromatic excitation

$$|P_1+P_2|^2 = |P_1|^2+|P_2|^2+P_1{P_2}^*+{P_1}^*P_2 \cong \left|\frac{\omega\rho_0 v_0}{2R_{0_1}}\right|^2 \{a_1^4{D_1}^2(\theta)+ a_2^4{D_2}^2(\theta)+a_1^2a_2^2D_1(\theta)D_2(\theta)\left[e^{-ik\left(R_{0_1}-R_{0_2}\right)}+e^{+ik\left(R_{0_1}-R_{0_2}\right)}\right]\} = \left|\frac{\omega\rho_0 v_0}{2R_{0_1}}\right|^2 \{a_1^4{D_1}^2(\theta)+a_2^4{D_2}^2(\theta)+a_1^2a_2^2D_1(\theta)D_2(\theta)\left[2\cos\left(k(R_{0_1}-R_{0_2})\right)\right]\} \tag{A.1}$$

and note that,

$$\frac{R_{0_1}}{R_0} = \sqrt{\left(\frac{z}{R_0}\right)^2 + \left(\frac{y}{R_0}\right)^2 + \left(\frac{x + d/2}{R_0}\right)^2} = \sqrt{\frac{z^2 + y^2}{R_0^2} + \frac{x^2}{R_0^2} + \frac{2x(d/2)}{R_0^2} + \frac{(d/2)^2}{R_0^2}}$$

$$= \sqrt{1 + \frac{2x(d/2)}{R_0^2} + \frac{(d/2)^2}{R_0^2}} \approx \sqrt{1 + \frac{2x(d/2)}{R_0^2}} \approx 1 + \alpha \tag{A.2}$$

by using the binomial expansion and taking only first-order terms of the R_{0_1}/R_0 expression, and also by considering the defined coordinate system in Fig. 3.1, with

$$\alpha = \frac{1}{2}\frac{xd}{R_0^2} = \frac{1}{2}\frac{d}{R_0} sin\theta sin\varphi. \tag{A.3}$$

Similarly,

$$\frac{R_{0_2}}{R_0} = \sqrt{\left(\frac{z}{R_0}\right)^2 + \left(\frac{y}{R_0}\right)^2 + \left(\frac{x - d/2}{R_0}\right)^2} \approx 1 - \alpha \tag{A.4}$$

Thus,

$$R_{0_1} \cong R_0(1 + \alpha),$$

$$R_{0_2} \cong R_0(1 - \alpha). \tag{A.5}$$

which yields to,

$$|P_1 + P_2|^2 = \left|\frac{\omega\rho_0 v_0}{2R_{0_1}}\right|^2 \{a_1^4 {D_1}^2(\theta) + a_2^4 {D_2}^2(\theta) + 2a_1^2 a_2^2 D_1(\theta) D_2(\theta)[\cos{(2k\alpha R_0)}]\} \tag{A.6}$$

Then,

$$|K(\theta,\varphi)|^2 = \left(\left|\frac{\omega\rho_0 v_0}{2R_{0_1}}\right|^2 \{a_1^4 {D_1}^2(\theta) + a_2^4 {D_2}^2(\theta) + 2a_1^2 a_2^2 D_1(\theta) D_2(\theta)[\cos(2k\alpha R_0)]\}\right) / \left|\frac{\omega\rho_0 v_0 (a_1^2 + a_2^2)}{2R_{0_1}}\right|^2 = \{a_1^4 {D_1}^2(\theta) + a_2^4 {D_2}^2(\theta) + 2a_1^2 a_2^2 D_1(\theta) D_2(\theta)[\cos(2k\alpha R_0)]\}/(a_1^2 + a_2^2)^2 \quad \text{(A.7)}$$

Finally, by utilizing the Eq. (A.3), a comprehensive expression for $|K(\theta,\varphi)|^2$ which is valid for any types of circular disks of different sizes is obtained as Eq. (3.9).

A.2 Calculation of the Self-Radiation Acoustic Impedance

By using Eq. (3.14), the self-radiation impedances Z_{nn} (n is the cell number) can be written as

$$Z_{nn} = R_{nn} + j\, X_{nn} = \rho c(\pi a_n^2)\frac{(ka_n)^2}{2}\int_0^{(\pi/2)+j\infty} {D_n}^2(\theta) sin\theta d\theta \quad \text{(A.8)}$$

According to $\int_0^{(\pi/2)+j\infty} = \int_0^{\pi/2} + \int_{(\pi/2)+j0}^{(\pi/2)+j\infty}$, the real and imaginary parts of the self-radiation impedance are given by

$$R_{nn} = \rho c(\pi a_n^2)\frac{(ka_n)^2}{2}\int_0^{\pi/2} {D_n}^2(\theta) sin\theta d\theta \quad \text{(A.9)}$$

and

$$X_{nn} = \rho c(\pi a_n^2)\frac{(ka_n)^2}{2}\int_{(\pi/2)+j0}^{(\pi/2)+j\infty} {D_n}^2(\theta) sin\theta d\theta \quad \text{(A.10)}$$

If we consider two disks as identical pistons ($a_1 = a_2 = a$), the directivity function will be $D(\theta) = 2\,\frac{J_1(kasin\theta)}{(kasin\theta)}$ and then Z_{11} and Z_{22} become equal and reduce to the d independent part of the Eq. (3.8) of Pritchard and then, can be written in terms of Bessel and Struve function of order one and $2ka$.

$$Z_{11} = Z_{22} = 2\rho c(\pi a^2) \int_0^{(\pi/2)+j\infty} \frac{{J_1}^2(kasin\theta)}{sin^2\theta}\, sin\theta d\theta$$
$$= \rho c(\pi a^2)\left\{\left[1 - \frac{J_1(2ka)}{ka}\right] + \left[\frac{H_1(2ka)}{ka}\right]\right\} \tag{A.11}$$

A.3 Calculation of the Mutual Radiation Acoustic Impedance

According to Eq. (3.15) and by using $\int_0^{2\pi} \cos\,(kdsin\theta sin\varphi\,)\,d\varphi = 2\pi J_0(kdsin\theta)$ the mutual radiation impedance can be expanded as

$$Z_{12} = R_{12} + j\,X_{12}$$
$$= \frac{\rho c(\pi a_1^2)(ka_2)^2}{2\left(\sum \frac{\alpha_n}{n+2}\right)^2} \sum_{\mu=1}^{3} \sum_{\nu=1}^{3} \beta_\mu \gamma_\nu$$
$$\times \frac{1}{(ka_1)^\mu (ka_2)^\nu} \left\{ \int_0^{(\pi/2)+j\infty} \frac{J_\mu(ka_1 sin\theta) J_\nu(ka_2 sin\theta)}{sin^\mu\theta sin^\nu\theta} \right. \tag{A.12}$$
$$\left. \times [J_0(kdsin\theta)] sin\theta d\theta \right\}$$

If we consider two disks as separated identical piston radiators ($\beta_\mu = \gamma_\nu = \beta_1 = \gamma_1 = 1$) and the directivity function equal to $D(\theta) = 2\,\frac{J_1(kasin\theta)}{(kasin\theta)}$, then Z_{12} or Z_{21} reduce to the Eq. (3.11) of Pritchard.

$$Z_{12} = R_{12} + j\,X_{12} \tag{A.13}$$
$$= 2\rho c(\pi a^2) \int_0^{(\pi/2)+j\infty} \frac{{J_1}^2(kasin\theta)}{sin^2\theta} \times J_0(kdsin\theta) sin\theta d\theta$$

A.4 Calculation of the Approximated Version of the Mutual Radiation Acoustic Impedance

By employing a change of variables $p = m + n$ for the mutual radiation impedance expression, the Eq. (3.17) can be simplified as.

$$Z_{12} = \frac{\rho c(\pi a_1^2)(ka_2)^2}{4\left(\sum \frac{\alpha_n}{n+2}\right)^2} \sum_{\mu=1}^{3} \sum_{\nu=1}^{3} \beta_\mu \gamma_\nu \times \frac{1}{(ka_1)^\mu (ka_2)^\nu} \left\{ \sum_{p=0}^{\infty} \sigma_p(ka_{1,2}) \left(\frac{1}{d}\right)^p \zeta_{m+n^{(2)}}(kd) \right\} \tag{A.14}$$

where

$$\sigma_p(ka_{1,2}) = \sum_{n=0}^{p} \frac{2\Gamma\left(p+\frac{1}{2}\right)}{\pi^{\frac{1}{2}}(p-n)!\,n!} (a_1^{p-n} a_2^n) J_{\mu+p-n}(ka_1) J_{\nu+n}(ka_2) \tag{A.15}$$

For the disks are separated by a distance large relative to the radius, $\left(\frac{a_{1,2}}{d}\right) \ll 1$, all terms of order $\left(\frac{a}{d}\right)$ and higher in Eq. (A.14) may be neglected. Then we only need to consider the first term of $\sigma_p(ka_{1,2})$.

According to $J_{\frac{1}{2}}(kd) + jJ_{-\frac{1}{2}}(kd) = (\frac{2}{\pi kd})^{\frac{1}{2}}[\sin(kd) + j\cos(kd)]$, we obtain

$$Z_{12} = \frac{\rho c(\pi a_1^2)(ka_2)^2}{2\left(\sum \frac{\alpha_n}{n+2}\right)^2} \left\{ \frac{\sin(kd)}{kd} + j\frac{\cos(kd)}{kd} \right\} \times \sum_{\mu=1}^{3} \sum_{\nu=1}^{3} \beta_\mu \gamma_\nu \frac{1}{(ka_1)^\mu (ka_2)^\nu} \left[J_\nu(ka_2) J_\mu(ka_1)\right] \tag{A.16}$$

Another approximate condition can be considered when $(ka_{1,2})^2 \ll 1$ which means only the first terms of the series expansion of Eq. (A.16) are needed. The second condition is applied separately for pistons and clamped-edge disks to find the approximate expressions of the mutual radiation impedances. Considering the first and second approximate conditions and according to the β_μ and γ_ν values for the pistons,

$$\sum_{\mu=1}^{3}\sum_{\nu=1}^{3}\beta_\mu\gamma_\nu \times \frac{1}{(ka_1)^\mu(ka_2)^\nu} \times \left[J_\nu(ka_2)J_\mu(ka_1)\right] \cong \frac{\beta_1\gamma_1}{k^2a_1a_2}J_1(ka_1)J_1(ka_2) \cong \frac{\beta_1\gamma_1}{k^2a_1a_2} \times \frac{ka_1}{2} \times \frac{ka_2}{2} = \frac{1}{4} \tag{A.17}$$

Similarly, by considering the approximate conditions, the result of Eq. (A.17) for clamped edge disks is,

$$\frac{\beta_3\gamma_3}{(ka_1)^3(ka_2)^3}J_3(ka_1)J_3(ka_2) \cong \frac{\beta_3\gamma_3}{(ka_1)^3(ka_2)^3} \times \frac{(ka_1)^3}{48} \times \frac{(ka_2)^3}{48} \tag{A.18}$$

Then, Eqs. (3.19) and (3.20) are obtained as approximate versions of the piston and clamped edge radiators, respectively.

A.5 Polynomial Coefficients of Approximate Mutual Radiation Expressions

The polynomial coefficients $A(ka)$ and $B(ka)$ of Eq. (3.23) for identical membranes are computed using a tenth-order polynomial curve fitting method to give a best-fit to Eq. (3.22) and are shown in Table A.I below.

TABLE A.I. POLYNOMIAL COEFFICIENTS OF FUNCTIONS $A(ka)$ AND $B(ka)$ FOR APPROXIMATE SUPPORT EDGE AND CLAMPED EDGE DISKS.

	Approx. supported edge $0.5 < ka < 4.5$		Clamped edge $0.5 < ka < 5.5$	
n	a_n	b_n	a_n	b_n
0	1.2510e-2	-1.330e-2	4.2800e-2	1.0000e-2
1	-1.6030e-1	1.6820e-1	-3.0480e-1	1.3490e-2
2	1.643000	3.8390e-1	1.875000	9.0530e-1
3	-1.117000	1.020000	-1.130000	1.8320e-1
4	8.5200e-1	-1.045000	6.6730e-1	-2.7980e-1
5	-5.3710e-1	4.2310e-1	-3.3070e-1	6.4890e-2
6	1.8350e-1	-1.0360e-1	9.2680e-2	-5.6560e-3
7	-3.3090e-2	1.7030e-2	-1.3890e-2	4.7550e-4
8	3.0140e-3	-1.7040e-3	1.0580e-3	-8.6770e-5
9	-1.0970e-4	7.5050e-5	-3.2022e-5	6.1840e-6
10	5.0000e-9	2.5380e-8	-1.0000e-7	-1.000e-11

Likewise, the polynomial coefficients $A(ka_1, ka_2)$ and $B(ka_1, ka_2)$ of Eq. (3.25) for non-identical membranes are computed using 5x5 multivariate polynomial curve fitting to give a best-fit to Eq. (3.24) and are shown in Table A.II and III below for different intervals.

TABLE A.II. POLYNOMIAL COEFFICIENTS OF FUNCTIONS $A(ka_1, ka_2)$ AND $B(ka_1, ka_2)$ FOR APPROXIMATE SUPPORT EDGE AND CLAMPED EDGE DISKS FOR $0.05 < ka_1, ka_2 < 0.8$.

Clamped edge disks for $0.05 < ka_1, ka_2 < 0.8$					
ij	a_{ij}	b_{ij}	ij	a_{ij}	b_{ij}
00	-4.679e-3	-8.319e-3	20	4.889e-1	-2.475e-1
01	-2.268e-2	2.097e-2	21	-5.27600	-4.04300
02	-3.456e-1	-3.991e-1	22	4.22000	1.74600
03	1.700000	1.51900	23	2.51100	6.428e-1
04	-3.27100	2.48900	30	2.81500	5.69300
05	2.224000	1.53600	31	12.0000	9.85200
10	5.614e-2	1.416e-1	32	-3.38500	-3.49400
11	-8.271e-1	4.969e-1	40	-7.36000	-12.1800
12	-5.508e-1	5.349e-1	41	-9.73700	-7.55100
13	-1.01800	-2.28700	50	6.84400	9.54800
14	1.90900	1.76100	The a_{ij} and b_{ij} coefficients for the rest of the ij values are zero.		
Goodness of fit		SSE		0.01587	
		R-square		0.9986	
		Adjusted R-square		0.9986	
		RMSE		0.002752	

TABLE A.III. POLYNOMIAL COEFFICIENTS OF FUNCTIONS $A(ka_1, ka_2)$ AND $B(ka_1, ka_2)$ FOR APPROXIMATE SUPPORT EDGE AND CLAMPED EDGE DISKS FOR $0.8 < ka_1, ka_2 < 6$.

Clamped edge disks for $0.8 < ka_1, ka_2 < 6$					
ij	a_{ij}	b_{ij}	ij	a_{ij}	b_{ij}
00	8.152e-1	8.154e-1	20	2.72000	2.6930
01	-5.128e-1	-5.343e-1	21	-6.375e-1	-6.317e-1
02	1.448e-1	1.462e-1	22	4.392e-2	4.519e-2
03	-2.004e-2	-1.617e-2	23	-4.341e-3	-4.479e-3
04	2.180e-3	1.229e-3	30	-6.183e-1	-6.138e-1
05	-2.226e-4	-1.594e-4	31	1.300e-1	1.279e-1
10	-2.10600	-2.07800	32	-2.773e-4	-2.421e-4
11	1.14500	1.16700	40	2.952e-2	2.964e-2
12	-2.970e-1	-3.113e-1	41	-8.750e-3	-8.618e-3
13	3.042e-2	3.234e-2	50	1.281e-3	1.237e-3
14	1.390e-5	-5.918e-5	The a_{ij} and b_{ij} coefficients for the rest of the ij values are zero.		
Goodness of fit			SSE	1.767	
			R-square	0.9998	
			Adjusted R-square	0.9998	
			RMSE	0.02185	

Appendix B

Polynomial Coefficients for Nonlinear Capacitance Calculations

The polynomial coefficients of Eq. (6.7) for different normalized deflection areas of $x_p(t)/t_{ge}$ are computed using a polynomial curve fitting method to give a best fit to numerical solutions of Eq. (6.5) and are shown in Table B.I.

TABLE B.I. POLYNOMIAL COEFFICIENTS OF FUNCTION $g(u)$ FOR CAPACITANCE CALCULATION.

$u = \frac{x_p(t)}{t_{ge}}$	$0 < u < 10^{-3}$	$10^{-3} < u < 0.5$	$0.5 < u < 0.99$
n	a_n	a_n	a_n
0	1	1	1.47200
1	0.30370	0.3037	0.21400
2	0.17990	0.1798	0.03438
3	0.03161	0.1293	-0.0244
4	426.400	0.08433	0.08047
5	-1.112e6	0.1801	0.08518
6	1.759e9	-0.3259	-0.05122
7	-1.657e12	1.0070	-0.04796
8	8.547e14	-1.2320	0.01346
9	-1.859e17	0.8414	0.01037
	$(Goodness\ of\ fit)$		
SSE	4.187e-26	1.509e-11	5.058e-3
R-square	1	1	0.9999
Adjusted R-square	1	1	0.9999
RMSE	2.047e-15	5.504e-8	3.277e-3

Appendix C

Sacrificial Release Single-Gap Multi-Frequency and Multi-Gap Multi-Frequency CMUT Detailed Process Flow

1) ***Wafer Preparation and Cleaning*****:** Piranha cleaning of the wafers in a 3:1 solution of sulphuric acid and hydrogen peroxide for 15 minutes and then buffered oxide etching (BOE) to remove the native oxide on the wafers for 1 minute. Rinse the wafers in a deionized water for 5 times after each cleaning step.

2) ***Low pressure chemical vapor deposition (LPCVD) of the bottom silicon nitride insulation layer*****:** 250 nm silicon nitride deposition using the recipe shown in Table C.I. The Piranha cleaning of the wafers must be done right before each LPCVD step. It is recommended to add an extra wafer for thickness measurements and calculating the proper etching time.

TABLE C.I. LPCVD THIN SILICON NITRIDE DEPOSITION RECIPE.

Temperature (ºC)	835
Pressure (mTorr)	150
NH_3 Flow Rate (sccm*)	10
Dichlorosilane Flow Rate (sccm)	50
Time (hr:min:sec)	01:18:00
*standard cubic centimeters per minute.	

3) ***Plasma enhanced chemical vapor deposition (PECVD) of a silicon dioxide protection layer*:** 50 nm deposition (100 nm for multi-gap multi-frequency CMUTs) using the recipe shown in Table C.II with a Trion Technology PECVD.

Note: It is recommended to perform Piranha cleaning right before each deposition step to reduce the contamination.

TABLE C.II. PECVD PROTECTION SILICON DIOXIDE DEPOSITION RECIPE.

Temperature (ºC)	300
Pressure (mTorr)	800
Oxygen Flow Rate (sccm)	85
TEOS Flow Rate (sccm)	100
RF Power (W)	60
Deposition Rate (nm/sec)	1.47

4) ***Wafer cleaning*:** Piranha cleaning of the wafers in a 3:1 solution of sulphuric acid and hydrogen peroxide for 15 minutes. Rinse the wafers in a deionized water for 5 times after each cleaning step.

5) ***Low pressure chemical vapor deposition (LPCVD) of the first large grain poly-silicon sacrificial layer*:** 250 nm deposition (500 nm for multi-gap multi-frequency CMUTs) using the recipe shown in Table C.III.

TABLE C.III. LPCVD First Poly-Silicon Sacrificial Layer Deposition Recipe.

Temperature (ºC)	660
Pressure (mTorr)	300
SiH_4 (sccm)	75
Time (min)	10
* 20 minutes for 500 nm poly-silicon deposition.	

6) ***Promoting the adhesion between the photoresist and the poly-silicon film***: Coating the wafers with Hexamethyldisilizane (HMDS) using a Yield Engineering Systems (YES) Vapor tool, or equivalent, with a standardized recipe shown in Table C.IV.

TABLE C.IV. HMDS VAPOR DEPOSITION RECIPE.

Temperature (ºC)	150
Pressure (Torr)	1
Time (min)	5

7) ***Lithography mask 1*****:** Photoresist patterning of the first sacrificial layer with the recipe shown in Table C.V. The average thickness of the resist is 1.2 – 1.3 µm.

TABLE C.V. STANDARD HPR-504 PATTERNING RECIPE.

Spread	10 s @ 500 rpm
Spin	40 s @ 3500 rpm
Baking	90 s @ 115 ºC
Rehydration Time (min)	15
Exposure Time (s)	2.6
Developing Time in 354 (s)	22
Exposure Intensity (mJ/cm^2)	60

8) ***Reactive ion etching (RIE) of the 250 nm (500 nm for multi-gap multi-frequency CMUTs) poly-silicon sacrificial layer*:** Etching using the recipe shown in Table C.VI with a Trion Technology RIE, or equivalent.

TABLE C.VI. RIE OF POLY-SILICON RECIPE.

Pressure (mTorr)	50
SF_6 Flow Rate (sccm)	25
RF Power (W)	30
Time (s)	250*
* 285 seconds for etching 500 nm poly-silicon.	

9) ***Strip the photoresist*:** Expose the entire wafer in UV flood exposure system for 3 minutes and then remove the photoresist using 354 developer. To make sure no photoresist left on the wafer, rinse the wafer with acetone and isopropanol. Finally, dry the wafer with nitrogen.

10) ***Wafer cleaning*:** Piranha cleaning of the wafers in a 3:1 solution of sulphuric acid and hydrogen peroxide for 15 minutes. Rinse the wafers in a deionized water for 5 times after each cleaning step.

11) ***Low pressure chemical vapor deposition (LPCVD) of the second large grain poly-silicon sacrificial layer*:** 100 nm deposition using the recipe shown in Table C.III except the time is 4 minutes.

12) ***Promoting the adhesion between the photoresist and the poly-silicon film*:** Coating the wafers with Hexamethyldisilizane (HMDS) using a Yield Engineering Systems (YES) Vapor tool, or equivalent, with a standardized recipe shown in Table C.IV.

13) ***Lithography mask 2*:** Photoresist patterning of the second sacrificial layer with the recipe shown in Table C.V. The average thickness of the resist is 1.2 – 1.3 µm.

14) ***Reactive ion etching (RIE) of the 350 nm (100 nm for multi-gap multi-frequency CMUTs) poly-silicon sacrificial layer*:** Etching using the recipe shown in Table C.VI with a Trion Technology RIE, or equivalent except the time is 325 and 44 seconds for multi-frequency and multi-gap multi-frequency CMUT devices, respectively.

15) ***Strip the photoresist*:** Expose the entire wafer in UV flood exposure system for 3 minutes and then remove the photoresist using 354 developer. To make sure no photoresist left on the wafer, rinse the wafer with acetone and isopropanol. Finally, dry the wafer with nitrogen.

16) ***(Only for multi-gap multi-frequency devices) Low pressure chemical vapor deposition (LPCVD) of the third large grain poly-silicon sacrificial layer*:** 200 nm deposition using the recipe shown in Table C.III except the time is 8 minutes.

17) ***(Only for multi-gap multi-frequency devices) Lithography mask 3*:** Photoresist patterning of the second sacrificial layer with the recipe shown in Table C.V. The average thickness of the resist is 1.2 – 1.3 μm.

18) ***(Only for multi-gap multi-frequency devices) Reactive ion etching (RIE) of the 300 nm poly-silicon sacrificial layer*:** Etching using the recipe shown in Table C.VI with a Trion Technology RIE, or equivalent except the time is 200 seconds.

19) ***(Only for multi-gap multi-frequency devices) Strip the photoresist*:** Expose the entire wafer in UV flood exposure system for 3 minutes and then remove the photoresist using 354 developer. To make sure no photoresist left on the wafer, rinse the wafer with acetone and isopropanol. Finally, dry the wafer with nitrogen.

20) ***Buffered oxide etching (BOE) of exposed silicon dioxide protection layer*:** Etching silicon dioxide for 2 minutes in BOE bath. Then rinse the wafers 5 times in a deionized water dump rinser.

21) ***Wafer cleaning*:** Piranha cleaning of the wafers in a 3:1 solution of sulphuric acid and hydrogen peroxide for 15 minutes. Rinse the wafers in a deionized water for 5 times after each cleaning step.

22) ***Low pressure chemical vapor deposition (LPCVD) of the top silicon nitride membrane layer*:** Deposition of 1 and 1.5 μm low-stress silicon nitride thick membranes with the parameters shown in Table C.I for multi-frequency and multi-gap multi-frequency CMUTs, respectively. The required time (hr:min:sec) for 1 and 1.5 μm silicon nitride deposition is 05:37:30 and 07:48:30, respectively.

23) ***Promoting the adhesion between the photoresist and the poly-silicon film*:** Coating the wafers with Hexamethyldisilizane (HMDS) using a Yield Engineering Systems (YES) Vapor tool, or equivalent, with a standardized recipe shown in Table C.IV.

24) ***Lithography mask 3 for multi-frequency and Lithography mask 4 for multi-gap multi-frequency CMUTs*:** Photoresist patterning of the sacrificial release holes with the recipe shown in Table C.VII. The average thickness of the resist is 3 μm.

TABLE C.VII. STANDARD HPR-506 PATTERNING RECIPE.

Spread	10 s @ 500 rpm
Spin	40 s @ 2000 rpm
Baking	90 s @ 115 ºC
Rehydration Time (min)	15
Exposure Time (s)	7.3
Developing Time in 354 (s)	35
Exposure Intensity (mJ/cm^2)	60

25) ***Reactive ion etching (RIE) of the 1.0 (multi-frequency) and 1.5 μm (multi-gap multi-frequency) silicon nitride membrane layer*:** Etching using the recipe shown in Table C.VIII with a Trion Technology RIE, or equivalent except the time is 470 and 650 seconds for multi-frequency and multi-gap multi-frequency CMUTs, respectively.

TABLE C.VIII. RIE OF SILICON NITRIDE RECIPE.

Pressure (mTorr)	150
CF_4 Flow Rate (sccm)	45
Oxygen (O_2) Flow Rate (sccm)	5
RF Power (W)	125
Time (s)	470*
* 650 seconds for etching 1.5 μm silicon nitride.	

26) ***Strip the photoresist*:** Expose the entire wafer in UV flood exposure system for 3 minutes and then remove the photoresist using 354 developer. To make sure no photoresist left on the wafer, rinse the wafer with acetone and isopropanol. Finally, dry the wafer with nitrogen.

27) ***Potassium hydroxide (KOH) chemical etching of poly-silicon sacrificial layers*****:** Etch the exposed poly-silicon layers in a heated 32% KOH solution mixed with deionized water. Mix 970 ml potassium hydroxide with 570 ml deionized water in KOH bath. Heat the solution to 90 ºC and stir using a magnetic stirring rod with the speed of 60 rpm. Etch the wafers for 30 and 150 minutes in the heated KOH solution to ensure complete releasing of the membranes for multi-frequency and multi-gap multi-frequency CMUTs, respectively. Rinse the wafers in three large containers of deionized water to remove any remaining KOH.

28) ***Critical point drying (CPD)*****:** After completing the KOH and rinsing the wafers three times in deionized water, transfer the wafers into a container of high purity isopropanol. Filling the chamber with high purity isopropanol before transferring the wafers quickly for CPD of the membranes using a Tousimis AutoSamdri 815B, or equivalent.

29) ***Plasma enhanced chemical vapor deposition (PECVD) of silicon dioxide to seal the sacrificial release holes*****:** 1.6 and 2.5 µm silicon dioxide deposition using the parameters shown in Table C.II with a Trion Technology PECVD for multi-frequency and multi-gap multi-frequency CMUTs, respectively.

30) ***Promoting the adhesion between the photoresist and the poly-silicon film*****:** Coating the wafers with Hexamethyldisilizane (HMDS) using a Yield Engineering Systems (YES) Vapor tool, or equivalent, with a standardized recipe shown in Table C.IV.

31) ***Lithography mask 4 for multi-frequency and Lithography mask 5 for multi-gap multi-frequency CMUTs*****:** Photoresist patterning of the sacrificial release plugs with the recipe shown in Table C.VII. The average thickness of the resist is 3 µm.

32) ***Reactive ion etching (RIE) of the 1.6 (multi-frequency) and 2.5 µm (multi-gap multi-frequency) silicon dioxide plug layer*****:** Etching using the recipe shown in Table C.IX with an Oxford PlasmaPro NGP80 RIE, or equivalent.

Note**:** It is strongly recommended to split the etching time by 5 and rotate the wafer 90 degrees each time manually to reduce the etching non-uniformity across the wafer. For example, for etching 2.5 µm of silicon dioxide, etch the SiO_2 layer in the format of 7.5 minutes and each time rotate the wafer by 90 degrees. Similarly, for etching the 1.6 µm of silicon dioxide, etch the SiO_2 layer in the format of four times of 5 minutes. Remained SiO_2 thickness for next step (BOE) is around 500 nm.

TABLE C.IX. RIE OF SILICON DIOXIDE RECIPE.

<table>
<tr><td colspan="2">Pressure (mTorr)</td><td>70</td></tr>
<tr><td colspan="2">CHF_3 Flow Rate (sccm)</td><td>50</td></tr>
<tr><td colspan="2">SF_6 Flow Rate (sccm)</td><td>10</td></tr>
<tr><td colspan="2">Ar Flow Rate (sccm)</td><td>25</td></tr>
<tr><td rowspan="2">Helium Backing</td><td>Pressure (Torr)</td><td>10</td></tr>
<tr><td>Flow Rate (sccm)</td><td>3.6</td></tr>
<tr><td colspan="2">Time (min)</td><td>20*</td></tr>
<tr><td colspan="3">* 37.5 minutes for etching 2.5 µm silicon nitride.</td></tr>
</table>

33) ***Buffered oxide etching (BOE) of the remained exposed silicon dioxide layer*:** Etching the remaining silicon dioxide for 12 and 18 minutes in BOE bath for multi-frequency and multi-gap multi-frequency CMUTs, respectively. Then rinse the wafers 5 times in a deionized water dump rinser.

34) ***Strip the photoresist*:** Expose the entire wafer in UV flood exposure system for 3 minutes and then remove the photoresist using 354 developer. To make sure no photoresist left on the wafer, rinse the wafer with acetone and isopropanol. Finally, dry the wafer with nitrogen.

35) ***Promoting the adhesion between the photoresist and the poly-silicon film*:** Coating the wafers with Hexamethyldisilizane (HMDS) using a Yield Engineering Systems (YES) Vapor tool, or equivalent, with a standardized recipe shown in Table C.IV.

36) ***Lithography mask 5 for multi-frequency and Lithography mask 6 for multi-gap multi-frequency CMUTs*:** Photoresist patterning of the bottom electrode openings with the recipe shown in Table C.VII. The average thickness of the resist is 3 µm.

37) ***Reactive ion etching (RIE) of the 1.25 (multi-frequency) and 1.75 µm (multi-gap multi-frequency) silicon nitride layers to reach the bottom silicon substrate*:** Etching using the recipe shown in Table C.VIII with a Trion Technology RIE, or equivalent except the time is 620 and 700 seconds for multi-frequency and multi-gap multi-frequency CMUTs, respectively.

Note: To make sure all the nitride is gone in bottom electrode areas, the considered etching time is more than calculated time for etching the entire nitride layers.

38) ***Strip the photoresist*:** Expose the entire wafer in UV flood exposure system for 3 minutes and then remove the photoresist using 354 developer. To make sure no photoresist left on the wafer, rinse the wafer with acetone and isopropanol. Finally, dry the wafer with nitrogen.

39) ***Wafer Cleaning and Quick BOE*:** Piranha cleaning of the wafers in a 3:1 solution of sulphuric acid and hydrogen peroxide for 15 minutes and then buffered oxide etching (BOE) to remove the native oxide on the bottom electrode areas for 30 seconds. Rinse the wafers in a deionized water for 5 times after each cleaning step.

40) ***Sputtering deposition of the aluminum electrodes*:** Sputtering of 400 nm aluminum using the recipe shown in Table C.X with a load-locked, computer-controlled, planar magnetron sputter system with four sputter guns and RF etch back, or equivalent.

TABLE C.X. RIE OF SILICON NITRIDE RECIPE.

Pressure (mTorr)	7
Argon Flow rate (sccm)	10.5
RF Power (W)	300
Time (s)	2400

41) ***Annealing the sputtered aluminum film*:** Annealing the sputtered 400 nm aluminum layer at 200 ºC for 3 hours using a Yamato DNF400 oven, or equivalent.

42) ***Lithography mask 6 for multi-frequency and Lithography mask 7 for multi-gap multi-frequency CMUTs*:** Photoresist patterning of the aluminum electrode layer with the recipe shown in Table C.V. The average thickness of the resist is 1.2 – 1.3 μm.

43) ***Wet aluminum etching in a solution of AD Aluminum Etch*:** Semiconductor Grade (Fugifilm Puretch #881772) for 26-27 minutes. Following the aluminum etch rinse the wafers 5 times in a deionized water dump rinser.

44) ***Strip the photoresist*:** Expose the entire wafer in UV flood exposure system for 3 minutes and then remove the photoresist using 354 developer. To make sure no photoresist left on the wafer, rinse the wafer with acetone and isopropanol. Finally, dry the wafer with nitrogen.

45) ***Characterization, Dicing, and Bonding*****:** Now the wafers are ready for wafer level characterization. The wafer is then diced into CMUT arrays and diced arrays are wire-bonded to custom PCB designs for ultrasound imaging and therapeutic applications.